High-Nuclearity Lanthanide(III) Complexes as Single-Molecule Magnets and Luminescent Materials

Eleni C. Mazarakioti

A thesis submitted to the Department of Chemistry in partial fulfillment of the

requirements for the Degree of Doctor of Philosophy

Supervised by

Professor Theocharis C. Stamatatos

Brock University

St. Catharines Ontario, Canada

April 2017

Abstract

The employment of the bridging/chelating Schiff base ligands, *N*-salicylidene-*o*-aminophenol ($saphH_2$), *N*-salicylidene-*o*-aminocyclohexanol ($sachH_2$) and *N*-salicylidene-2-amino-5-chlorobenzoic acid ($sacbH_2$), in lanthanide (Ln^{III}) cluster chemistry has afforded four families of polynuclear and dinuclear complexes with new structural motifs, and interesting magnetic and optical properties.

Chapter 1 deals with most of the fundamental aspects within the areas of polynuclear metal complexes, molecular magnetism and optics as these are applied to 4*f*-metal based systems, while the research results are reported in Chapters 2, 3 and 4. In the first project (Chapter 2), the coordination chemistry of the organic chelating/bridging ligand, *N*-salicylidene-*o*-aminophenol ($saphH_2$) in lanthanide cluster chemistry was investigated. The general Ln^{III}/X^{-} /$saphH_2$/base reaction system has led to a family of $(NHEt_3)[Ln_7(OH)_2(saph)_{10}(Me_2CO)_2]$ (Ln = Gd (**1**); Tb (**2**); Dy (**3**)) clusters with a new core topology that comprises two $\{Ln_4\}$ butterflies sharing a common metal vertex. The $\{Dy^{III}_7\}$ analogue exhibits slow magnetization relaxation, whereas all heptanuclear compounds show ligand-centered blue-green emissions.

The second project of this thesis, which is discussed in Chapter 3, comprises the first use of the Schiff base ligand *N*-salicylidene-2-aminocyclohexanol ($sachH_2$; mixture of *cis*- and *trans*-analogue) in metal cluster chemistry which has afforded a new family of $[Ln_7(OH)_6(CO_3)_3(sach)_3(sachH)_3(MeOH)_6]$ (Ln = Gd (**4**); Tb (**5**); Dy (**6**)) clusters with ideal D_{3h} point group symmetry and metal-centered trigonal prismatic topology. Solid-state and solution studies revealed single-molecule magnetism (SMM) and photoluminescence behaviors. Moreover, in order to investigate the steric and stereoisomerism effects of the ligand on the chemical and structural identity of the $\{Ln_7\}$ clusters, the pure *trans*-analogue of the $sachH_2$

ligand was utilized. As a result, a new family of octanuclear $[Ln_8(OH)_4(CO_3)_2(trans\text{-}sach)_8(EtOH)_4]$ (Ln = Gd (**7**); Tb (**8**); Dy (**9**); Eu (**10**)) clusters were obtained, while the solid-state studies revealed SMM behavior and lanthanide-centered emissions.

In the last chapter of this thesis (Chapter 4), the Schiff base ligand *N*-salicylidene-2-amino-5-chlorobenzoic acid ($sacbH_2$) was introduced for a first time in lanthanide cluster chemistry. This has afforded a family of dinuclear $[Ln_2(NO_3)_4(sacbH)_2(H_2O)_2(MeCN)_2]$ compounds (Ln = Gd (**11**); Tb (**12**); Dy (**13**)) with the Dy-analogue exhibiting SMM behaviour with a high-energy barrier for the magnetization reversal and interesting magnetization dynamics.

All research-based Chapters (Chapters 2-4) are divided into subsections in order to facilitate the understanding of the research concepts by the familiar and non-familiar readers and contextualize the messages, goals and conclusions of each individual project. I felt it prudent to always begin with a short preface of the work that summarizes the most important aspects of the specific project, followed by the complete experimental part and discussion of the results, and finishing up with conclusions and some future perspectives.

Acknowledgements

First and foremost, I would like to express my immense appreciation and thanks to my supervisor Professor Theocharis C. Stamatatos. It has been an honor to be one of his first PhD students of his academic career. He has taught me how to think as a chemist and behave as a professional scientist. Words cannot express how much I appreciate his time, his continuous support and his patience throughout these four difficult years for me. His love and enthusiasm for his research has encouraged and motivated me even during the toughest times of my PhD studies. You have been the best supervisor, mentor, and human! Besides my supervisor I would also like to thank the rest of my thesis advisory committee: Professor Melanie Pilkington and Professor Paul Zelisko. They have generously offered me valuable comments towards improving my work; their insightful comments at different stages of my research are much appreciated.

I would also like to thank our research collaborators for their valuable contributions to the successful completion of the present thesis. In particular, my sincere thanks go to Dr. Luís Cunha-Silva and Dr. Simon J. Teat for solving and refining the structures of all the reported complexes. Furthermore, I am grateful to Professor George Christou and all his group members, Professor Wolfgang Wernsdorfer and Professor Jinkui Tang who acquired the magnetic data of all synthesized compounds, as well as Dr. Vlasoula Bekiari who performed some of the solid-state photoluminescence studies from selected compounds. My sincere thanks also goes to Professor Albert Escuer who provided me with an opportunity to join his research team as an intern, allowing me access to the laboratory and research facilities at University of Barcelona for five months. His knowledge on molecular magnetism has helped me to further support my

studies. I am also grateful to Professor Pilkington and her graduate student, Mr. Jeffery Regier, for performing theoretical calculations on the $\{Dy^{III}_2\}$ compound.

I would also like to thank my fellow labmates for being there through the good and bad moments the four years. A special thanks to my labmate Alysha Alaimo for being my personal English teacher all these years!

Finally, I would like to thank the Ontario Trillium Foundation and Brock University for the financial support of my PhD research over the last 4 years.

Last but not least, I would like to thank from the bottom of my heart all of my Greek best friends and my family: my parents, Christos and Eleftheria, and my sister, Andriana, for supporting me spiritually throughout my studies and my life in general. They were always standing by me even from far away, from my lovely country Greece.

Table of Contents

Chapter 1: **Introduction**

Chapter 2: **New structural topologies in 4*f*-metal cluster chemistry from vertex-sharing butterfly units: {Ln_7} complexes exhibiting slow magnetization relaxation and ligand-centered emissions**

Chapter 3: **First use of the Schiff base ligand *N*-salicylidene-2-aminocyclohexanol in metal cluster chemistry: {Ln_7} and {Ln_8} complexes with novel structures, and SMM and photoluminescence behaviors**

Chapter 4: **A family of {Ln_2} complexes with spherical tricapped trigonal prismatic Ln^{III} ions bearing the Schiff base ligand *N*-salicylidene-2-amino-5-chlorobenzoic acid: Large energy barrier and magnetization hysteresis at 5 K for the {Dy_2} analogue**

List of Schemes

List of Figures

List of Tables

List of Publications

Chapter 2

E. C. Mazarakioti, L. Cunha-Silva, V. Bekiari, A. Escuer and Th. C. Stamatatos. "New structural topologies in 4*f*-metal cluster chemistry from vertex-sharing butterfly units: $\{Ln^{III}_7\}$ complexes exhibiting slow magnetization relaxation and ligand-centred emissions", *RSC Advances*, *5*, 92534, **2015**.

Chapter 3

E. C. Mazarakioti, K. M. Poole, L. Cunha-Silva, G. Christou and Th. C. Stamatatos. "A new family of Ln_7 clusters with an ideal D_{3h} metal-centered trigonal prismatic geometry, and SMM and photoluminescence behaviors", *Dalton Transactions*, *43*, 11456, **2014**.

Chapter 4

E. C. Mazarakioti, J. Regier, L. Cunha-Silva, W. Wernsdorfer, M. Pilkington, J. Tang and Th. C. Stamatatos. "Large energy barrier and magnetization hysteresis at 5 K for a symmetric $\{Dy_2\}$ complex with spherical tricapped trigonal prismatic Dy^{III} ions", *Inorganic Chemistry*, **2017**, in press.

List of Abbreviations

Å	Angstrom
ac	alternating current
C	Curie constant
CH_2Cl_2	Dichloromethane
$CHCl_3$	Chloroform
CShM	Continuous Shape Measurement
cm^{-1}	Wavenumbers
D	Zero-field splitting parameter
dc	direct current
DMSO	Dimethylsulfoxide
ESI-MS	Electrospray Ionization Mass Spectroscopy
ET	Energy Transfer
EtOH	Ethanol
F	Fluorescence Emission
g	Landé factor
H	Magnetic field
$\hat{H}$	Heisenberg spin-Hamiltonian
HSAB	Hard Soft Acid Base
Hz	Hertz
IR	Infrared
IC	Internal Conversion
ISC	Intersystem Crossing

IVR	Internal Vibrational Relaxation
K	Boltzmann's constant
K	Kelvin
L	Ligand
$\boldsymbol{l}$	Orbital Angular Momentum
$\boldsymbol{L}$	Total Orbital Angular Momentum
$\boldsymbol{LS}$	Russell-Saunders Coupling
Ln	Lanthanide
M	Metal
M	Magnetization
Me	Methyl group
MeCN	Acetonitrile
MeOH	Methanol
Me_2CO	Acetone
N_3^-	Azide anion
NEt_3	Triethylamine
NIR	Near Infrared
nm	Nanometer
NMR	Nuclear Magnetic Resonance
N_A	Avogadro's number
o	Ortho position
Ph	Phenyl group
P	Phosphorescence Emission

QTM	Quantum tunneling of magnetization
S	Ground-state spin
$\boldsymbol{S}$	Total Spin Angular Momentum
$\boldsymbol{s}$	Spin Angular Momentum
$S_{0,1,2}$	Singlet states
sacbH_2	*N*-salicylidene-2-amino-5-chlorobenzoic acid
sachH_2	*N*-salicylidene-*o*-aminocyclohexanol
saphH_2	*N*-salicylidene-*o*-aminophenol
SMM	Single-molecule magnet
SOC	Spin-Orbit Coupling
SQUID	Superconducting quantum interference device
T	Temperature
T	Tesla
TA-QTM	Thermally-assisted quantum tunneling of magnetization
$T_{1,2,3}$	Triplet states
T_B	Blocking temperature
T_C	Curie temperature
THF	Tetrahydrofuran
T_N	Néel temperature
U	Energy barrier for magnetization reversal
UV	Ultraviolet
Vis	Visible
η^1, η^2, η^3	Coordination modes of ligands

θ	Weiss constant
μ, μ_3, μ_4	Bridging modes of ligands
μ_B	Bohr magneton
ν	stretching frequency
π	Pi-orbital
σ	Sigma-orbital
τ	relaxation time
τ_0	pre-exponential factor
χ	Magnetic susceptibility
χ'	real or in-phase susceptibility
χ''	imaginary or out-of-phase susceptibility
ω	angular frequency

Chapter 1

Introduction

1.1 *Introduction to Lanthanides*

The series of lanthanides (Ln) consists of fifteen 4*f*-block elements from $_{57}$La to $_{71}$Lu in the sixth period of periodic table. In 1787, a black mineral, today known as Gadolinite, was discovered by Carl Axel Arrhenius in Ytterby, Sweden. Initially, the "earth" (oxide) yttria (Y_2O_3) was successfully isolated by Johann Gadolin in 1794. During the following years scientists isolated more lanthanide oxides while Henry Moseley analyzed the X-ray spectra of 15 elements confirming the existence of the lanthanides. Although lanthanides were first classified as "rare earth elements" (including $_{21}$Sc and $_{39}$Y) because of the rare minerals used to extract them, their abundance in earth's crust is unlimited.[1] In 1885, lanthanides were introduced in industry by Carl Auer Welsbach. Since then, 4*f* elements have been widely used in various applications such as optics, optical fiber telecommunications, magnets, biomedical applications and catalysis (Table 1.1).[2] Currently, China dominates in the lanthanide global market producing the largest amounts of rare earth elements. The following graphic (Figure 1.1) depicts the world's mine production and reserves for 2015-2016 (estimated percentages).[3,4]

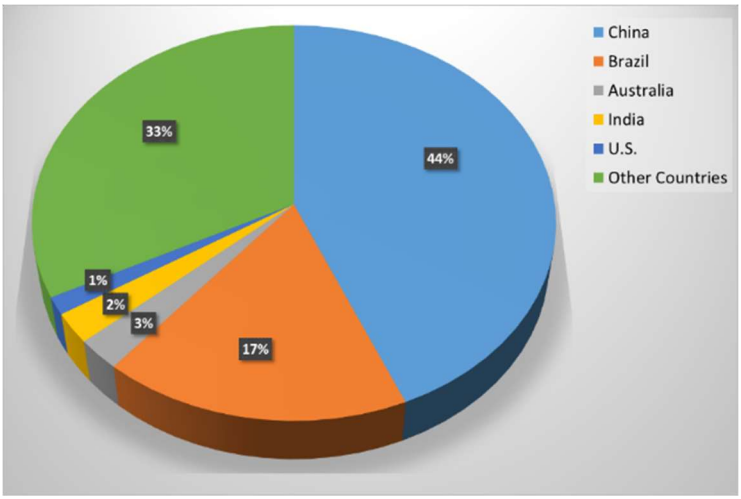

Figure 1.1. Rare earth reserves by country for 2015-2016 using data from *statista.com*.[4]

Table 1.1. Common applications of lanthanide elements in industry.[5]

Name of the Element	***Symbol***	***Application***
Lanthanum	**La**	Visualization of images in medicine, optical and magnetic detection, ceramics, glasses, crystal scintillators
Cerium	**Ce**	Phosphors
Praseodymium	**Pr**	Phosphors, ceramics, nuclear industry
Neodymium	**Nd**	Ceramics, lasers, nuclear industry
Promethium	**Pm**	Ceramics, dyes for glass, optical fibers, lasers, nuclear industry
Samarium	**Sm**	Electron bean tubes, visualization of images in medicine
Europium	**Eu**	Metallurgy, chemical industry
Gadolinium	**Gd**	Single crystal scintillators
Terbium	**Tb**	Visualization of images in medicine, optical and magnetic detection, ceramics, glasses, crystal scintillators

Dysprosium	**Dy**	Phosphors
Holmium	**Ho**	Phosphors, ceramics, nuclear industry
Erbium	**Er**	Ceramics, lasers, nuclear industry
Thulium	**Tm**	Ceramics, dyes for glass, optical fibers, lasers, nuclear industry
Ytterbium	**Yb**	Electron beam tubes, visualization of images in medicine
Lutetium	**Lu**	Metallurgy, chemical industry

The 4*f*-orbitals are characterized by the quantum numbers $n = 4$, $l = 3$ and $m_l = +3, +2, +1, 0, -1, -2, -3$ and they are 7-fold degenerate.[6] Depending on their bonding environment, the two main ways that a set of 4*f*-orbitals can be presented are the cubic and general set. The 4*f*-orbitals penetrate the Xe core and are shielded by the fully occupied $5s^2$ and $5p^6$ orbitals (Figure 1.2). Due to the insufficient shielding of the 5*s* and 5*p* electrons, they contract as the effective nuclear charge increases. Consequently, along the lanthanide series, from the left to the right, both atomic and ionic radii steadily decrease; this effect is known as the lanthanide contraction (Figure 1.3).

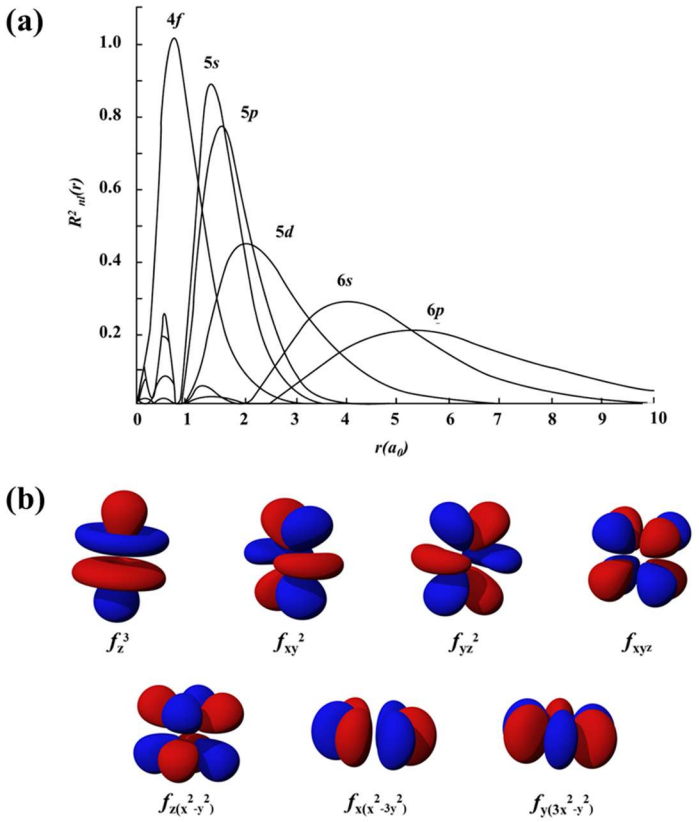

Figure 1.2. **(a)** Radial distribution functions of 4*f*, 5*s*, 5*p*, 5*d*, 6*s*, and 6*p* electrons for Ce. Reproduced from Ref. 6(b). **(b)** Cubic set representation of the 4*f*-orbitals. Adapted through Creative Common License (Public Domain) from Ref. 7.

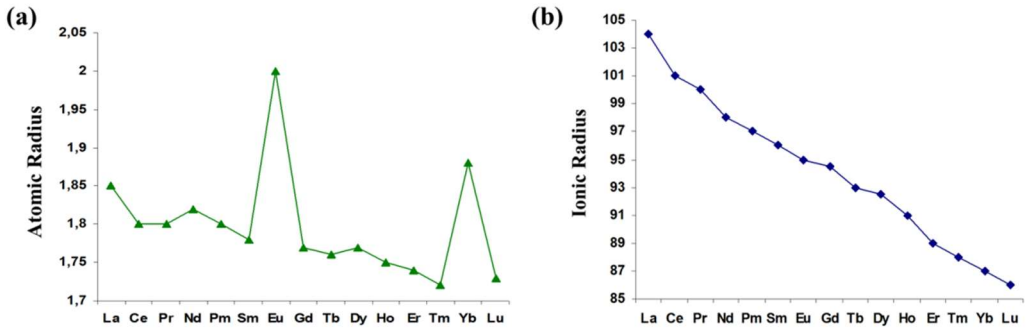

Figure 1.3. Trend of **(a)** atomic and **(b)** ionic radii of lanthanide elements in the 3+ oxidation state.

Along the series of lanthanides, electrons are progressively added in the 4*f*-orbitals with concomitant increase of the atomic number of the elements. This filling of their nuclei with protons leads to the steady increase of the attraction to the poorly protected 4*f* electrons. As a consequence, the 4*f*-orbitals are more stable than the 5*s*. Thus, in general, the ground state electronic configurations of lanthanides are depicted as $[Xe]4f^n6s^2$ ($1 \leq n \leq 14$). However, La, Ce, and Gd adopt the $[Xe]4f^{n-1}5d^16s^2$ configuration due to its lower energy than the former one (Table 1.2). All lanthanides tend to lose three electrons from their outer shells adopting a very stable 3+ oxidation state. Diverse oxidation states can also exist for some lanthanides (Table 1.2). Hund's rule states that empty, half-full, and full electron shells are more stable. Therefore, Ce^{3+} and Tb^{3+} can relatively easily lose one electron and be oxidized to the 4+ oxidation state. Similarly, Eu^{3+} and Yb^{3+} can gain one electron adopting a more stable electronic configuration in the 2+ oxidation state. The general trends of the lanthanides' ionization energies further support all the above (Figure 1.4).[1]

Table 1.2. Electronic properties of lanthanide elements.[a]

Element	***Z***	***Electronic Configuration***		***Common Oxidation States***
		Ln	***Ln^{3+}***	
La	57	$[Xe]4f^05d^16s^2$	$[Xe]4f^0$	3+
Ce	58	$[Xe]4f^15d^16s^2$	$[Xe]4f^1$	3+, 4+
Pr	59	$[Xe]4f^36s^2$	$[Xe]4f^2$	3+, (4+)
Nd	60	$[Xe]4f^46s^2$	$[Xe]4f^3$	3+
Pm	61	$[Xe]4f^56s^2$	$[Xe]4f^4$	3+

Sm	62	[Xe]$4f^6 6s^2$	[Xe]$4f^5$	(2+), 3+
Eu	63	[Xe]$4f^7 6s^2$	[Xe]$4f^6$	2+, 3+
Gd	64	[Xe]$4f^7 5d^1 6s^2$	[Xe]$4f^7$	3+
Tb	65	[Xe]$4f^9 6s^2$	[Xe]$4f^8$	3+, (4+)
Dy	66	[Xe]$4f^{10} 6s^2$	[Xe]$4f^9$	3+
Ho	67	[Xe]$4f^{11} 6s^2$	[Xe]$4f^{10}$	3+
Er	68	[Xe]$4f^{12} 6s^2$	[Xe]$4f^{11}$	3+
Tm	69	[Xe]$4f^{13} 6s^2$	[Xe]$4f^{12}$	3+
Yb	70	[Xe]$4f^{14} 6s^2$	[Xe]$4f^{13}$	2+, 3+
Lu	71	[Xe]$4f^{14} 5d^1 6s^2$	[Xe]$4f^{14}$	3+

[a] The less common oxidation states are shown in parentheses.

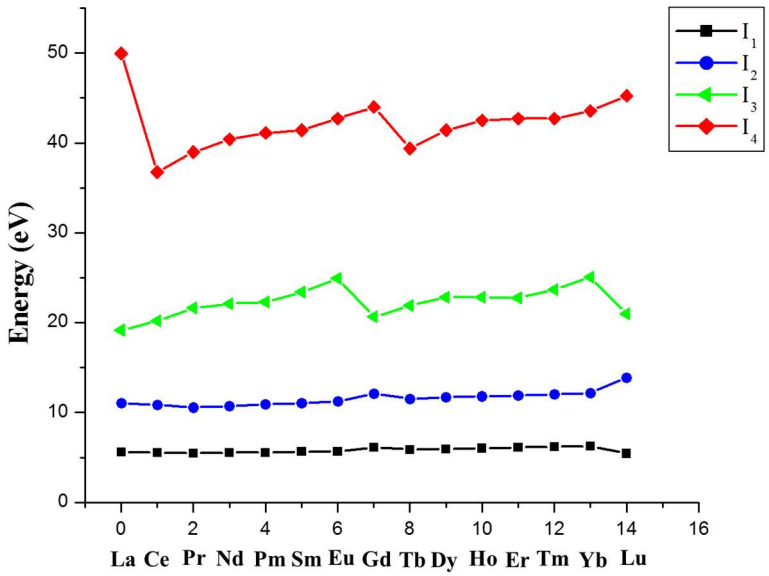

Figure 1.4. Trend of the first four ionization energies ($I_{1\rightarrow4}$) for the lanthanide elements. Reproduced from Ref. 8.

According to Hard Soft Acid Base (HSAB) theorem, Ln^{III} are hard acids and thus they form strong bonds with elements that belong to hard bases (*i.e.*, O). The nature of the bonds between Ln^{III} and a hard base atom exhibit a polar covalent behavior due to the inner character of the 4*f*-orbitals. As a result, the orbitals of lanthanides are unable to overlap with the orbital(s) of the donor atom(s). Consequently, the chemical and physical properties of 4*f*-based complexes are considered to often originate purely from the lanthanide ions.

Generally, the interactions between electrons in a multielectronic system must be considered. It is well known that an electron in an atom is characterized by the spin around its own axis known as *spin angular momentum*, ***s***. Moreover, the orbitals motion in an atom gives rise to the *orbital angular momentum*, ***l***. Consequently, in a polyelectronic atom the coupling of the spins of individual electrons results in the *spin quantum number* ***S*** and similarly the coupling of individual angular momenta results in the *total orbital angular momentum*, ***L***. The Russell-Saunders coupling scheme, or *LS* coupling, is an approximation to determine the interaction between the total spin angular momentum, ***S***, and the total angular orbital momentum, ***L*** (Figure 1.5). This type of interaction, known as *spin-orbit coupling* (SOC), affords the *total angular momentum quantum number*, ***J***, which is given by the vector sum of ***S*** and ***L*** and takes values between $\boldsymbol{L}+\boldsymbol{S}$, …, $|\boldsymbol{L}-\boldsymbol{S}|$.

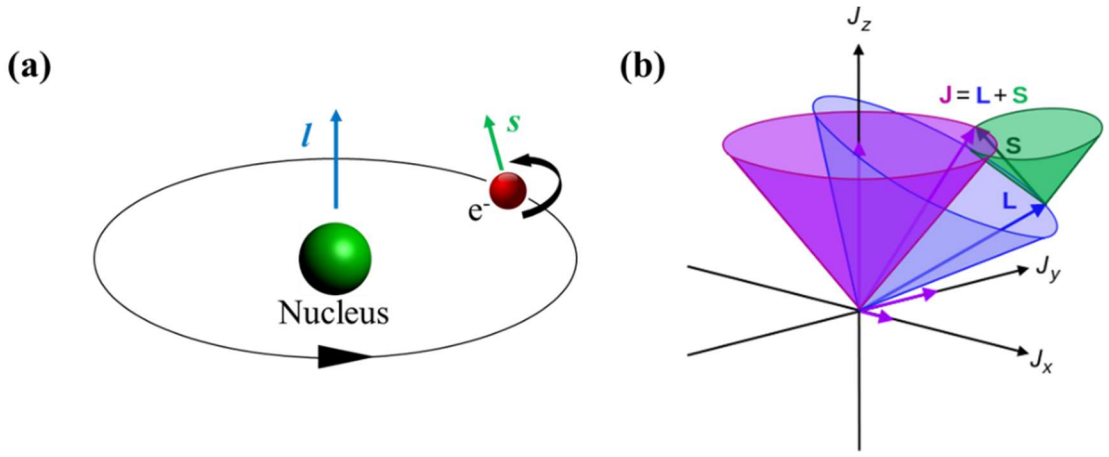

Figure 1.5. Graphical representation of **(a)** spin angular momentum (***s*****,** green) and orbital angular momentum (***l***, blue) in an one-electron system. **(b)** Russell-Saunders (*LS*) coupling scheme for a polyelectronic atom: the summation of ***S*** and ***L*** results the overall angular momentum (***J***, purple). Adapted through Creative Commons License (Public Domain).[9]

In the case of 4*f*-electron systems, the SOC dominates over the interelectronic repulsions yielding the electronic terms $^{(2S+1)}$L which are further split into multiplet $^{(2S+1)}L_J$ states. By applying Hund's rules, the ground-state multiplet term symbol of a lanthanide ion can be determined. According to these rules the ground state is characterized by the highest spin multiplicity (2*S*+1) and the largest *L* value. In addition, *J* takes the lowest value when the shell is less than half-filled and the highest value when the shell is more than half-filled.[10] The SOC within a given *LS* multiplet term is expressed as a function of the ***L*** and ***S***, as shown in the following Hamiltonian (Eqn. 1.1),

$$H_{SO} = \lambda \boldsymbol{L} \cdot \boldsymbol{S} \qquad \textbf{Eqn. 1.1}$$

where λ is the spin-orbit coupling parameter derived from the spin-orbit coupling constant of the free-ion, ζ, and the spin multiplicity, *S* (Eqn. 1.2). The single electron spin-orbit coupling constant, ζ, is a positive quantity.[6b] The positive sign in Eqn. 1.2 corresponds to a shell that is

less than half-filled and the negative sign to a shell more than half-filled if the hole formalism is assumed.[6b] According to Benelli and Gatteschi, the negative sign has the effect of placing the state with the highest *J* at the lowest energy level with an inversion of the splitting with respect to the less than half-filled shell.[6b] The spin-orbit coupling constants, ζ, for Ln^{3+} ions increase on passing from the lighter to the heavier elements in the same row. The lanthanide ions, especially the late lanthanides ($4f^n$, $n > 7$), demonstrate strong spin-orbital coupling interactions, mainly due to their higher effective nuclear charge and the screening effects of outer $5d$ and $6s$ electrons. For a given multiplet the energy is given by Eqn. 1.3a. In addition, the energy difference between two states with quantum numbers *J* and *J*+1 is given by Eqn. 1.3b.

$$\lambda = \pm\frac{\zeta}{2S} \qquad \textbf{Eqn. 1.2}$$

$$E_J = \frac{1}{2}\,\lambda\,[J(J+1) - L(L+1) - S(S+1)] \qquad \textbf{Eqn. 1.3a}$$

$$\Delta E_{J,J+1} = \lambda(J+1) \qquad \textbf{Eqn. 1.3b}$$

Due to their large ionic radii, Ln^{III} ions can adopt various coordination numbers (3-12) with the most common being 8 and 9. The steric properties of the ligands highly affect the geometry of the coordination polyhedra around the lanthanide atom. For this reason, bulky ligands such as bis(trimethylsilyl)amine result in small coordination numbers whereas large coordination numbers can be adapted by using smaller bidentate and/or macrocyclic ligands.[1d] In order to determine the coordination polyhedron, which is defined by the number of the donor atoms around a lanthanide atom, the *continuous symmetry method* is used.[11] This method compares the edges of the ideal polyhedron with those experimentally determined.

The general chemistry and fundamental rules of lanthanide elements have been briefly discussed. In the following sections the coordination chemistry, magnetic and photoluminescence properties of lanthanides will be described in more detail.

1.2 ***Polynuclear 4f-Metal Complexes - Synthetic Routes***

In 1893, Alfred Werner described a novel class of compounds named coordination compounds, and subsequently created the field of coordination chemistry. He proposed that a coordination compound consists of a central transition metal ion surrounded by ligands. Due to his work on this new area of research he won the Nobel Prize in Chemistry in 1913 and is considered as the "father" of coordination chemistry.[12] Since then, coordination chemistry has been further developed and has been oriented towards the synthesis of molecular species with large number of metal ions. These species are well-known as polynuclear metal complexes or "coordination clusters"[13] or simply "clusters".[14] They can be described by the general formula $[M_x(L)_y(L')_z]^n$, where "x" is an integer number larger than or equal to three, "y" and "z" are also integer numbers, and "*n*" can be any integer number, including zero; if "*n*" is negative, the cluster compound is anionic, if it is positive the complex is cationic, and if it is zero the complex is neutral.[15] These zero-dimensional molecular species generally consist of a large number of metal ions (M^{n+}; "n" varies) and various bridging and terminal ligands that will aggregate the metal ions by increasing the overall nuclearity of the compound and simultaneously block the extensive polymerization, which would otherwise lead to multidimensional coordination polymers. Particularly important for the synthesis of a thermodynamically stable cluster compound is the choice of the bridging and/or terminal chelating and/or non-chelating ligands.

Based on the HSAB principle, the isolation of stable polynuclear clusters may result from the combination of metals ions in moderate-to-high oxidation states, which are considered as relatively hard acids, with moderate-to-hard bases as ligands. The classification of the latter type of ligands results from the nature of their donor atoms (*i.e.*, O, N). The type of donor atoms also affects the physical properties of the resulting complexes as will be discussed later in this thesis.

A plethora of polynuclear metal complexes have been reported especially since the development of single-crystal X-ray crystallography which is the main tool for their structural elucidation. These molecular species have diverse nuclearities, geometries and sizes reaching up to nanoscale dimensions.[16] The synthesis of polynuclear metal clusters is not limited to their aesthetically beautiful structures, but they also have numerous potential applications. Molecular materials are shown to exhibit interesting physicochemical properties (magnetic, optical, catalytic, etc.) combining macroscopic properties at the molecular level. Monodispersity, crystallinity, solubility, and mild synthetic conditions are some of the most important advantages of molecular materials as opposed to traditional, bulk materials, which are synthesized under high temperatures and pressures, thus rendering their uniform shape and size an extremely difficult synthetic task. The Nobel Prize in Chemistry for 2016 confirms the importance of this field as it was awarded for the *design and synthesis of molecule-based machines*.[17]

Transition metal cluster chemistry is the most explored and developed field of coordination chemistry and has afforded a large number of high-nuclearity complexes with various metal topologies and nanoscale dimensions. Figure 1.6 depicts a representative example of a high-nuclearity 3*d*-metal cluster comprising 84 Mn^{III} ions that are bridged by oxido, alkoxido and carboxylate groups to yield a "wheel"-like metal arrangement.[18] On the other hand, 4*f*-metal cluster chemistry has been developed only in the last two decades or so.[19] The record

nuclearity of a lanthanide cluster is shared between the $\{Gd^{III}_{104}\}$ reported by Zheng and coworkers in 2014 (Figure 1.7),[20] and a $\{Dy^{III}_{104}\}$ reported by Gu and Xue in 2007 (Figure 1.8).[21] The molecular structure of the former is described as "Keplerate"-like, while the latter can be considered as a tetramer of linked $\{Dy^{III}_{26}\}$ clusters.

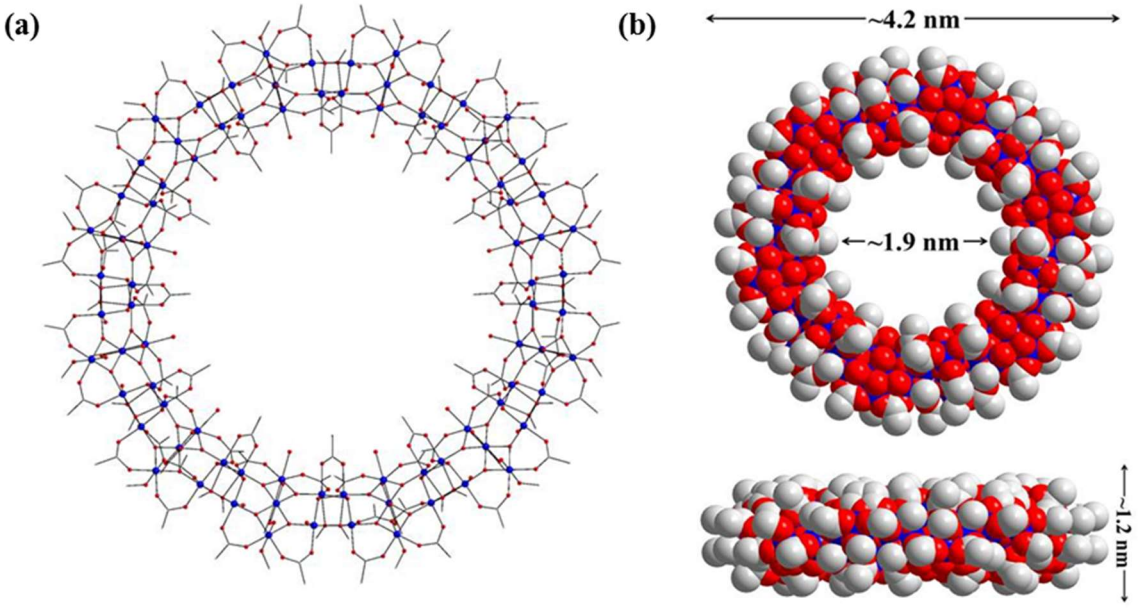

Figure 1.6. (a) Molecular structure of the $\{Mn^{III}_{84}\}$ torus-like cluster. **(b)** Space-filling representations of the $\{Mn^{III}_{84}\}$. The cluster possesses a diameter of about 4.2 nm and a thickness of about 1.2 nm, with a central hole of diameter 1.9 nm. H atoms are omitted for clarity. Colour scheme: Mn^{III}, blue; O, red; C, gray. Used with the permission of Wiley, from Ref. 18.

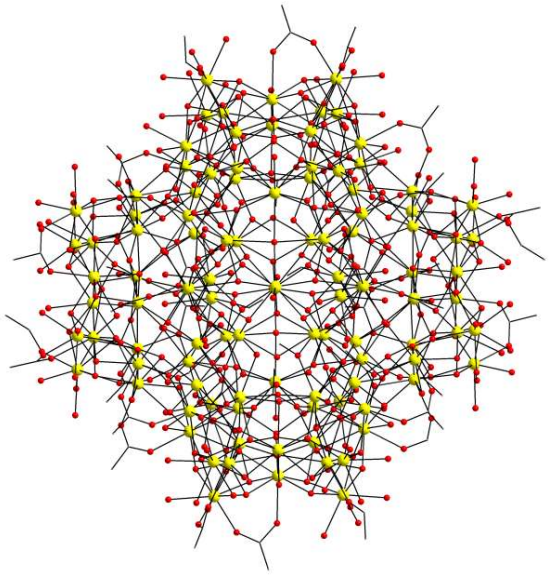

Figure 1.7. Molecular structure of the $\{Gd^{III}_{104}\}$. H atoms are omitted for clarity. Colour scheme: Gd^{III}, yellow; O, red; C, gray. Reproduced from Ref. 20.

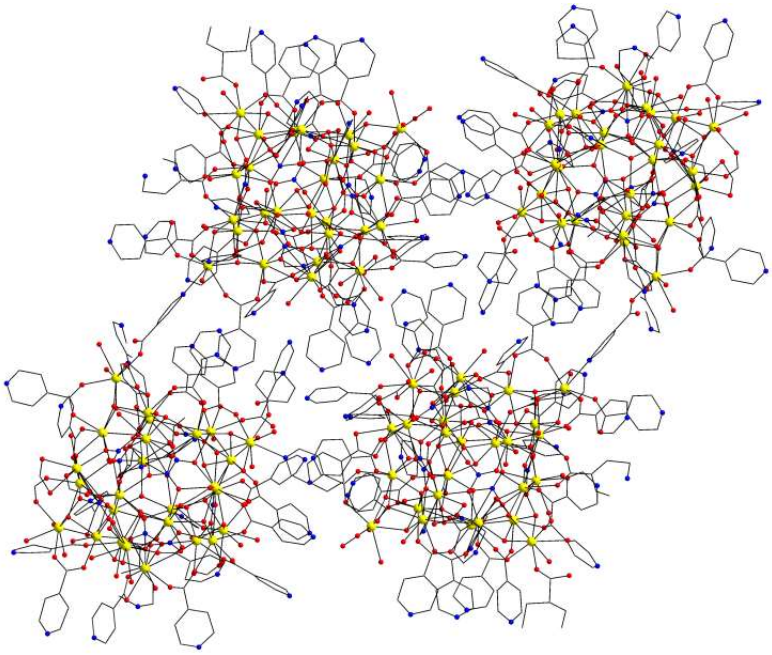

Figure 1.8. Structure of the $\{Dy^{III}_{104}\}$ cluster reported by Gu and Xue. H atoms are omitted for clarity. Colour scheme: Dy^{III}, yellow; N, blue; O, red; C, gray. Reproduced from Ref. 21.

Lanthanide coordination complexes have been shown to exhibit interesting physicochemical properties and consequently can be potentially employed as catalysts,[22] luminescent materials,[23] magnetic coolers,[20] and single-molecule magnets (SMMs).[24] In comparison to transition metal complexes, lanthanide clusters are fundamentally different. The inner character of the lanthanides' orbitals does not allow for the direct interaction of the 4*f*-orbitals of different metal centers with the orbitals of the ligands, as it is the case for 3*d*-metals. Lanthanide ions in non-organometallic complexes can accommodate diverse and high coordination numbers (7 to 12) due to their large size, with the energy differences between these numbers being small.[25] As a result, the synthesis of polynuclear 4*f*-metal clusters is often more challenging and difficult than that of 3*d*-metal cluster compounds. The use of Lewis-base organic ligands (i.e, O-containing ligands such as alkoxides and aryloxides) may be the first good step for the isolation of stable 4*f*-metal clusters due to the hard Lewis-acid character of the lanthanide ions. Moreover, the electronic and steric effects of the selected ligands and the type of bridging entities[26] that link the lanthanide ions can affect the size of the resulting complexes. These small and flexible ligands, such as oxido, hydroxido, halogenido and chalcogenido groups, are able -in most of the cases- to play a crucial role in the structural integrity, size and properties of the resulting coordination compounds. It is believed that these ligands foster the formation of the core unit of the cluster allowing for the peripheral ligands to complete the coordination spheres of the lanthanide ions, rendering possible the crystallization and isolation of these species in the solid state.[26-30]

A general synthetic strategy that is followed for the preparation of lanthanide clusters is based on the reaction between different lanthanide sources and the selected ligand(s), in the presence or absence of an external base. The addition of an external base may further support the

deprotonation of the OH-group(s) of the primary organic ligand, thus allowing the ligand to bind to more metal ions. The reactions can take place in a variety of solvents, or mixture of solvents, which could enhance the solubility of the precursors and improve the crystallinity of the resulting complexes. Consequently, a variety of different reactions can be performed, hopefully leading to interesting chemical reactivity studies with unpredictable yet, still exciting, results. To this end, it has been shown[19,26] that lanthanide complexes consisting of oxido and/or hydroxido bridging groups exhibit interesting luminescent,[27] magnetic,[28] and catalytic[22a] properties. Thus, the scientific interest in high-nuclearity lanthanide cluster chemistry is oriented towards the synthesis of compounds with as many oxido and/or hydroxido bridging groups as possible. Although these types of polynuclear 4*f*-metal clusters are almost always isolated from serendipitous synthetic approaches, two basic routes have been recently proposed.[29]

The first approach follows the hydrolytic process of anhydrous lanthanide sources which are sensitive in water, such as $LnCl_3$.[29] According to this synthetic method the ligand partially controls the hydrolysis of the metal starting material. This procedure is directly related with the ligand's ability to prevent the extensive polymerization of lanthanide salts. In 2000, Roesky and his group first followed the above method and they isolated tetradecanuclear clusters with the formula $[Ln_{14}(o\text{-}O_2NC_6H_4O)_{24}(\mu_4\text{-}OH)_2(\mu_3\text{-}OH)_{16}]$ (Ln = Dy, Er, Tm, Yb; Figure 1.9).[30] Scheme 1.1 depicts the synthetic route that was followed for the isolation of the $\{Ln^{III}_{14}\}$ complexes.[29] The authors used the ligand *o*-nitrophenolate to control both the hydrolysis of moisture-sensitive anhydrous lanthanide sources and the arrangement of lanthanide-oxido/hydroxide groups. The resulting compounds comprise an inorganic core that was described as a chain of three corner-sharing Ln octahedra, in which one corner of the two outer octahedra is missing. The metal ions

are linked through 18 hydroxido groups while peripheral ligation is provided by the *O*,*O*-chelating *o*-nitrophenolate ligands.[30]

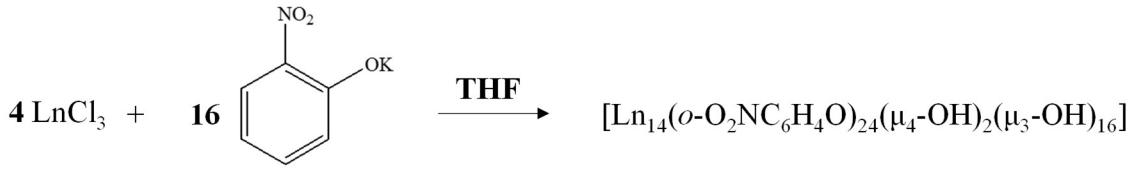

Scheme 1.1. Synthetic route for the isolation of the $\{Ln^{III}_{14}\}$ complexes. Reproduced from Ref. 29.

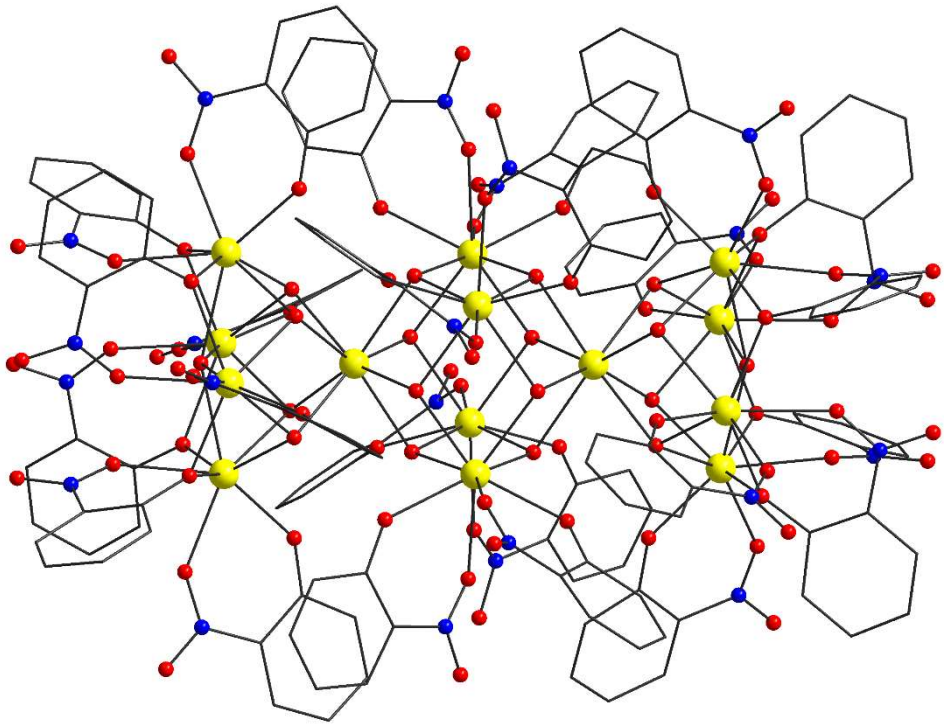

Figure 1.9. Structure of the $[Er_{14}(o\text{-}O_2NC_6H_4O)_{24}(\mu_4\text{-}OH)_2(\mu_3\text{-}OH)_{16}]$ cluster. Colour scheme: Er^{III}, yellow; O, red; N, blue; C, gray. Reproduced from Ref. 30.

In 1999, Zheng and coworkers also proposed a synthetic method for the synthesis of polynuclear lanthanide complexes which was based on the controlled deprotonation of the crystal water molecules on the lanthanide precursor (*i.e.*, $Ln(ClO_4)_3 \cdot xH_2O$).[31] The key in this synthetic approach was the ancillary ligand which should block the complete hydrolytic process of the lanthanide starting material. The authors reacted amino acids, as supporting ligands, with $Ln(ClO_4)_3 \cdot xH_2O$, and they were able to crystallize and structurally characterize a new pentadecanuclear compound (Figure 1.10). The cluster compound consisted of 15 lanthanide ions, 10 tyrosine ligands and hydroxido and aqua bridges originating from the hydrolysis of the lanthanide salt. The inorganic core of the complex was described as a "cubane-wheel".[31]

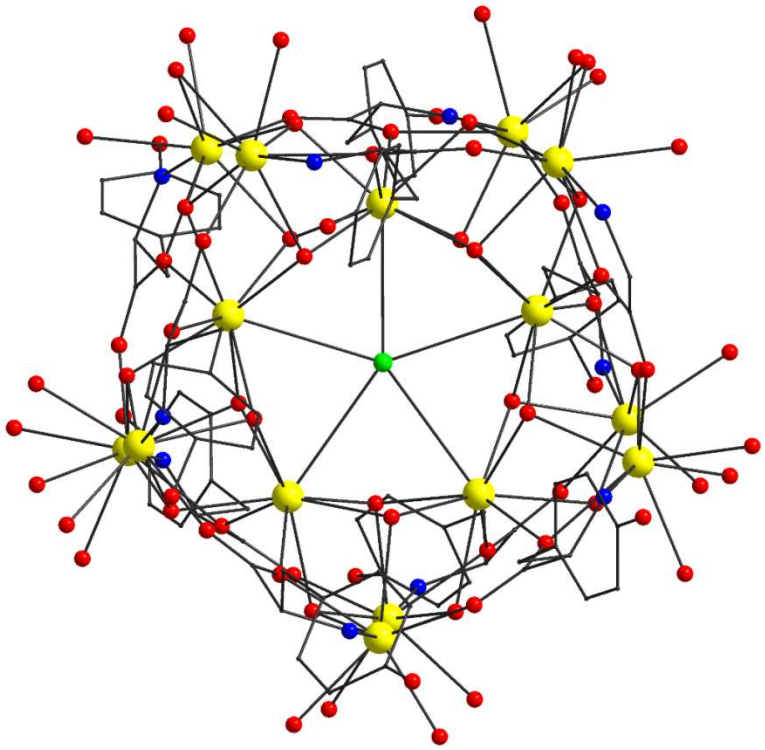

Figure 1.10. Structure of the $[Eu_{15}Cl(\mu_3\text{-}Tyr)_{10}(\mu_3\text{-}OH)_{20}(\mu_2\text{-}H_2O)_5(OH)_{12}(H_2O)_8]^{2+}$ cation. Colour scheme: Eu^{III}, yellow; Cl, green; O, red; N, blue; C, gray. Reproduced from Ref. 31.

1.3 *Aromatic Schiff Bases as Bridging/Chelating Ligands in Metal Cluster Chemistry*

The key for the synthesis of oligo- and polynuclear metal complexes in coordination chemistry is the selection of the organic ligand that bridges the metal centers. The physical properties (magnetic,[32] optical,[33] conductive,[34] catalytic,[35] etc.) and chemical identities of the resulting coordination compounds are affected by the nature, stereoconfiguration and electronic properties of the primary organic bridging/chelating ligand.[36] Depending on the type of donor atoms (i.e., N and/or O) that a ligand comprises, clusters with metal ions in high-to-moderate oxidation states (i.e., Ln^{III}, Mn^{III}, Ni^{II} etc.) can be isolated. This capacity of the polydentate organic ligands leads to the isolation of complexes with a large number of metal ions, nanoscale dimensions and beautiful metal topologies. Moreover, it is well known that the type of bridging donor atom affects the nature and strength of intramolecular magnetic exchange interactions between the paramagnetic centers that they bridge. Specifically, in 3*d*-metals the resulting magnetic properties of the compound are influenced by the way that the orbitals of metal ions and ligands interact.[37]

In addition to all of the above properties, it is essential to consider the remaining part of the organic ligand as it brings various physicochemical properties into the resulting complexes. In coordination chemistry, ligands based on aromatic or polyaromatic chelates are commonly used due to their ability to enhance the stability and crystallinity of the resulting metal clusters. Furthermore, the aromatic rings may act as "antennas" to promote energy transfer effects, thus leading to the enhancement of the optical properties of the complexes.[33] Unusual and unpredictable metal-ion assisted transformations that lead to new organic groups with novel electronic and steric properties have been also reported.[35]

One of the most common families of ligands employed in metal cluster chemistry are Schiff bases. In 1864, Hugo Schiff reported the synthesis of Schiff bases as the organic compounds that contain the azomethine (>C=N-) group and have the general formula RR′C=NR″.[38] The substituents for the R can be alkyl, aryl or heteroaryl groups, for the R′, alkyl or aryl groups or a single hydrogen atom, and for the R″ substituent at the imino N-atom can be an alkyl, aryl or heteroaryl group. Commonly, Schiff bases are condensation products of primary amines and carbonyl-based precursors (aldehydes or ketones). The nucleophilic addition of the amine to the carbonyl-based precursor forms an intermediate hemiaminal (or carbinolamine) which -upon the elimination of a water molecule- leads to the desirable compound. The reaction usually takes place in alcoholic solvent media and under refluxing conditions (Scheme 1.2).[39,40] Schiff bases can be hydrolyzed to their initial precursors under acidic, basic or metal-assisted conditions.[40]

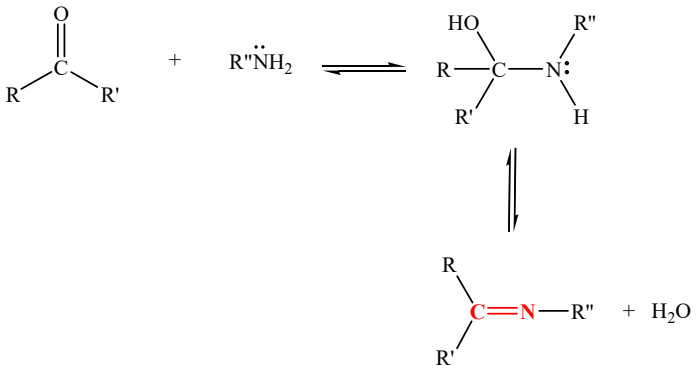

Scheme 1.2. General synthetic route and mechanism for the formation of Schiff bases. R, R′, R″ are various substituents.

The appearance of the characteristic band in the 1680-1600 cm^{-1} region of an infrared (IR) spectrum confirms the formation of a carbon-nitrogen double bond. Depending on the

nature of the substituents (alkyl, aryl, heteroaryl groups or hydrogen) on these atoms the characteristic band of the azomethine group may be shifted towards lower or higher wavenumbers within this region. A general trend of the *ν*(C=N) IR frequency to shift to lower wavenumbers is observed when the Schiff base is bound to a metal ion. The presence of an unconjugated chromophore in a compound gives rise to the characteristic n→π* transition in its electronic spectrum (UV-Vis spectrum). Generally, this transition is shown in the 235-271 nm range, whereas aryl or alkene substituents alter the resulting UV-Vis spectra. These deviations are due to the strong bands from the π→π* transitions, which overlap with the weaker n→π* transitions. It is important to note that the UV-Vis spectra of compounds bearing Schiff base ligands are often solvent-dependent.[39b] Classification of Schiff bases is based on the number of their donor atoms. According to that, there are mono-, bi-, tri-, tetra-and poly-dentate Schiff base ligands if they comprise of more than four donor atoms (Figure 1.11).[41]

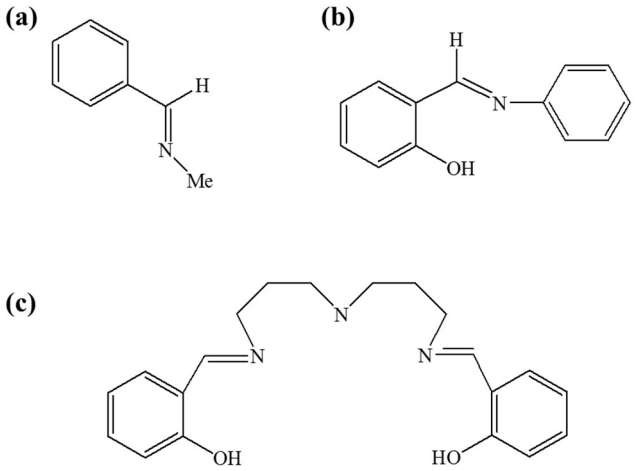

Figure 1.11. Selected examples of **(a)** monodentate, **(b)** bidentate, **(c)** multidentate Schiff base ligands.

Schiff base ligands hold a special position in the field of coordination chemistry. Generally, they are able to coordinate to metal ions through their *O*, *N* or *S*-donor atoms, as well as through the *N* of the azomethine group.[41] Further classification of each type of Schiff base is provided by the type of donor atoms that they bear (*N*, *O*, or *S*), thus leading to a huge variety of families, which can potentially be used as ligands in metal cluster chemistry. Aromatic Schiff bases are most commonly used in coordination chemistry as chelating/bridging ligands, forming stable metal complexes. Moreover, they fulfill all the essential requisites for a good ligand as these have already been described. Aromatic bridging/chelating Schiff bases have been shown to form 3*d*-, 4*f*- and 3*d*/4*f*-metal clusters with various nuclearities and unprecedented topologies, and they have contributed to the observation of numerous interesting physicochemical properties.

Recently, Andruh published a review article describing the coordination chemistry of Schiff base ligands based on the *o*-vanillin scaffold.[42] The variety of isolated and structurally characterized 3*d*-, 3*d*/4*f*- and 4*f*-metal complexes with different metal topologies and enhanced magnetic and photoluminescence properties have further supported the choice of Schiff bases as efficient bridging/chelating ligands for the synthesis of novel clusters with both magnetic and optical properties. Figure 1.12 depicts two examples with Schiff base ligands derived from *o*-vanillin.[43,44]

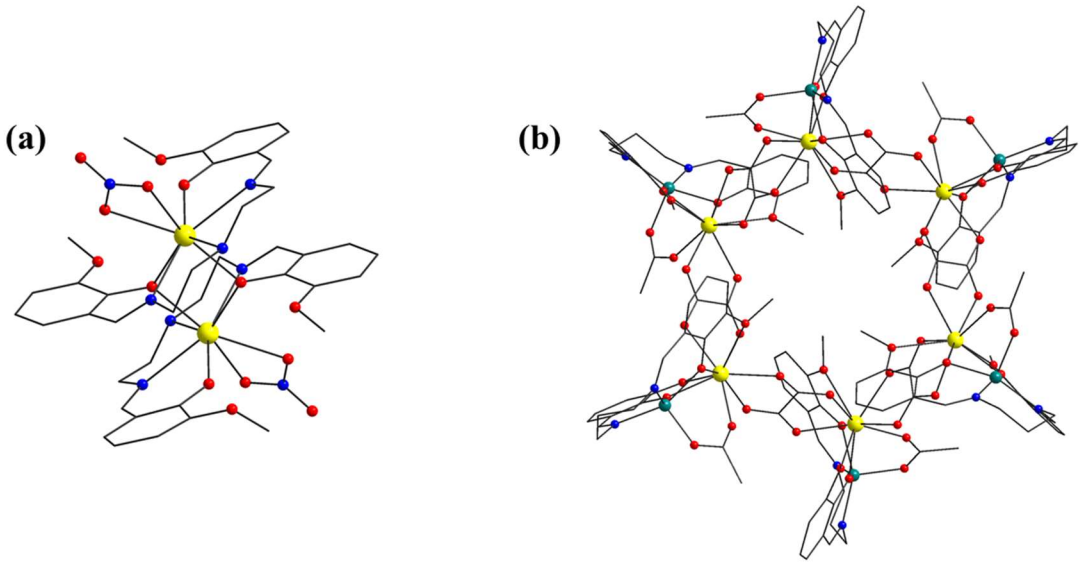

Figure 1.12. Molecular structures of the **(a)** $[Dy^{III}_2(valdien)_2(NO_3)_2]$ and **(b)** $[Cu^{II}_6Dy^{III}_6(CH_3CO_2)_6(C_2O_4)_6(valpn)_6]$ complexes, where $valdien^{2-}$ and $valpn^{2-}$ are the anions of N1,N3-bis(3-methoxysalicylidene)diethylenetriamine and 1,3-propanediyl-bis(2-iminomethylene-6-methoxyphenol), respectively. Colour scheme: Dy^{III}, yellow; Cu^{II}, cyan; O, red; N, blue; C, gray. Reproduced from Refs. 42 and 44.

Substituted derivatives that are based on the scaffold of *N*-salicylidene-*o*-aminophenol ($saphH_2$, Scheme 1.3) Schiff base ligand are of particular interest in the Stamatatos research group. $SaphH_2$ is a well-studied ligand in metal cluster chemistry due to the ability of the relatively soft *N* atom and the two hard, upon deprotonation, *O* atoms to bind to a single or multiple metal centers. The ligand $saphH_2$ has also been involved within the synthesis of new SMMs as well as luminescent materials that exhibit strong emissions in the blue-green region of the visible spectrum. Consequently, $saphH_2$ has proved its ability to act as an excellent bridging/chelating ligand for the synthesis of molecules with dual physical properties (SMMs and emissive materials).

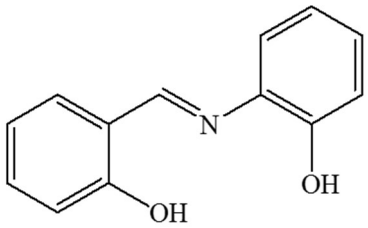

Scheme 1.3. Molecular structure of the Schiff base ligand *N*-salicylidene-*o*-aminophenol ($saphH_2$).

Stamatatos' research group has focused on the employment of $saphH_2$ and its substituted derivatives in coordination chemistry. The use of $saphH_2$ in heterometallic 3*d*/4*f*-metal cluster chemistry has led to the isolation of $\{Mn^{III}_4Dy^{III}_5\}$ and $\{Mn^{III}_4Dy^{III}_3\}$ complexes with unprecedented topologies and interesting SMM properties (Figure 1.13).[45] Additionally, Perlepes and coworkers reported a family of dinuclear $\{Ln^{III}_2\}$ complexes (Ln = Sm, Eu, Gd, Tb, Dy, Ho, Er) with $saphH_2$ acting as a bridging/chelating ligand (Figure 1.14a); the dimers exhibited SMM behaviors and ligand-centered emissions.[46] Mukherjee and coworkers have also isolated a hexanuclear $\{Dy^{III}_6\}$ complex (Figure 1.14b) with $saphH_2$, which showed weak SMM behavior.[47]

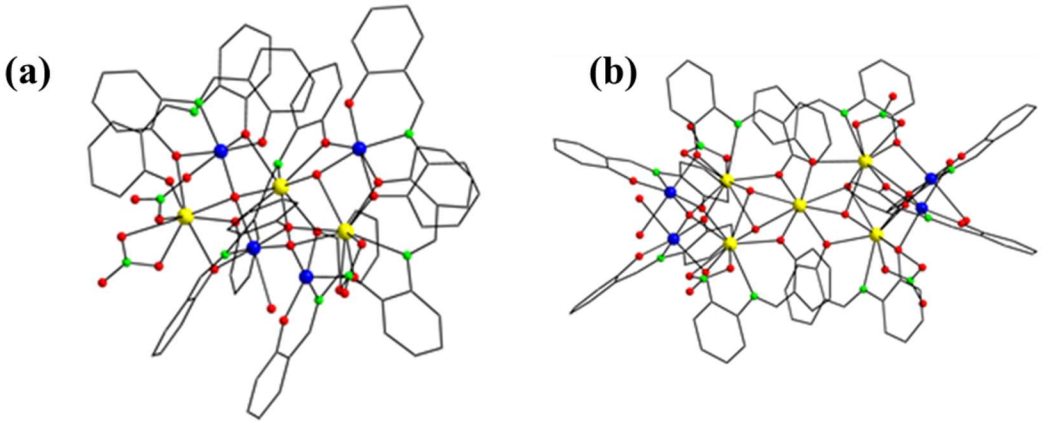

Figure 1.13. Molecular structures of the **(a)** $[Mn_4Dy_3O_2(OH)(NO_3)_3(saph)_6(saphH)(H_2O)]$ and **(b)** $[Mn_4Dy_5O_2(OH)_4(NO_3)_4(saph)_8(H_2O)_4]^-$ cluster compounds obtained from the initial use of *N*-salicylidene-*o*-aminophenol Schiff base ligand in 3*d*/4*f*-metal chemistry. Colour scheme: Mn^{III}, blue; Dy^{III}, yellow; O, red; N, green; C, gray. Reproduced from Ref. 45.

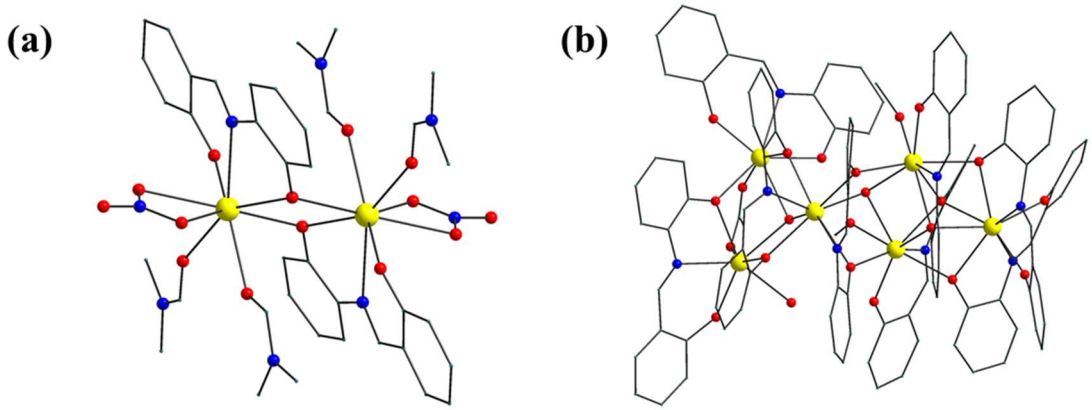

Figure 1.14. Molecular structures of the **(a)** $[Dy^{III}_2(NO_3)_2(saph)_2(DMF)_4]$ and **(b)** $[Dy^{III}_6(OH)_2(O_2CMe)(saph)_7(saphH)(MeOH)_2(H_2O)]$ complexes. Colour scheme: Dy^{III}, yellow; O, red; N, blue; C, gray. Reproduced from Refs. 46 and 47.

Moreover, different ring-substituted derivatives of $saphH_2$, either on the *o*-aminophenol or the salicylidene moieties or both, have been employed by Stamatatos' research group for the synthesis of new cluster compounds with new metal topologies and magneto-optical properties. Scheme 1.4 shows two representative examples of these types of Schiff base ligands. The employment of the aforementioned ligands in Ni^{II} cluster chemistry has afforded complexes with diverse nuclearities. It is noteworthy to mention that $sacbH_2$ has led to the isolation of the highest in nuclearity, non-organometallic Ni^{II} cluster to date, namely a $\{Ni_{26}\}$ with a 'rabbit-face' topology (Figure 1.15).[48a] In contrast, the bulkier $nacbH_2$ ligand, which bears the naphthalene

moiety in place of the phenyl ring of $sacbH_2$, has been responsible for the stabilization and isolation of a large family of $\{Ni_5\}$, $\{Ni_6\}$ and $\{Ni_{12}\}$ clusters with new metal topologies, large spin ground state values, emissive properties, and unprecedented organic ligand transformations.[48b,48c] Undoubtedly, the reported results have demonstrated the rich coordination chemistry of both $sacbH_2$ and $nacbH_2$ in the presence of Ni^{II} metal ions and the ability of these chelates to adopt a variety of different modes, thus fostering the formation of high-nuclearity molecules with multiple physical properties.

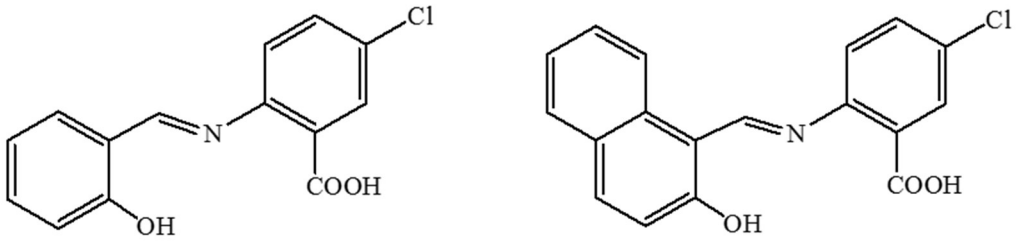

$sacbH_2$ $nacbH_2$

Scheme 1.4 Structural formulae and abbreviations of the ligands *N*-salicylidene-2-amino-5-chlorobenzoic acid ($sacbH_2$) and *N*-naphthalidene-2-amino-5-chlorobenzoic acid ($nacbH_2$) discussed in the text.

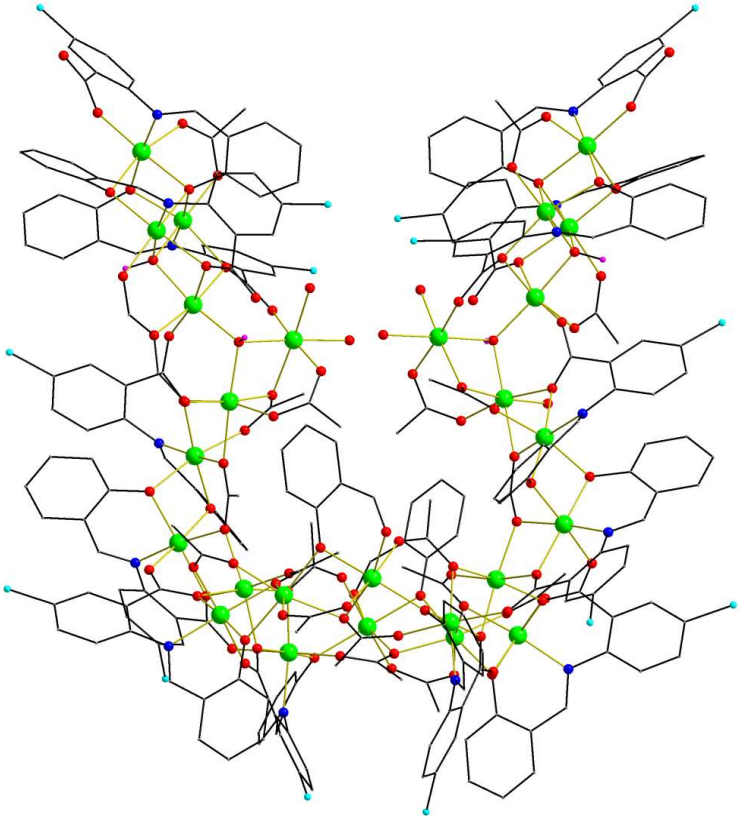

Figure 1.15. Molecular structure of the $\{Ni^{II}_{26}\}$ cluster. All H atoms except from the ones belonging to the μ_3-OH^- groups are omitted for clarity. Colour scheme: Ni^{II}, green; O, red; N, blue; C, dark gray; Cl, cyan; H, magenta. Reproduced from Ref. 48a.

1.4 ***Lanthanide Complexes in the Field of Molecular Magnetism***

Magnetism is one of the most widely used properties of materials in daily used devices (data storage devices, power converters, medical devices etc.). There is a variety of classical amorphous magnetic materials which cover the needs of modern technology. On the other hand, the growing demand for smaller and cheaper technological devices has led research into the synthesis of molecule-based magnetic materials; molecular analogues of traditional "atom-based" magnets.[24a] Molecular magnetism has been a well-known field since the end of twentieth

century when an early example of a molecule-based ferromagnet was discovered comprising organic radicals.[49] Compared with the amorphous magnetic materials used in industry, molecule-based magnetic materials show some synthetic and practical benefits. Relatively controllable and mild chemical synthetic procedures can be performed for the synthesis of these molecular species. Moreover, molecular magnets are more soluble than the bulk-magnets, an effective property that allows their employment in a variety of applications. There are different types of molecular magnets with regards to their magnetic behavior and the nature or dimensionality of their consisting molecules.[50] An important class of discrete molecules that have the ability to be magnetized by an external magnetic field, retain their magnetization upon removal of the field and exhibit slow relaxation of magnetization over an energy barrier U, below their blocking temperature (T_B), are *single-molecule magnets* (SMMs).[51] Single-molecule magnetism was first introduced as a term by Christou, Gatteschi, Hendrickson and coworkers.[52]

In 1980, the dodecanuclear cluster compound $[Mn_{12}O_{12}(O_2CMe)_{16}(H_2O)_4]$ (Figure 1.16)[53] was first synthesized and reported by Lis, but it was not until the early 1990s when its SMM properties were first elucidated.[54] This $\{Mn_{12}\}$ compound is the most widely investigated SMM and its complete magnetic characterization has revealed an S = 10 ground state, a magnetic anisotropy value of D = -0.5 cm^{-1} and an effective energy barrier for spin reversal of U_{eff} = 50 cm^{-1} (72 K).

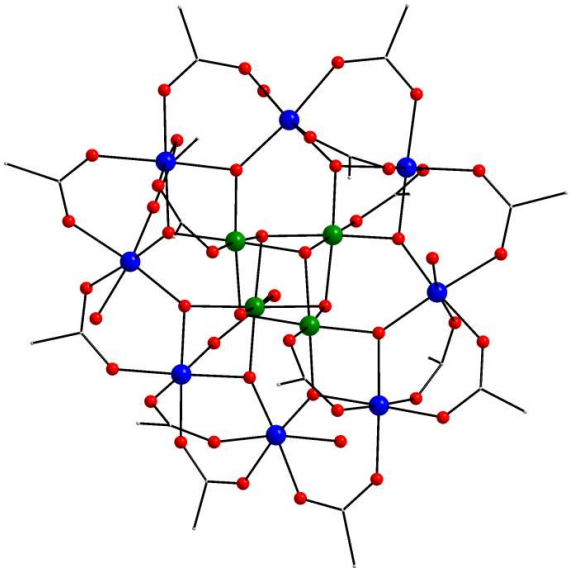

Figure 1.16. Molecular structure of the $\{Mn_{12}\}$ SMM. Colour scheme: Mn^{III}, blue; Mn^{IV}, olive green; O, red; C, gray. H atoms are not shown for clarity. Reproduced from Ref. 53.

In the early years, SMMs attracted the interest of scientists for extending their knowledge in the physicochemical properties of these novel molecule-based materials. Today, this area of research is still fascinating due to the potential applications that these 0-D molecular species could find in high-density data storage,[55] quantum computation,[56] among others. However, the temperatures that these species operate must increase to become more technologically applicable.[24a] Since the discovery of the first $\{Mn_{12}\}$ SMM, a continuous research development of this area has been observed, resulting in some important breakthroughs by means of enhancing the relaxation dynamics and overall properties of SMMs. Larger effective energy barriers (U_{eff}) for magnetization reversal and higher blocking temperatures (T_B) were some of the problems that scientists in this field had to resolve for the accomplishment of more effective SMMs. In 2003, a family of complexes with the general formula $[Pc_2Ln]^-$, where Pc^{2-} is the macrocycle-type ligand phthalocyanine and Ln^{III} are Tb^{III}, Dy^{III}, Ho^{III}, Er^{III}, Tm^{III} and Yb^{III}, was

reported by Ishikawa and coworkers (Figure 1.17). The Tb^{III} and Dy^{III} analogues of the sandwich-like mononuclear compounds exhibited slow relaxation of their magnetization, with the $[Pc_2Tb]^-$ analogue exhibiting a U_{eff} of 584 cm^{-1} (836 K).[57] The temperature ranges in which the magnetization relaxations were observed for this new class of mononuclear single-molecule magnets (or, alternatively, single-ion magnets (SIMs)) were significantly higher than those of the transition-metal-cluster SMMs. The resulting magnetic behavior of this family of complexes was the first step towards the systematic exploration of highly anisotropic lanthanide ions for the synthesis of efficient SMMs.

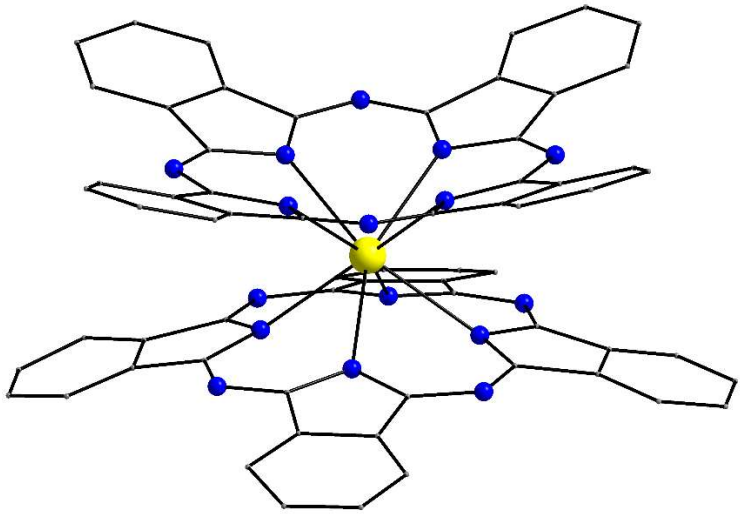

Figure 1.17. Structure of the $[Pc_2Tb]^-$ single-ion magnet. H atoms are omitted for clarity. Colour scheme: Tb^{III}, yellow; N, blue; C, gray. Reproduced from Ref. 57.

In order to further understand the magnetic profile of SMMs, the fundamentals of molecular magnetism and the employment of lanthanide ions in this field will be discussed. As it is well known, magnetism arises from the electron's motion around its own axis and around the nucleus. As it has already been mentioned earlier in this thesis, the motion of electrons leads to a

spin angular momentum, *S*, and an orbital angular momentum, *L*, the interaction of which gives rise to a small magnetic moment. As a consequence, the overall magnetic moment of an atom is the vector sum of each electron's magnetic moment, resulting in the observed magnetic behavior.[58] In order to determine the magnetic behavior of a species it is useful to define the magnetic susceptibility, χ (dimensionless), which describes the magnetization response (M) of a material to an applied magnetic field (H). The measurement is given in the volume magnetic susceptibility, χ_v, by the following equation:

$$\boldsymbol{\chi_v = \frac{M}{H}} \qquad \textbf{Eqn. 1.4}$$

The most commonly used expression of the magnetic susceptibility is the molar magnetic susceptibility, χ_M (cm^3mol^{-1}), which can be derived by the χ_v.[59] Depending on the presence or absence of unpaired electrons in an atom, ion or molecule, there are two fundamental magnetic behaviors of materials: paramagnetism and diamagnetism. The latter is a property of all matter as it refers to the interaction of the paired electrons of the material with the external magnetic field. It is known that, at the atomic level, weak magnetic dipoles are produced due to the small atomic current loops created by the orbital's motion. These small magnetic fields are aligned in the opposite direction of the external magnetic field and are temperature independent. However, in the presence of unpaired electrons the diamagnetism is very small and the paramagnetic behavior of the material dominates. Paramagnetic materials are characterized by randomized spins, which under an external magnetic field, are aligned parallel exhibiting attractive forces between them. Despite that, paramagnetic materials cannot retain their magnetization upon field removal as the spins are randomized again (Figure 1.18).[37d,60]

Figure 1.18. Randomized spins in a paramagnetic material.

As a consequence, in any material the total molar susceptibility comprises two factors: the paramagnetic (χ_p) and diamagnetic (χ_d) susceptibilities (Eqn. 1.5). The paramagnetic component, affected by the unpaired electrons, has a positive value and the diamagnetic component is negative. In a given molecule the overall diamagnetism can be calculated by adding the diamagnetic susceptibilities of every atom (χ_{D_i}), and bond (λ_i) in the molecule (Eqn. 1.6). The values of χ_{D_i} and λ_i are known as "Pascal's constants".[61]

$$\boldsymbol{\chi_m = \chi_p + \chi_d} \qquad \textbf{Eqn. 1.5}$$

$$\boldsymbol{\chi_d = \sum_i \chi_{D_i} + \sum_i \lambda_i} \qquad \textbf{Eqn. 1.6}$$

Further classification of magnetic interactions depends on the long-range magnetic ordering of the unpaired spins (retention and direction of spin alignments), thus leading to ferromagnetic, antiferromagnetic and ferrimagnetic behavior (Figure 1.19). They are described as critical phenomena, as at a certain temperature these species behave as paramagnets. These temperatures are known as the Curie temperature (T_C) for ferromagnetic and Néel temperature (T_N) for antiferromagnetic materials. Above these temperatures, the thermal energy dominates over the magnetic order resulting in the loss of the long-range magnetic ordering of the material. In bulk magnets, when the magnetic moments are aligned parallel within a domain the material is described as a ferromagnet. Despite the fact that each domain is characterized by a non-zero magnetic moment, the random spatial orientation of them leads to a zero net magnetic moment. The most common type of magnetism is the antiferromagnetism, where the magnetic moments

are aligned antiparallel to each other. In this case, the resulting net magnetic moment of the material in the absence of an external magnetic field equals to zero. Antiparallel magnetic moments with different magnitudes give rise to the ferrimagnetic behavior of a material. The net magnetic moment of these materials is usually non-zero; however, a zero-net magnetic moment may also be observed in few cases.[59]

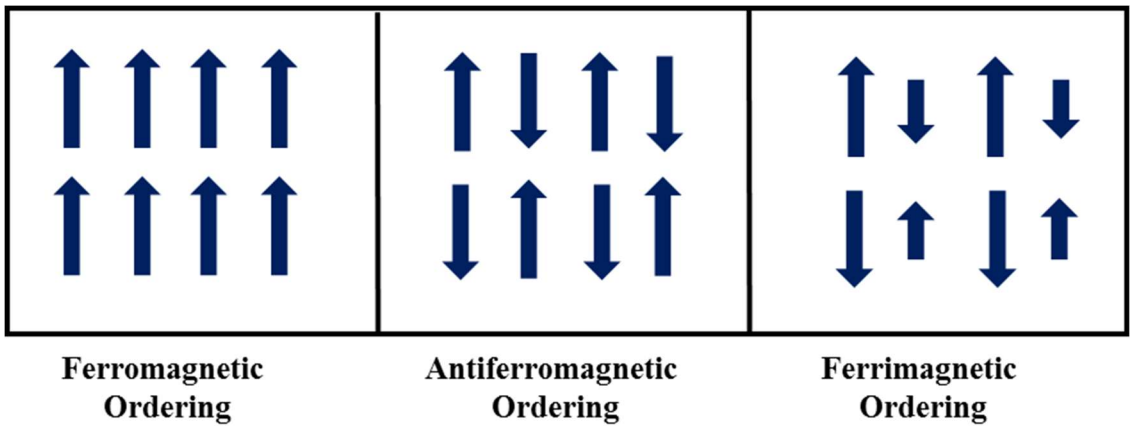

Figure 1.19. Spin ordering in different types of magnetic materials.

In the case of 0-D molecular magnets consisting of paramagnetic metal ions, each molecule represents a discrete entity with its own total magnetic moment. The spin of each metal center can interact (or couple) ferro- or antiferromagnetically with the spin of a neighboring metal atom resulting in an overall ferromagnetic, antiferromagnetic or ferrimagnetic response for the coordination compound.

Lanthanide ions have an effective spin-orbit coupling which results in a strong single-ion anisotropy. Furthermore, there is a large separation between the ground-state multiplet level and the excited one (except for Eu^{III} and Sm^{III}). Thus, it is reasonable to assume that the origin of magnetism for the lanthanide ions arises mainly from their ground-state level, which is described

by the angular momentum, J.[6] Earlier, the ground-state multiplet $^{2S+1}L_J$ of a free trivalent lanthanide ion was described. The presence of an applied direct current (*dc*) field can lift the degeneracy of the (2J+1) levels of the ground-state with the energy of each of them given by Eqn. 1.7, where μ_0 is the magnetic permeability of free space ($\mu_0 = 4\pi \times 10^{-7}$ TmA^{-1}), μ_B is the Bohr magneton, H is the applied magnetic field, and g_J is the Landè factor.

$$\boldsymbol{E_H = -g_J m_J \mu_0 \mu_B H} \qquad \textbf{Eqn. 1.7}$$

In a weak applied magnetic field, the Landè splitting factor, g_J, describes the separation of the field-dependent energy levels of an atom and is given by the following Eqn. 1.8.

$$\boldsymbol{g_J = \frac{3}{2} + \frac{S(S+1) - L(L+1)}{2J(J+1)}} \qquad \textbf{Eqn. 1.8}$$

At the point where the field and temperature allow only the lowest microstate to be populated, the magnetization reaches a saturation value, M_S, which is given by Eqn. 1.9, where N is the number of paramagnetic centers (Figure 1.20).

$$\boldsymbol{M_S = N g_J J \mu_B} \qquad \textbf{Eqn. 1.9}$$

However, in highly anisotropic systems and/or in systems described by the presence of low-lying excited states, the magnetization, M, does not reach a saturation value even at high fields and low temperatures. This is a common characteristic in polynuclear metal complexes, where the metal centers are often weakly coupled to each other and the resulting ground states are close in energy with the low-lying excited states. The relative population of the excited levels at a given temperature, T, and a given field strength, H, can be determined by assuming a Boltzmann distribution. Hence, the magnetization of such a system can be eventually given by the so-called Brillouin function (Eqn. 1.10), where the terms $B_J(y)$ and y are described by Eqns 1.11 and 1.12, respectively, and k is the Boltzmann constant.

$$\boldsymbol{M = N g_J J \mu_B \cdot B_J(y)} \qquad \textbf{Eqn. 1.10}$$

$$B_J(y) = \frac{2J+1}{2J}\coth\frac{2J+1}{2J} - \frac{1}{2J}\coth\frac{y}{2J} \qquad \textbf{Eqn. 1.11}$$

$$y = \frac{g_J J \mu_B \mu_0 H}{kT} \qquad \textbf{Eqn. 1.12}$$

Furthermore, at low magnetic fields and high temperatures the y term is far less than 1, and the magnetization (Figure 1.20), as well as the magnetic susceptibility, increases linearly with the field following the so-called Curie law (Eqn. 1.13).

$$\chi = \frac{M}{H} = \frac{N\mu_0 g_J{}^2 J(J+1)\mu_\beta{}^2}{3kT} = \frac{C}{T} \qquad \textbf{Eqn. 1.13}$$

In the above equation, C is the Curie constant and is given in units of $cm^3 \cdot K \cdot mol^{-1}$. Pierre Curie experimentally determined that when a paramagnetic material is placed into a magnetic field, the molar susceptibility (χ_M) is temperature and field dependent.[6] Importantly, the χT values for lanthanide ions can be calculated through Eqn. 1.13.

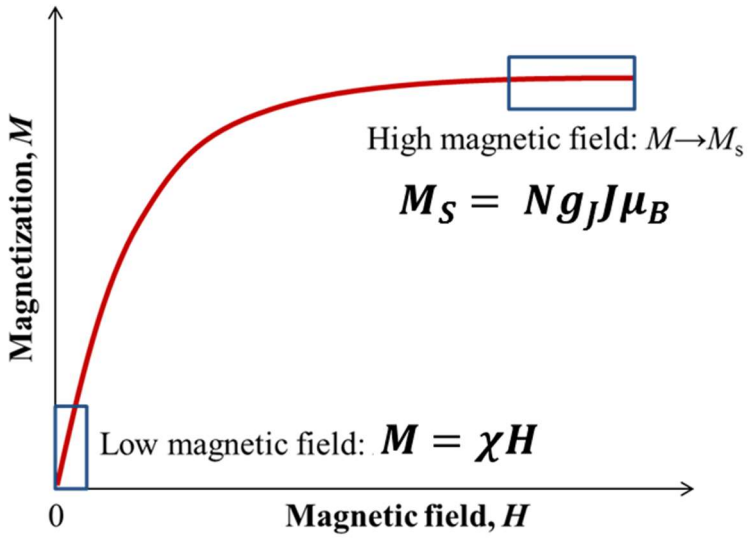

Figure 1.20. Plot of *M vs. H* for a paramagnetic material. Reproduced from Ref. 59.

The Curie law describes an ideal paramagnetic behavior. Consequently, the majority of real paramagnetic compounds do not follow the Curie law but instead they obey the phenomenological Curie-Weiss law (Eqn. 1.14). In this case, the ideal Currie law is modified by inserting into equation 1.13 the parameter, θ (in Kelvin), or otherwise the Curie-Weiss constant (Eqn. 1.14). The θ parameter is extracted from the interception of the linear plot of $1/\chi$ versus T with the x-axis (Figure 1.21). In most cases, θ describes the nature of the magnetic exchange interactions, but it can also be attributed to the presence of spin-orbit coupling effects depending on the paramagnetic metal center.

$$\chi = \frac{C}{T-\theta} \qquad \textbf{Eqn. 1.14}$$

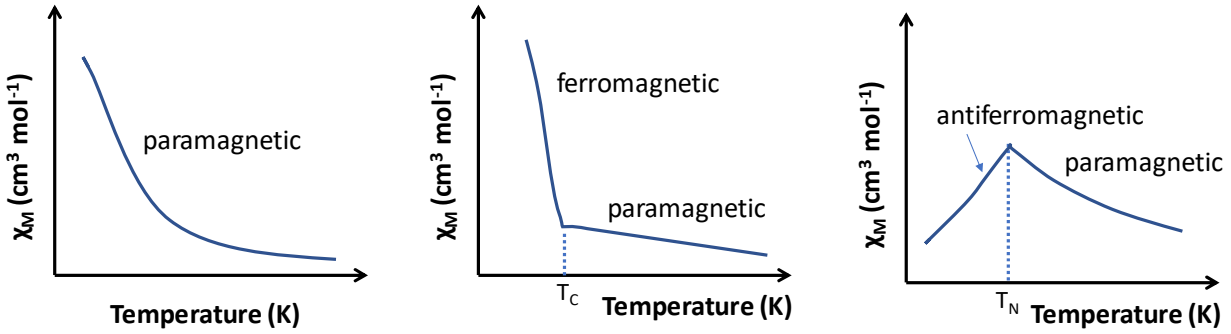

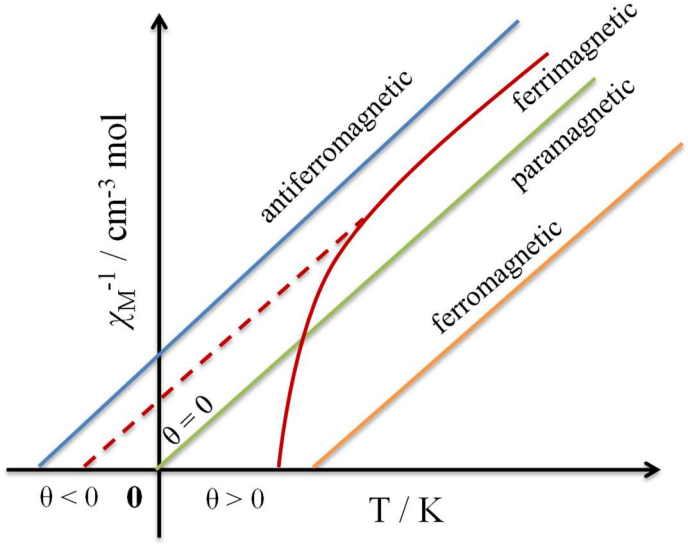

Figure 1.21. (top) Plots of the molar magnetic susceptibility (χ_M) versus temperature (T) for three different classes of magnetic materials. (bottom) Plots of inverse susceptibility $\frac{1}{\chi_M}$ *vs.* T for a paramagnetic species and ferromagnetically-, ferrimagnetically- and antiferromagnetically-coupled compounds. Reproduced from Ref. 58a.

Generally, the magnetic behavior of a material can be described by using a $\chi_M T$ *vs.* T plot. Considering all that has been mentioned, the susceptibility-temperature product, $\chi_M T$ *vs.* T, in all ideal paramagnetic materials is a straight line. However, this is not the case for species with ferromagnetic, antiferromagnetic and ferrimagnetic behaviors, where the $\chi_M T$ *vs.* T plots deviate significantly from that line as is depicted in the following Figure 1.22.[58]

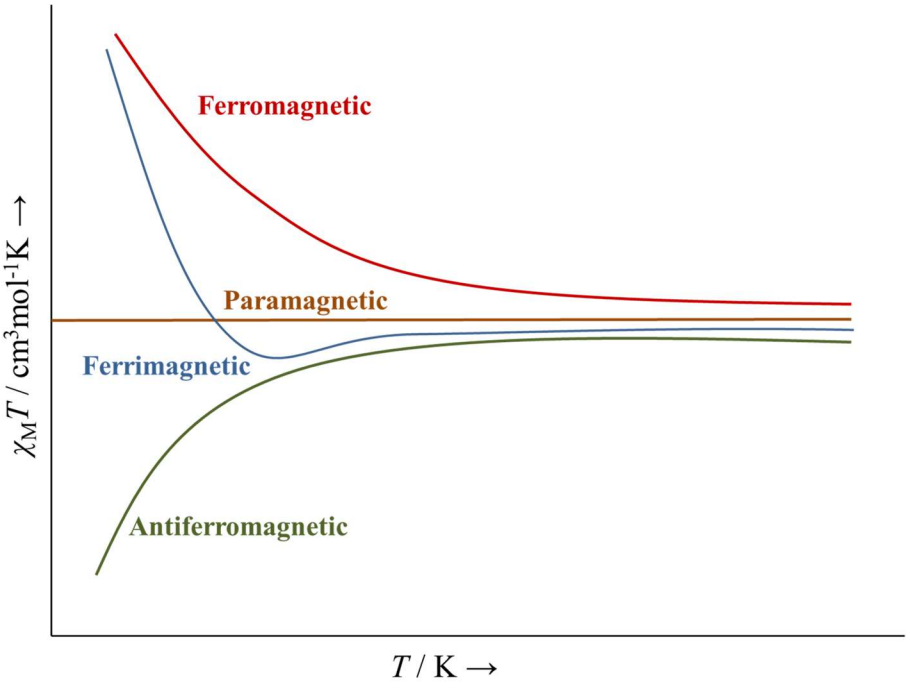

Figure 1.22. Plots of the susceptibility-temperature product, $\chi_M T$, *vs.* T for the different magnetic materials. Reproduced from Ref. 58a.

The importance of synthesizing and utilizing new SMMs has already been documented. However, it is necessary to describe and comment on the basic requirements that a functional lanthanide single-molecule magnet must fulfill. First, the ground state should be bistable. This is always the case for Kramer's ions (odd number of electrons, i.e. Dy^{III}) but for non-Kramer's ions the degeneracy of their ground-state is established when the ligand field around the metal ions has the proper symmetry. Moreover, the ground state must be ideally characterized by the highest possible $\pm m_J$ quantum number in order to ensure the retention of the magnetic moment when the temperature allows for the ground-state to be the only populated state.[24a] Secondly, the presence of axial magnetic anisotropy (D) is required, which would lead to an effective energy barrier (U_{eff}) separating the opposite orientations ($\pm m_J$) of the spin ground-state. Assuming a thermal-assisted (TA) relaxation mechanism the energy that the magnetization requires to relax can be defined by that separation.[62]

Lanthanides are excellent candidates for the development of efficient SMMs due to their intrinsic free-ion anisotropy resulting from strong spin-orbit coupling. In lanthanide complexes the coordination environment of the metal centers affects the ground-state magnetic anisotropy of the metal ions. Furthermore, the ground degenerate multiplet state is split into $2J+1$ microstates (or "Stark" sublevels), each with an m_J quantum number. Ligand field effects appear to be one of the most important factors towards the synthesis of efficient Ln-SMMs. Their interaction with the ground spin-orbit coupled J state leads to the generation of the magnetic anisotropy barrier, which further separates the opposite orientations of spins in the ground state (Figure 1.23).[62]

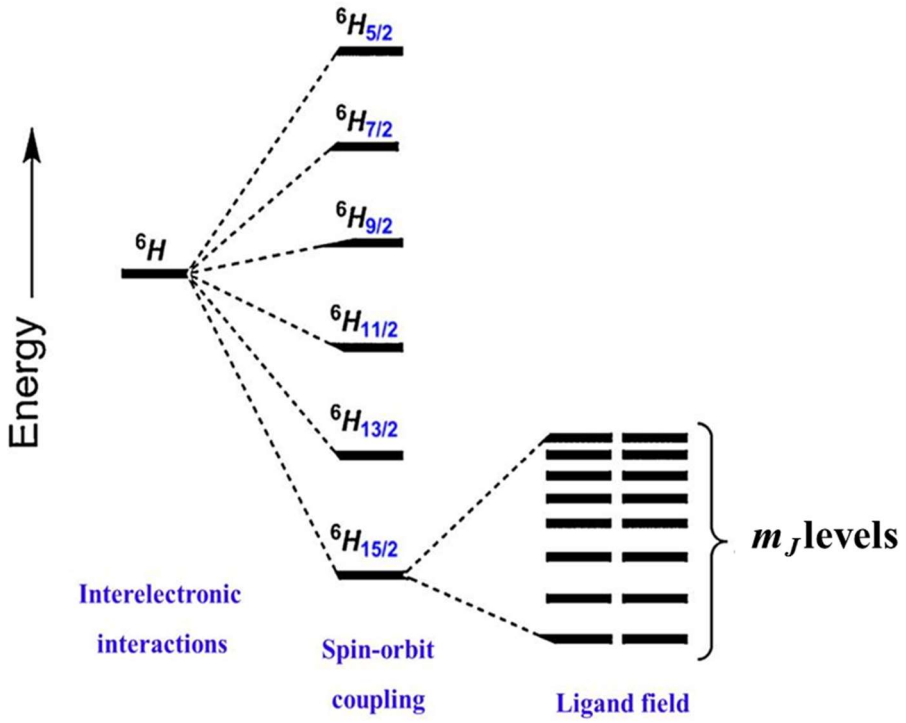

Figure 1.23. Representation of the electronic structure of a Dy^{3+} ion in its free ion form (left) and in the presence of spin-orbit coupling (middle) and ligand field (right), generating (2*J*+1) sublevels with the respective quantum numbers, m_J. The $^6H_{15/2}$ spin ground state is split into sixteen sublevels (eight Kramer's doublets). Reproduced from Ref. 58a.

Depending on the ion (Kramer's or non-Kramer's) the microstates can be single- or doubly-degenerate. In a doubly-degenerate scenario, the ground-state magnetization relaxes through the m_J microstates over the energy barrier. In an attempt to increase the magnetic anisotropy in a Ln-based complex, the optimum coordination environment must be achieved. According to mathematical calculations, the quadrupole moment has been adapted to describe the basic shapes of the lowest *J* states. By considering this approach, the shape of the quadrupole moment of the 4*f*-electron densities can be prolate (axially elongated), oblate (equatorially

elongated) or isotropic (spherical). The strong angular dependence of the *f*-orbitals results in the observed different shapes across lanthanide series (Figure 1.24).[62]

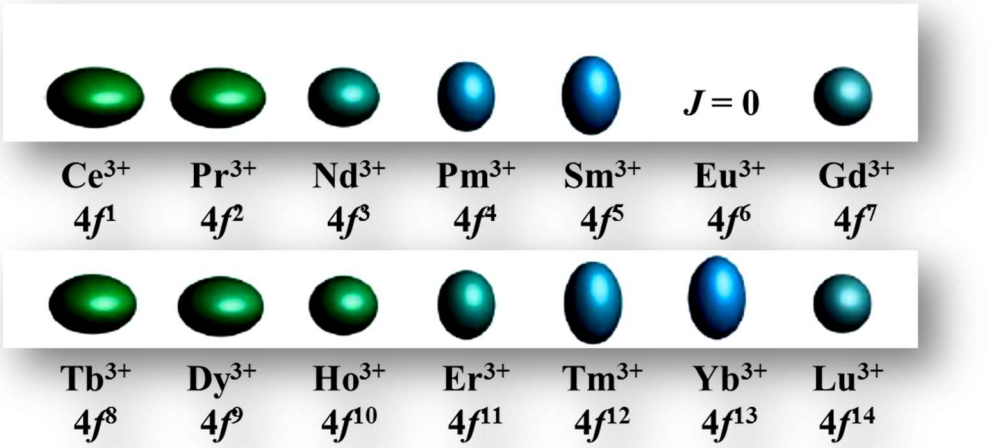

Figure 1.24. Quadrupole approximations of the *f*-electron distribution of the Ln^{3+} free-ions. Due to $J = 0$, there is no electron distribution for the Eu^{3+} ion. Reproduced from Ref. 62.

By knowing the shape of free-ion charge density the favorable type of ligand field around each lanthanide ion, which maximizes their overall anisotropy in the ground-state, can be predicted. Considering all the above, an ion with oblate electron density must be placed in an axially coordinated ligand environment in order for the highest possible anisotropy to be achieved. On the other hand, ions with prolate electron distribution prefer equatorially-coordinated ligand fields (Figure 1.25).

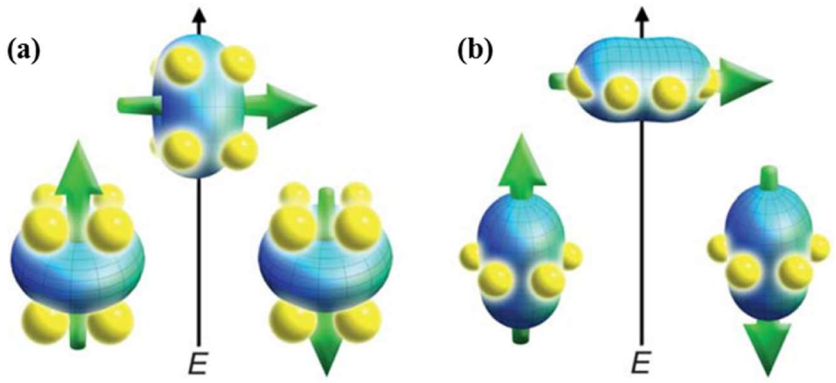

Figure 1.25. Depictions of the combination of the ligand field (yellow spheres) with the electron distribution (blue ovoid) of **(a)** an oblate or **(b)** a prolate Ln^{III} metal ion. Oblate lanthanides prefer axial "sandwich"-type ligand fields, while prolate lanthanides prefer equatorial ligand fields. Adapted from Ref. 62 with permission from the Royal Society of Chemistry.

In order to gain any further insights into the field of SMMs and analyze their magnetization dynamics, it is essential to define the two basic factors that characterize an SMM: the effective energy barrier, U_{eff}, and the pre-exponential factor, τ_0. The former is referred to the experimental anisotropy barrier which is almost always smaller than the maximum calculated energy barrier, U, for a particular system, while the latter describes quantitatively the relaxation time of the spin-phonon interactions (*vide infra*). In general terms, the magnetization relaxation process can occur through two different processes; these are the thermally assisted process and the quantum tunneling. In the thermally assisted process, the magnetization passes through each individual m_J state stepwise over the barrier to the reversal of magnetization, and relaxes back down to the opposite m_J level. This process is the slowest of all, and therefore the magnetization of the compound is retained for a long period of time. However, a competing relaxation process is also present, especially in 4*f*-metal based SMMs, known as the quantum tunneling of magnetization (QTM). Quantum tunneling can only occur through degenerate m_s or m_J states and

it is a fast process since it is not dictated by the anisotropy barrier. At low temperatures, if there is a mixing of energetically degenerate m_S or m_J states, the magnetization can pass through the barrier as opposed to relaxing over it, and it takes an immediate opposite spin (Figure 1.26). Because of the presence of QTM, the barrier frequently takes on a value smaller than the expected one of U, leading to an effective anisotropy barrier, U_{eff}. It is desirable for quantum tunneling to be absent in a single-molecule magnet, or if present, very slow. Quantum tunneling can evolve through two different mechanisms. One is the ground state quantum tunneling and the other involves a combination of thermal relaxation and quantum tunneling. In the latter case, the magnetization ascends to an excited m_S or m_J state through a thermally-assisted process, and then it finds a degenerate excited m_S or m_J state which allows it to tunnel through the barrier, and consequently relaxes down to the ground state of opposite direction. This process is called thermally-assisted quantum tunneling, or excited state quantum tunneling.

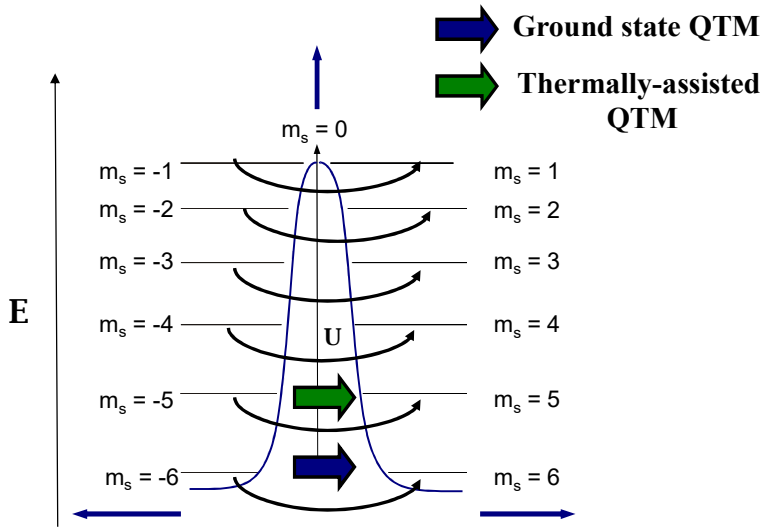

Figure 1.26. Representation of the two different forms of quantum tunnelling of magnetization (QTM) for an SMM with S = 6 and axial magnetic anisotropy. The ground state QTM (blue arrow) describes the fast relaxation of magnetization from the m_S = -6 to the m_S = +6 microstate.

The thermally-assisted QTM (green arrow) describes the relaxation of the magnetization through the first excited state (for this system) *via* a thermally-assisted process from m_s = -6 to the m_s = -5 followed by tunneling from the m_s = -5 to the m_s = +5 (resonant states) and down to the m_s = +6.

At this point it is noteworthy to briefly explain the main thermally-assisted relaxation processes that have taken place in 4*f*-metal based SMMs to date. Therefore, in lanthanide SMMs the magnetization can relax *via* one or two steps through a mechanism which is known as the spin-lattice relaxation. The system gains the required energy from the lattice by absorbing one phonon in order to be excited, followed by its relaxation to the opposite direction with a phonon emission. Commonly, the magnetization relaxes through the first excited state and only in few cases where there are low-lying excited states does the magnetization relax through the second excited state.[63] Due to the distorted symmetries of the real structures of complexes, the above process deviates, resulting in the mixing of the ground and excited states. In that case, a direct process may take place, in which the magnetization is directly transferred from one microstate to the other by absorbing an acoustic phonon, i.e. a single quantum of a long wavelength lattice vibration. Furthermore, the anisotropy axes of the ground and excited states do not coincide which is a result of the symmetry distortion of the complex, enhancing the Orbach and Raman mechanisms (Figure 1.27). In the Raman process, a superposition of two lattice waves absorbs the energy that is released by a relaxing spin system. The superposed lattice waves have the same frequency as the released energy. The first-order Raman transition occurs *via* a virtual intermediate lattice state and can be considered as a two-phonon process. However, when the spin system also makes a transition from a virtual lattice state the relaxation is then called a second-order Raman process.[6,64] The Orbach process (Figure 1.27), which is a direct, resonant

two-phonon process, evolves *via* a real intermediate state involving two phonons related to each other by $h(\nu_2-\nu_1)$. In this case, the relaxation time is found to vary exponentially with $1/T$ with a slope of Δ/k. In contrast to the other two processes (Raman and direct), the presence of this mechanism is more important in characterizing a SMM (Figure 1.28), because it allows a spin to reorient by ascending over the anisotropy barrier, a key characteristic for single-molecule magnets.

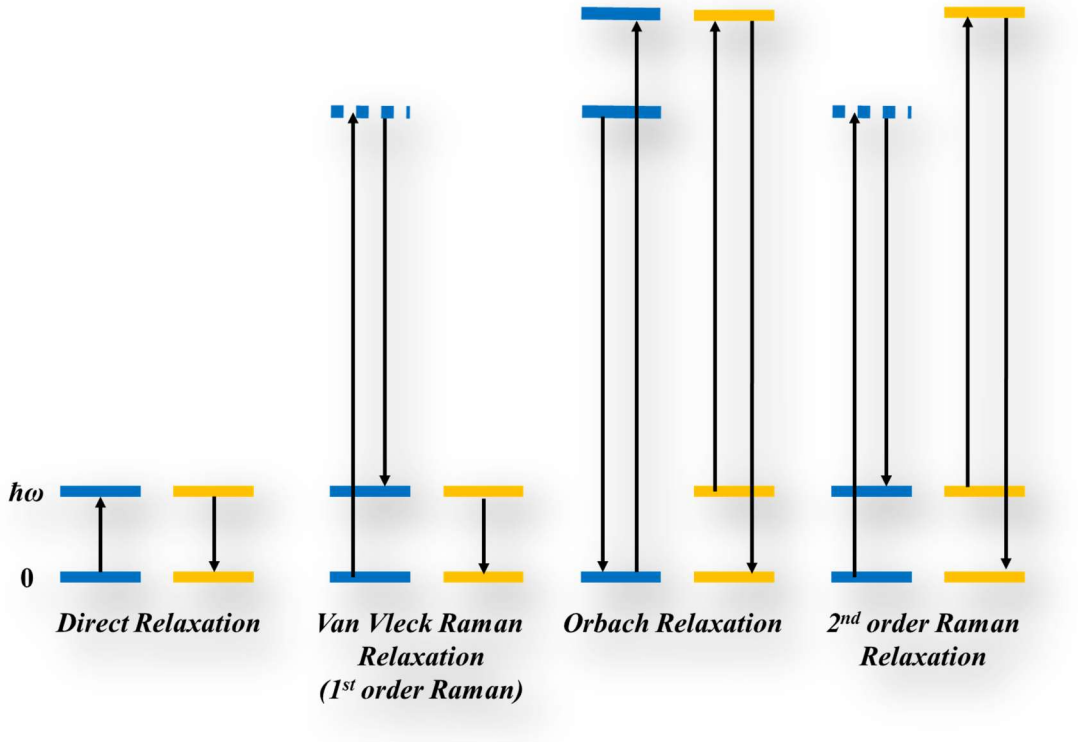

Figure 1.27. Different relaxation (spin-lattice relaxation) mechanisms of magnetization for a (Kramer's) doublet split by the Zeeman interaction. The blue lines represent the levels of the lattice, while the red lines represent the crystal field levels of the lanthanide ion. The black arrows show the energy direction. Reproduced from Ref. 64.

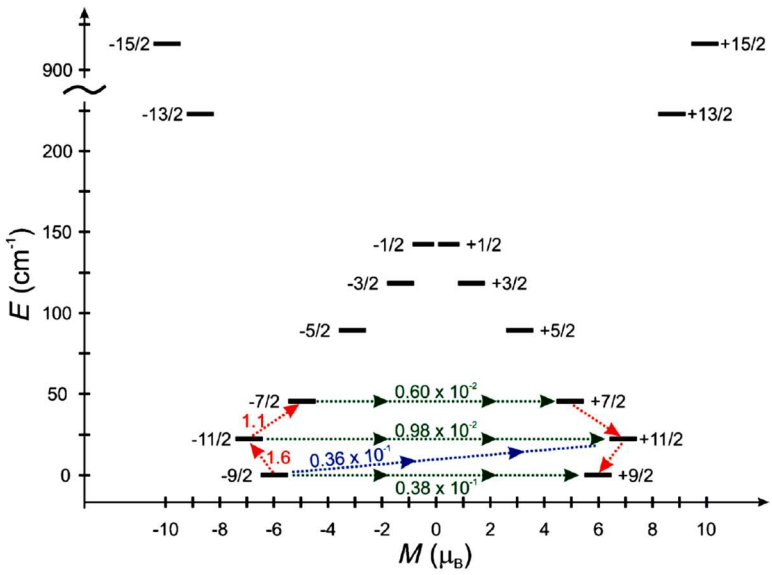

Figure 1.28. Relaxation pathways in a lanthanide-based SMM. Relaxation processes: **(i)** red arrows show the thermally-assisted quantum tunneling (TA-QTM); **(ii)** green arrows show the quantum tunneling (QTM); and **(iii)** blue arrows show the Orbach relaxation of magnetization. Reproduced from Ref. 63.

A number of magnetic measurements are performed in order to detect and study the single-molecule magnetic behavior of a molecule. The magnetic properties of the lanthanide complexes in the present thesis have been studied according to these measurements, a discussion of which follows. A series of measurements using a Superconducting QUantum Interference Device known as a SQUID magnetometer are performed in order to investigate the magnetization dynamics. The appearance of peaks in the frequency-dependent out-of-phase (χ'') *vs.* temperature (T) diagram and the presence of hysteresis loops in the magnetization (M) *vs.* field (H) plot confirm the single-molecule magnetic behavior of a molecular system.

Specifically, in alternating current (*ac*) magnetic susceptibility studies an oscillating magnetic field (~2-5 Oe) of a frequency ω is applied to the sample. The *ac* susceptibility consists

of the real, in-phase (χ'), and the imaginary, out-of-phase (χ''), components with respect to the frequency ω (Eqn. 1.15).

$$\chi_{ac}(\omega) = \chi'(\omega) - i\chi''(\omega) \qquad \textbf{Eqn. 1.15}$$

At the high temperature region, the in-phase susceptibility is equal to the total susceptibility. In this case the out-of-phase component (χ'') is zero as the magnetization follows the applied oscillating field.

When the magnetization is unable to follow, the switching direction of the field leads to the appearance of an in-phase and out-of-phase peak in the χ_M' and χ_M'' *vs. T* plots, respectively (Figure 1.29).[43] The observed out-of-phase (χ'') signals, which indicate the presence of slow relaxation of magnetization, are due to the phase shift between the magnetization and the applied field. The magnetization dynamics are measured in various angular frequencies (ω) according to the following Eqn. 1.16, where χ_T and χ_S are the isothermal (when $\omega \rightarrow 0$) and adiabatic (when $\omega \rightarrow \infty$) susceptibilities, respectively.

$$\chi(\omega) = \chi_S + \frac{\chi_T - \chi_S}{1+i} \qquad \textbf{Eqn. 1.16}$$

Therefore, the in-phase and out-of-phase components are expressed as:

$$\chi' = \chi_S + \frac{\chi_T - \chi_S}{1+\omega^2\tau^2} \qquad \textbf{Eqn. 1.17}$$

$$\chi'' = \frac{(\chi_T - \chi_S)\,\omega\tau}{1+\omega^2\tau^2} \qquad \textbf{Eqn. 1.18}$$

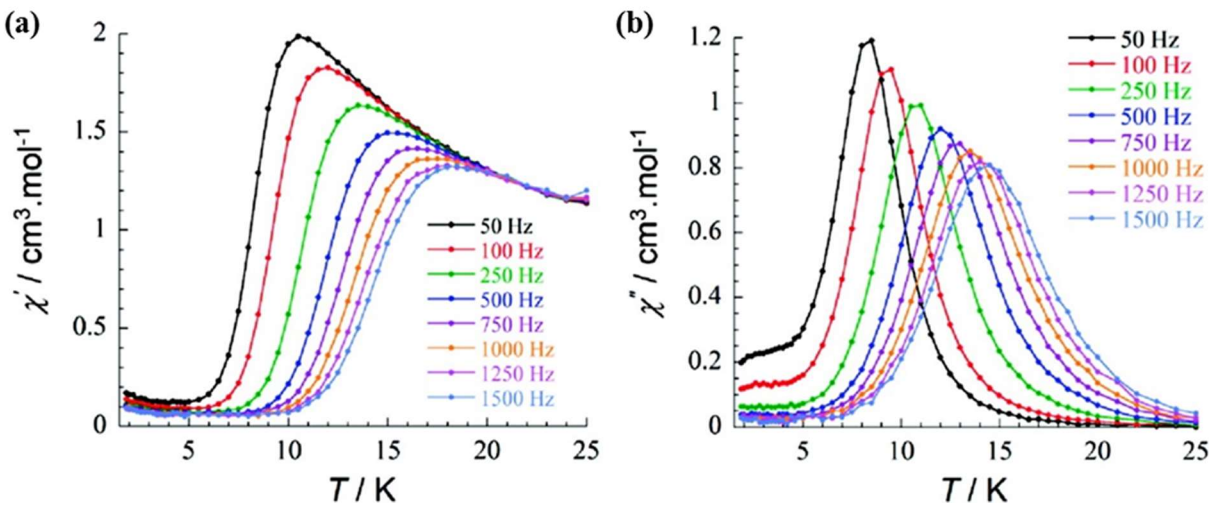

Figure 1.29. Example of *ac* magnetic susceptibility data plotted as: **(a)** in-phase (χ_M'), and **(b)** out-of-phase (χ_M'') *vs.* temperature (T) diagrams showing frequency-dependent signals at different temperatures under a zero static field. Adapted from Ref. 43 with permission from the American Chemical Society.

The relaxation of magnetization is a kinetic process in the thermally activated regime and can be described by the Arrhenius law (Eqn. 1.19). From an ln(τ) *vs.* 1/T plot it is possible to calculate the effective energy barrier for the magnetization reversal (U_{eff}) and the pre-exponential factor, τ_0 (Figure 1.30). The U_{eff} is determined by the gradient of the ln(τ) *vs.* 1/T plot. The largest energy barrier been reported to date is 1815 K for a $[Dy(O^tBu)_2(py)_5]^+$ SIM with a pentagonal bipyramidal coordination geometry and a blocking temperature of 14 K.[65] At each peak maxima in the χ_M'' *vs.* T plot, for a given temperature and frequency, the relaxation time, τ, can be determined using Eqn. 1.20.

$$\tau(T) = \tau_0 \, exp(\frac{U_{eff}}{k_B T}) \qquad \textbf{Eqn. 1.19}$$

$$\tau = \frac{1}{2\pi\nu} \qquad \textbf{Eqn. 1.20}$$

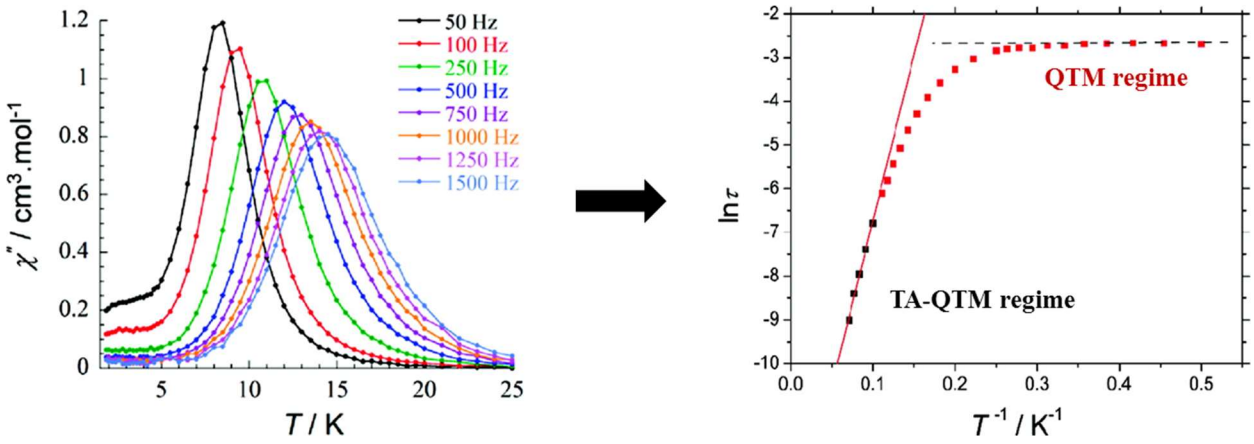

Figure 1.30. Example of an Arrhenius-type plot which includes the temperature dependence of the magnetization relaxation time in the form of an ln(τ) *vs.* T^{-1} diagram (right). The relaxation times for each temperature and frequency are calculated by Eqn. 1.20 based on the χ_M'' *vs.* T diagram (left). Adapted from Ref. 43 with permission from the American Chemical Society.

In the majority of SMMs, instead of entirely visible peaks in the out-of-phase component of the *ac* diagrams, tails of peaks are observed in the operating temperature limit of the conventional SQUID magnetometers (T > 1.8 K); these tails of peaks are indicative of the presence of quantum tunneling of magnetization (QTM). This phenomenon is usually observed at low temperatures (T < 10 K), where the magnetization can relax through the energy barrier. The application of a small, static *dc* field may shift the tails of *ac* peaks to higher temperatures and therefore the χ'' signals can become entirely visible. In this case, the QTM is reduced or even vanished completely. However, in some cases, the application of an external *dc* field induces the appearance of more than one thermally-activated relaxation processes and therefore two (or sometimes even more) peaks for the out-of-phase *ac* signals may be observed.

For systems that are not characterized by a single relaxation time, the $\chi_{ac}(\omega)$ is determined by Eqn. 1.21, where *a* is the distribution parameter of relaxation times and takes values between 0 and 1. When *a* is zero, Eqn. 1.21 is related to the Debye process with a single relaxation time, τ. The wider the distribution in relaxation times the larger the value of α.

$$\boldsymbol{\chi(\omega) = \chi_S + \frac{\chi_T - \chi_S}{1+(i\omega\tau)^{1-a}}} \qquad \textbf{Eqn. 1.21}$$

The χ'' *vs.* χ' plot at a certain temperature is known as a Cole-Cole (or Argand) plot (Figure 1.31). It is used for the detailed investigation of the relaxation times in a SMM. For a single relaxation time process, the shape of the Cole-Cole plot is a semicircle (Figure 1.31). Eqn. 1.22a describes the peak maximum, χ''_{max}, of the Cole-Cole plot for both single- and multiple-relaxation processes. In an ideal, single relaxation process, where $a = 0$, the χ''_{max} is determined by Eqn. 1.22b. However, when multiple relaxation processes are present and overlap with each other, the α value is larger than zero and thus the shape of Cole-Cole plot appears as unsymmetrical (Figure 1.32).

$$\chi''_{max} = \boldsymbol{\frac{1}{2}\,(\chi_T - \chi_S)\tan(\frac{\pi}{4}(1-\alpha))} \qquad \textbf{Eqn. 1.22a}$$

$$\chi''_{max} = \boldsymbol{\frac{1}{2}\,(\chi_T - \chi_S)} \qquad \textbf{Eqn. 1.22b}$$

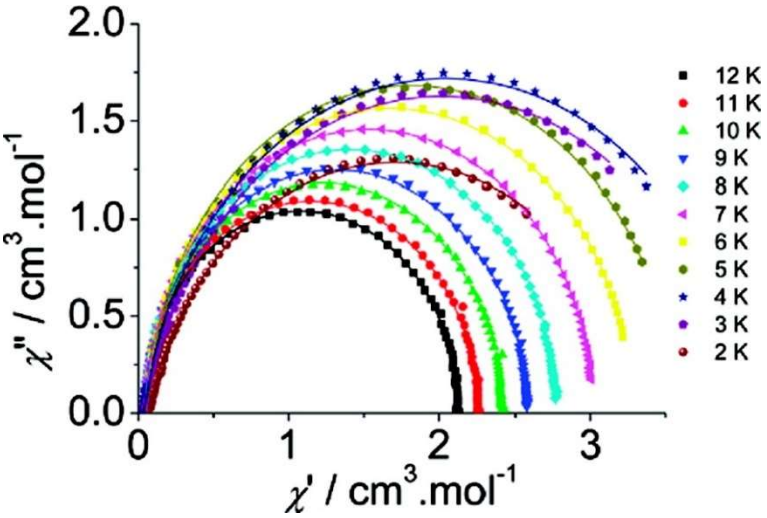

Figure 1.31. Example of Cole-Cole (Argand) plot for a {Dy_2} SMM with a single relaxation process and $a < 0.03$. The solid lines correspond to the best fit obtained with a generalized Debye model. Adapted from Ref. 43 with permission from the American Chemical Society.

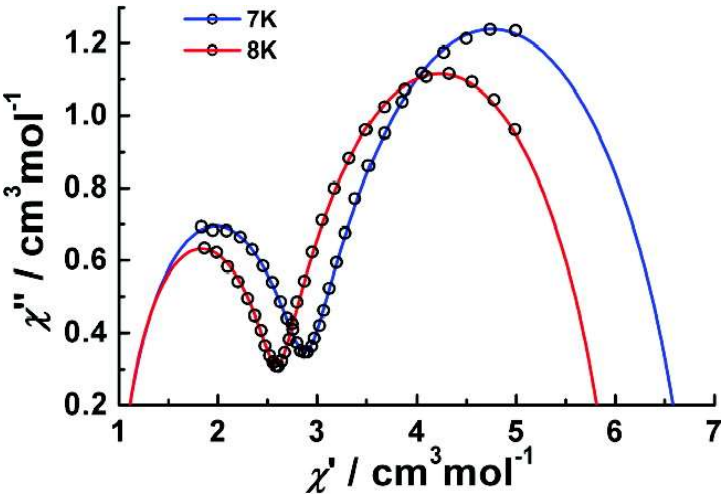

Figure 1.32. Example of Cole-Cole plot for a {Dy_4} SMM with a two-step relaxation. The solid lines correspond to the best fit obtained with a generalized Debye model accounting for the presence of two relaxation times (τ_1 and τ_2) and two distribution parameters, α_1 and α_2. Adapted from Ref. 66 with permission from the American Chemical Society.

To confirm the SMM behavior, the magnetization of a sample is measured under a cycling magnetic field starting from $+H$ to $-H$ and from $-H$ back to $+H$ at different low temperatures and field sweep rates. The magnetization in the presence of an energy barrier to spin reversal does not reach zero directly when the field is switched off; the spins are still aligned due to the presence of magnetic anisotropy. The spins that are driven by the thermal energy (kT) change their orientation, thus yielding a remnant magnetization (M_r) at zero field, where M_r is smaller than M_{sat}. Then, the opposite direction of the field is applied in order to reorient the direction of the spins. When $M = 0$, the magnetic field is known as the coercive magnetic field (H_c). A cycle of the measurement is completed when the field returns back to $+H$. When a compound retains its magnetization in the absence of external magnetic field a hysteresis loop in the *M vs. H* diagram is observed (Figure 1.33). The highest temperature that an open hysteresis loop is observed is the blocking temperature (T_B) of an SMM. It is important to mention that T_B depends on the sweep-rate of the magnetic field and a comparison of blocking temperatures among SMMs must be considered carefully. The highest T_B reported to date is 14 K for a N_2^{3-} radical-bridged $\{Tb_2\}$ SMM (Figure 1.33).[67]

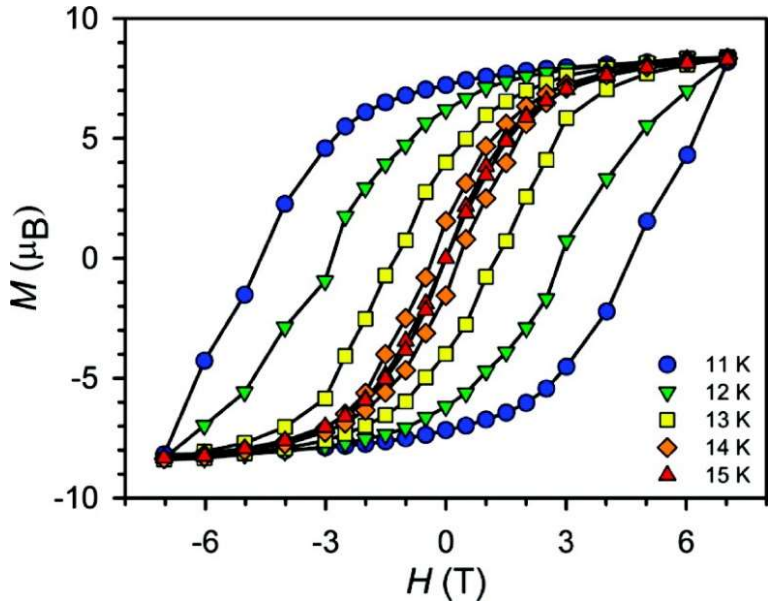

Figure 1.33. Example of hysteresis loops in magnetization (*M*) *vs. dc* magnetic field (*H*) plot for a {Tb_2} SMM from 11 to 15 K at an average sweep rate of 0.9 mT/s. Adapted from Ref. 67 with permission from the American Chemical Society.

As mentioned earlier, lanthanide SMMs often exhibit fast QTM resulting in a small or negligible remnant magnetization at $H = 0$. Thermally-assisted QTM occurs when the magnetization relaxes through the U_{eff} barrier from one microstate to its degenerate one. This phenomenon decreases the actual energy barrier while in the case that the magnetization relaxes between the ground-state $\pm m_J$ levels (pure QTM) the energy barrier becomes very small to zero. Ideally, the QTM can be observed and studied in magnetization *vs. dc* field hysteresis loops, appearing as distinct step-like features at periodic field values, at which levels on either side of the anisotropy barrier to relaxation are in resonance. The steps are thus field positions at which the magnetization relaxation rate increases owing to the onset of QTM. Such steps are a diagnostic signature of resonant QTM, and have been clearly seen only for a few classes of SMMs.[6,32,51]

Due to the increase in number of experimental data for Ln-based SMMs, the development of theoretical models for the determination of the lanthanide's electronic and magnetic properties has become more and more necessary. Despite the fact that *ab initio* studies are not relatively easy for some classes of lanthanide complexes (i.e. high nuclearity 4*f*-metal cluster compounds) due to the structural complexity and the large number of inequivalent metal ions with different coordination polyhedra (among other reasons), efforts were recently made to apply *ab initio* studies on various SMMs. This helped both theoretical and synthetic scientists to further understand the relationship between the electronic structure of the compound, which is resulted from the ligand-field splitting, and the magnetization dynamics.[68] CASSCF is a type of *ab initio* calculation based on the complete active space self-consistent field which is an approach that provides a model for the magnetic properties of Ln-based SMMs. By using MOLCAS software,[69] or other computational packages, it is feasible to evaluate the magnetic properties arising from the ligand field environment of the lanthanide ions (g_x, g_y, g_z values, single-ion anisotropic axes, etc.) followed by a comparison of the theoretical findings with the experimental data.

1.5 ***Lanthanide Complexes in the Field of Optics***

Luminescence is a property of molecules (organic and inorganic) or ions that leads to the emission of light as a result of chemical reactions, electrical energy or absorption of electromagnetic radiation (in the form of photons). The latter is known as photoluminescence (PL) emission. As electrons absorb light with certain energy they proceed to an excited state and due to their energetically unstable situation they return back to the ground state. This transition to

a lower energy state, after the excitation, releases energy either as radiative, with simultaneous light emission, or non-radiative decays. Relaxation can be either from a singlet excited-state, where the spin is antiparallel with regards to the spin in the ground-state, or from a triplet excited state in which the spin is parallel to the one in the ground state. Depending on the relaxation pathway luminescence can be either fluorescence or phosphorescence, respectively.[70]

A typical Jablonski diagram (Figure 1.34)[71] for an organic chromophore describes the energy states of the compound with respect to the electronic transitions between them (absorption and emission). The absorption and emission of light arises from the electrons in the π-orbitals of the organic chromophore. In particular, the S_0, S_1 and S_2 symbols describe the singlet ground-state, the first-excited, and the second-excited electronic states, respectively, while the symbol *T* represents the triplet state. The vibrational energy levels of each state are shown with the integral numbers 0, 1, 2, etc., and they are arranged as vertical and horizontal lines in order to account for the energy and spin multiplicity. The excitation process always occurs *via* a singlet-to-singlet transition and the emission decays following certain selection rules, such as the spin selection rule. According to this rule, the transitions between states with different spin multiplicity are forbidden, although they may take place if the metal center possesses strong spin-orbit coupling.[72]

An electron in an excited state can follow different ways to relax back to the ground state depending on its energy. These processes can potentially be non-radiative, including *internal vibrational relaxation* (IVR), *internal conversion* (IC) or *intersystem crossing* (ISC). An electron rapidly decays from an energetically disfavored, higher in energy state than the first excited level, to a smaller-energy level *via* vibrational relaxation losing kinetic energy. This relaxation process has a lifetime of 10^{-14} - 10^{-12} s. In internal conversion, an electron decays from a second

excited singlet state to the first excited singlet state with a lifetime of 10^{-12} s. An electron in the first excited state can either return back to the ground state with a concomitant photon emission [fluorescence process (F)] or undergo intersystem crossing to an excited triplet state and then relax to the ground state *via* phosphorescence emission (P). According to the spin selection rule, phosphorescence emission is a spin forbidden process which is accompanied by a lifetime in the range of microseconds or greater.[73] Moreover, lifetimes for fluorescence emission decay are near 10 ns. In some cases, quenching of fluorescence decay may occur decreasing the intensity of the resulting emission. Quenching originates from excited state reactions, energy transfer, complex-formation, and collisional quenching. In the majority of cases, significant fluorescence quenchers are paramagnetic species and dissolved oxygen.[70]

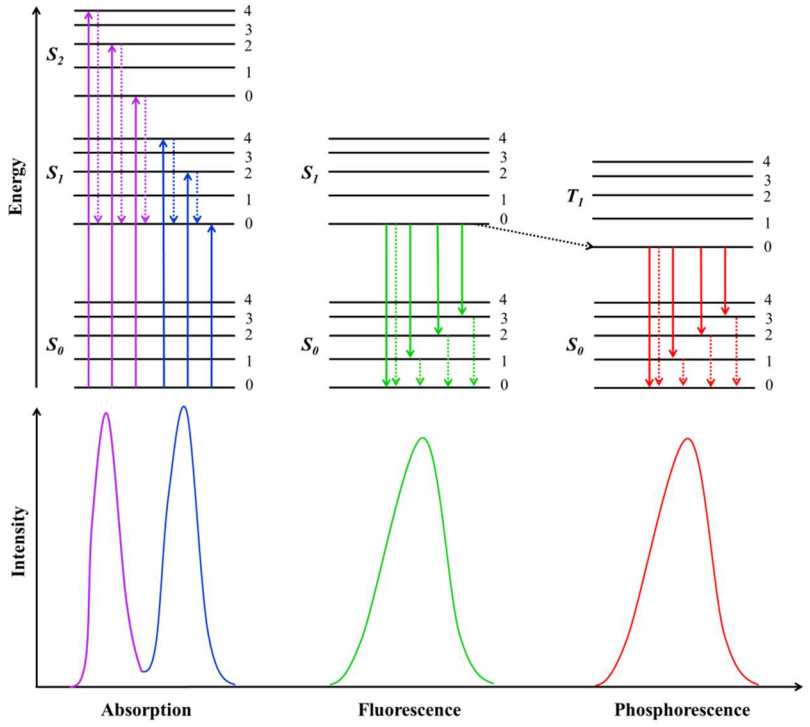

Figure 1.34. A general representation of a Jablonski energy diagram. Radiative transitions indicating absorption (violet, blue) or emission (green for fluorescence and red for

phosphorescence) of light are depicted by solid arrows. Non-radiative transitions (violet, blue, green and red) are represented by dashed arrows. Reproduced from Ref. 58a.

Lanthanides are well-known for their optical properties and therefore they find numerous applications in industry and technology. Some selected examples of their employment as devices in our daily life are in lighting equipment, televisions, computer displays, biomedical analysis techniques, medical diagnosis and photodynamic therapy. Due to the large variety of applications, lanthanide ions and their compounds have attracted the interest of many researchers from diverse disciplines.[74] Across the lanthanide series, except for La^{III} and Lu^{III} which show no emissions, the 4*f*-metal luminescence emissions cover the entire electromagnetic spectrum. Gd^{III} emits at the UV region, Sm^{III}, Eu^{III}, Tb^{III}, Dy^{III}, Tm^{III} at the visible part, and Pr^{III}, Nd^{III}, Ho^{III}, Er^{III} and Yb^{III} at the near-infrared region of the electromagnetic spectrum. Typical emission spectra of lanthanide ions consist of sharp lines/bands resulting from the *f-f* transitions (Figures 1.35 and 1.36).[1e]

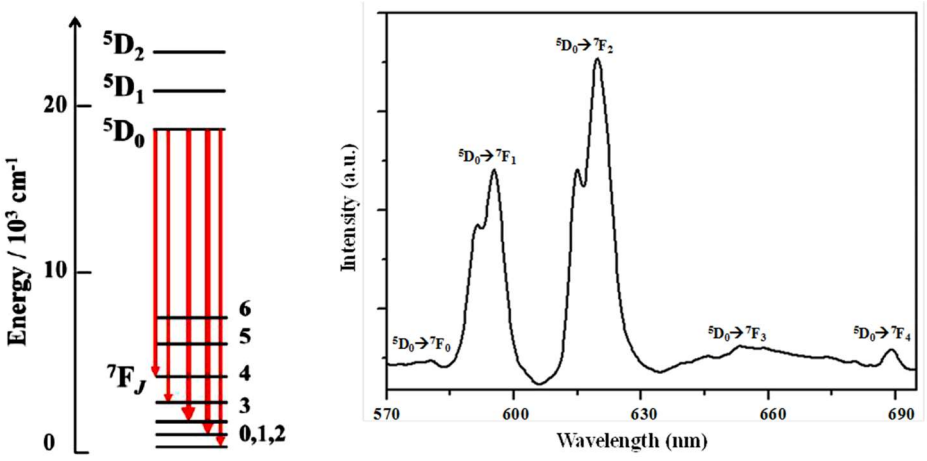

Figure 1.35. The energy levels (left) and emission spectrum (right) of Eu^{3+} in complex $[Eu^{III}(SO_4)_2]^-$. Reproduced from Ref. 75.

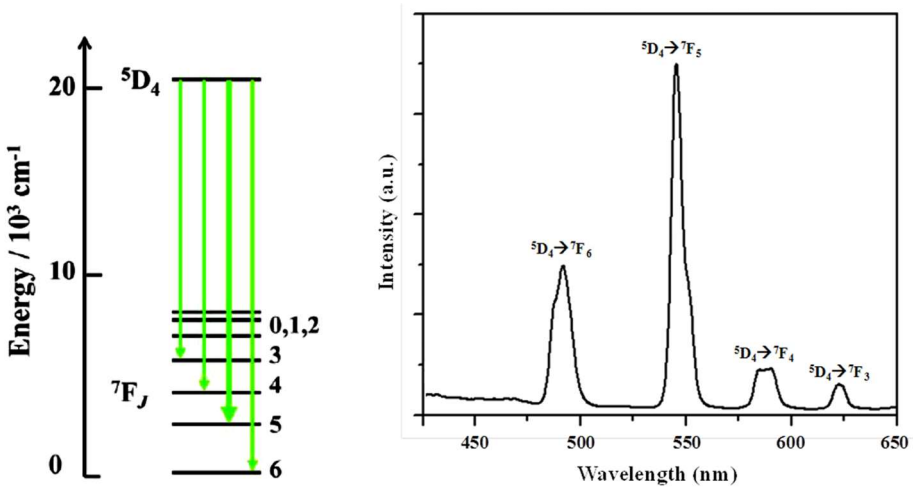

Figure 1.36. The energy levels (left) and emission spectrum (right) of Tb^{3+} in complex $[Tb_2(SO_4)_3(H_2O)_8]$. Reproduced from Ref. 75.

Due to the inner character of 4*f*-orbitals, the internuclear distances are not affected by the bonding environment. As a consequence, the distances between the ground and excited states remain almost constant leading to narrow, sharp bands and small Stokes' shifts. On the contrary, broad emission bands and large Stokes' shifts are observed in the emission spectra of organic molecules (Figure 1.37).[76]

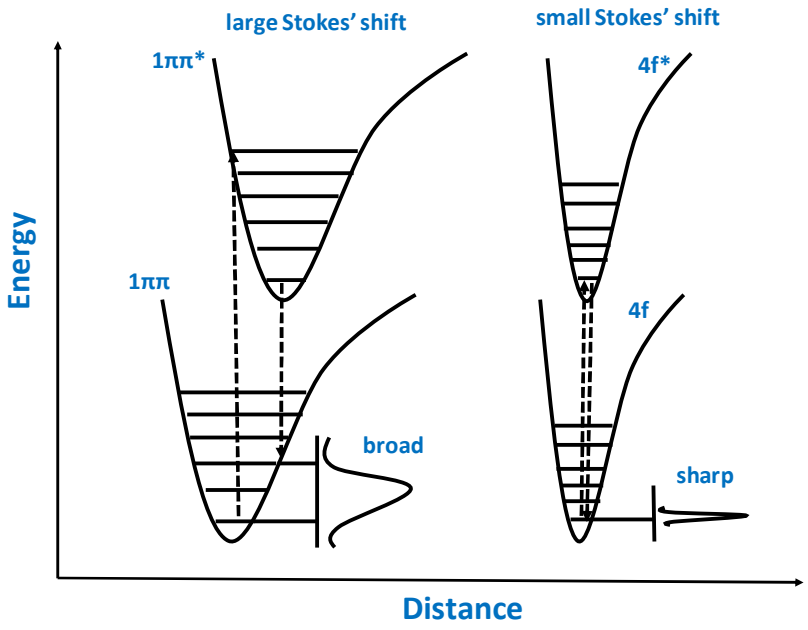

Figure 1.37. Schematic representation of Stokes' shifts for an organic compound (left) and a lanthanide element (right). Reproduced from Ref. 76.

Direct excitation into the 4*f* excited states hardly leads to intense photoluminescence emission as a result of the weak dipole strength of the *f-f* transitions. Alternatively, in order to enhance the energy of these transitions different chromophore groups are used to coordinate to emissive lanthanide ions, an effect which is known as the luminescence sensitization or the "antenna effect".[77] The idea is based on the ability of chromophores to absorb light acting as "antenna" and consequently transferring this energy to the Ln^{3+} ion(s) *via* intramolecular energy transfer. This results in the characteristic metal-centered photoluminescence emission for the lanthanide coordination complex (Figure 1.38). Moreover, for the redox-active Ln^{3+} ions (Sm^{3+}, Eu^{3+} and Yb^{3+}) the sensitization may occur through a charge-transfer process. This process is possible when an intense ligand-to-metal charge transfer state absorbs light followed by an energy transfer to the 4*f*-states of the Ln^{3+} ion.[78]

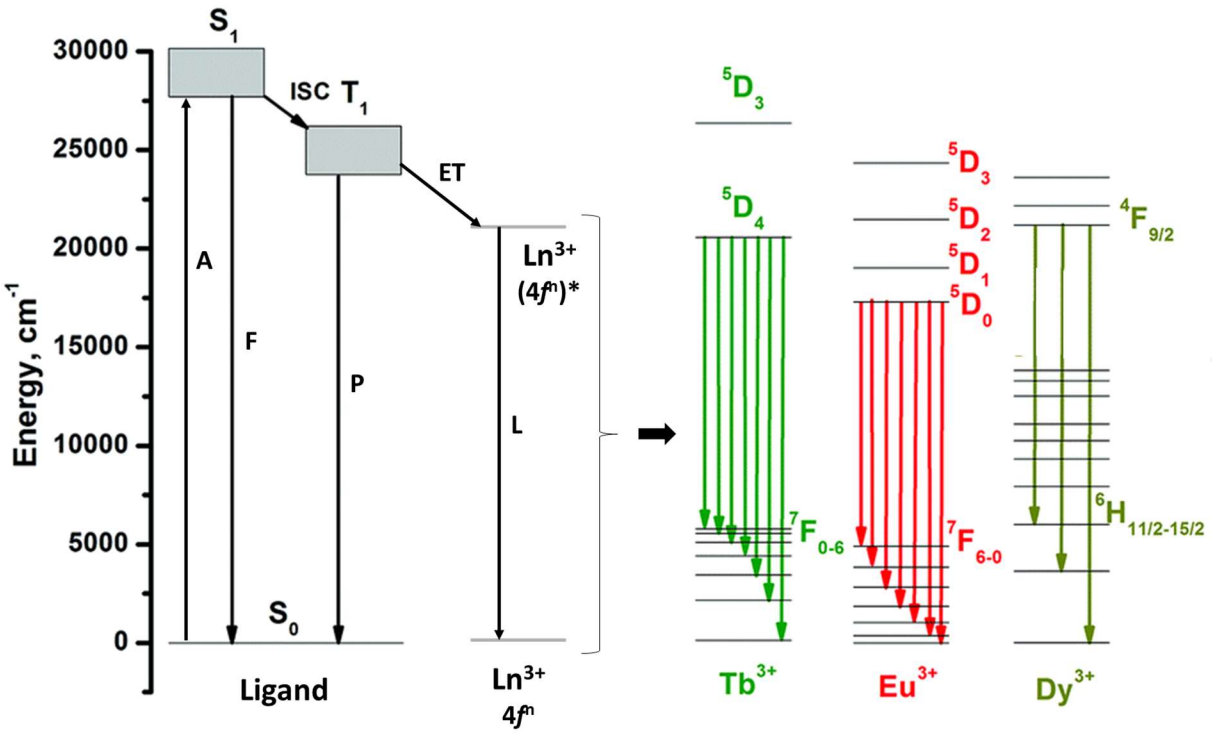

Figure 1.38. Schematic representation of the photophysical processes that could potentially take place in Ln^{3+} coordination complexes ("antenna effect"). Abbreviations: A = absorption; F = fluorescence; P = phosphorescence; L = lanthanide-centered luminescence; ISC = intersystem crossing; ET = energy transfer; S = singlet; T = triplet. Solid vertical lines indicate radiative transitions. Reproduced from the Ref. 79.

According to the literature, one of the most common processes for the sensitization of near-infrared emitted lanthanides (Nd^{3+}, Er^{3+} and Yb^{3+}) is the attachment of strongly absorbing chromophore containing *d*-block metal ions (Ru^{2+}, Ir^{2+}, Pt^{2+} etc.) on the Ln^{3+} ion. The former has the ability to absorb at long wavelengths compared to the common organic chromophores.[80] Scheme 1.5 shows an example of these structures that have been used for many years as inorganic phosphors for lighting applications.

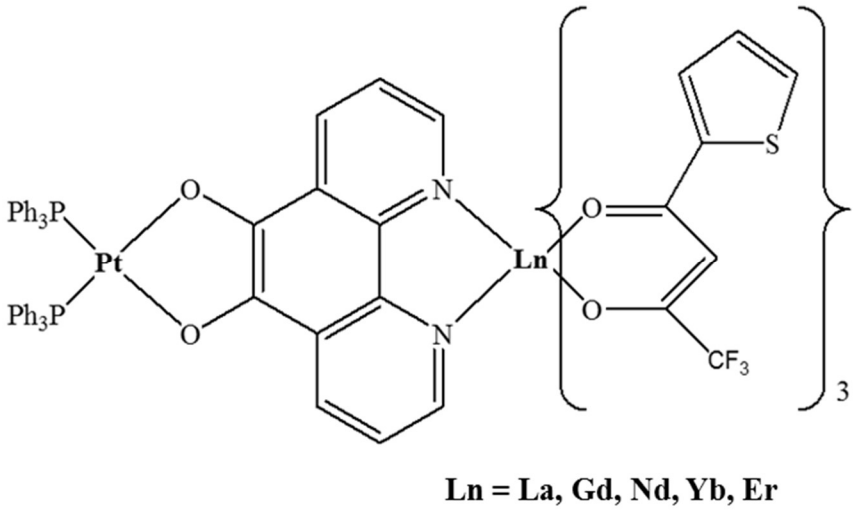

Scheme 1.5. Example of a complex with an attached chromophore that contains coordinated *d*-block metal ions.[80e]

The present thesis is focused on the synthesis of lanthanide complexes with photoluminescence properties by sensitizing the metal ions with organic ligands comprising chromophore groups. As a consequence, the choice of the ligand plays a crucial role for the enhancement of the photoluminescence properties. Towards that end, it should be considered that lanthanide ions are able to emit only when the *f-f* transitions are from the resonance states, which are different for each 4*f*-metal ion. Metal-centered emission can be observed when the excitation energy is deactivated by internal conversion to the resonance state of the Ln^{3+} ion. An organic ligand can be an effective "antenna" when its triplet state lies almost in the same or relatively higher energy with the resonant state of the metal ion in order for the energy transfer to occur (Figure 1.38). In some cases, the energy transfer process is not very efficient, resulting in the concomitant appearance of ligand- and metal-centered emissions or solely ligand-centered emissions.

1.6 ***Long- and Short-Term Research Objectives***

The long-term research objective of the present thesis is the synthesis of new oligo- and polynuclear 4*f*-metal complexes with interesting structural, magnetic and luminescent properties. In an attempt to reach this research goal, the project was divided into the following short-term research objectives: (i) the synthesis of novel lanthanide clusters bearing different Schiff base ligands; (ii) the growth of single-crystals suitable for X-ray diffraction studies in order to elucidate the crystal structures of the targeted compounds; (iii) the complete spectroscopic and physicochemical characterization of all compounds in solution and/or solid-state, utilizing IR, UV/Vis, ESI-MS, and elemental analyses techniques; (iv) the performance of *dc* and *ac* magnetic susceptibility studies in order to assess the bulk magnetic properties and magnetization dynamics of the paramagnetic 4*f*-metal complexes; and (v) the performance of photoluminescence studies in order to evaluate the optical response of the synthesized coordination compounds and the organic Schiff base ligands.

For the synthesis of new lanthanide clusters, three different types of Schiff bases were used in the present thesis as primary organic bridging and chelating ligands. Specifically, the ligands *N*-salicylidene-*o*-aminophenol ($saphH_2$), *N*-salicylidene-2-aminocyclohexanol ($sachH_2$; mixture of *trans*- and *cis*-, and the pure *trans*-analogue), and *N*-salicylidene-2-amino-5-chlorobenzoic acid ($sacbH_2$) have been explored for their ability to form lanthanide clusters with magnetic and luminescent properties.

Chapter 2

New structural topologies in 4*f*-metal cluster chemistry from vertex-sharing butterfly units: {Ln_7} complexes exhibiting slow magnetization relaxation and ligand-centered emissions

2.1. *Preface*

One of the current most attractive directions in modern inorganic and coordination chemistry is towards the synthesis of complex molecular materials with appealing structures and multiple physical properties. The goal is undoubtedly to construct multifunctional (or hybrid) materials, where two or more properties will cooperate synergistically in the presence of an external stimulus, such as light, electric current or magnetic field.[81] In order to achieve the synthesis of such molecular, zero-dimensional (0-D) species, the nature of metals and bridging ligands is of vital importance.

In terms of metal ions, lanthanides have shown a remarkable ability to yield beautiful structures with interesting magnetic and optical properties.[20,21] This is due to the preference of 4*f*-metal ions to bind to *O*- and/or *N*-based ligands, the nature of the *f*-electrons and orbitals, and the unique electronic structures they possess (ground state: $^{2S+1}L_J$). The large number of unpaired electrons, in conjunction with the appreciable magnetoanisotropy originating from the spin-orbit coupling and ligand field effects, of some 4*f*-metal ions (i.e., Dy^{III} and Tb^{III}) make them suitable candidates for single-molecule magnetism behaviors.[24a,62,82] Single-molecule magnets (SMMs) derive their properties from the combination of a large magnetic moment in the ground state with

a large magnetic anisotropy, as reflected in a large and negative zero-field splitting parameter (D).[83] As a result, SMMs often possess an appreciable barrier to magnetization relaxation at low temperatures, and they display out-of-phase *ac* magnetic susceptibility signals and magnetization hysteresis loops.[51a,84] In addition, 4*f*-metal complexes have also shown intense, sharp and long-lived emissions;[2,85] they can thus be used for a variety of optical and medical applications such as display devices, luminescent sensors, and probes for clinical use.[33] This particularly applies to Eu^{III} and Tb^{III} complexes with red and green luminescence due to $^5D_0 \rightarrow {}^7F_J$ and $^5D_4 \rightarrow {}^7F_J$ transitions, respectively, and occasionally to Dy^{III} compounds with characteristic blue or yellow-centred $^4F_{9/2} \rightarrow {}^6H_J$ transitions.[1,86]

Thus, it becomes apparent that polynuclear 4*f*-metal clusters can satisfy all the above requirements and yield both structurally interesting molecular species and emissive SMMs.[87] The nature of the organic bridging ligand becomes of great importance because it will not only foster the formation of a high-nuclearity species but also dictate the nature of the intramolecular magnetic exchange interactions between the metal ions and the efficiency of the energy transfer from its triplet state to the metals' accessible emissive states ("antenna" effect). For these reasons, it was decided to follow up with the group's previous success in employing Schiff base bridging ligands in 3*d*-metal cluster chemistry,[48] but this time to explore their use in lanthanide chemistry as a means of obtaining novel compounds with unprecedented topologies and magneto-optical behaviors. Herein it is shown that the use of tridentate chelating/bridging ligand *N*-salicylidene-*o*-aminophenol ($saphH_2$) in 4*f*-metal chemistry can lead to a new family of heptanuclear clusters with an unforeseen metal vertex-sharing double-butterfly topology, and SMM and emission behaviors. It is also demonstrated that although $saphH_2$ is not a new ligand in

lanthanide chemistry,[46,47] the hydrolysis of the metal ions *via* the use of a different combination of solvent and starting materials can lead to higher nuclearity products.

2.2. ***Experimental Section***

2.2.1. Physical Measurements

Elemental analysis: Elemental analyses (C, H, and N) were performed on a Perkin-Elmer 2400 Series II Analyzer.

FT-IR spectroscopy: Infrared (IR) spectra were recorded in the solid state on a Bruker FT-IR spectrometer (ALPHA Platinum ATR single reflection) in the 4000-450 cm^{-1} range. Notation for IR bands: vs = very strong; s = strong; m = medium; w = weak; b = broad; wb = weak broad.

Magnetic susceptibility measurements: Variable-temperature direct current (*dc*) magnetic susceptibility studies were performed at the Chemistry Department of the University of Barcelona using a Quantum Design SQUID magnetometer equipped with a 7 T magnet and operating in the 1.8-300 K range. The Superconducting QUantum Interference Device (SQUID) allows for the complete *dc* and *ac* study of the magnetic properties of bulk and molecule-based materials at various temperatures and magnetic fields. The *dc* scan mode provides continual plotting and capture of raw magnetic data points at static or sweeping fields and temperatures. All the studied solid-state samples were embedded in solid eicosane to prevent torquing. Pascal's constants were used to estimate the diamagnetic corrections, which were subtracted from the experimental susceptibilities to give the molar paramagnetic susceptibilities (χ_M).[61]

Photoluminescence studies: Excitation and emission spectra for all complexes were recorded in the solid state using a Cary Eclipse spectrofluorometer.

2.2.2. Synthesis

General considerations: All manipulations were performed under aerobic conditions using materials as received. All chemicals were purchased from Sigma-Aldrich and Alfa Aesar. Chemicals and solvents were used as received without further purification. The organic ligand saphH_2 (orange crystalline solid) was synthesized by following a well-known synthetic protocol for the synthesis of Schiff base ligands. This includes the condensation in refluxing absolute methanol of equimolar amounts of 2-aminophenol and salicylaldehyde, in accordance with literature methods for the same ligand.[88]

(NHEt$_3$)[Gd$_7$(OH)$_2$(saph)$_{10}$(Me$_2$CO)$_2$] (1): To a stirred, orange solution of saphH_2 (0.043 g, 0.2 mmol) and NEt_3 (84 μL, 0.6 mmol) in Me_2CO (20 mL) was added solid $Gd(NO_3)_3 \cdot 6H_2O$ (0.045 g, 0.1 mmol). The resulting yellow solution was stirred for 30 min, during which time all the solids dissolved and the color of the solution became more intense yellow. The solution was filtered, and the filtrate was left to evaporate slowly at room temperature. After 2 days, very thin needle-like crystals of **1** had appeared, and these were found to be suitable enough for X-ray diffraction studies. The crystals were collected by filtration, washed with cold Me_2CO (2 x 2 mL) and dried in air. The yield was 45 %. The air-dried solid was found to be slightly hygroscopic and analyzed as **1**$\cdot 2H_2O$: C, 48.71; H, 3.57; N, 4.40 %. Found: C, 48.62; H, 3.42; N, 4.49 %. Selected IR data (ATR): ν = 3010 (w), 1690 (w), 1601 (m), 1580 (m), 1533 (m), 1463 (m), 1441 (m), 1385 (m), 1342 (w), 1325 (w), 1274 (m), 1249 (m),

1169 (w), 1144 (m), 1106 (w), 1030 (w), 966 (w), 913 (m), 867 (w), 846 (m), 826 (w), 736 (s), 646 (wb), 597 (m), 537 (w), 496 (m), 444 (w).

$(NHEt_3)[Tb_7(OH)_2(saph)_{10}(Me_2CO)_2]$ (2): This complex was prepared in the same manner as complex **1** but using $Tb(NO_3)_3 \cdot 6H_2O$ (0.045 g, 0.1 mmol) as the Ln salt. Again, after 2 days, very thin needle-like crystals of **2** had appeared, albeit this time the crystals were not of sufficient quality (very small in size) to allow for a complete X-ray diffraction analysis. The crystals were collected by filtration, washed with cold Me_2CO (2 x 2 mL) and dried in air. The yield was 52 %. The air-dried solid was analyzed as **2**·$2H_2O$: C, 48.55; H, 3.56; N, 4.39 %. Found: C, 48.36; H, 3.44; N, 4.55 %. Selected IR data (ATR): ν = 3011 (w), 1690 (w), 1601 (m), 1580 (m), 1533 (m), 1463 (m), 1441 (m), 1385 (m), 1342 (w), 1325 (w), 1274 (m), 1251 (m), 1169 (w), 1144 (m), 1107 (w), 1030 (w), 965 (w), 914 (m), 868 (w), 847 (m), 827 (w), 737 (s), 659 (wb), 599 (m), 538 (w), 497 (m), 447 (w).

$(NHEt_3)[Dy_7(OH)_2(saph)_{10}(Me_2CO)_2]$ (3): This complex was prepared in the same manner as complex **1** but using $Dy(NO_3)_3 \cdot 6H_2O$ (0.046 g, 0.1 mmol) as the Ln salt. Again, after 2 days, very thin needle-like crystals of **3** had appeared and these were not suitable for a complete X-ray diffraction analysis. The crystals were collected by filtration, washed with cold Me_2CO (2 x 2 mL) and dried in air. The yield was 55 %. The air-dried solid was analyzed as **3**·$2H_2O$: C, 48.21; H, 3.53; N, 4.35 %. Found: C, 48.16; H, 3.29; N, 4.48 %. Selected IR data (ATR): ν = 3013 (w), 1690 (w), 1602 (m), 1580 (m), 1533 (m), 1463 (m), 1441 (m), 1384 (m), 1342 (w), 1325 (w), 1274 (m), 1252 (m), 1169 (w), 1143 (m), 1106 (w), 1029 (w), 966 (w), 913 (m), 868 (w), 846 (m), 827 (w), 737 (s), 666 (wb), 598 (m), 538 (w), 498 (m), 447 (w).

2.2.3. Single-crystal X-ray Crystallography

Crystalline material of the compounds $(NHEt_3)[Ln_7(OH)_2(saph)_{10}(Me_2CO)_2]$ [Ln^{3+} = Gd^{3+} (**1**), Tb^{3+} (**2**) and Dy^{3+} (**3**)] were manually harvested and mounted on cryoloops using an appropriate inert oil.[89] Complete diffraction data have been collected only for compound **1** at 150.0(2) K on a Bruker X8 Kappa APEX II Charge-Coupled Device (CCD) area-detector diffractometer controlled by the APEX2 software package (Mo K_α graphite-monochromated radiation, $\lambda = 0.71073$ Å),[90] and equipped with an Oxford Cryosystems series 700 cryostream monitored remotely with the software interface Cryopad.[91] As mentioned previously, the small size and apparently the weak diffraction of several crystals of compounds **2** and **3** tested in the X-ray diffractometer prevented the acquisition of full data sets; however, it was possible to obtain unequivocal indexations of the respective unit cells.

The images collected for compound **1** were processed with the software SAINT+,[92] and the absorption effects were corrected by the multi-scan method implemented in SADABS.[93] The structure was solved using the algorithm implemented in SHELXT-2014,[94,95] allowing the immediate location of all the Gd^{3+} centers. Remaining non-hydrogen elements were located from difference Fourier maps and calculated by successive full-matrix least-squares refinement cycles on F^2 using SHELXL-v.2014.[94,96] All non-hydrogen atoms of the anionic Gd_7 cluster compound were successfully refined with anisotropic displacement parameters, except from the carbon atoms of the coordinated acetone (Me_2CO) molecules and the $NHEt_3^+$ counter-cation which were only refined with isotropic parameters. Hydrogen atoms were placed at their geometrical positions and included in subsequent refinement cycles. A substantial dispersed electron density was found, most probably due to disordered lattice solvate molecules. The effort to locate and model these solvent molecules revealed to be unsuccessful, and the investigation of the total

potential solvent area using the software package PLATON[97] revealed the presence of voids with potential solvent accessible void volume. Consequently, the contribution of these highly disordered molecules was removed using the program SQUEEZE.[98] Unit cell parameters, structure solution and refinement details for all complexes are listed in Table 2.1.

Table 2.1. Crystal and structure refinement details for complexes **1**-**3**.

	1	**2**	**3**
Formula	$C_{142}H_{120}Gd_7N_{11}O_{24}$	$C_{142}H_{120}Tb_7N_{11}O_{24}$	$C_{142}H_{120}Dy_7N_{11}O_{24}$
Fw / g mol^{-1}	3465.23	3477.06	3502.08
Crystal type	Yellow needle	Yellow needle	Yellow needle
Crystal size / mm^3	0.16×0.08×0.06	0.12×0.04×0.03	0.10×0.05×0.03
Crystal system	Triclinic	Triclinic	Triclinic
Space group	*P*-1	Bravais Lattice *P*	Bravais Lattice *P*
a / Å	15.5132(16)	15.793(2)	15.642(2)
b / Å	20.762(2)	20.459(3)	20.753(2)
c / Å	24.831(3)	25.003(3)	25.149(3)
α / º	106.288(4)	106.025(5)	105.978(5)
β / º	103.085(5)	102.852(6)	102.976(2)
γ / º	105.827(4)	105.789(5)	106.012(4)
Volume / Å^3	6977.1(1)	7074.6(2)	7134.0(2)
Z	2	-	-
ρ_{calc} / g cm^{-3}	1.649	-	-
μ / mm^{-1}	3.348	-	-

θ range / °	3.68 – 25.03	-	-
Index ranges	$-18 \le h \le 18$	-	-
	$-24 \le k \le 24$		
	$-28 \le l \le 28$		
Collected reflections	121671	-	-
Independent	23766	-	-
reflections	(R_{int} = 0.0507)		
Final $R^{a,b}$ indices	$R1$ = 0.0652	-	-
[I>2σ(I)]	$wR2$ = 0.1398		
Final $R^{a,b}$ indices	$R1$ = 0.0864	-	-
(all data)	$wR2$ = 0.1489		
$(\Delta\rho)_{max,min}$ / e Å^{-3}	1.881 and −1.151	-	-

[a] $R1 = \Sigma(||F_o| - |F_c||)/\Sigma|F_o|$. [b] $wR2 = [\Sigma[w(F_o^2 - F_c^2)^2]/\Sigma[w(F_o^2)^2]]^{1/2}$, $w = 1/[\sigma^2(F_o^2) + (ap)^2 + bp]$, where $p = [\max(F_o^2, 0) + 2F_c^2]/3$.

2.3. ***Results and Discussion***

2.3.1. Synthetic Comments

Based on the proposed synthetic approaches for lanthanide clusters, as these were previously mentioned, and considering the requirements needed in order for these complexes to exhibit single-molecule magnetic and luminescent properties, a general synthetic scheme was followed. The general synthetic route for the isolation of these 0-D complexes includes reactions

between LnX_3 starting materials (X^- = various) and a suitable organic chelating/bridging ligand that contains acidic H-atoms. The nature of the X^- group and the organic ligand play crucial role for the isolation of the reported complexes. X^- can be various organic or inorganic anions capable of bridging the lanthanide ions and therefore increasing the overall nuclearity of the compounds. X^- can also terminate the aggregation of the metal ions, thus eliminating the formation of multidimensional coordination polymers which was out of the scope of the present project. Moreover, the X^- groups can act as counter-anions stabilizing any possible cationic cluster.

In the present study, various LnX_3 starting materials containing inorganic anions such as halides, NO_3^-, ClO_4^- or $CF_3SO_3^-$, in the presence of the chelating/bridging Schiff base ligand $saphH_2$, were employed in an attempt to isolate new polynuclear Ln/$saphH_2$ complexes. A series of one-pot reactions between the $LnX_3{\cdot}6H_2O$ and the ligand, in a variety of molar ratios and solvents or mixtures of solvents and in the presence of external base, were performed. The employment of the base NEt_3 was found to facilitate the deprotonation of $saphH_2$. The reaction of $Ln(NO_3)_3{\cdot}6H_2O$, $saphH_2$, and NEt_3 in a 1:2:6 molar ratio in Me_2CO gave a yellow solution that upon slow evaporation at room temperature afforded yellow, very thin needle-shaped crystals of $(NHEt_3)[Ln_7(OH)_2(saph)_{10}(Me_2CO)_2]$ (Ln = Gd (**1**); Tb (**2**); Dy (**3**)) in 45-55% isolated yields. The formation of **1** as a representative example can be summarized by the balanced Eqn. 2.1.

$$7\ Gd(NO_3)_3{\cdot}6H_2O + 10\ saphH_2 + 22\ NEt_3 + 2\ Me_2CO \rightarrow$$

$$(NHEt_3)[Gd_7(OH)_2(saph)_{10}(Me_2CO)_2] + 21\ (NHEt_3)(NO_3) + 40\ H_2O \qquad \textbf{Eqn. 2.1}$$

The reported reaction was performed in various solvents and mixture solvents with different polarities but only Me_2CO afforded a crystalline product suitable for X-ray diffraction studies. All the other solvents gave very soluble products, without leading to the formation of single-crystals from the corresponding solutions, or amorphous precipitates. Apart from facilitating the complete deprotonation of $saphH_2$, the organic base NEt_3 was also necessary for providing the Et_3NH^+ cations which were essential for the stabilization of the $[Ln_7(OH)_2(saph)_{10}(Me_2CO)_2]^-$ cluster anions. Different bases were also utilized albeit these have led to non-crystalline precipitates which were not able to further crystallize. The replacement of the NO_3^- groups in the lanthanide starting material by other anions did not lead to any new products. The chemical and structural identities of the complexes were confirmed by single-crystal X-ray crystallography (complete data set for **1** and unit cell determination for **2** and **3**), elemental analyses, IR spectral comparison (see the Appendix), and powder-XRD studies (Figure 2.1).

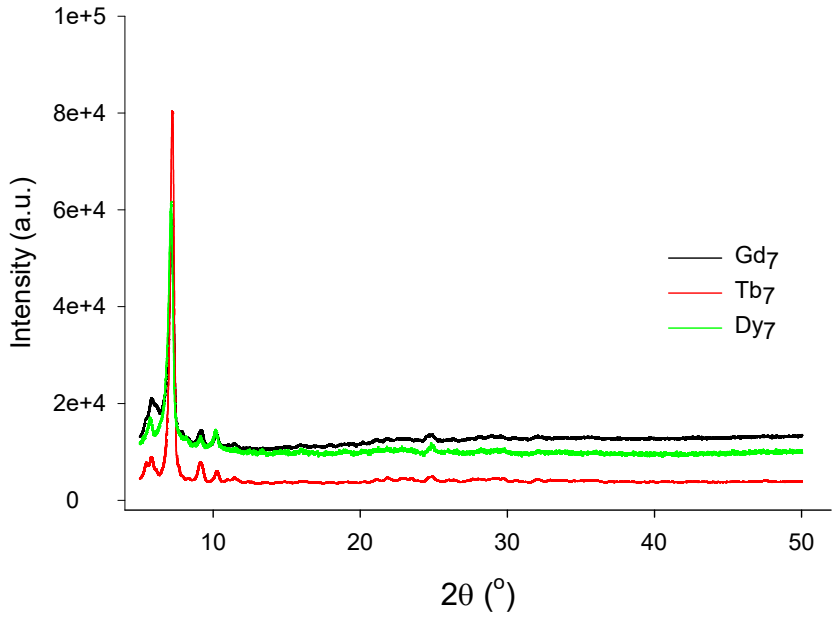

Figure 2.1. Powder-XRD spectra of complexes **1**-**3**.

2.3.2. Description of Structures

The formula of **1** is based on metric parameters (Table 2.2), charge balance considerations and O BVS calculations; the latter confirmed the assignment of the μ_3-bridging groups as OH^- ions (BVS 1.11-1.12).[99] The molecular structure of the anion of **1** (Figure 2.2) reveals the presence of seven Gd^{III} atoms bridged together by two μ_3-OH^- ions (O8, O11) and the phenoxido arms of two η^2:η^1:η^2:μ_3, four η^1:η^1:η^2:μ and four η^1:η^1:η^3:μ_3 $saph^{2-}$ ligands (Scheme 2.1).

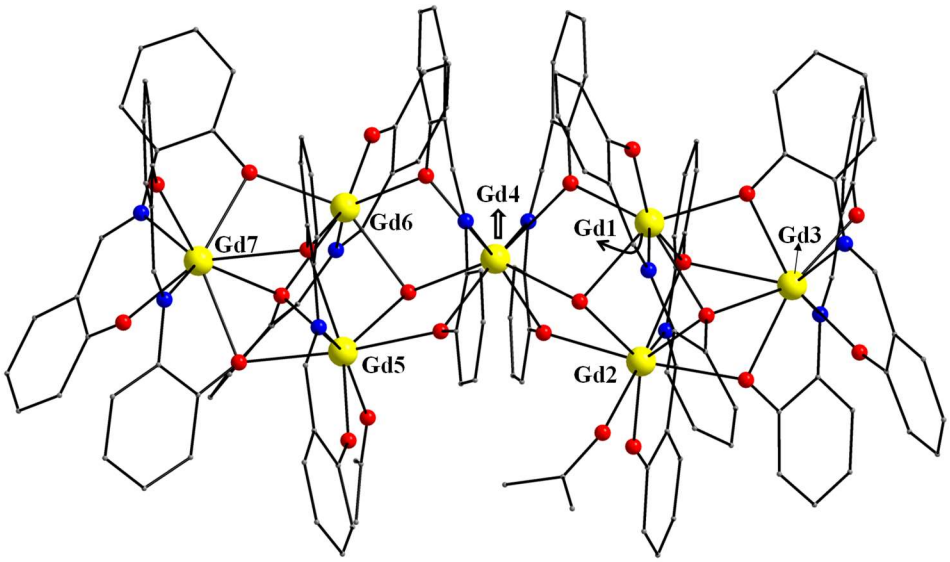

Figure 2.2. Molecular structure of the $[Gd_7(OH)_2(saph)_{10}(Me_2CO)_2]^-$ anion of complex **1.** H atoms are omitted for clarity. Color scheme: Gd^{III}, yellow; O, red; N, blue; C, dark gray.

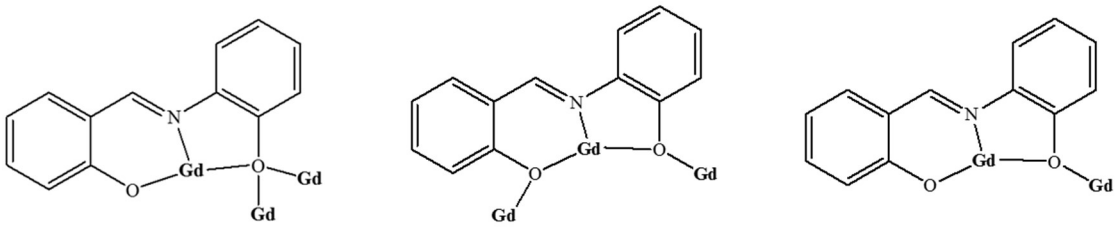

$\eta^1:\eta^1:\eta^3:\mu_3$ $\eta^2:\eta^1:\eta^2:\mu_3$ $\eta^1:\eta^1:\eta^2:\mu$

Scheme 2.1 Coordination modes of $saph^{2-}$ in complex **1**.

The complete $[Gd_7(\mu_3\text{-}OH)_2(\mu_3\text{-}OR)_4(\mu\text{-}OR)_8]^{7+}$ core of **1** (Figure 2.3) can be conveniently described as two $[Gd_4(\mu_3\text{-}OH)(\mu_3\text{-}OR)_2(\mu\text{-}OR)_4]^{5+}$ butterflies that share a common metal vertex (Gd4) at the wing-tip position. The $\mu_3\text{-}OH^-$ and $\mu_3\text{-}OR^-$ bridging groups are all displaced by 1.04-1.40 Å away from the Gd_4 best-mean-planes, implying a significant distortion of the butterflies and a subsequent asymmetrization of the overall structure. Peripheral ligation about the core is provided by the chelating part of the $saph^{2-}$ ligands and two terminally bound Me_2CO molecules on Gd2 and Gd5.

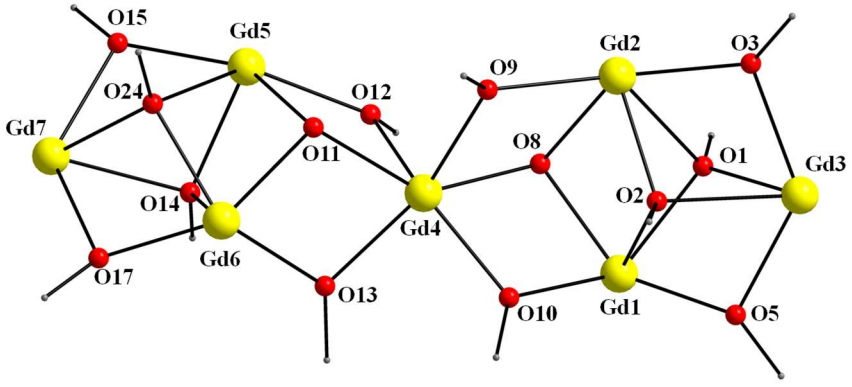

Figure 2.3. The complete $[Gd_7(\mu_3\text{-}OH)_2(\mu_3\text{-}OR)_4(\mu\text{-}OR)_8]^{7+}$ core of complex **1**. Color scheme: Gd^{III}, yellow; O red; C, dark gray.

Table 2.2. Selected interatomic distances (Å) and angles (°) for complex **1**.

Intermetallic distances			
Gd1···Gd2	3.686(8)	Gd2···Gd4	3.930(8)
Gd1···Gd3	3.656(8)	Gd4···Gd5	3.916(8)
Gd1···Gd4	3.805(7)	Gd5···Gd7	3.775(8)
Gd2···Gd3	3.770(8)		
Bond distances			
Gd1-O23	2.180(8)	Gd4-O9	2.380(7)
Gd1-O5	2.264(7)	Gd4-O12	2.384(7)
Gd1-O10	2.337(7)	Gd4-N5	2.534(1)
Gd1-O8	2.342(7)	Gd4-N4	2.558(2)
Gd1-O1	2.385(7)	Gd5-O20	2.216(8)
Gd1-O2	2.488(7)	Gd5-O15	2.288(7)
Gd1-N11	2.507(1)	Gd5-O12	2.382(7)
Gd2-O7	2.206(8)	Gd5-O14	2.384(7)
Gd2-O3	2.328(7)	Gd5-O21	2.408(1)
Gd2-O2	2.370(6)	Gd5-O11	2.492(7)
Gd2-O9	2.390(7)	Gd5-N10	2.504(9)
Gd2-O22	2.457(9)	Gd5-O24	2.754(8)
Gd2-N3	2.499(9)	Gd6-O19	2.195(8)
Gd2-O8	2.501(7)	Gd6-O17	2.253(7)
Gd2-O1	2.770(7)	Gd6-O11	2.342(7)
Gd3-O6	2.197(8)	Gd6-O13	2.362(7)

Gd3-O4	2.264(9)	Gd6-O24	2.380(7)
Gd3-O5	2.418(7)	Gd6-N9	2.523(1)
Gd3-O1	2.435(7)	Gd6-O14	2.537(7)
Gd3-O3	2.442(7)	Gd7-O18	2.217(8)
Gd3-N1	2.545(1)	Gd7-O16	2.241(8)
Gd3-O2	2.579(6)	Gd7-O17	2.440(8)
Gd3-N2	2.582(1)	Gd7-O24	2.453(7)
Gd4-O10	2.346(6)	Gd7-O15	2.474(7)
Gd4-O8	2.369(7)	Gd7-N6	2.534(9)
Gd4-O11	2.371(6)	Gd7-O14	2.547(6)
Gd4-O13	2.375(7)	Gd7-N7	2.551(1)

Bond angles

Gd1-O1-Gd2	91.0(2)	Gd4-O11-Gd5	107.3(3)
Gd1-O1-Gd3	98.7(3)	Gd4-O12-Gd5	110.5(3)
Gd1-O2-Gd2	98.7(2)	Gd4-O11-Gd6	107.9(3)
Gd1-O2-Gd3	92.4(2)	Gd4-O13-Gd6	107.1(3)
Gd1-O5-Gd3	102.7(3)	Gd5-O11-Gd6	100.0(2)
Gd1-O8-Gd2	99.1(2)	Gd6-O24-Gd5	92.1(2)
Gd1-O8-Gd4	107.7(3)	Gd7-O24-Gd5	92.8(2)
Gd1-O10-Gd4	108.7(3)	Gd5-O15-Gd7	104.9(3)
Gd1-O10-Gd4	108.7(3)	Gd5-O14-Gd7	99.9(2)
Gd2-O1-Gd3	92.6(2)	Gd6-O17-Gd7	102.4(3)
Gd2-O3-Gd3	104.5(3)	Gd6-O24-Gd7	98.4(2)

Gd2-O8-Gd4	107.6(3)

Two Gd^{III} atoms (Gd1, Gd6) are 7-coordinate with capped octahedron geometries, while the remaining metal ions are 8-coordinate with different coordination geometries (triangular dodecahedral for Gd2 and Gd5; biaugmented trigonal prismatic for Gd3 and Gd7; square antiprismatic for Gd4). All coordination features of the individual Gd^{III} ions have been derived from the program SHAPE (Figure 2.4).[11a] The so-called Continuous Shape Measures (CShM) approach essentially allows one to numerically evaluate by how much a particular structure deviates from an ideal shape. Values of CShM between 0.1 and 3 usually correspond to a not negligible but still small distortion from ideal geometry, while values larger than 3 refer to very distorted coordination environments (Tables 2.3 and 2.4).

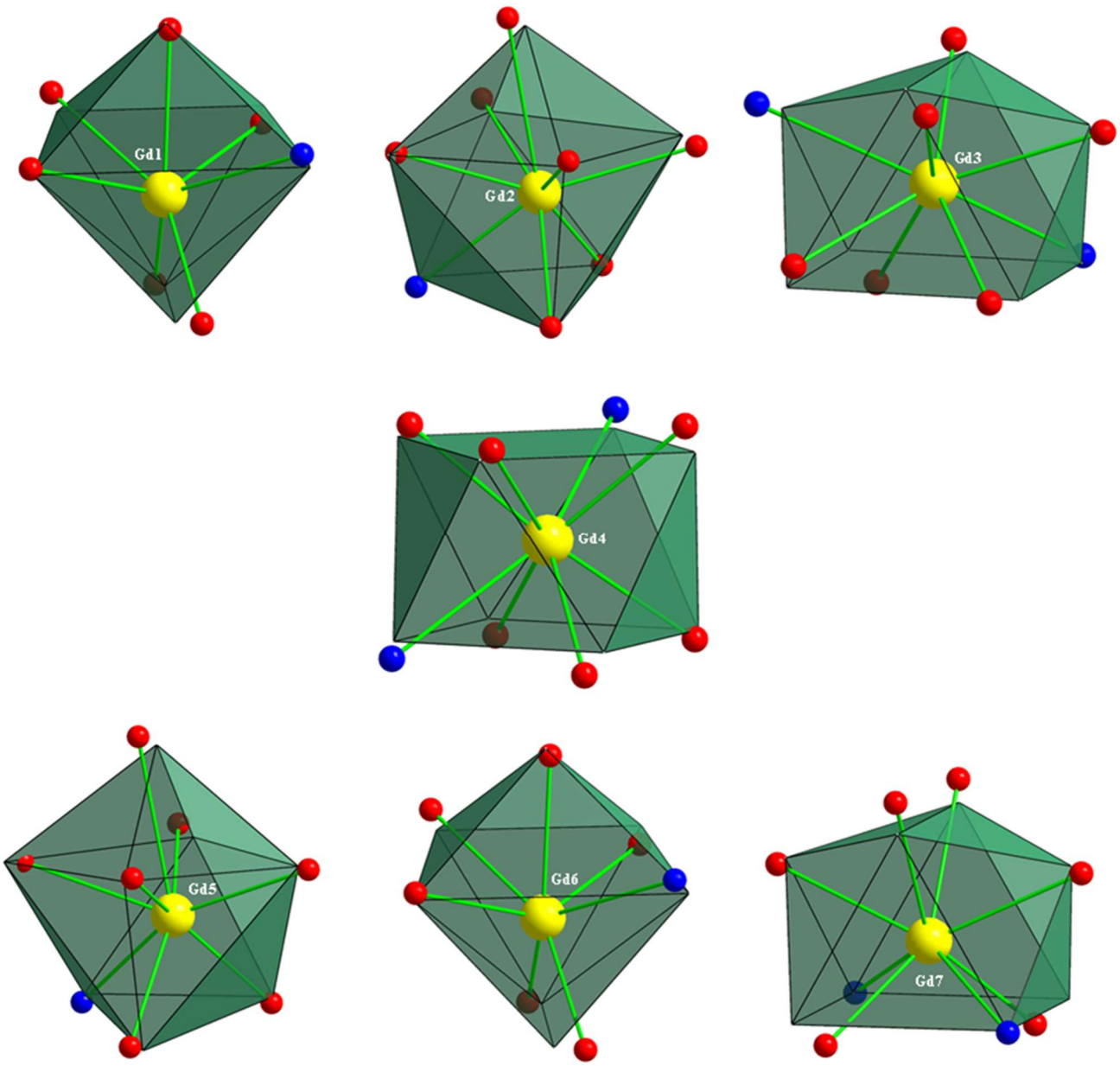

Figure 2.4. Capped octahedron (Gd1 and Gd6), triangular dodecahedral (Gd2 and Gd5), biaugmented trigonal prismatic (Gd3 and Gd7) and square antiprismatic (Gd4) geometries of the gadolinium atoms in the structure of **1**. The points connected by the black lines define the vertices of the ideal polyhedron. Color scheme: Gd^{III}, yellow; O, red; N, blue.

Table 2.3. Continuous Shape Measures (CShM) of the 7-coordinate Gd1 and Gd6 coordination polyhedra in complex **1**.[a]

Polyhedron[b]	Gd1	Gd6
HP-7	33.844	32.443
HPY-7	21.765	22.694
PBPY-7	5.883	5.035
COC-7	**1.697**	**2.359**
CTPR-7	2.490	2.433
JPBPY-7	8.426	7.359
JETPY-7	19.388	19.730

[a]The values in boldface indicate the closest polyhedron according to the Continuous Shape Measures (CShM). [b]Abbreviations: HP-7, heptagon; HPY-7, hexagonal pyramid; PBPY-7, pentagonal bipyramid; COC-7, capped octahedron; CTPR-7, capped trigonal prism; JPBPY-7, Johnson pentagonal bipyramid; JETPY-7, Johnson elongated triangular pyramid.

Table 2.4. Continuous Shape Measures (CShM) of the 8-coordinate Gd2, Gd3, Gd4, Gd5 and Gd7 coordination polyhedra in complex **1**.[a]

Polyhedron[b]	Gd2	Gd3	Gd4	Gd5	Gd7
OP-8	29.274	27.691	34.645	30.124	28.452
HPY-8	24.265	21.366	22.261	24.163	21.037
HBPY-8	15.272	15.369	14.754	15.513	14.902
CU-8	12.609	12.145	8.046	12.202	13.605
SAPR-8	3.313	3.713	**1.423**	3.848	4.851

TDD-8	**1.540**	3.296	1.935	**1.372**	3.264
JGBF-8	10.668	10.791	16.826	11.244	11.420
JETBPY-8	28.668	25.570	28.243	27.983	25.206
JBTPR-8	3.134	3.065	3.392	2.256	3.650
BTPR-8	2.635	**2.841**	3.070	2.325	**2.691**
JSD-8	2.863	3.553	4.883	2.616	3.495
TT-8	12.986	12.740	8.662	12.536	14.169
ETBPY-8	22.682	21.253	24.613	24.002	20.432

[a]The values in boldface indicate the closest polyhedron according to the Continuous Shape Measures (CShM). [b]Abbreviations: OP-8, octagon; HPY-8, heptagonal pyramid; HBPY-8, hexagonal bipyramid; CU-8, cube; SAPR-8, square antiprism; TDD-8, triangular dodecahedron; JGBF-8, Johnson gyrobifastigium; JETBPY-8, Johnson elongated triangular bipyramid; JBTPR-8, Johnson biaugmented trigonal prism; BTPR-8, biaugmented trigonal prism; JSD-8, Johnson snub diphenoid; TT-8, triakis tetrahedron; ETBPY-8, elongated trigonal bipyramid.

Finally, the $\{Gd^{III}_7\}$ anions are well-isolated in the crystal (Figure 2.5), with the shortest Gd···Gd intermolecular separation being 12.2 Å. Although heptanuclear metal complexes are of precedence, with the majority of them comprising two vertex-sharing dicubanes,[100] there is no previous report on a topology similar to that of **1**, other than a mixed-valence $\{Mn^{II/III}_7\}$ with diethylenetriamine chelate ligand.[101]

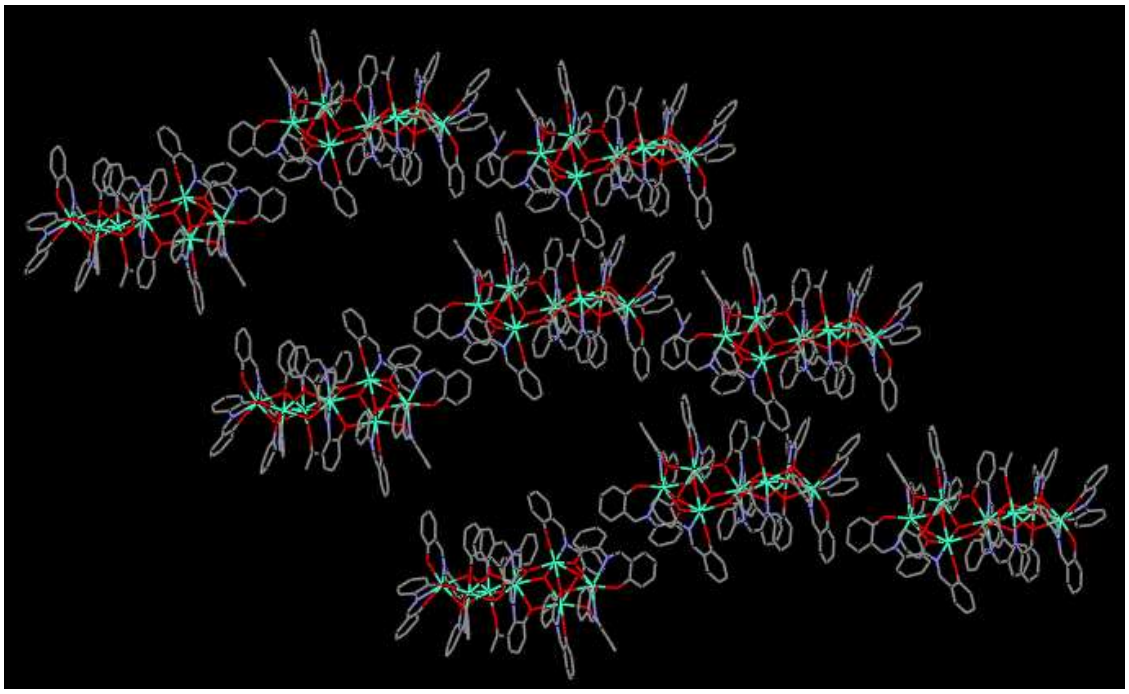

Figure 2.5. The packing of the $\{Gd^{III}_7\}$ clusters in the crystal of **1**.

2.3.3. Magnetic Susceptibility Studies

Variable-temperature direct current (*dc*) magnetic susceptibility studies were carried out on freshly prepared, crystalline samples of complexes **1**-**3** in the temperature range 2.0-300 K under an applied field of 0.3 T. The low-temperature (30-2 K) susceptibility data were re-collected at a very small applied *dc* field of 0.02 T to avoid saturation effects; these data were identical with the ones collected under 0.3 T. The obtained data for all studied compounds are shown as $\chi_M T$ *vs.* T plots in Figure 2.6. The experimental $\chi_M T$ values at room temperature are in good agreement with the theoretical ones (55.13 cm^3Kmol^{-1} for **1**; 82.74 cm^3Kmol^{-1} for **2**; 99.19 cm^3Kmol^{-1} for **3**) for seven non-interacting Gd^{III} ($^8S_{7/2}$, $S = 7/2$, $L = 0$, $g = 2$), Tb^{III} ($^7F_6$, $S = 3$, $L = 3$, $g = 3/2$) and Dy^{III} ($^6H_{15/2}$, $S = 5/2$, $L = 5$, $g = 4/3$) ions. For the isotropic $\{Gd^{III}_7\}$ (**1**), the $\chi_M T$ product remains almost constant at a value of ~55 cm^3Kmol^{-1} from 300 K to ~40 K and then

steadily decreases to a minimum value of 22.21 cm^3Kmol^{-1} at 2.0 K. The identical response under the two measured fields precludes the presence of any anisotropy, and is indicative of the presence of weak intramolecular antiferromagnetic exchange interactions between the seven Gd^{III} centers. For the anisotropic $\{Tb^{III}_7\}$ (**2**) and $\{Dy^{III}_7\}$ (**3**) complexes, the thermal evolution of the magnetic susceptibility is similar, in which the $\chi_M T$ product remains essentially constant at a value of ~78 and ~98 cm^3Kmol^{-1} from 300 K to ~130 K and then steadily decreases to a minimum value of 44.07 and 63.60 cm^3Kmol^{-1} at 2.0 K, respectively. Such a low temperature decrease of the $\chi_M T$ product is mainly due to depopulation of the excited Stark sublevels of the Tb^{III} and Dy^{III} ions and some weak antiferromagnetic interactions between the metal centers, which cannot be quantified due to the strong orbital momentum.[102]

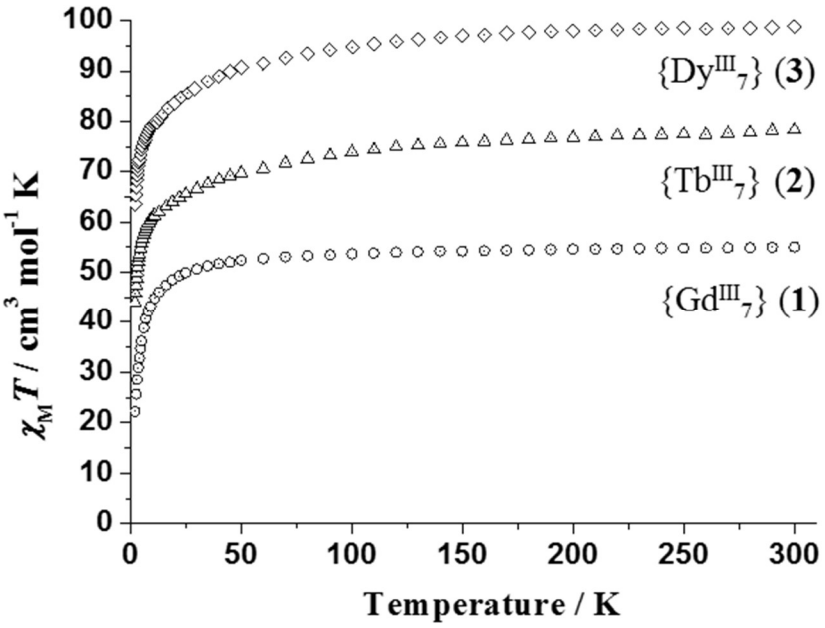

Figure 2.6. Plots of $\chi_M T$ *vs. T* for complexes **1**-**3**.

The field dependence of magnetization (M) at low temperatures shows all the expected characteristics for polynuclear, weakly coupled Ln^{III} clusters. Briefly, the lack of saturation in magnetization for complexes **2** and **3** (Figure 2.7) indicates the presence of magnetic anisotropy and/or population of low-lying excited states.[103] In the case of **1**, the magnetization reaches a quasi-saturated value of 47.7 μ_B at the highest fields (Figure 2.8), which is in excellent agreement with the expected value of 49 μ_B for seven non-coupled Gd^{III} ions. The deviation of M *vs.* H for **1** at low fields (below the shape and values expected for a simply Brillouin behavior for 7 Gd^{III}) confirms the weak antiferromagnetic interactions.

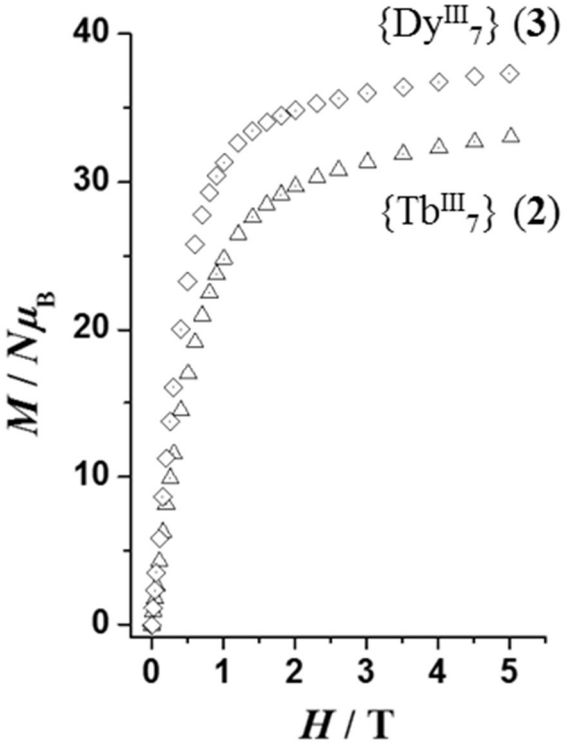

Figure 2.7. Plots of magnetization (M) *vs.* field (H) for complexes **2** and **3** at 2 K.

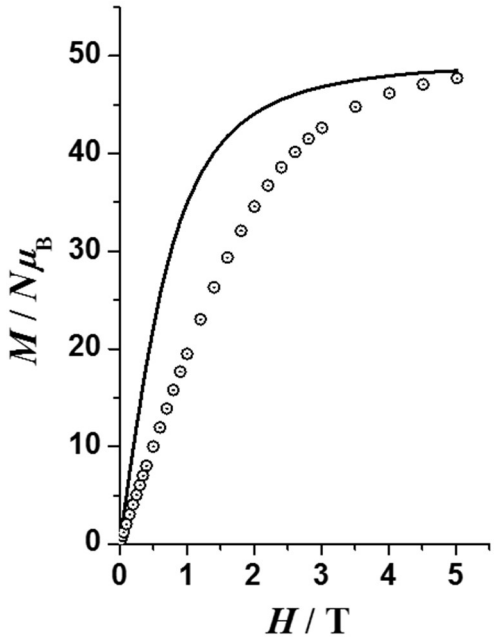

Figure 2.8. Plot of magnetization (*M*) *vs.* field (*H*) for complex **1** at 2 K; the solid line corresponds to the Brillouin function for seven non-coupled Gd^{III} ions.

Alternating current (*ac*) magnetic susceptibility studies have been also performed in order to investigate the magnetization dynamics of the anisotropic $\{Tb^{III}_7\}$ and $\{Dy^{III}_7\}$ clusters under a zero *dc* magnetic field. Complex **2** does not show any out-of-phase signals (Figure 2.9); this is somehow usual in polynuclear Tb^{III} complexes because Tb^{III} is a non-Kramers ion and so its complexes will have a bistable ground state only if the ligand-field has an axial symmetry.[57,104] This is particularly difficult and rare when the aggregation of Tb^{III} ions results in a polymetallic cluster compound where many metal ions are present in different coordination environments. In contrast, complex **3** shows frequency-dependent out-of-phase χ_M'' tails of signals at temperatures below ~7 K (Figure 2.10), indicative of the slow magnetization relaxation of an SMM with a small energy barrier for magnetization reversal. This is most likely due to the fast tunneling which is frequently observed in high-nuclearity Dy^{III} SMMs, and mainly originates from single-

ion anisotropy effects of the individual Dy^{III} Kramers ions.[105] In an attempt to quantify the energy barrier and relaxation time for **3**, and given the absence of χ'' peak maxima, it was decided to apply the below equation (Eqn. 2.2) developed by Bartolomé et al.[106]

$$\ln(\chi''/\chi') = \ln(\omega\tau_0) + E_a/k_BT \qquad \textbf{Eqn. 2.2}$$

Considering a single relaxation process, the least-squares fit of the experimental data (inset of Figure 2.10) gave an energy barrier of ~3.0(1) cm^{-1} (~4.3(1) K) and a $\tau_0 = 8.3(2) \times 10^{-6}$ s.

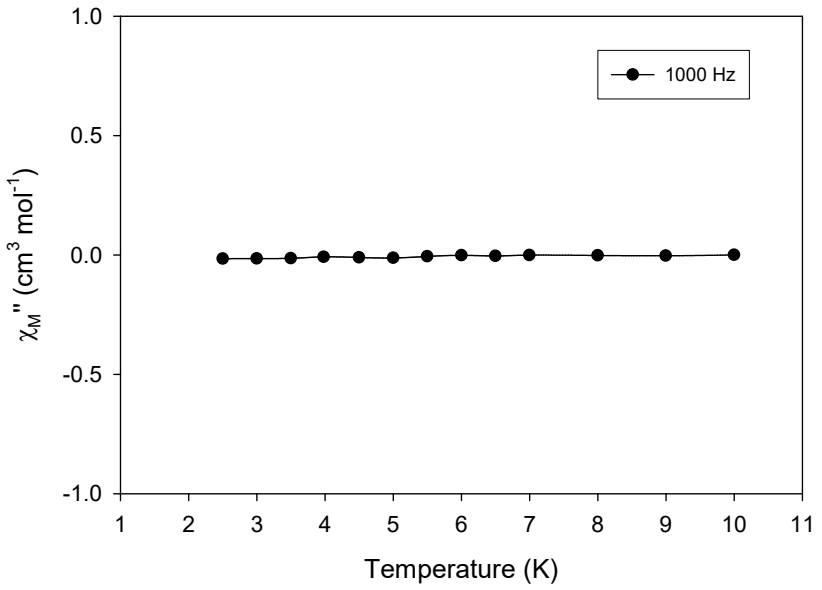

Figure 2.9. The out-of-phase (χ_M'') *vs. T ac* susceptibility signals for **2** in a 4.0 G field oscillating at 1000 Hz.

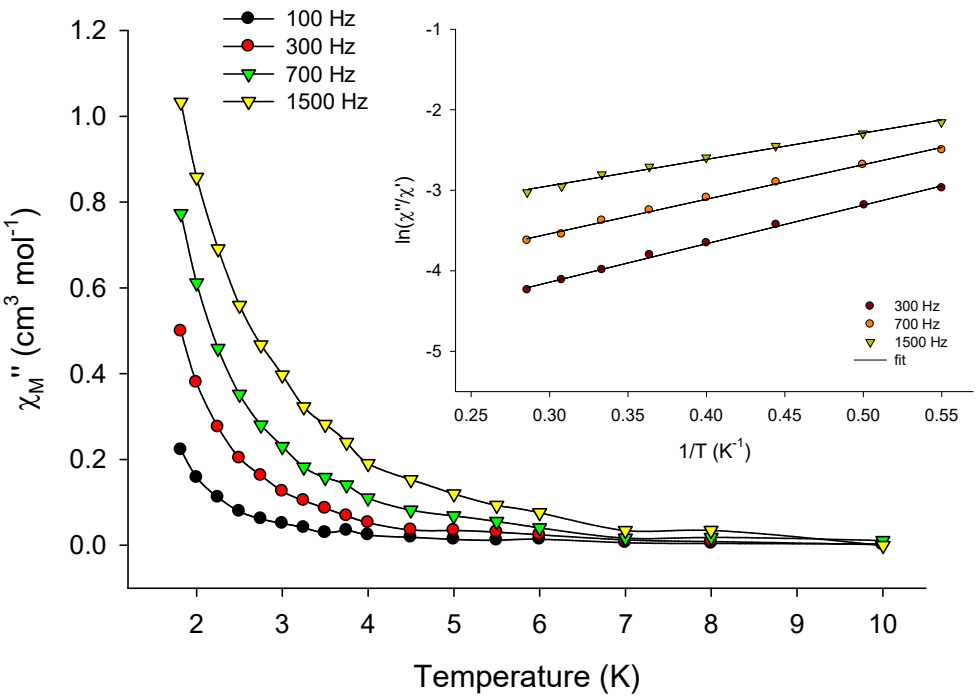

Figure 2.10. Out-of-phase (χ_M'') *vs. T ac* susceptibility signals for **3** in a 4.0 G field oscillating at the indicated frequencies. (inset) Plots of ln(χ''/χ') *vs.* 1/*T* for **3** at different *ac* frequencies; the solid lines are the best-fit curves.

2.3.4. Photoluminescence Studies

In order to gain any possible access into additional physical properties for this family of {Ln_7} complexes, it was decided to perform photoluminescence studies in the solid-state and at room temperature. 4*f*-metal complexes usually exhibit metal-centered emission bands, which are sharp, intense, and narrow. These bands arise from an efficient energy transfer mechanism which includes the 'sensitization' of the metal's excited levels from the triplet (or occasionally singlet) state of the coordinated organic ligand(s).[107] In contrast, quenching of Ln emission is relatively rare, but -when it occurs- it is associated with either negligible emission or red-shifted ligand-

centered emissions, which are both broad and weak. Reasons for such quenching vary but they are mainly related to structural parameters, such as the coordination of solvate ligands and the presence of lattice solvents and counterions in the crystal, the temperature, as well as the energy of the lowest triplet state of the ligand.[108]

The free ligand saphH_2, and its dianionic form (saph^{2-}),[109] appear to have very similar photophysical behaviors. Upon maximum excitation at 490 nm, the ligand shows two strong and broad emission bands at 510 and 540 nm (Figure 2.11a), which are located at the blue-green range on the visible spectrum. Although saphH_2 seemed to be a promising 'sensitizer' for 4*f*-metal luminescence, the photophysical properties of all three reported {Ln_7} compounds are identical and consistent with a ligand-centered emission. In detail, upon maximum excitation of **1-3** at 400 nm, a green emission at 540 nm has been detected, supplemented with a weaker intensity band at 485 nm (Figures 2.11b, 2.11c, 2.11d). The recorded emissions of **1-3** are obviously red-shifted with respect to the metal-free ligand, implying a significant effect of the metal-ligand interactions on the overall optical response. Such a Ln-independent emission can be ascribed to an efficient Ln-to-saph^{2-} back energy transfer process.[110] There is no doubt that quenching from the coordinated Me_2CO molecules, the presence of Et_3NH^+ countercations and lattice solvents in the crystals of **1-3**, might also contribute to the diminishing of the Ln emission.

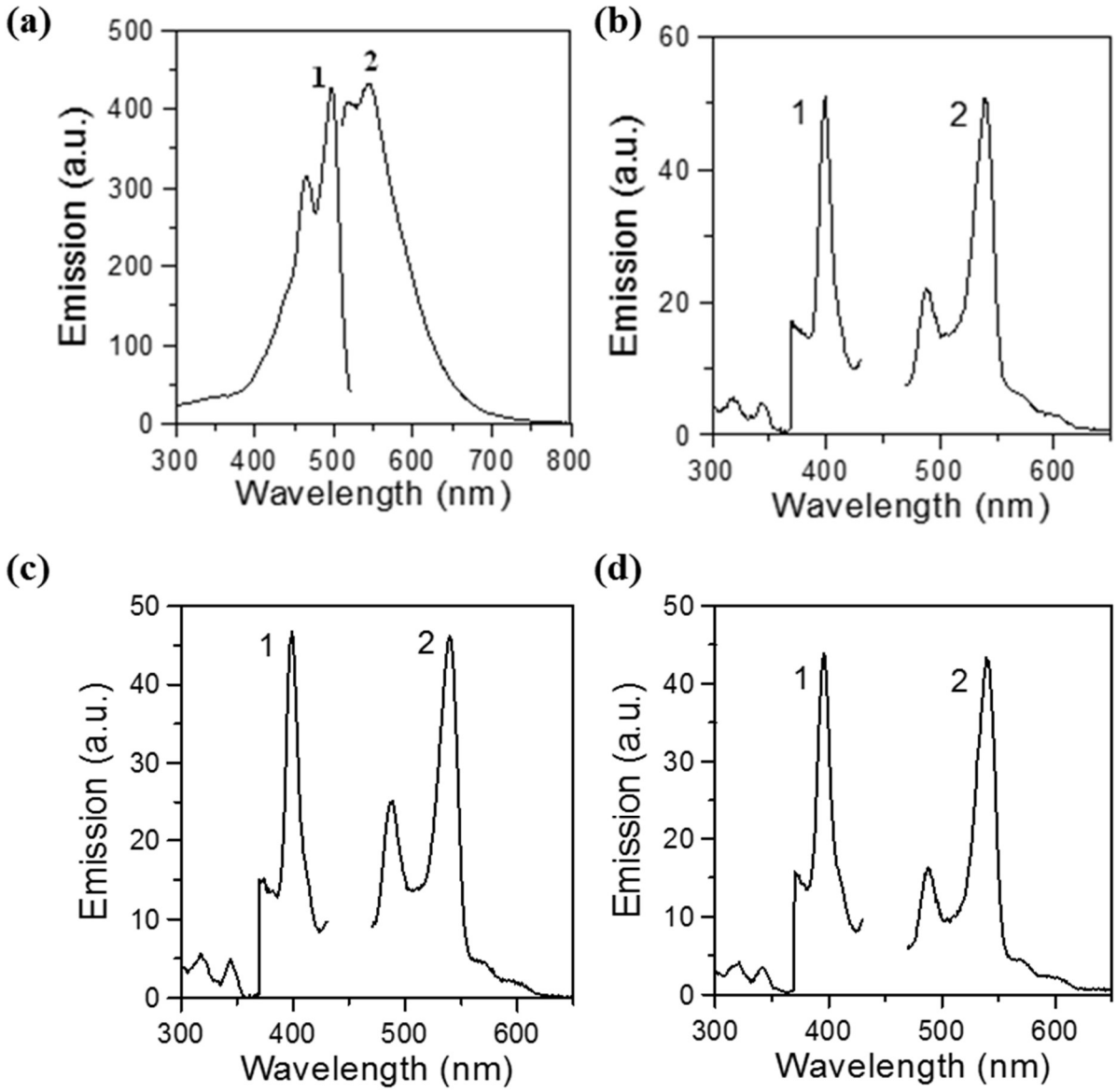

Figure 2.11. Excitation (1) and emission (2) spectra of solid-state: **(a)** saphH$_2$, **(b)** {Dy$^{III}_7$}, **(c)** {Gd$^{III}_7$}, and **(d)** {Tb$^{III}_7$} at room temperature.

2.4. Conclusions and Perspectives

In conclusion, it was shown in this chapter that a new family of heptanuclear Ln^{III} complexes, bearing the known Schiff base ligand *N*-salicylidene-*o*-aminophenol (saphH$_2$), has

now joined the growing family of 4*f*-metal clusters with large nuclearities, unprecedented topologies and interesting physicochemical properties, such as single-molecule magnetism and optics. The reported complexes possess an unusual topology of two $\{Ln_4\}$ butterflies sharing a common, central metal ion at the wing-tip position. This results from the co-presence of μ_3-OH^-, and μ_3- and μ-OR^- groups from the double-deprotonated form of $saphH_2$ under the prevailing basic conditions. Work in progress may include the incorporation of β-diketones as ancillary bridging/chelating ligands and the introduction of pseudohalides (i.e., azides) as bridging ligands in the $Ln^{III}/saphH_2$ reaction system. It would be also pertinent to explore the effect of various R-substituents (R = -Cl, $-NO_2$, -Me, -Ph, etc.) of the $saphH_2$ scaffold on the structural, magnetic and emission properties of the resulting coordination compounds.

Chapter 3

First use of the Schiff base ligand *N*-salicylidene-2-aminocyclohexanol in metal cluster chemistry: {Ln_7} and {Ln_8} complexes with novel structures, and SMM and photoluminescence behaviors

3.1 *Preface*

One of the current major challenges in molecular nanoscience is the synthesis of new polynuclear metal complexes (clusters) exhibiting more than one physical property within the same entity. Of significant importance is the combination of their magnetic properties with one or more additional properties, such as conductivity,[111] chirality[112] and luminescence.[113] This is due to the fact that such multifunctional (or 'hybrid') molecular magnetic materials can find potential applications in the fields of molecular electronics and spintronics.[114] Molecular electronics is undoubtedly an emerging area of research which is based on the construction and fabrication of molecular species with intriguing magnetic properties, pronounced stability, robustness, and capability to be deposited on electrical conducting surfaces.[81c,115] Such deposition of 'hybrid' molecular materials is actually one of the ultimate goals, but at the same time one of the most difficult challenges for synthetic chemists to unravel.[116] It primarily requires the molecules to retain their structures and properties in solution, and subsequently to allow anchoring of the peripheral sites.

The unique electronic and physical properties of the 4*f*-metal ions render polynuclear lanthanide(III) metal clusters as excellent candidates for the construction of dual-acting molecular species. An appreciable number of 4*f*-metal clusters with various interesting structural

topologies and SMM behaviors have been reported to date, from linear[66] and linked-triangular[117a] to more complex ones such as cubanes,[117b] trigonal prismatic[117c] and disc-like.[117d] Polynuclear 4*f*-metal complexes have also shown intense, sharp and long-lived emissions, which make these compounds particularly interesting for a variety of optical uses such as display devices and luminescent sensors.[33] This is also applied to the 'magnetic' Tb^{III}- and Dy^{III}-based clusters which show photoluminescence properties with metal-centered emissions at different regions of the visible spectrum. Due to the forbidden electronic transitions between the 4*f*-orbitals on symmetry grounds, which lead to poor absorption cross-sections, population of the emitting levels of the Ln^{III} ion is best achieved by employing light-harvesting ligands.[107a,108a]

It therefore becomes apparent that one of the most important factors for the construction of new 4*f*-metal clusters with dual physical properties, unprecedented topologies and possible structural integrity in solution is the choice of the primary organic bridging/chelating ligand. This often dictates not only the topology and the number of paramagnetic metal ions present, but also the nature of the intramolecular magnetic exchange interactions and the efficiency of metal ion's sensitization by the intramolecular energy transfer from the ligand's triplet state. A family of such potentially multi-acting organic ligands is Schiff bases, and particularly the ones which are based on the scaffold of *N*-salicylidene-*o*-aminophenol ($saphH_2$, Scheme 3.1). The latter is a well-explored precursor in coordination chemistry because of the ability of the relatively soft *N*-atom and the two hard, upon deprotonation, *O*-atoms to bind to a single or multiple metal centers.[118] In the present study, it was decided to slightly "tweak" the *o*-aminophenol moiety of $saphH_2$ and replace the bulky phenyl ring with the more flexible cyclohexane functionality. The latter could, in principle, differentiate the electronic and steric properties of the resulting precursor, and subsequently lead to the formation of new polynuclear 4*f*-metal complexes with

new topologies and interesting physical properties. In this chapter, the use for a first time of *N*-salicylidene-2-aminocyclohexanol (sachH_2, Scheme 3.1) in metal cluster chemistry is presented. In particular, the synthesis, structures, and solid-state and solution characterization of two new families of heptanuclear and octanuclear Ln^{III} clusters are reported. The structures and nuclearities of the reported compounds appear to be influenced by the stereo-configuration of the employed sachH_2 ligand. To that end, {Ln_7} clusters with an ideal metal-centered trigonal prismatic topology were isolated from the *cis*/*trans*-mixture of sachH_2, while {Ln_8} complexes consisting of six edge- and vertex-sharing triangular subunits were the only isolated products from the *trans*-analogue of sachH_2. Unfortunately, due to limited resources of the corresponding starting materials for the synthesis of the *cis*-sachH_2, I was not able to investigate its employment in *4f*-metal chemistry.

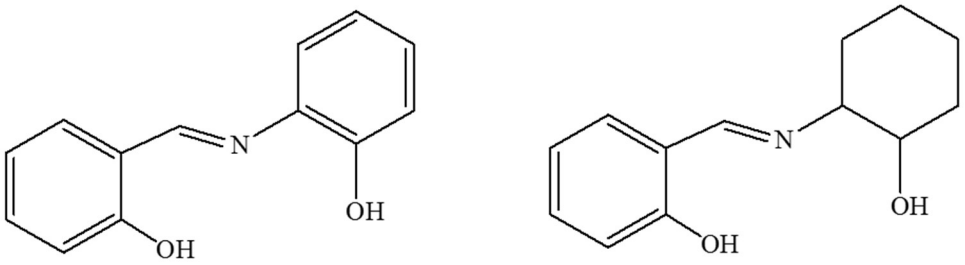

Scheme 3.1. Structural formulas and abbreviations of the ligands *N*-salicylidene-*o*-aminophenol (saphH_2) and *N*-salicylidene-2-aminocyclohexanol (sachH_2) discussed in the text.

3.2 ***Experimental Section***

3.2.1 Physical Measurements

Elemental analysis: Elemental analyses (C, H, and N) were performed on a Perkin-Elmer 2400 Series II Analyzer.

FT-IR spectroscopy: Infrared (IR) spectra were recorded in the solid state on a Bruker FT-IR spectrometer (ALPHA Platinum ATR single reflection) in the 4000-400 cm^{-1} range. Notation for IR bands: vs = very strong; s = strong; m = medium; w = weak; b = broad.

NMR spectroscopy: NMR spectra were recorded on a Bruker Avance III HD 400 Digital NMR spectrometer with a 9.4 Tesla Ascend Magnet at Brock University. Data for proton spectra are reported as follows: chemical shift multiplicity [singlet (s), double (d), and triplet (t)].

UV-Visible studies: UV-Visible (UV-Vis) spectra were recorded in solution at concentrations ~10^{-5} M on a Beckman Coulter DU Series 700 dual beam spectrophotometer.

Mass spectroscopy: Electrospray ionization (ESI) mass spectra (MS) were taken on a Bruker HCT Ultra mass spectrometer at Brock University.

Photoluminescence studies: Excitation and emission spectra were recorded in solution using a PTI FeliX32 spectrofluorometer. Excitation and emission spectra were recorded in the solid state using a Cary Eclipse spectrofluorometer.

Magnetic susceptibility measurements: Variable-temperature direct current (*dc*) and alternating current (*ac*) magnetic susceptibility data were collected at the Chemistry Department of the University of Florida using a Quantum Design MPMS-XL SQUID magnetometer equipped with a 7 T magnet and operating in the 1.8-300 K range. Samples were embedded in solid eicosane to prevent torquing. Pascal's constants were used to estimate the diamagnetic corrections, which were subtracted from the experimental susceptibilities to give the molar paramagnetic susceptibilities (χ_M).[61]

3.2.2 Synthesis

General considerations: All experiments were performed under aerobic conditions. All chemicals were purchased from Sigma-Aldrich and Alfa Aesar. Chemicals and solvents were used as received without further purification. ***Caution!*** *Although no such behavior was observed during the present work, perchlorate salts are potentially explosive; such compounds should be synthesized and used in small quantities, and treated with utmost care at all times.*

Synthesis of *cis*/*trans*-mixture of *N*-salicylidene-2-aminocyclohexanol (sachH_2): The Schiff base ligand sachH_2 was prepared in 85 % yield by the condensation of 2-aminocyclohexanol (*cis*- and *trans*-mixture; 4.61 g, 40.0 mmol) with salicylaldehyde (4.88 g, 40.0 mmol) in a 1:1 molar ratio in refluxing absolute EtOH (20 mL). The resulting yellow microcrystalline solid was washed with cold EtOH (2 × 5 mL), dried under vacuum, and analyzed as solvent-free. Elemental analysis (%) calculated for *cis*/*trans*-sachH_2: C, 71.87; H, 6.96; N 6.45; Found: C, 71.65; H, 6.80; N, 6.58. Selected IR data (ATR): ν = 2923 (m), 2848 (m), 1633 (s), 1607 (s), 1525(m), 1496 (s), 1391 (m), 1334 (w), 1273 (m), 1225 (m), 1188 (s), 1150 (m), 1128 (m), 1047 (m), 985 (m), 942 (w), 849 (w), 791 (w), 757 (m), 677 (s), 655 (w), 589 (w), 539 (w), 512 (m), 482 (m), 453 (m). ^{1}H NMR ($CDCl_3$, ppm): 13.47 (singlet, -OH), 8.44-8.43 (doublet, -CH=N-), 7.34-6.87 (doublet and double-of-doublets, Ar-H), 1.92-1.76 (doublet and double-of-doublets, cyclohexane-H).

Synthesis of *trans*-*N*-salicylidene-2-aminocyclohexanol (*trans*-sachH_2): The Schiff base ligand *trans*-sachH_2 was prepared in 95 % yield by the condensation of *trans*-2-aminocyclohexanol (0.97 g, 6.4 mmol) with salicylaldehyde (0.78 g, 6.4 mmol) in a 1:1 molar ratio in refluxing absolute EtOH (20 mL). The resulting yellow microcrystalline solid was

washed with cold EtOH (2 × 5 mL), dried under vacuum, and analyzed as solvent-free. Elemental analysis (%) calculated for *trans*-sachH$_2$: C, 71.87; H, 6.96; N 6.45; Found: C, 71.75; H, 6.88; N, 6.51. Selected IR data (ATR): ν = 2925 (m), 2855 (m), 1628 (s), 1580 (s), 1498 (s), 1448 (m), 1414 (m), 1355 (w), 1309 (w), 1229 (s), 1206 (m), 1133 (m), 1080 (m), 1042 (m), 939 (w), 904 (m), 860 (s), 791 (w), 749 (s), 697 (m), 646 (m), 581 (w), 563 (m), 529 (w), 479 (w), 441 (m). ^{1}H NMR ($CDCl_3$, ppm): 13.27 (singlet, -OH), 8.43 (singlet, -CH=N-), 7.33-6.87 (doublet and double-of-doublets, Ar-H), 2.09-1.62 (doublet and double-of-doublets, cyclohexane-H).

[Gd$_7$(OH)$_6$(CO$_3$)$_3$(sach)$_3$(sachH)$_3$(MeOH)$_6$] (4): To a stirred, yellow solution of the *cis*/*trans*-mixture of sachH$_2$ (0.13 g, 0.6 mmol) and Me$_4$NOH·5H$_2$O (0.11 g, 0.6 mmol) in MeOH (20 mL) was added Gd(ClO$_4$)$_3$·6H$_2$O (0.11 g, 0.2 mmol). The resulting yellow solution was stirred for 10 min, during which time all of the solids dissolved and the color of the solution became more intense yellow. The solution was filtered, and the filtrate was left to evaporate slowly at room temperature. After 12 days, X-ray quality pale yellow plate-like crystals of **4**·11MeOH had appeared and were collected by filtration, washed with cold MeOH (2 × 2 mL) and dried in air. The yield was 32 %. The air-dried solid was analyzed as **4**. Elemental analysis (%) calculated for **4**: C, 36.26; H, 4.30; N, 2.92 %. Found: C, 36.02; H, 4.12; N, 2.99 %. Selected IR data (ATR): ν = 2928 (m), 2910 (m), 1627 (s), 1594 (m), 1543 (m), 1471 (m), 1442 (m), 1357 (m), 1304 (mb), 1194 (m), 1151 (m), 1129 (w), 1060 (m), 984 (m), 901 (m), 840 (m), 820 (w), 756 (s), 603 (m), 579 (w), 507 (w).

[Tb$_7$(OH)$_6$(CO$_3$)$_3$(sach)$_3$(sachH)$_3$(MeOH)$_6$] (5): This complex was prepared in the same manner as complex **4** but using Tb(ClO$_4$)$_3$·6H$_2$O (0.11 g, 0.2 mmol) as the Ln salt. After 6 days, pale yellow plate-like crystals of **5**·3MeOH had appeared and were collected by filtration,

washed with cold MeOH (2 × 2 mL) and dried in air. The yield was 25 %. The air-dried solid was analyzed as **5**. Elemental analysis (%) calculated for **5**: C, 36.12; H, 4.28; N, 2.90 %. Found: C, 36.16; H, 4.44; N, 2.80 %. Selected IR data (ATR): ν = 2930 (m), 2914 (m), 1628 (s), 1591 (m), 1541 (m), 1467 (m), 1440 (m), 1360 (m), 1301 (mb), 1198 (m), 1148 (m), 1134 (w), 1062 (m), 990 (m), 900 (m), 843 (m), 822 (w), 751 (s), 600 (m), 583 (w), 505 (w).

$[Dy_7(OH)_6(CO_3)_3(sach)_3(sachH)_3(MeOH)_6]$ (6): This complex was prepared in the same manner as complex **4** but using $Dy(ClO_4)_3 \cdot 6H_2O$ (0.11 g, 0.2 mmol) as the Ln salt. After ~10 days, pale yellow plate-like crystals of **6**·6MeOH had appeared and were collected by filtration, washed with cold MeOH (2 × 2 mL) and dried in air. The yield was 35 %. The air-dried solid was analyzed as **6**. Elemental analysis (%) calculated for **6**: C, 35.81; H, 4.25; N, 2.88 %. Found: C, 36.12; H, 4.56; N, 2.72 %. Selected IR data (ATR): ν = 2928 (m), 2911 (m), 1631 (s), 1590 (m), 1544 (m), 1472 (m), 1444 (m), 1361 (m), 1299 (mb), 1203 (m), 1152 (m), 1130 (w), 1060 (m), 998 (m), 905 (m), 840 (m), 825 (w), 750 (s), 601 (m), 589 (w), 504 (w).

$[Gd_8(OH)_4(CO_3)_2$(*trans*-sach$)_8(EtOH)_4]$ (7): To a stirred, yellow solution of *trans*-sachH_2 (0.07 g, 0.3 mmol) and $Me_4NOH \cdot 5H_2O$ (0.06 g, 0.3 mmol) in EtOH (20 mL) was added $Gd(ClO_4)_3 \cdot 6H_2O$ (0.06 g, 0.1 mmol). The resulting yellow solution was kept under stirring for approximately 15 min, during which time all of the solids dissolved. The resulting solution became more intense yellow, filtered, and the filtrate was left in fridge. After 7 days, X-ray quality pale yellow plate-like crystals of **7**·3EtOH had appeared and were collected by filtration, washed with cold EtOH (2 × 2 mL) and dried in air. The yield was 42 %. The air-dried solid was analyzed as **7**. Elemental analysis (%) calculated for **7**: C, 40.85; H, 3.97; N, 3.34 %. Found: C, 40.97; H, 4.15; N, 3.29 %. Selected IR data (ATR): ν = 2923(m), 2853 (m), 1627 (s), 1596 (w),

1542 (m), 1469(m), 1447 (m), 1399 (w), 1331 (s), 1192 (m), 1148 (m), 1088 (m), 1041 (m), 1019 (m), 908 (m), 847 (m), 805 (m), 754 (s), 697 (w), 603 (m), 565 (m), 494 (m), 430 (m).

[$Tb_8(OH)_4(CO_3)_2$(*trans*-sach)$_8(EtOH)_4$] (8): This complex was prepared in the same manner as complex **7** but using $Tb(ClO_4)_3 \cdot 6H_2O$ (0.06 g, 0.1 mmol) as the Ln salt. After 5 days, pale yellow plate-like crystals of **8**·3EtOH had appeared and were collected by filtration, washed with cold EtOH (2 × 2 mL) and dried in air. The yield was 38 %. The air-dried solid was analyzed as **8**. Elemental analysis (%) calculated for **8**: C, 40.68; H, 3.95; N, 3.33 %. Found: C, 40.75; H, 4.04; N, 3.26 %. Selected IR data (ATR): ν = 2922 (m), 2852 (m), 1628 (s), 1596 (w), 1539 (m), 1468 (m), 1446 (m), 1400 (w), 1328 (s), 1192 (m), 1146 (m), 1089 (m), 1043 (m), 1018 (m), 907 (m), 849 (m), 805 (m), 755 (s), 738 (m), 697 (w), 601 (m), 563 (m), 429 (m).

[$Dy_8(OH)_4(CO_3)_2$(*trans*-sach)$_8(EtOH)_4$] (9): This complex was prepared in the same manner as complex **7** but using $Dy(ClO_4)_3 \cdot 6H_2O$ (0.06 g, 0.1 mmol) as the Ln salt. After 7 days, pale yellow plate-like crystals of **9**·3EtOH had appeared and were collected by filtration, washed with cold EtOH (2 × 2 mL) and dried in air. The yield was 44 %. The air-dried solid was analyzed as **9**. Elemental analysis (%) calculated for **9**: C, 40.34; H, 3.92; N, 3.30 %. Found: C, 40.50; H, 3.99; N, 3.13 %. Selected IR data (ATR): ν = 2922 (m), 2852 (m), 1629 (s), 1596 (w), 1540 (m), 1468 (m), 1447 (m), 1400 (w), 1329 (s), 1192 (m), 1146 (m), 1090 (m), 1043 (m), 1019 (m), 907 (m), 849 (m), 805 (m), 755 (s), 738 (m), 698 (w), 601 (m), 563 (m), 498 (m), 434 (m).

[$Eu_8(OH)_4(CO_3)_2$(*trans*-sach)$_8(EtOH)_4$] (10): This complex was prepared in the same manner as complex **7** but using $Eu(ClO_4)_3 \cdot 6H_2O$ (0.06 g, 0.1 mmol) as the Ln salt. After 6 days, pale yellow plate-like crystals of **10**·3EtOH had appeared and were collected by filtration, washed with cold EtOH (2 × 2 mL) and dried in air. The yield was 46 %. The air-dried solid was

analyzed as **10**. Elemental analysis (%) calculated for **10**: C, 41.37; H, 4.02; N, 3.39 %. Found: C, 40.49; H, 4.90; N, 3.33 %. Selected IR data (ATR): ν = 2922 (m), 2852 (m), 1597 (w), 1539 (m), 1468 (m), 1445 (m), 1398 (w), 1330 (s), 1190 (m), 1146 (m), 1086 (m), 1018 (m), 906 (m), 848 (m), 804 (m), 755 (s), 737 (m), 692 (w), 597 (m), 562 (m), 492 (m), 473 (m).

3.2.3 Single-crystal X-Ray Crystallography

Single-crystals of the complexes $[Ln_7(OH)_6(CO_3)_3(sach)_3(sachH)_3(MeOH)_6]\cdot n(MeOH)$ ($Ln^{3+} = Gd^{3+}$ and $n = 11$ for complex **4**; $Ln^{3+} = Tb^{3+}$ and $n = 3$ for **5**; $Ln^{3+} = Dy^{3+}$ and $n = 6$ for **6**) and $[Ln_8(OH)_4(CO_3)_2(trans\text{-}sach)_8(EtOH)_4]\cdot 3EtOH$ ($Ln^{3+} = Gd^{3+}$ for complex **7**; $Ln^{3+} = Dy^{3+}$ for **9**) were manually harvested and mounted on cryoloops using inert oil.[89] For the $\{Tb_8\}$ (**8**) and $\{Eu_8\}$ (**10**) analogues, I have not been able to collect a complete diffraction data set because the crystals were found to lose lattice solvate molecules and, subsequently, their diffraction has become less intense due to a partial loss of their crystallinity. Regardless, the identity of these products (**8** and **10**) was confirmed by (i) unit cell determination and comparison with the unit cell of compounds **7**·3EtOH and **9**·3EtOH, (ii) IR spectroscopic comparison with all isostructural $\{Ln_8\}$ complexes, and (iii) elemental analysis. Diffraction data were collected at 150.0(2) K on a Bruker X8 Kappa APEX II Charge-Coupled Device (CCD) area-detector diffractometer controlled by the APEX2 software package[119] (Mo Kα graphite-monochromated radiation, λ = 0.71073 Å), and equipped with an Oxford Cryosystems series 700 cryostream monitored remotely with the software interface Cryopad.[91] Images were processed with the software SAINT+,[120] and absorption effects were corrected with the multi-scan method implemented in SADABS.[121] The structures were solved by direct methods employed in SHELXS-97,[94,122]

allowing the immediate location of the Ln atoms. The remaining non-H-atoms of the complexes were located from difference Fourier maps and calculated by successive full-matrix least-squares refinement cycles on F^2 using SHELXL-97,[94,122] and have been successfully refined with anisotropic displacement parameters, while the MeOH or EtOH solvate molecules were refined with isotropic parameters.

The H-atoms attached to the C-atoms of the ligands were placed at their geometrical positions using appropriate *HFIX* instructions in SHELXL and incorporated in subsequent refinement cycles in riding-motion approximation with isotropic thermal displacements parameters (U_{iso}) fixed at 1.2 or 1.5 × U_{eq} of the parent C-atom. Furthermore, the H-atoms of the coordinated OH-, MeOH- and EtOH-groups were clearly visible in the difference Fourier maps, and included in subsequent refinement stages with the O-H distances restrained to 0.92(2) Å, using a riding-motion approximation with an isotropic thermal displacement parameter fixed at 1.5 × U_{eq} of the respective O-atom. Besides the identification and successful refinement of several crystallization MeOH solvate molecules in all structures of complexes **4**-**6**, the spaces originated by the close packing of complexes also contained some electron density, mainly due to disordered solvate molecules, which was not possible to modulate and refine properly (particularly in the structures of complexes **4** and **6**). Searches for the total potential solvent area using the software package PLATON[97,123] revealed the existence of cavities with a potential solvent accessible voids in both the structures of **4** and **6**. The original data sets were then treated with SQUEEZE[98] to remove the contribution of these disordered molecules in the solvent-accessible volume, and the calculated solvent-free reflection lists were consequently utilized for the final refinement of the structures. Unit cell parameters and structure solution and refinement data for complexes **4**-**6** and **7**/**9** are listed in Tables 3.1 and 3.2, respectively.

Table 3.1. Crystal and structure refinement details for complexes **4**-**6**.

	4·11MeOH	**5**·3MeOH	**6**·6MeOH
Formula	$C_{98}H_{164}Gd_7N_6O_{44}$	$C_{90}H_{132}Tb_7N_6O_{36}$	$C_{93}H_{144}Dy_7N_6O_{39}$
Fw / g mol^{-1}	3231.10	2986.46	3107.64
Crystal type	Pale yellow plates	Pale yellow plates	Pale yellow plates
Crystal size / mm^3	0.44×0.12×0.12	0.10×0.08×0.06	0.10×0.05×0.03
Crystal system	Hexagonal	Hexagonal	Hexagonal
Space group	$P6_3/m$	$P6_3/m$	$P6_3/m$
a / Å	17.237(2)	15.7469(9)	15.5912(7)
b / Å	17.237(2)	15.7469(9)	15.5912(7)
c / Å	25.135(4)	27.7469(3)	28.0106(13)
α / º	90	90	90
β / º	90	90	90
γ / º	120	120	120
Volume / Å^3	6467.6(16)	5977.5(8)	5896.7(5)
Z	2	2	2
T / K	150.0(2)	150.0(2)	150.0(2)
ρ_{calc} / g cm^{-3}	1.659	1.659	1.750
μ / mm^{-1}	3.614	4.156	4.455
Index ranges	$-22 \le h \le 22$	$-18 \le h \le 18$	$-17 \le h \le 18$
	$-22 \le k \le 22$	$-18 \le k \le 18$	$-18 \le k \le 18$
	$-32 \le l \le 32$	$-33 \le l \le 33$	$-30 \le l \le 33$

Reflections collected	83384	64198	61297
Independent	5046	3555	3537
reflections	(R_{int} = 0.0418)	(R_{int} = 0.0517)	(R_{int} = 0.0388)
Data completeness	to θ = 27.48°, 99.3%	to θ = 25.03°, 99.4%	to θ = 25.02°, 99.4%
Final *R* indices	*R*1 = 0.0334	*R*1 = 0.0893	*R*1 = 0.0726
[I>2σ(I)][a,b]	*wR*2 = 0.0764	*wR*2 = 0.2180	*wR*2 = 0.1541
Final *R* indices	*R*1 = 0.0420	*R*1 = 0.0957	*R*1 = 0.0759
(all data)	*wR*2 = 0.0780	*wR*2 = 0.2228	*wR*2 = 0.1554
$(\Delta\rho)_{max,min}$ / e Å^{-3}	2.045 and -2.267	6.336 and -1.869	3.030 and -3.869

[a] $R1 = \Sigma(||F_o| - |F_c||)/\Sigma|F_o|$. [b] $wR2 = [\Sigma[w(F_o^2 - F_c^2)^2]/\Sigma[w(F_o^2)^2]]^{1/2}$, $w = 1/[\sigma^2(F_o^2) + (ap)^2 + bp]$, where $p = [\max(F_o^2, 0) + 2F_c^2]/3$.

Table 3.2. Crystal and structure refinement details for complexes **7** and **9**.

	7·3EtOH	**9**·3EtOH
Formula	$C_{120}H_{150}Gd_8N_8O_{33}$	$C_{120}H_{150}Dy_8N_8O_{33}$
Fw / g mol^{-1}	3490.57	3532.57
Crystal type	Pale yellow plates	Pale yellow plates
Crystal size / mm^3	0.28×0.13×0.07	0.06×0.15×0.16
Crystal system	Monoclinic	Monoclinic
Space group	$P2_1/c$	$P2_1/c$
a / Å	19.214(2)	19.026(3)
b / Å	22.109(3)	22.129(4)
c / Å	16.6741(19)	16.595(3)

α / º	90	90
β / º	106.902(5)	106.867(7)
γ / º	90	90
Volume / Å^3	6777.2(14)	6686(2)
Z	2	2
T / K	150.0(2)	150.0(2)
ρ_{calc} / g cm^{-3}	1.699	1.699
μ / mm^{-1}	3.931	4.483
Index ranges	$-24 \le h \le 24$	$-22 \le h \le 22$
	$-27 \le k \le 27$	$-24 \le k \le 26$
	$-20 \le l \le 20$	$-19 \le l \le 19$
Reflections collected	13805	11469
Independent	12233	9673
reflections	(R_{int} = 0.0507)	(R_{int} = 0.0546)
Data completeness	to θ = 26.37°, 99.3%	to θ = 25.03°, 99.3%
Final R indices	$R1$ = 0.0752	$R1$ = 0.0841
[I>2σ(I)]^{a,b}	w$R2$ = 0.1653	w$R2$ = 0.1798
Final R indices	$R1$ = 0.0842	$R1$ = 0.0997
(all data)	w$R2$ = 0.1699	w$R2$ = 0.1873
$(\Delta\rho)_{max,min}$ / e Å^{-3}	6.097 and -1.875	4.614 and -1.746

^{a} $R1 = \Sigma(||F_o| - |F_c||)/\Sigma|F_o|$. ^{b} $wR2 = [\Sigma[w(F_o^2 - F_c^2)^2]/\Sigma[w(F_o^2)^2]]^{1/2}$, $w = 1/[\sigma^2(F_o^2) + (ap)^2 + bp]$, where $p = [\max(F_o^2, 0) + 2F_c^2]/3$.

3.3. ***Results and Discussion***

3.3.1. Synthetic Comments

In the present chapter, the organic ligand *N*-salicylidene-*o*-aminocyclohexanol ($sachH_2$), either as a *cis*/*trans*-mixture or in its pure *trans*-form, was explored for the first time in lanthanide cluster chemistry. One-pot reactions were performed between various LnX_3 salts and the $sachH_2$ ligand in different molar ratios and solvents, in the presence of external organic or inorganic bases to facilitate the deprotonation of the neutral $sachH_2$ and any other acidic H atoms from H_2O-containing solvents and starting materials. Hence, the reaction of $Ln(ClO_4)_3 \cdot 6H_2O$ (Ln = Gd, Tb and Dy), $sachH_2$, and $Me_4NOH \cdot 5H_2O$ in a 1:3:3 molar ratio in MeOH gave deep yellow solutions that upon slow evaporation at room temperature afforded yellowish crystals of $[Ln_7(OH)_6(CO_3)_3(sach)_3(sachH)_3(MeOH)_6]$ (Ln = Gd (**4**); Tb (**5**); Dy (**6**)) in 25-35% isolated yields. The formation of **4** as a representative example is summarized in the balanced Eqn. 3.1.

$$7\ Gd(ClO_4)_3 \cdot 6H_2O + 6\ sachH_2 + 21\ Me_4NOH \cdot 5H_2O + 6\ MeOH + 3\ CO_2 \rightarrow$$
$$[Gd_7(OH)_6(CO_3)_3(sach)_3(sachH)_3(MeOH)_6] + 21\ (Me_4N)(ClO_4) + 159\ H_2O \qquad \textbf{Eqn. 3.1}$$

In the next step of my synthetic attempts, the same general reaction scheme was followed but with the pure *trans*-$sachH_2$ ligand in place of the *cis*/*trans*-mixture of the same ligand. However, all of my efforts failed to give me single-crystals suitable for X-ray diffraction studies. Thus, it was decided to perform these reactions in solvent EtOH instead of MeOH but preserving the reactions conditions similar to those followed for the synthesis of **4**-**6** (i.e., same starting

materials, molar ratios, etc.). Indeed, this time, I was able to grow single-crystals of a new family of octanuclear 4*f*-metal complexes, the chemical identities of which are most likely determined by the solvent media and -most importantly- the stereoconfiguration of the *trans*-form of the sachH$_2$ ligand (*vide infra*). The reaction of Ln(ClO$_4$)$_3$·6H$_2$O (Ln = Gd, Tb, Dy and Eu), *trans*-sachH$_2$, and Me$_4$NOH·5H$_2$O in a 1:3:3 molar ratio in EtOH gave deep yellow solutions that upon maintenance in the fridge afforded yellowish crystals of complexes [Ln$_8$(OH)$_4$(CO$_3$)$_2$(*trans*-sach)$_8$(EtOH)$_4$] (Ln = Gd (**7**); Tb (**8**); Dy (**9**); Eu (**10**)) in 38-46% isolated yields. The formation of **7** as a representative example is summarized in the balanced Eqn. 3.2.

$$8\ Gd(ClO_4)_3\cdot 6H_2O + 8\ \textit{trans}\text{-sachH}_2 + 24\ Me_4NOH\cdot 5H_2O + 4\ EtOH + 2\ CO_2 \rightarrow$$
$$[Gd_8(OH)_4(CO_3)_2(\textit{trans}\text{-sach})_8(EtOH)_4] + 24\ (Me_4N)(ClO_4) + 186\ H_2O \qquad \textbf{Eqn. 3.2}$$

The same reactions but with different external bases (i.e., NEt$_3$, LiOH, etc.) did not yield any crystalline products other than amorphous precipitates with negligible solubility in common organic solvents. Furthermore, the use of Ln(NO$_3$)$_3$ starting materials has indeed led to the same two families of {Ln$_7$} and {Ln$_8$} complexes albeit the products were always contaminated with (Me$_4$N)(NO$_3$) salts. The CO_3^{2-} groups found in the structures of **4**-**10** were presumably derived from the fixation of atmospheric CO$_2$ during the aerobic reactions.[124] The pivotal role of carbonates as multidentate bridging ligands in the synthesis of 4*f*- and 3*d*/4*f*-metal clusters with unprecedented topologies has been recently documented by Brechin and coworkers.[125] The carbonate-related IR absorption bands in complexes **4**-**10** are located at ~1440 and 845 cm^{-1}, as seen for other carbonato 4*f*-metal complexes.[124,125]

3.3.2 Description of Structures

The formulas of all complexes are based on metric parameters, charge balance considerations and O BVS calculations; the latter confirmed the assignment of the μ_3-bridging groups as OH^- ions (BVS values in the range 1.10-1.12).[99] As a result of the calculations, the formulas of **4**-**6** initially appeared to be $[Ln_7(OH)_6(CO_3)_3(sach)_6(MeOH)_6]^{3-}$, their trianionic nature disagreeing with the absence of three countercations from the crystal lattice. To maintain the neutral charge of each cluster, it is very likely that the crystallographic C_3 axis of the molecule is masking the presence of three protons statically disordered between three $sach^{2-}$/$sachH^-$ pairs, or even among other groups (i.e., CO_3^{2-}/HCO_3^-).[126]

Complexes **4**-**6** are isomorphous and differ only in the number of lattice MeOH solvate molecules; thus, only the structure of representative complex **4** will be described in detail. Selected bond distances and angles for complex **4** are shown in Table 3.3. Complex **4**·11MeOH crystallizes in the high-symmetry hexagonal space group $P6_3/m$ and comprises seven Gd^{III} ions linked through six μ_3-OH^- and three $\eta^1{:}\eta^1{:}\eta^3{:}\mu_3$-$CO_3^{2-}$ bridges to form an ideal metal-centered trigonal prism with a perfect D_{3h} point group symmetry (Figure 3.1). Such a metal topology has never been seen before in homometallic 4*f*-metal cluster chemistry, although heptanuclear Ln^{III} compounds with cage-/disc-like[127] and centered-octahedral[87d] topologies have been reported. Of interest is also the unusual $\eta^1{:}\eta^1{:}\eta^3{:}\mu_3$-binding mode of the carbonate group which has been previously seen only in complex $[Er_3(CO_3)(MQ)_7]$ (MQ^- = 8-quinaldinolate).[128]

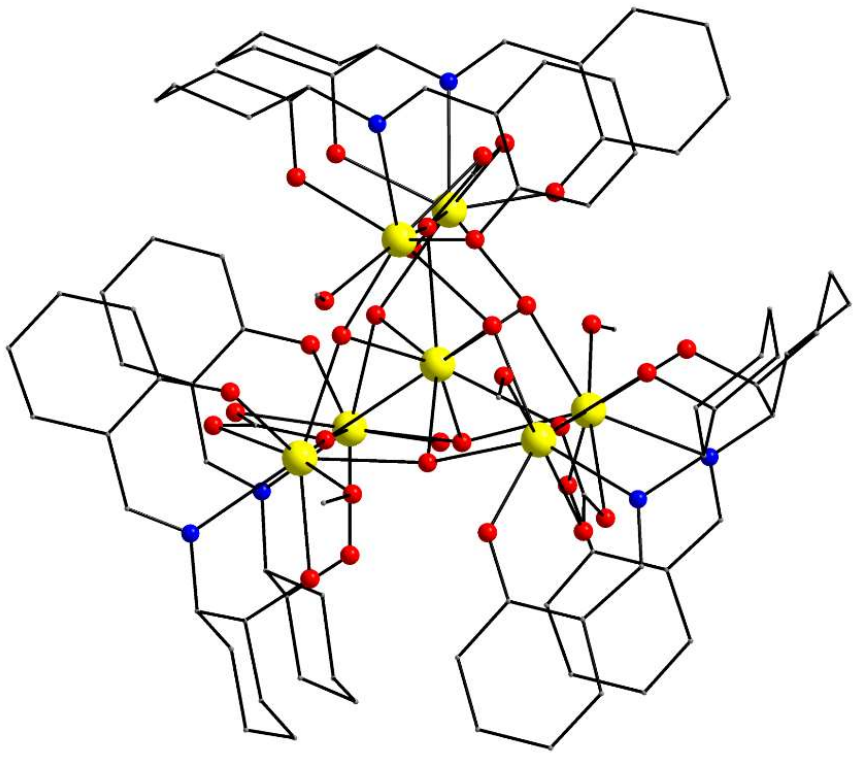

Figure 3.1. Molecular structure of complex **4.** H-atoms and lattice solvate molecules have been omitted for clarity. Color scheme: Gd^{III}, yellow; O, red; N, blue; C, gray.

Table 3.3. Selected interatomic distances (Å) and angles (°) for complex **4**.[a]

Intermetallic distances			
Gd1···Gd2	3.636(3)	Gd2···Gd2′	4.495(3)
Bond distances			
Gd1-O2	2.298(3)	Gd2-O3	2.399(3)
Gd1-O1	2.344(3)	Gd2-O3′	2.399(3)
Gd1-O3′	2.389(3)	Gd2-O3″	2.399(3)
Gd1-O4	2.392(3)	Gd2-O3‴	2.399(3)
Gd1-O6	2.398(3)	Gd2-O3⁗	2.399(3)

Gd1-O3	2.430(3)	Gd2-O3′′′′′	2.399(3)
Gd1-O5	2.547(4)	Gd2-O5	2.550(4)
Gd1-N1	2.518(4)	Gd2-O5′	2.550(4)
		Gd2-O5′′	2.550(4)
Bond angles			
Gd1-Gd2-Gd1′	88.9(1)	Gd1-O5-Gd2	91.0(1)
Gd1-Gd2-Gd1′′	76.4(1)	Gd1′-O5-Gd2	91.0(1)
Gd1-O5-Gd1′	176.9(2)		

[a] All primed atoms are related to the unprimed ones by the corresponding symmetry operations.

The compound has therefore an overall $[Gd_7(\mu_3\text{-}OH)_6(\mu_3\text{-}CO_3)_3]^{9+}$ core (Figure 3.2a), with peripheral ligation provided by six *N*,*O*,*O*-tridentate chelating $sach^{2-}$/$sachH^{-}$ ligands (Scheme 3.2) and six terminally-bound MeOH molecules, each coordinated to one of the external Gd^{III} ions. The six external, symmetry equivalent Gd^{III} ions (Gd1 and its symmetry-related partners) constitute the two trigonal faces. The two parallel trigonal faces are ideal equilateral triangles with Gd···Gd distances of 4.495 Å and Gd···Gd···Gd angles of 60°. Two Gd^{III} ions from each trigonal face make up three ideal and symmetry-related Gd_4 rectangles with Gd···Gd distances of 4.495 and 5.093 Å, and Gd···Gd···Gd angles of 90°; these units constitute the three tetragonal faces of the prism (Figure 3.2b). The crystallographically unique Gd2 atom is located exactly at the center of the prism (Gd1···Gd2 = 3.636 Å).

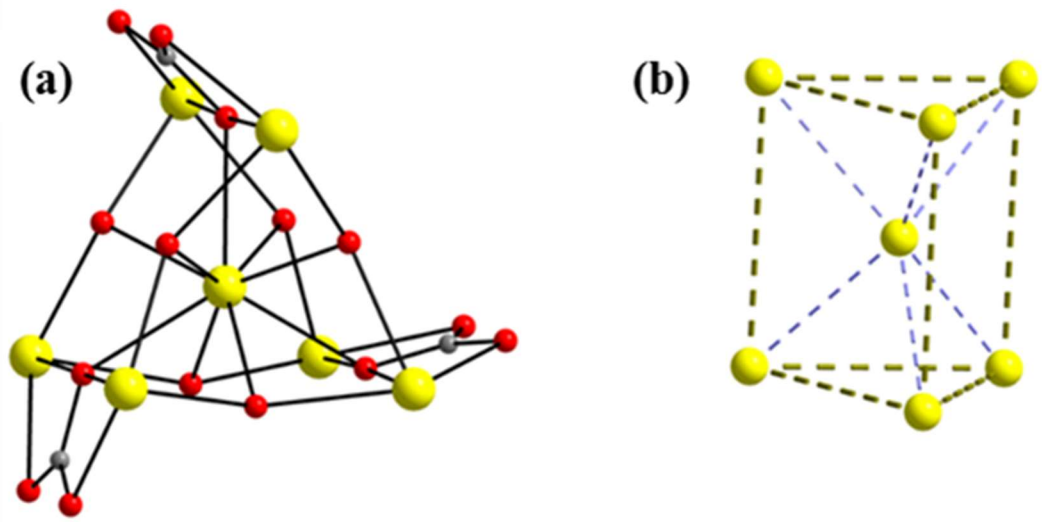

Figure 3.2. (a) The $[Gd_7(\mu_3\text{-}OH)_6(\mu_3\text{-}CO_3)_3]^{9+}$ complete core of complex **4**, and **(b)** a different view of the ideal metal-centered trigonal prismatic topology. Green and blue dashed lines indicate the trigonal and tetragonal faces of the prism and their connectivity with the central metal atom, respectively. Color scheme: Gd^{III}, yellow; O, red; C, gray.

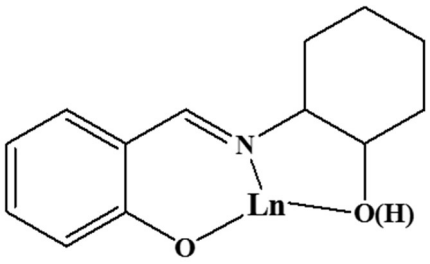

$\eta^1:\eta^1:\eta^1$

Scheme 3.2. Coordination modes of $sach^{2-}$ in complexes **4-6**.

All the external Gd atoms are eight-coordinate with slightly distorted triangular dodecahedral geometries whereas the central Gd2 is nine-coordinate with a perfect spherical tricapped trigonal prismatic geometry (Figure 3.3). To estimate the closer coordination polyhedra

defined by the donor atoms around all Gd atoms in **4**, a comparison of the experimental structural data with the theoretical data for the most common polyhedral structures with eight and nine vertices was performed by means of the program SHAPE (Tables 3.4 and 3.5).[11a] Finally, the $\{Gd^{III}_7\}$ molecules, as well as the other members of this family of $\{Ln^{III}_7\}$ clusters, are well-isolated in the crystal, with the shortest Gd···Gd intermolecular separation being 12.767 Å.

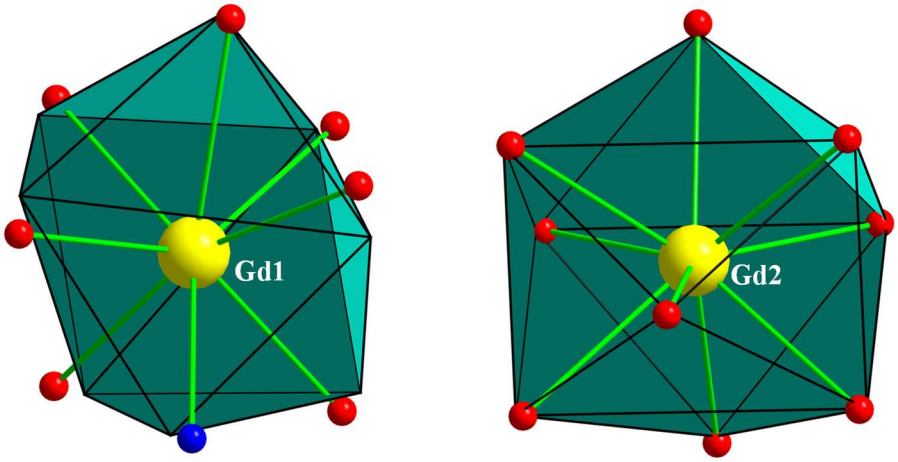

Figure 3.3. Triangular dodecahedral (Gd1) and spherical tricapped trigonal prismatic (Gd2) geometries of the gadolinium atoms in the structure of **4**. The points connected by the black lines define the vertices of the ideal polyhedron. Color scheme: Gd^{III}, yellow; O, red; N, blue.

Table 3.4. Continuous Shape Measures (CShM) of the eight-coordinate Gd1 coordination polyhedra in complex **4**.[a]

Polyhedron[b]	Gd1
OP-8	32.133
HPY-8	21.595
HBPY-8	14.244

CU-8	10.636
SAPR-8	2.326
TDD-8	**2.006**
JGBF-8	11.853
JETBPY-8	27.967
JBTPR-8	2.571
BTPR-8	2.291
JSD-8	3.693
TT-8	11.204
ETBPY-8	23.584

[a]The value in boldface indicate the closest polyhedron according to the Continuous Shape Measures (CShM). [b]Abbreviations: OP-8, octagon; HPY-8, heptagonal pyramid; HBPY-8, hexagonal bipyramid; CU-8, cube; SAPR-8, square antiprism; TDD-8, triangular dodecahedron; JGBF-8, Johnson gyrobifastigium; JETBPY-8, Johnson elongated triangular bipyramid; JBTPR-8, Johnson biaugmented trigonal prism; BTPR-8, biaugmented trigonal prism; JSD-8, Johnson snub diphenoid; TT-8, triakis tetrahedron; ETBPY-8, elongated trigonal bipyramid.

Table 3.5. Continuous Shape Measures (CShM) of the nine-coordinate Gd2 coordination polyhedra in complex **4**.[a]

Polyhedron[b]	Gd2
EP-9	32.886
OPY-9	21.475
HBPY-9	21.780

JTC-9	17.129
JCCU-9	11.770
CCU-9	10.827
JCSAPR-9	1.885
CSAPR-9	1.114
JTCTPR-9	1.626
TCTPR-9	**0.122**
JTDIC-9	12.222
HH-9	13.878
MFF-9	1.991

[a]The value in boldface indicate the closest polyhedron according to the Continuous Shape Measures (CShM). [b]Abbreviations: EP-9, enneagon; OPY-9, octagonal pyramid; HBPY-9, heptagonal bipyramid; JTC-9, Johnson triangular cupola J3; JCCU-9, Capped cube J8; CCU-9, Spherical-relaxed capped cube; JCSAPR-9, Capped square antiprism J10; CSAPR-9, Spherical capped square antiprism; JTCTPR-9, Tricapped trigonal prism J51; TCTPR-9, Spherical tricapped trigonal prism; JTDIC-9, Tridiminished icosahedron J63; HH-9, Hula-hoop; MFF-9, Muffin.

The family of octanuclear complexes **7**-**10** appears also to consist of isostructural compounds and therefore only the structure of the $\{Gd^{III}_8\}$ (**7**) as a representative example will be described in detail. Selected bond distances and angles are listed in Table 3.6. Complex **7** crystallizes in the monoclinic space group $P2_1/c$ and comprises eight Gd^{III} ions linked through four μ_3-OH^-, the alkoxido fragments of eight doubly deprotonated *trans*-$sach^{2-}$ ligands and two

η^1:η^1:η^4:μ_4-CO_3^{2-} groups (Figure 3.4). Surprisingly, the coordination mode of the carbonate groups -to my knowledge- has not been previously reported in coordination chemistry. Peripheral ligation about the metal-oxygen core is provided by four terminally-bound EtOH molecules. Impressively, the *trans*-sach^{2-} ions bind in three different modes (Scheme 3.3), emphasizing the binding affinity and rich bridging versatility of this Schiff base ligand. The compound has an overall $[Gd_8(\mu_3\text{-}OH)_4(\mu_4\text{-}CO_3)_2(\mu_3\text{-}OR)_2(\mu\text{-}OR)_8]^{6+}$ core (Figure 3.5a) and the arrangement of the eight Gd^{III} ions can be viewed as six edge- and vertex-sharing triangular subunits (Figure 3.5b).

The fact that the *trans*-form of the sach^{2-} led to a family of octanuclear Ln^{III} complexes, while the *cis*/*trans*-mixture of the same ligand yielded a family of $\{Ln_7\}$ clusters under similar reactions conditions, forced me to look for any helpful insights into the structural, stereochemical, and coordination features of the bound ligands in the representative $\{Ln_7\}$ and $\{Ln_8\}$ complexes. The ligands were found to bind differently, and I have thus tried to understand the reasons of such coordination dissimilarities, which would also allow me to tentatively interpret the structural variations between the Ln^{III}/*cis*-*trans*-sach^{2-} and Ln^{III}/*trans*-sach^{2-} products. In all the reported Ln_7/*cis*-*trans*-sach^{2-} compounds, the ligand's phenyl ring is almost perpendicular to the cyclohexane ring (calculated as the best-mean plane) forming an average angle of ~87° along the imino functionality. However, the corresponding average angle between the phenyl and cyclohexane rings of *trans*-sach^{2-} ligands in the Ln_8/*trans*-sach^{2-} products is ~40°, significantly smaller than that of *cis*/*trans*-sach^{2-} in $\{Ln_7\}$. As a result, it is very likely that the two rings of *trans*-sach^{2-} show a higher degree of rotation about the imino 'axle' compared to the phenyl-cyclohexane pair of the *cis*/*trans*-sach^{2-}, thus allowing *trans*-sach^{2-} to

have a greater flexibility and yield products with a variety of different coordination modes, including chelation and bridging to metal centers.

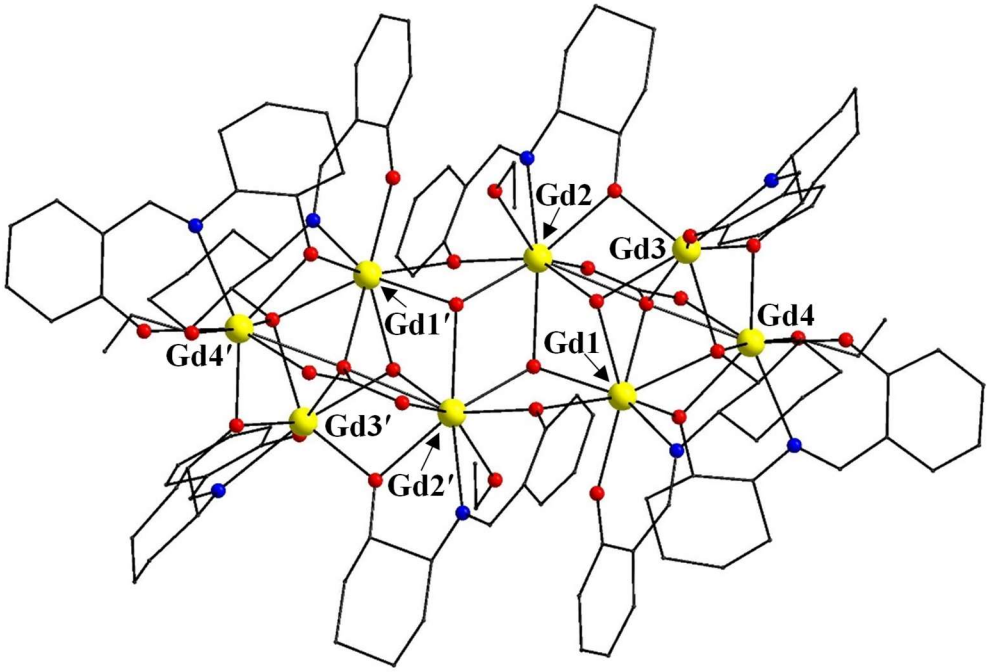

Figure 3.4. Molecular structure of complex **7**. H-atoms and lattice solvate molecules have been omitted for clarity. Symmetry code for the primed atoms: 1-*x*, 1-*y*, 1-*z*. Color scheme: Gd^{III}, yellow; O, red; N, blue; C, gray.

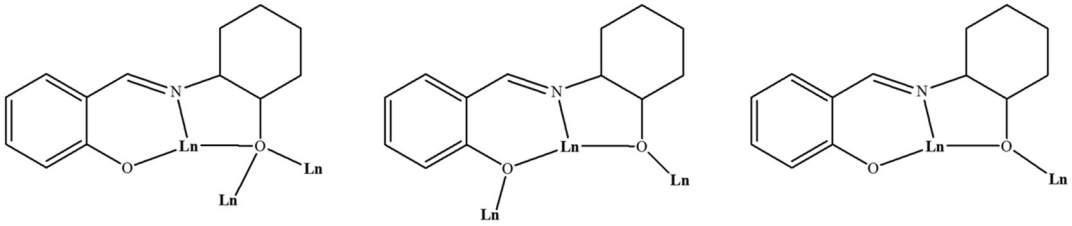

Scheme 3.3. Coordination modes of *trans*-$sach^{2-}$ in complex **7** (and **9**).

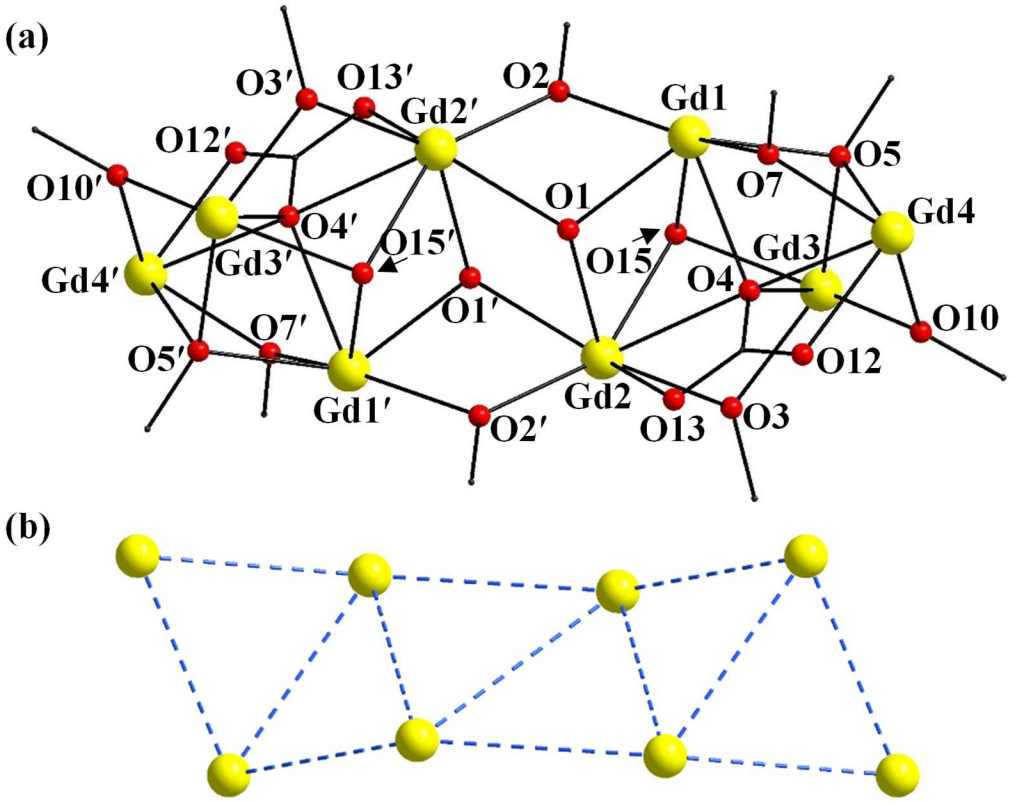

Figure 3.5. (a) The complete $[Gd_8(\mu_3\text{-}OH)_4(\mu_4\text{-}CO_3)_2(\mu_3\text{-}OR)_2(\mu\text{-}OR)_8]^{6+}$ core of complex **7**, and **(b)** a representation of the metal skeleton of the compound as six edge- and vertex-sharing triangular subunits. Color scheme: Gd^{III}, yellow; O, red; C, gray.

Table 3.6. Selected interatomic distances (Å) and angles (°) for complex **7**.[a]

Intermetallic distances			
Gd1···Gd2	3.7272(8)	Gd1···Gd4	3.6467(8)
Gd1···Gd2′	3.8656(8)	Gd2···Gd3	3.6608(8)
Gd1···Gd3	3.6916(8)	Gd3···Gd4	3.6124(9)
Bond distances			
Gd1-O6	2.289(8)	Gd3-O11	2.217(1)

Gd1-O7	2.304(9)	Gd3-O3	2.253(8)
Gd1-O1	2.368(8)	Gd3-O10	2.285(9)
Gd1-O5	2.428(8)	Gd3-O15	2.369(7)
Gd1-O15	2.445(7)	Gd3-O5	2.423(7)
Gd1-N2	2.498(1)	Gd3-O4	2.515(9)
Gd1-O4	2.514(8)	Gd3-N4	2.516(1)
Gd1-O2′	2.523(7)	Gd4-O9	2.251(9)
Gd2-O3	2.389 (8)	Gd4-O7	2.338(8)
Gd2-O15	2.412(8)	Gd4-O10	2.346(9)
Gd2-O13	2.428(9)	Gd4-O12	2.426 (9)
Gd2-O1′	2.474(7)	Gd4-O14	2.430(1)
Gd2-O1	2.475(8)	Gd4-O5	2.476(8)
Gd2-O16	2.530(8)	Gd4-N3	2.536(1)
Gd2-N1	2.547(9)	Gd4-O4	2.576(7)
Gd2-O4	2.715(7)		

Bond angles

Gd1-O1-Gd2	100.6(3)	Gd1′-O2-Gd2	105.1(3)
Gd1-O1-Gd2′	105.9(3)	Gd2-O1-Gd2′	112.2(3)
Gd1-O4-Gd2	90.9(2)	Gd2-O3-Gd3	104.1(3)
Gd1-O4-Gd3	94.5(3)	Gd2-O4-Gd3	88.8(2)
Gd1-O4-Gd4	91.5(2)	Gd2-O15-Gd3	99.9(3)
Gd1-O5-Gd4	96.1(3)	Gd3-O4-Gd4	90.4(2)
Gd1-O5-Gd3	99.1(3)	Gd3-O5-Gd4	95.0(2)

Gd1-O7-Gd4	103.6(3)	Gd3-O10-Gd4	102.5(3)
Gd1-O15-Gd2	100.3(3)	Gd4-O4-Gd2	177.5(3)
Gd1-O15-Gd3	100.1(3)		

[a] Primed and unprimed atoms are related by symmetry.

The octanuclear complex **7** comprises four crystallographically independent Gd^{III} ions that adopt four different coordination geometries. Figure 3.6 depicts the coordination polyhedra, which are defined by the donor atoms around the Gd atoms, in relation to the most common polyhedral geometries. Adopting the program SHAPE the coordination geometries, which better describe the environments around the eight-coordinate Gd1 and Gd4, are the triangular dodecahedral and biaugmented trigonal prismatic, respectively (Table 3.7). For the nine-coordinate Gd2, the polyhedron which is closer to the ideal one is that of the spherical capped square antiprism (Table 3.8), whereas for the seven-coordinate Gd3 the pentagonal bipyramidal geometry is the closest to the ideal polyhedron (Table 3.9).

There have been many $\{Ln_8\}$ complexes reported in the literature, and these possess a wide variety of metal topologies such as cages, squares and grids, dimers of tetramers, among others.[110,127f,129] However, complexes **7**-**10** are the first octanuclear 4*f*-metal clusters with a metal topology of six edge- and vertex-sharing triangles.

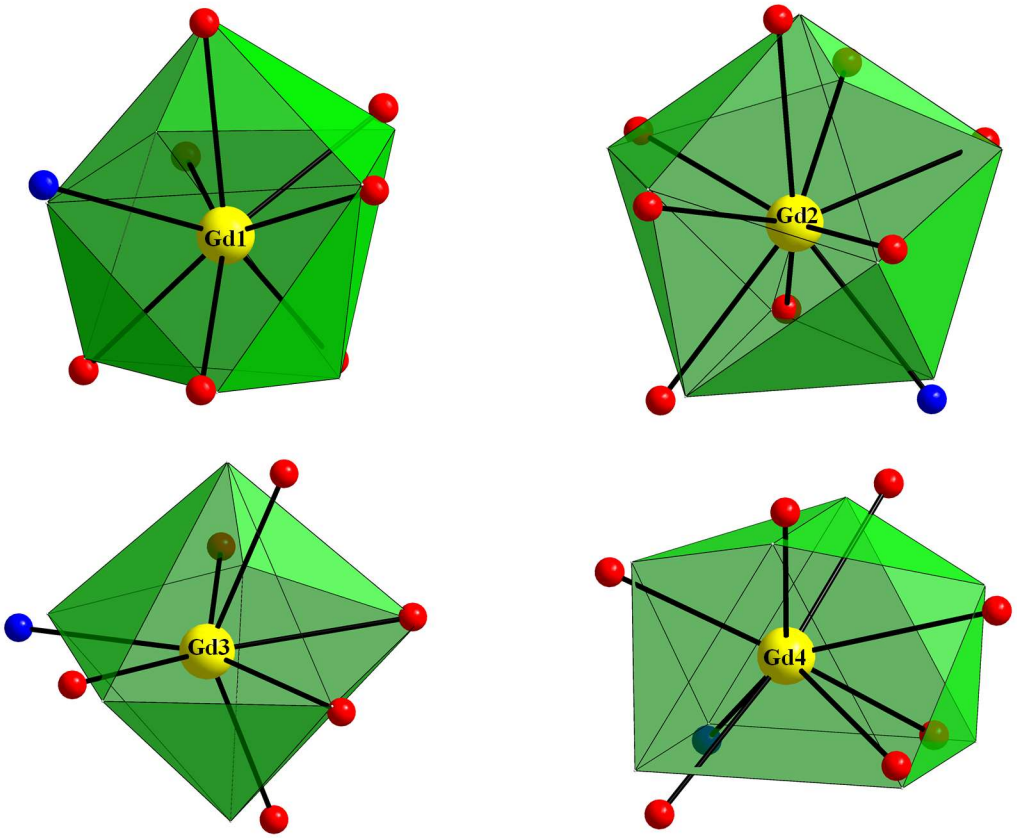

Figure 3.6. Triangular dodecahedral (Gd1), spherical capped square antiprismatic (Gd2), pentagonal bipyramidal (Gd3), and biaugmented trigonal prismatic (Gd4) geometries of the gadolinium atoms in the structure of **7**. The exact same polyhedra were adopted by the Dy atoms in the structure of complex **9**. Color scheme: Gd^{III}, yellow; O, red; N, blue; C, gray.

Table 3.7. Continuous Shape Measures (CShM) of the eight-coordinate Gd1 and Gd4 coordination polyhedra in complex **7**.[a]

Polyhedron[b]	Gd1	Gd4
OP-8	28.274	33.307
HPY-8	21.856	21.945
HBPY-8	16.692	14.350

CU-8	10.969	12.698
SAPR-8	3.299	6.163
TDD-8	**1.374**	4.326
JGBF-8	13.473	11.453
JETBPY-8	26.797	22.977
JBTPR-8	3.090	3.961
BTPR-8	2.546	**3.095**
JSD-8	3.429	4.833
TT-8	11.736	13.449
ETBPY-8	22.501	19.481

[a]The values in boldface indicate the closest polyhedron according to the Continuous Shape Measures (CShM). [b]Abbreviations: OP-8, octagon; HPY-8, heptagonal pyramid; HBPY-8, hexagonal bipyramid; CU-8, cube; SAPR-8, square antiprism; TDD-8, triangular dodecahedron; JGBF-8, Johnson gyrobifastigium; JETBPY-8, Johnson elongated triangular bipyramid; JBTPR-8, Johnson biaugmented trigonal prism; BTPR-8, biaugmented trigonal prism; JSD-8, Johnson snub diphenoid; TT-8, triakis tetrahedron; ETBPY-8, elongated trigonal bipyramid.

Table 3.8. Continuous Shape Measures (CShM) of the nine-coordinate Gd2 coordination polyhedra in complex **7**.[a]

Polyhedron[b]	Gd2
EP-9	32.843
OPY-9	23.995
HBPY-9	18.568

JTC-9	13.306
JCCU-9	10.047
CCU-9	9.656
JCSAPR-9	2.153
CSAPR-9	**1.867**
JTCTPR-9	2.495
TCTPR-9	2.144
JTDIC-9	11.662
HH-9	9.997
MFF-9	2.032

[a]The values in boldface indicate the closest polyhedron according to the Continuous Shape Measures (CShM). [b]Abbreviations: EP-9, enneagon; OPY-9, octagonal pyramid; HBPY-9, heptagonal bipyramid; JTC-9, Johnson triangular cupola J3; JCCU-9, Capped cube J8; CCU-9, Spherical-relaxed capped cube; JCSAPR-9, Capped square antiprism J10; CSAPR-9, Spherical capped square antiprism; JTCTPR-9, Tricapped trigonal prism J51; TCTPR-9, Spherical tricapped trigonal prism; JTDIC-9, Tridiminished icosahedron J63; HH-9, Hula-hoop; MFF-9, Muffin.

Table 3.9. Continuous Shape Measures (CShM) of the seven-coordinate Gd3 coordination polyhedra in complex **7**.[a]

Polyhedron[b]	Gd3
HP-7	28.277
HPY-7	19.531

PBPY-7	**3.844**
COC-7	4.669
CTPR-7	4.545
JPBPY-7	6.033
JETPY-7	20.046

[a]The values in boldface indicate the closest polyhedron according to the Continuous Shape Measures (CShM). [b]Abbreviations: HP-7, heptagon; HPY-7, hexagonal pyramid; PBPY-7, pentagonal bipyramid; COC-7, capped octahedron; CTPR-7, capped trigonal prism; JPBPY-7, Johnson pentagonal bipyramid; JETPY-7, Johnson elongated triangular pyramid.

3.3.3 Magnetic Susceptibility Studies

Variable-temperature direct current (*dc*) magnetic susceptibility studies were carried out on freshly prepared, crystalline samples of complexes **4**-**6** in the temperature range 5.0-300 K under an applied field of 0.1 T. The obtained data for all studied $\{Ln_7\}$ compounds are shown as $\chi_M T$ *vs.* T plots in Figure 3.7. The experimental $\chi_M T$ values at room temperature are in good agreement with the theoretical ones (55.13 cm^3Kmol^{-1} for **4**; 82.74 cm^3Kmol^{-1} for **5**; 99.19 cm^3Kmol^{-1} for **6**) for seven non-interacting Gd^{III} ($^8S_{7/2}$, $S = 7/2$, $L = 0$, $g = 2$), Tb^{III} ($^7F_6$, $S = 3$, $L = 3$, $g = 3/2$) and Dy^{III} ($^6H_{15/2}$, $S = 5/2$, $L = 5$, $g = 4/3$) ions. For the isotropic $\{Gd^{III}_7\}$ (**4**), the $\chi_M T$ product remains almost constant at a value of ~54 cm^3Kmol^{-1} from 300 K to ~50 K and then steadily decreases to a minimum value of 40.82 cm^3Kmol^{-1} at 5.0 K indicating the presence of weak intramolecular antiferromagnetic exchange interactions between the seven Gd^{III} centers and/or zero-field splitting. For the anisotropic $\{Tb^{III}_7\}$ (**5**) and $\{Dy^{III}_7\}$ (**6**) complexes, the

thermal evolution of the magnetic susceptibility is similar, in which the $\chi_M T$ product remains essentially constant at a value of ~81 and ~92 cm^3Kmol^{-1} from 300 K to ~140 K and then rapidly decreases to a minimum value of 55.63 and 73.79 cm^3Kmol^{-1} at 5.0 K, respectively. Such a low temperature decrease of the $\chi_M T$ product is mainly due to the depopulation of the excited Stark sublevels of the Tb^{III} and Dy^{III} ions and the presence of weak antiferromagnetic interactions between the metal centers, which cannot be quantified due to the strong orbital momentum.[24a,62,82,83a,b]

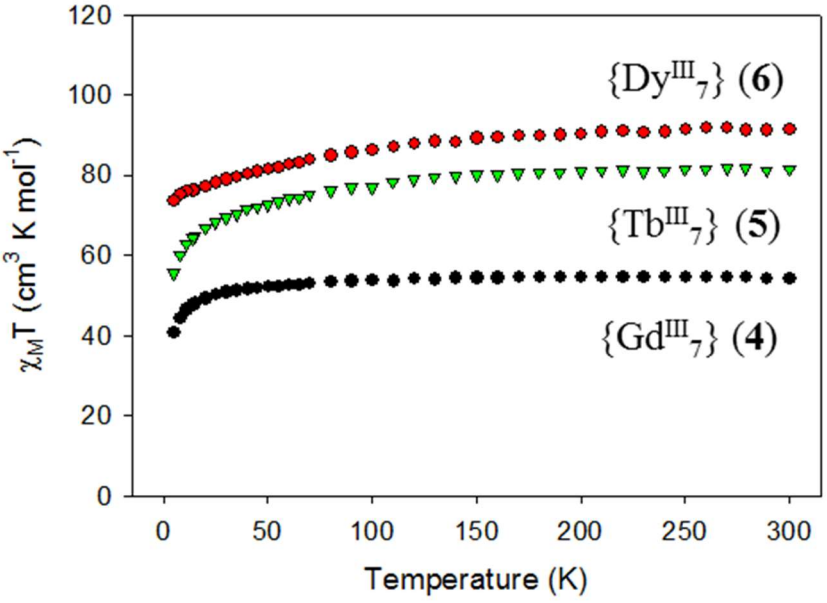

Figure 3.7. Plots of $\chi_M T$ *vs.* *T* products for complexes **4**-**6** at 0.1 T.

The field dependence of magnetization measurements at low temperatures shows all the expected characteristics for polynuclear, weakly coupled Ln^{III} clusters. Briefly, the lack of saturation in magnetization for complexes **5** and **6** (Figure 3.8) indicates the presence of magnetic anisotropy and/or population of low-lying excited states. In the case of **4**, the magnetization reaches a saturation of 48.9 $N\mu_B$ at the highest fields (Figure 3.9), which is in

excellent agreement with the expected value of 49 $N\mu_B$ for seven non-coupled Gd^{III} ions. The slight deviation of *M vs. H* for **4** at low temperatures and small magnetic fields is due to the population of low-lying excited states with *S* larger than the ground state.

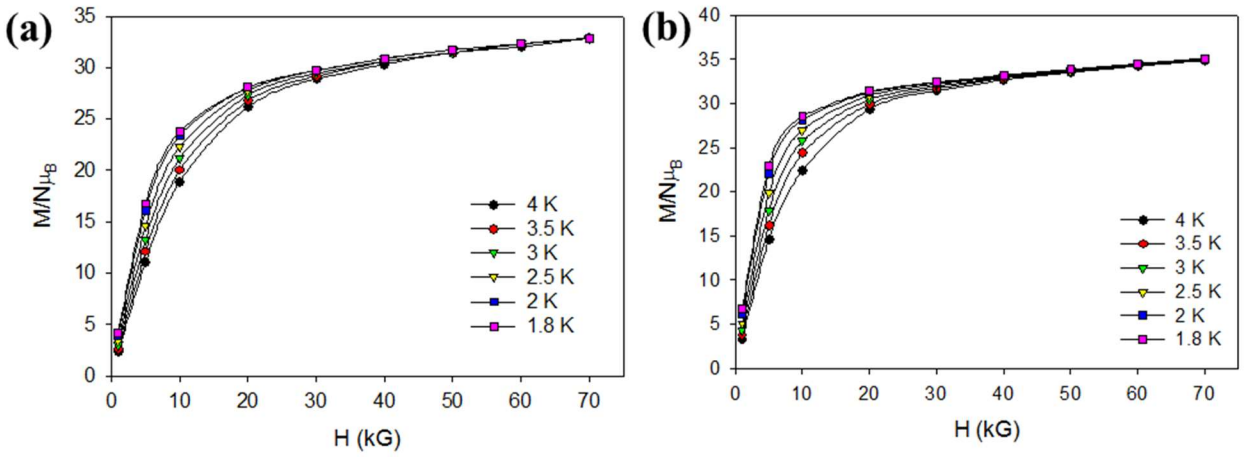

Figure 3.8. Plots of magnetization (*M*) *vs.* field (*H*) for complexes **(a) 5** and **(b) 6** at different low temperatures.

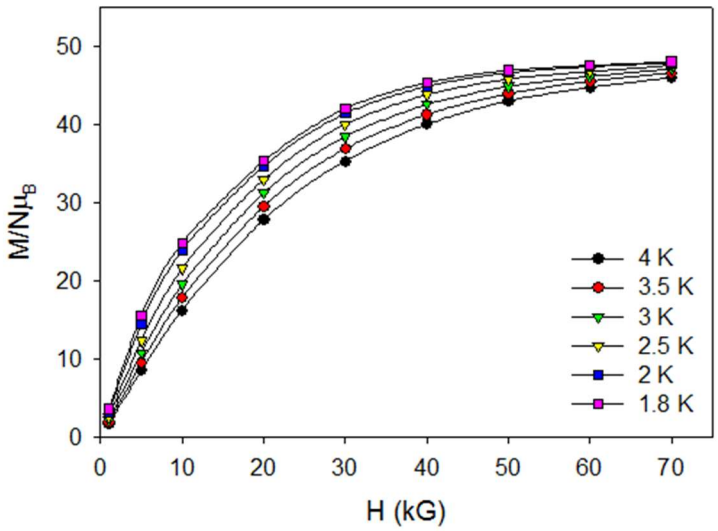

Figure 3.9. Plot of magnetization (*M*) *vs.* field (*H*) for complex **4** at different low temperatures.

Alternating current (*ac*) magnetic susceptibility studies have been also carried out in order to investigate the magnetization dynamics of the anisotropic $\{Tb^{III}_7\}$ and $\{Dy^{III}_7\}$ clusters under a zero *dc* magnetic field. Complex **6** shows strong frequency-dependent out-of-phase χ_M'' tails of signals at temperatures below ~10 K (Figure 3.10), indicative of the slow magnetization relaxation of an SMM with a small energy barrier for magnetization reversal. This is most likely due to the fast tunneling, which is usually observed in high-nuclearity and high-symmetry Dy^{III} SMMs,[87a,117d] and mainly originates from single-ion effects of the individual Dy^{III} Kramers ions.[24a,62,82,83a,b] There were no out-of-phase *ac* signals down to 1.8 K for the $\{Tb^{III}_7\}$ analogue (Figure 3.11).

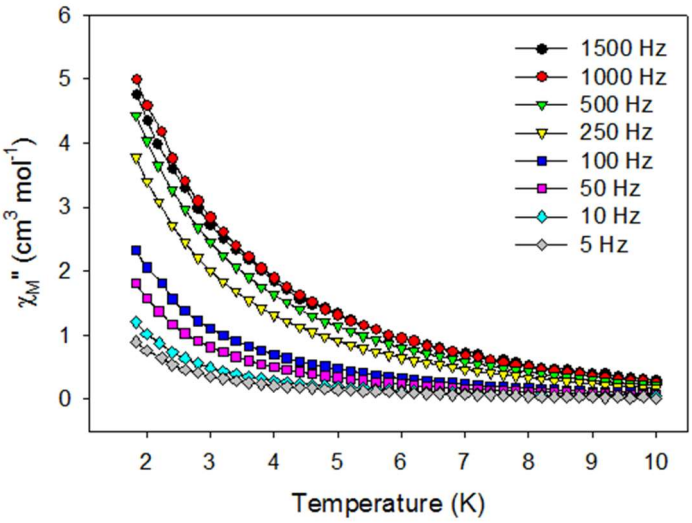

Figure 3.10. The out-of-phase (χ_M'') *vs. T ac* susceptibility signals for **6** in a 3.5 G field oscillating at the indicated frequencies.

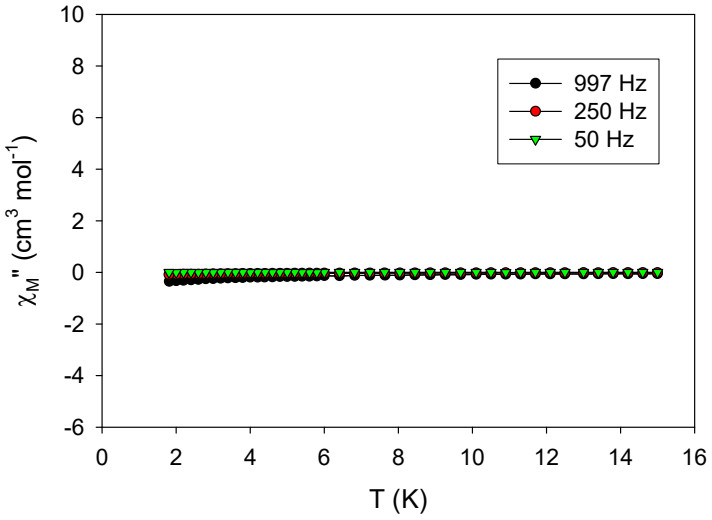

Figure 3.11. The out-of-phase (χ_M'') *vs. T ac* susceptibility signals for **5** in a 3.5 G field oscillating at the indicated frequencies.

In an attempt to quantify the energy barrier and relaxation time for **6**, and given the absence of χ'' peak maxima, it was decided to apply Eqn. 2.2 [$\ln(\chi''/\chi') = \ln(\omega\tau_0) + E_a/k_BT$] recently developed by Bartolomé and coworkers.[106] Considering a single relaxation process, the least-squares fits of the experimental data (Figure 3.12) gave an energy barrier of ~1.2 cm^{-1} (~1.7 K) and a relaxation time of 0.2×10^{-6} s, which is in agreement with previously reported τ_0 values for other fast relaxing 4*f*-metal based SMMs.[24a,62,82,83a,b]

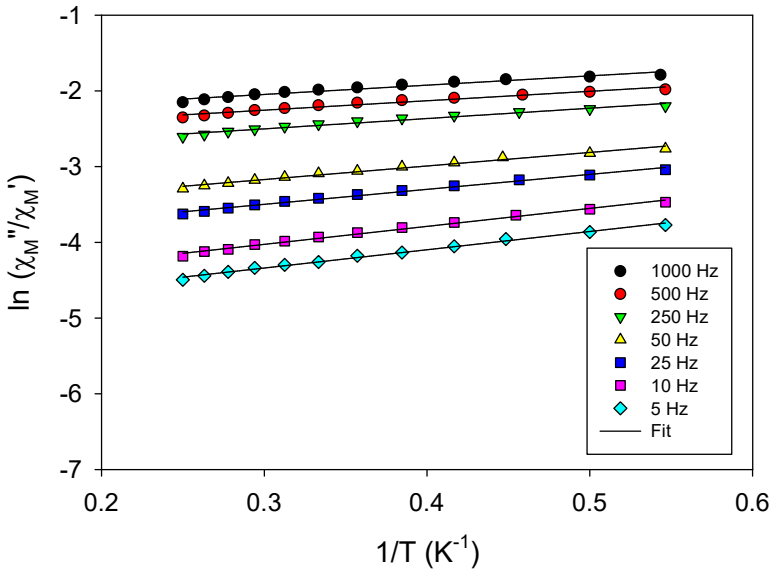

Figure 3.12. Plots of ln(χ''/χ') *vs.* 1/*T* for **6** at different frequencies of the 3.5 G oscillating *ac* field. The solid lines are the best-fit curves; see the text for the fit parameters.

The magnetic susceptibility data for the octanuclear complexes **7**, **8** and **9** are shown as $\chi_M T$ *vs.* *T* plots in Figure 3.13. Theoretically, the {Eu^{III}_8} analogue (**10**) should not exhibit any magnetic moment since Eu^{III} has an $^7F_0$ ground state with $J = 0$, although some contribution from thermally accessible levels such as $^7F_1$ and $^7F_2$ may appear. The experimental $\chi_M T$ values at room temperature are in good agreement with the theoretical ones (63.00 cm^3Kmol^{-1} for **7**; 94.56 cm^3Kmol^{-1} for **8**; 113.36 cm^3Kmol^{-1} for **9**) for eight non-interacting Gd^{III} ($^8S_{7/2}$, $S = 7/2$, $L = 0$, $g = 2$), Tb^{III} ($^7F_6$, $S = 3$, $L = 3$, $g = 3/2$) and Dy^{III} ($^6H_{15/2}$, $S = 5/2$, $L = 5$, $g = 4/3$) ions. The $\chi_M T$ product for the isotropic {Gd^{III}_8} (**7**) remains almost constant at a value of ~63 cm^3Kmol^{-1} until ~70 K and then steadily decreases to a minimum value of 38.83 cm^3Kmol^{-1} at 5.0 K indicating the presence of weak intramolecular antiferromagnetic exchange interactions between the eight Gd^{III} centers and/or zero-field splitting. For the anisotropic {Tb^{III}_8} (**8**) and {Dy^{III}_8} (**9**) complexes, the thermal evolution of the magnetic susceptibility is similar. The $\chi_M T$ values at 300

K are 96.4 and 109.1 cm^3Kmol^{-1} for **8** and **9**, respectively, and the products decrease smoothly until ~150 K, and then more rapidly to a minimum value of 58.18 and 76.85 cm^3Kmol^{-1} at 5.0 K, respectively. Such a low temperature decrease of the $\chi_M T$ products is mainly due to the depopulation of the excited Stark sublevels of the Tb^{III} and Dy^{III} ions and the possible presence of some weak antiferromagnetic interactions between the metal centers.

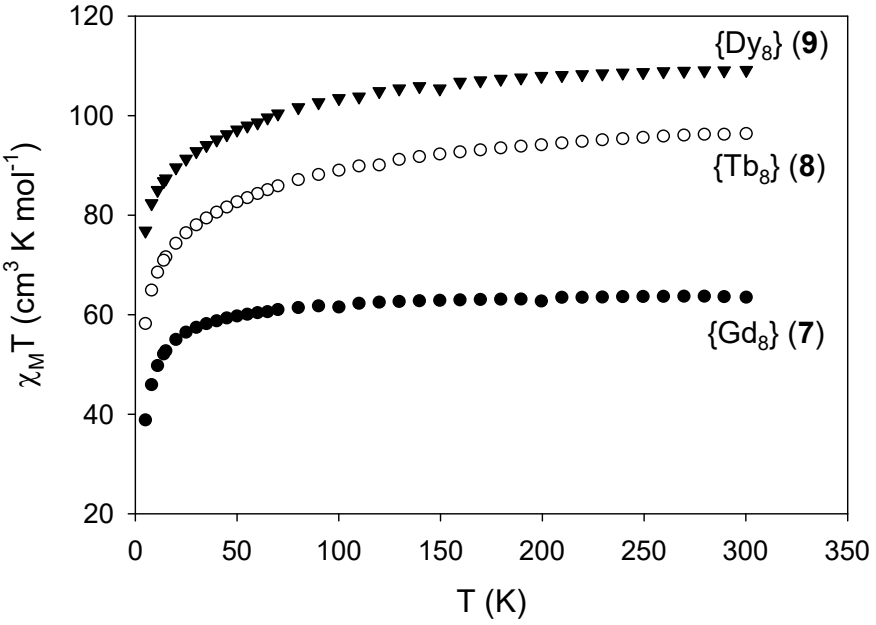

Figure 3.13. Plots of $\chi_M T$ *vs.* *T* for complexes **7-9** at 0.1 T.

With respect to the magnetization *vs.* field studies for all three complexes, again the lack of saturation of magnetization for **8** and **9** (Figure 3.14) indicates the presence of magnetic anisotropy and/or the population of low-lying excited states. In the case of **7** (Figure 3.15), the magnetization saturates at a value of ~55 $N\mu_B$ at the highest fields and lowest temperature, which is in good agreement with the expected value of 56 $N\mu_B$ for eight non-coupled Gd^{III} ions. This further supports the weak nature of the magnetic exchange interactions between the metal centers

($\chi_M T$ *vs.* *T* plot), meaning that the antiferromagnetic interactions are easily overcome by the external magnetic field. The slight deviation of *M vs. H* for **7** at low temperatures and small magnetic fields is due to the population of low-lying excited states with *S* larger than the ground state.

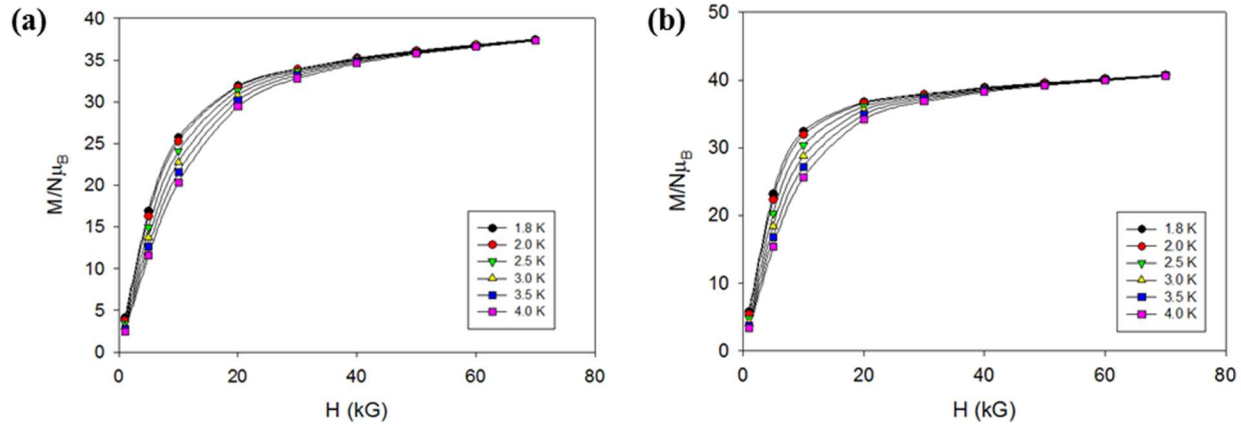

Figure 3.14. Plots of magnetization (*M*) *vs.* field (*H*) for **(a)** $\{Tb^{III}_8\}$ (**8**) and **(b)** $\{Dy^{III}_8\}$ (**9**) at different low temperatures.

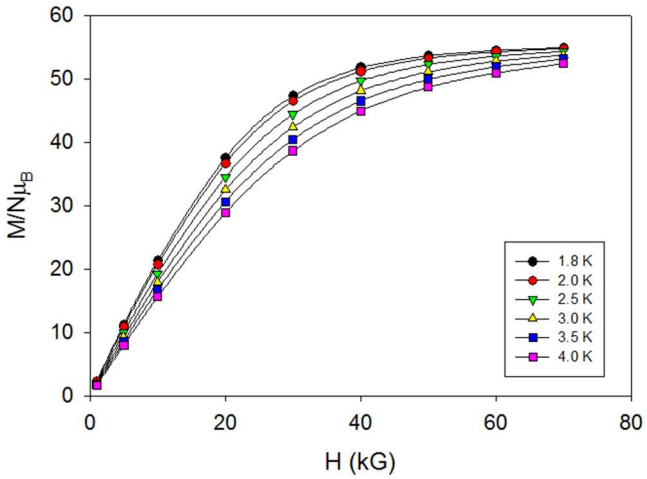

Figure 3.15. Plot of magnetization (*M*) *vs.* field (*H*) for the $\{Gd^{III}_8\}$ (**7**) complex at different low temperatures.

In order to probe the magnetization dynamics of the anisotropic $\{Tb^{III}_8\}$ and $\{Dy^{III}_8\}$ clusters, alternating current magnetic susceptibility studies have been also performed in the absence of a *dc* magnetic field. The $\{Dy^{III}_8\}$ complex shows weak frequency-dependent out-of-phase χ_M'' tails of signals at temperatures below ~10 K (Figure 3.16). This is an indication of the slow magnetization relaxation of an SMM with a small energy barrier for magnetization reversal. Such behavior is assumed to arise from predominant single-ion effects of the individual Dy^{III} Kramers' ions within the molecule, as was also the case for the $\{Dy_7\}$ cluster bearing the *cis*/*trans*-sach^{2-} ligand. In the case of $\{Tb^{III}_8\}$ complex, there were no out-of-phase *ac* signals (Figure 3.17).

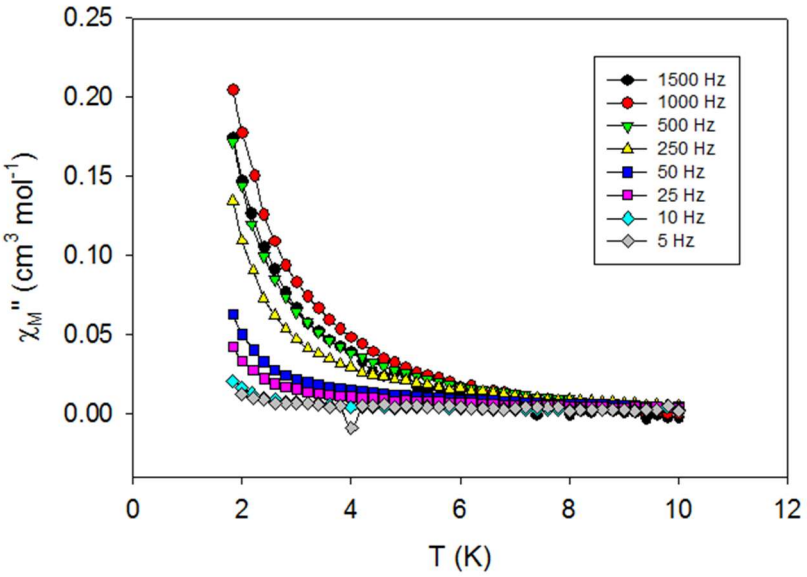

Figure 3.16. The out-of-phase (χ_M'') *vs. T ac* susceptibility signals for **9** in a 3.5 G field oscillating at the indicated frequencies.

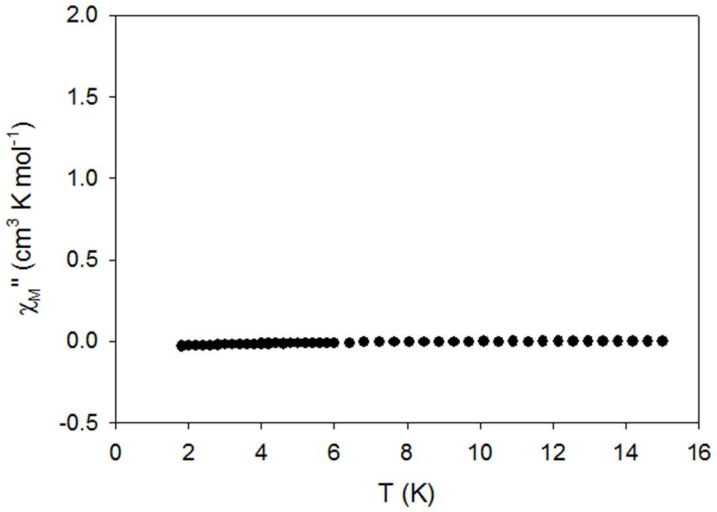

Figure 3.17. The out-of-phase (χ_M'') *vs. T ac* susceptibility signals for **8** in a 3.5 G field oscillating at a frequency of 1000 Hz.

Given the absence of χ_M'' peak maxima, the energy barrier and relaxation time for complex **9** were approximated using the Bartolomé method. Considering a single relaxation process, the least-squares fits of the experimental data (Figure 3.18) gave an energy barrier of ~2.3(1) cm^{-1} (3.3(1) K) and a relaxation time of 3.2(3) × 10^{-5} s. This is a very small energy barrier for the magnetization reversal, consistent with a very fast-relaxing SMM that is usually the case for high nuclearity Ln^{III} complexes consisting of many 4*f*-metal ions in different coordination environments. In this family of complexes, I have also performed *ac* studies in the presence of an external *dc* field. However, the application of an external *dc* field has not induced any significant shift of the out-of-phase signals to higher temperatures.

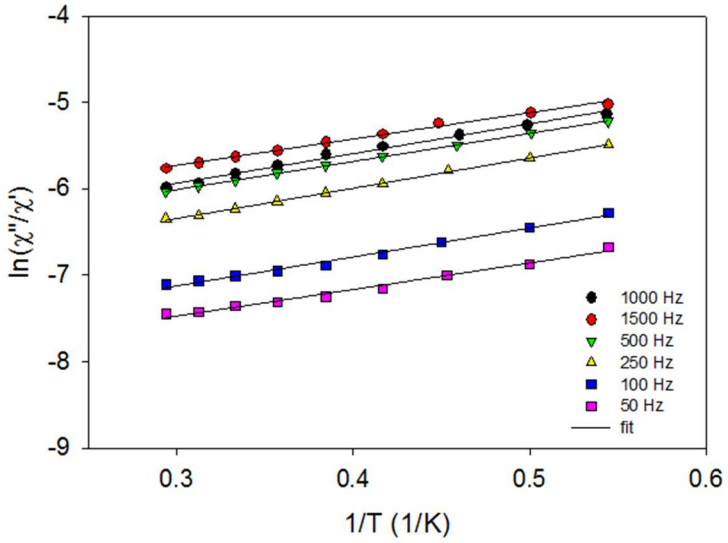

Figure 3.18. Plots of $\ln(\chi''/\chi')$ *vs.* $1/T$ for **9** at different frequencies of the 3.5 G oscillating *ac* field. The solid lines are the best-fit curves.

3.3.4 Solution and Solid-State Photoluminescence Studies

The characterization in solution of the free ligand sachH_2 and complexes **4-6** included UV/Vis, electrospray mass spectrometry (ES-MS) and excitation/emission studies at low-concentrations (~10^{-5} M) in solvent MeCN. These studies were performed in order to probe the integrity of the structures of **4-6** in solution and elucidate any possible photophysical properties. The absorption spectrum of sachH_2 exhibits three bands located at 215, 255 and 314 nm, which are characteristic bands of many Schiff bases,[130] and can be mainly assigned to $\pi \rightarrow \pi^*$ transitions. In all complexes **4-6**, these bands have been shifted to slightly higher wavenumbers (222, ~265 and 340 nm, respectively) consistent with coordination of the ligand to the metal centers (Figure 3.19).

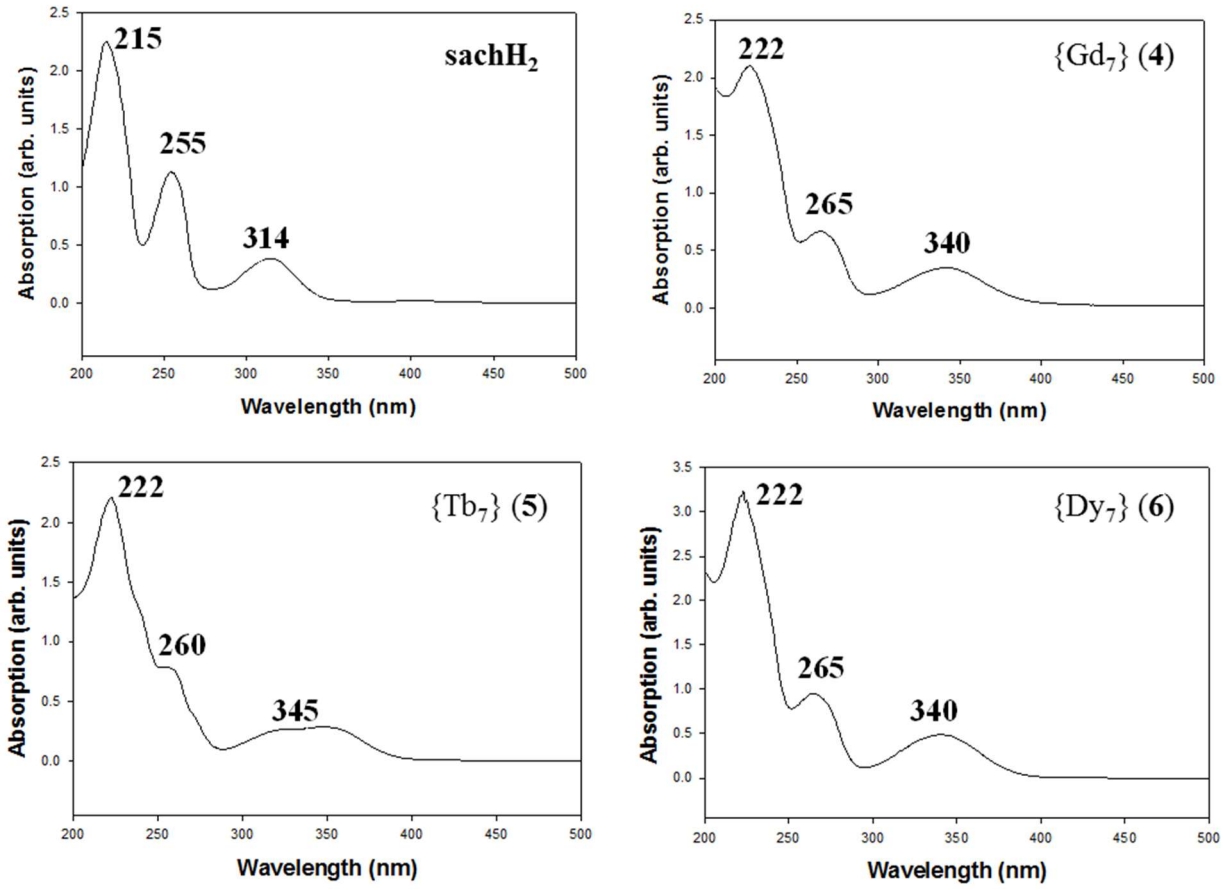

Figure 3.19. Absorption spectra of the free ligand $sachH_2$ and complexes **4**-**6** in MeCN (~10^{-5} M).

The negative ion electrospray mass spectrum (ESI-MS) of the representative $\{Gd^{III}_7\}$ compound **4** in MeCN shows a strong intensity peak at 2811 *m*/*z* which can be assigned to the singly charged anion $[Gd_7(OH)_6(CO_3)_3(sach)_4(sachH)_2(MeCN)_3]^-$, with the volatile coordinating MeOH molecules of the solid-state cluster being partially replaced by three terminal MeCN groups (Figure 3.20).[131] Isotopic pattern of the molecular ion was used to justify further the compositional assignment. Taking into advantage the characteristic isotopic patterns of molecules containing 4*f*-elements, a good agreement was observed between the experimentally

determined isotopic pattern for **4** and its theoretical one (Figure 3.21).[131] Complexes **5** and **6** showed similar compositions allowing me to confirm the structural integrity of **4**-**6** in MeCN.

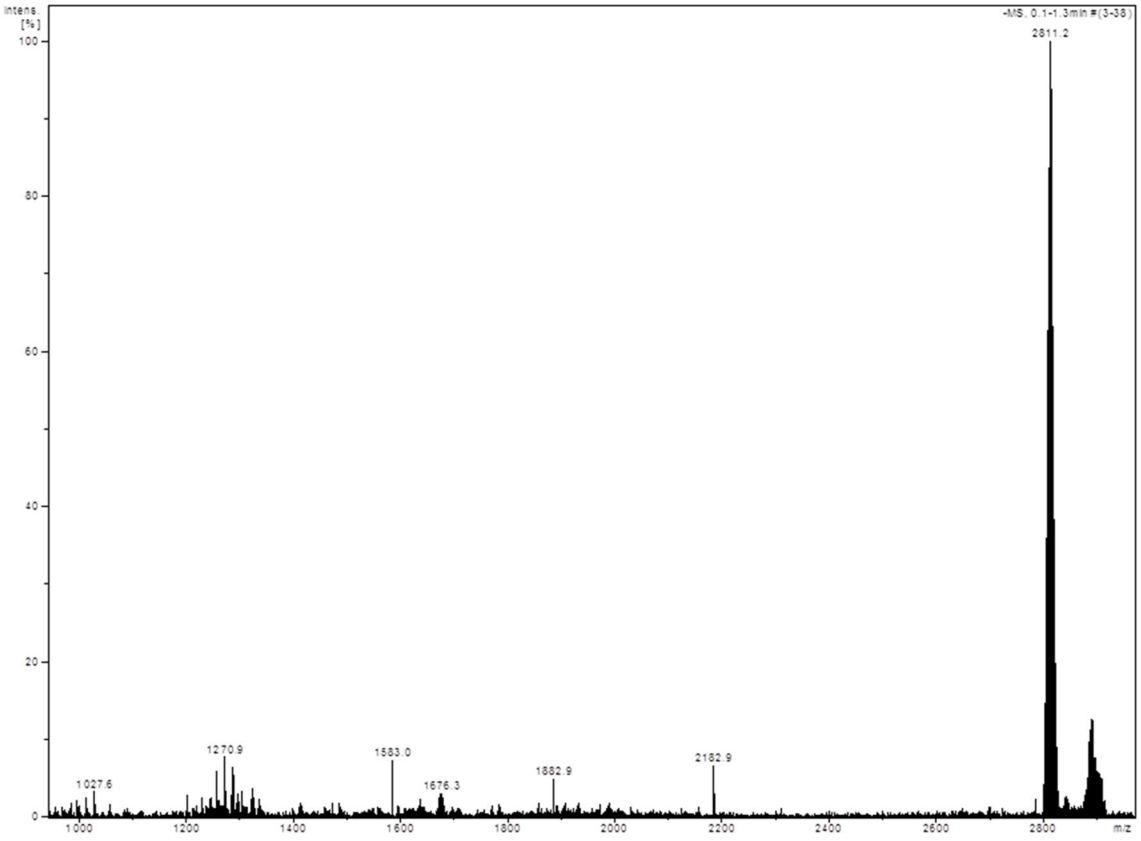

Figure 3.20. Negative ion ES mass spectrum of **4** shown in the 1000 to 3000 *m*/*z* range.

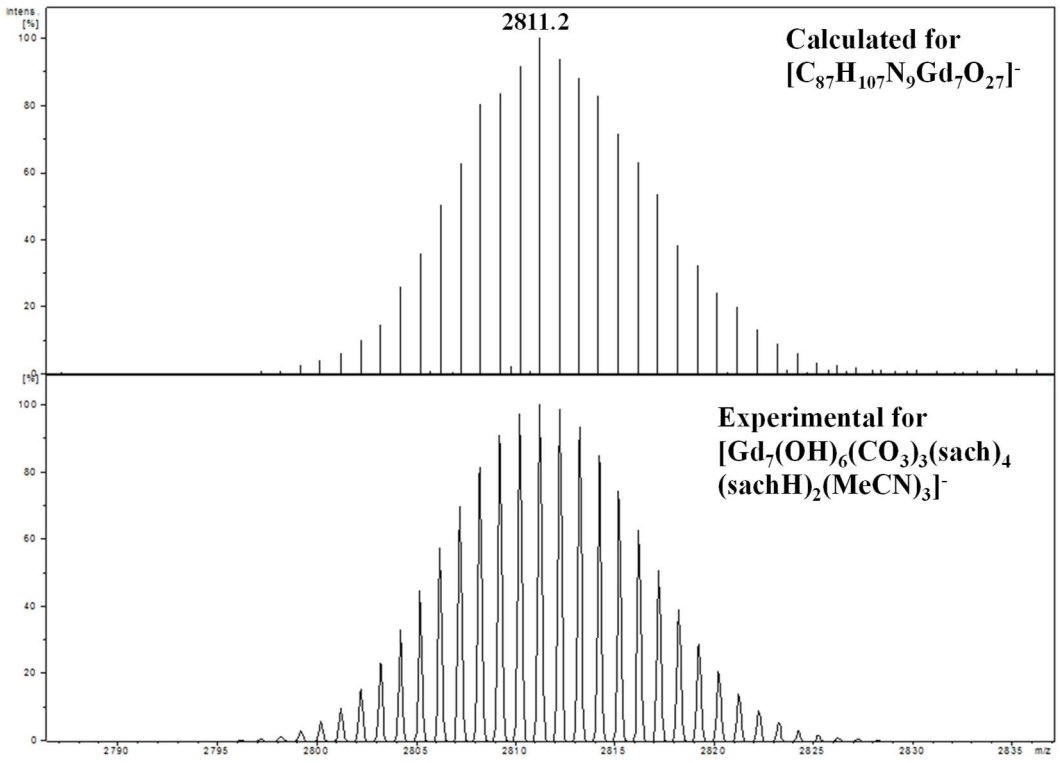

Figure 3.21. Comparison of the theoretical (top) and experimental (bottom) isotopic patterns of complex **4** under negative ion ES-MS.

In light of the stability of complexes **4**-**6** in MeCN, it was decided to perform photophysical studies in solution. The free ligand sachH$_2$ shows a broad blue-centered, fluorescence emission at 466 nm upon maximum excitation at 310 nm (Figure 3.22). The observed emission band is not concentration-dependent and is typical for organic molecules containing aromatic fragments.[108b,132] As expected, the {Gd^{III}_7} complex did not produce any metal-centered emission since the emissive state of Gd^{3+} is too high to accept energy transfer. Indeed, this state ($^6P_{7/2}$) lies at >30000 cm^{-1}, while that of Tb^{3+} ($^5D_4$) is located at ~20500 cm^{-1}.[107a,108,132] Thus, upon excitation at 340 nm, the {Tb^{III}_7} complex **5** exhibits a strong green luminescence emission with sharp and narrow bands (Figure 3.23, top) that can be ascribed to the characteristic $^5D_4 \rightarrow {}^7F_J$ (J = 3; 622 nm, J = 4; 583 nm, J = 5; 546 nm, J = 6; 490 nm)

transitions of Tb^{III}.[1,16e,86b] This means that the $sachH_2$ ligand promotes an efficient energy transfer to the Tb^{III} ions and can be considered as a prominent "antenna", although some ligand fluorescence is still observed as a broad band at ~430 nm which is due to a back-energy transfer from Tb^{III}.[74,76] In the case of $\{Dy^{III}_7\}$ complex **6**, a strong blue emission is clearly observed upon maximum excitation at 340 nm (Figure 3.23, bottom). The broad band at ~438 nm is assigned to a strong energy transfer from Dy^{III} to the ligand's excited state(s) leading to a ligand fluorescence, whereas the shoulder at 474 nm and the narrow band at 575 nm are ascribed to the characteristic $^4F_{9/2} \rightarrow {}^6H_{15/2}$ and $^4F_{9/2} \rightarrow {}^6H_{13/2}$ emissions of the Dy^{III} ions, respectively.[2,86c]

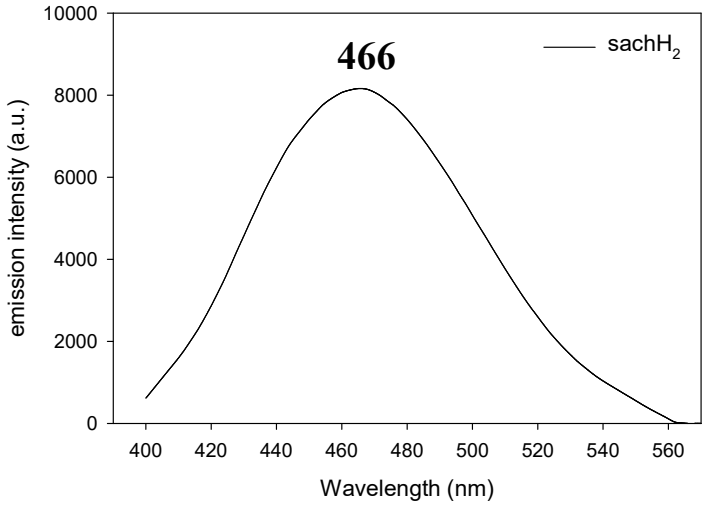

Figure 3.22. Emission spectrum of $sachH_2$ (excitation at 310 nm; MeCN solution 10^{-5} M) at room temperature.

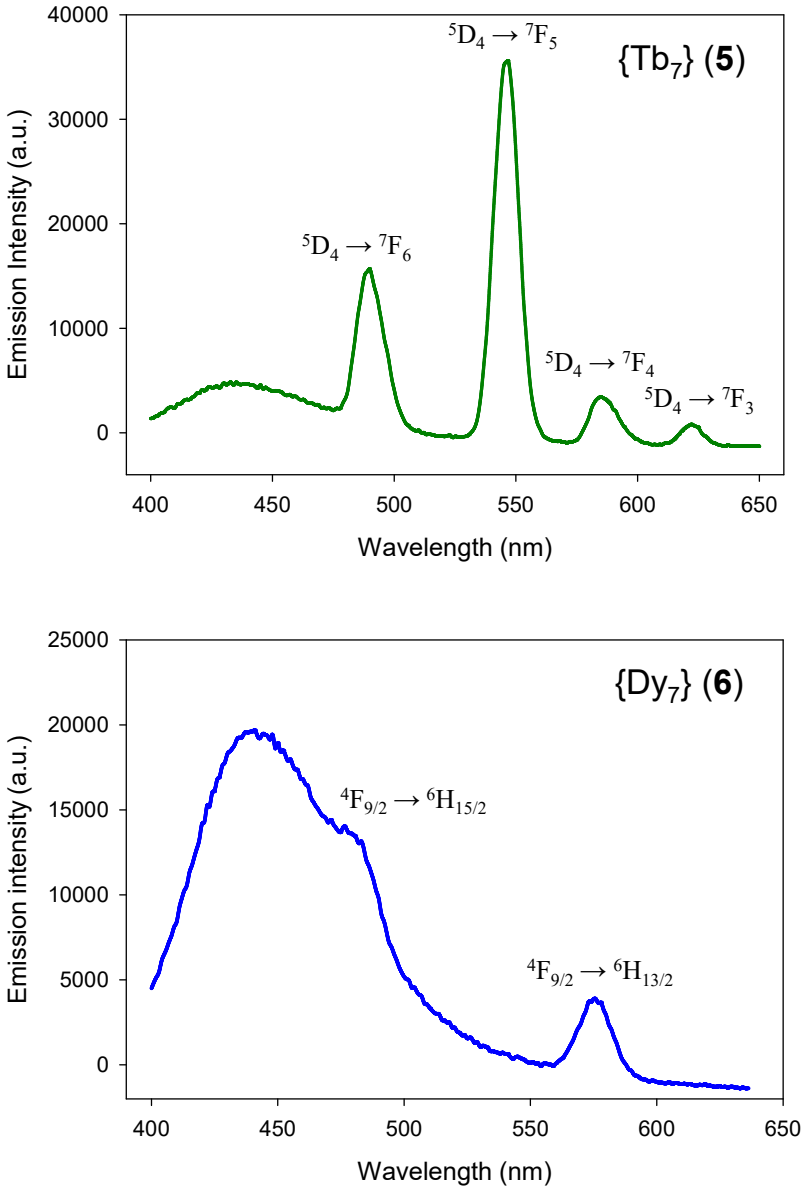

Figure 3.23. Room temperature emission spectra for **5** (top) and **6** (bottom) in MeCN (10^{-5} M). The excitation wavelength was 340 nm in both cases.

In contrast to the {Ln_7} complexes **4-6**, the octanuclear compounds **7-10** were found not to be stable in solution as determined by ESI-MS studies in various different solvate media (i.e., MeCN, CH_2Cl_2 and MeOH), which revealed multiple peaks of the same intensities at different values of *m*/*z*. I therefore concentrated on the characterization of these complexes and the *trans*-

sachH$_2$ ligand in the solid-state. Solid-state photoluminescence studies were performed for the free ligand and the {Tb$^{III}_8$} (**8**), {Dy$^{III}_8$} (**9**) and {Eu$^{III}_8$} (**10**) analogues. The free ligand shows a broad blue-centered emission at 514 nm (Figure 3.24a), upon excitation at 326 nm, which is red-shifted when compared to the emission of the *cis*/*trans*-sachH$_2$ in solution. For the metal cluster compounds, upon excitation at 325 nm, the {Tb$^{III}_8$} complex exhibits green luminescence emission with sharp and narrow bands that are ascribed to the characteristic *f-f* transitions of the Tb^{3+} ions (Figure 3.24b). In the case of the {Dy$^{III}_8$} complex, a blue-green luminescence emission is clearly observed, upon maximum excitation at 356 nm, while the {Eu$^{III}_8$} complex exhibits a strong red luminescence emission, upon excitation at 423 nm, which is attributed to the to the characteristic $^5D_0 \rightarrow {}^7F_J$ (J = 0-4) transitions of Eu^{3+} (Figures 3.24c,d). Specific assignments are as follows: $^5D_0 \rightarrow {}^7F_{0,1}$ (580-595 nm), $^5D_0 \rightarrow {}^7F_2$ (616 nm), $^5D_0 \rightarrow {}^7F_3$ (655 nm) and $^5D_0 \rightarrow {}^7F_4$ (702 nm). In all these cases of complexes **8**-**10**, the photoluminescence results clearly demonstrate the ability of the *trans*-sachH$_2$ ligand to act as an efficient "antenna" group by transferring energy to the Ln^{III} emission states and preventing back-transfer processes from the 4*f*-metal ions, which would otherwise quench or vanish the obtained emissions.

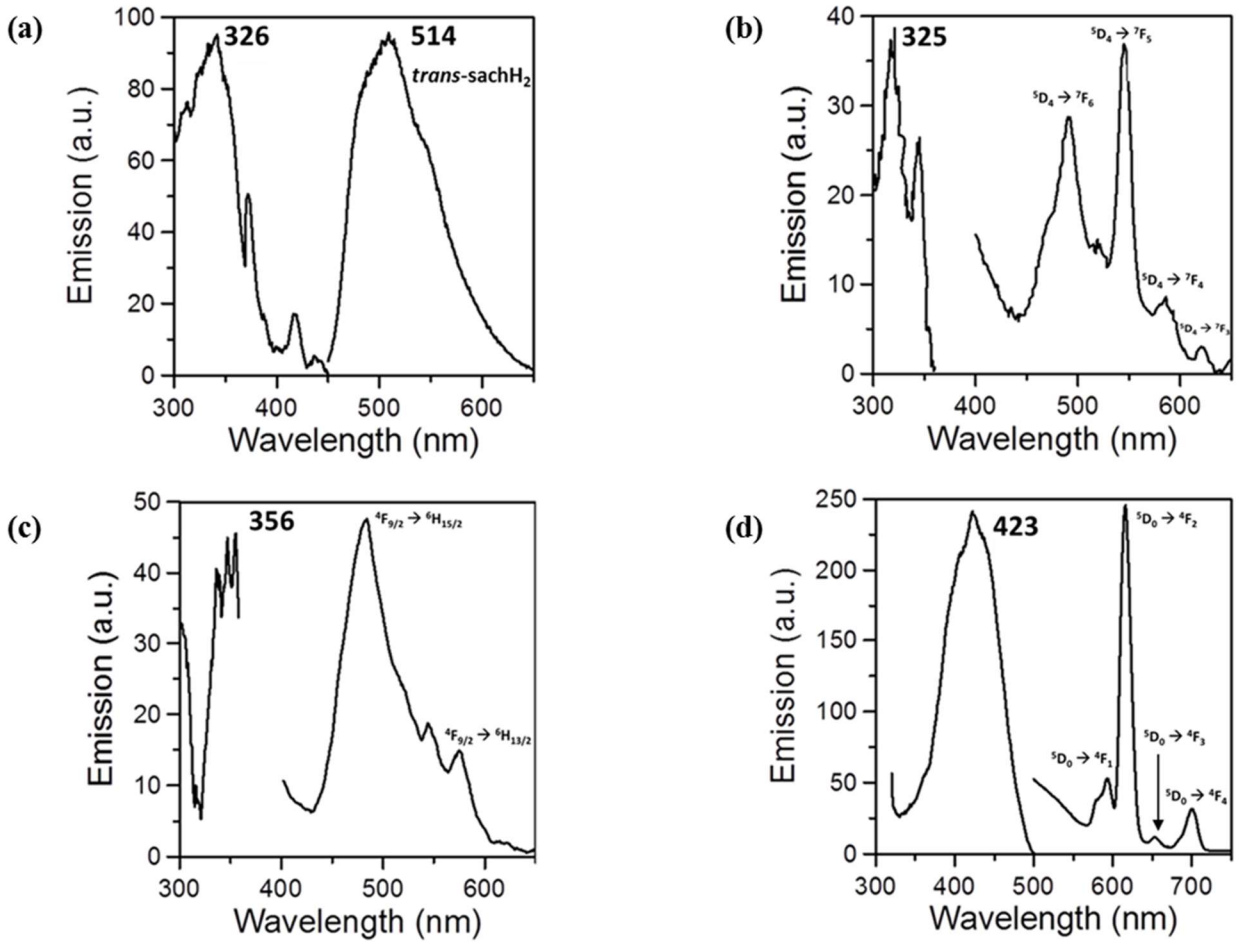

Figure 3.24. Room-temperature solid-state emission spectra of **(a)** *trans*-sachH$_2$, **(b)** complex **8**, **(c)** complex **9**, and (**d**) complex **10**.

3.4 ***Conclusions and Perspectives***

In this chapter it was shown that flexible analogues of the well-known bulky ligand *N*-salicylidene-*o*-aminophenol, such as the *cis*/*trans*-mixture and pure *trans*-isomer of *N*-salicylidene-2-aminocyclohexanol (sachH$_2$), can lead to 4*f*-metal clusters with diverse nuclearities, unprecedented topologies and interesting magneto-optical properties. The reported heptanuclear compounds, which have been resulted from the use of the *cis*/*trans*-sachH$_2$, are

very rare examples of polynuclear 4*f*-metal species that retain their structural conformations in solution. This could potentially allow for the deposition of the reported materials on a variety of surfaces, a perspective which is related to the field of molecular electronics. Furthermore, it was shown that the different stereoconfiguration of the *trans*-isomer of sachH$_2$ has a clear effect on the structural identity of the products, resulting in the isolation and complete characterization of a new family of octanuclear 4*f*-metal clusters. Both families of {Ln$_7$} and {Ln$_8$} complexes are further supported by bridging carbonate groups, which have been presumably derived by a metal-assisted CO_2 fixation process. The {Dy$_7$} and {Dy$_8$} complexes were found to exhibit weak SMM properties while most of the members of these families of clusters (except from the Gd-analogues) show metal-centered emissions in the visible region of the electromagnetic spectrum.

Work in progress with respect to this chapter has been oriented towards the use of other analogues of the Schiff base ligand *N*-salicylidene-*o*-aminophenol in 4*f*-metal cluster chemistry, and these results are presented in the following chapter 4. In addition, some future directions that someone could take are: (i) the modification of sachH$_2$ ligand by replacing the *para*-H atom with an anchoring -SR site, (ii) the synthesis of the pure *cis*-sachH$_2$ ligand and its use in 4*f*-metal chemistry, and (iv) the isolation and use in coordination chemistry of the corresponding pure enantiomers of the *cis*- and *trans*-diastereoisomers of sachH$_2$ in an attempt to prepare chiral SMMs.

Chapter 4

A family of {Ln_2} complexes with spherical tricapped trigonal prismatic Ln^{III} ions bearing the Schiff base ligand *N*-salicylidene-2-amino-5-chlorobenzoic acid: Large energy barrier and magnetization hysteresis at 5 K for the {Dy_2} analogue

4.1 *Preface*

The field of single-molecule magnets (SMMs) has entered a new era since the discovery of mononuclear[57,68,133] and oligonuclear[134] 4*f*-metal complexes exhibiting fascinating properties, distinctly different than those observed in traditional 3*d*-metal ions.[135] SMMs are discrete molecular compounds that show slow relaxation in the absence of an external magnetic field and hysteresis loops because of the presence of an energy barrier to the magnetization reversal.[49,83b,136] As a result, SMMs have been proposed as ideal candidates for potential applications in information storage, molecular spintronics, quantum computing, and other related areas of technological development.[114,137] The recent groundbreaking report of Google and NASA on the production of a new material that is able to perform complex calculations much faster than any conventional computer is undoubtedly the first strong evidence of quantum computing slowly entering our daily life.[138] Thus, molecule-based magnetic materials, such as SMMs, could in principle play a fundamental role in the advancement of new molecular electronic technologies with high densities and efficient performances. The basic requirements for SMM behavior are a bistable ground state, preferably with a large total angular momentum

(*J*), associated with a large magnetic anisotropy of the Ising (or easy-axis) type.[102,139] This combination often leads to large blocking temperatures (T_B), the temperature below which an SMM functions as magnet, and energy barriers to magnetic relaxation as high as 1815 K,[65] both of which are necessary features for the characterization of a molecular magnet as efficient and promising from a technological perspective.

Within the past decade, lanthanide ions have been increasingly exploited for the synthesis of SMMs. Their high single-ion anisotropies, resulting from substantial spin-orbit coupling, have led to slow relaxation of magnetization even in monometallic compounds. Much effort has been focused on understanding the effect of the crystal field (CF) on the size of the energy barrier in 4*f*-metal SMMs.[140] For these complexes it has been elucidated that an easy-axis magnetic anisotropy is favored when the ligand field stabilizes the state with the largest projection of the total angular momentum.[67,141] The application of a crystal field splits the degeneracy of the m_J microstates of the $^{2S+1}L_J$ ground term of the lanthanide ion.[24a,82] For Dy^{III}-based complexes with a non-integer value of *J*, this results in a Kramers doublet ground state, i.e. a degenerate pair of $\pm m_J$ microstates, which produces a bistable magnetic moment that can be used to store information at a molecular level. Therefore, one of the long-term challenges is to control the local symmetry of the 4*f*-metal ions *via* either a rational design or by synthesizing serendipitously low nuclearity complexes with high-symmetry coordination environments. This was theoretically shown and practically proved to allow for the control of the fast quantum tunneling of magnetization (QTM) by the disappearance of certain terms in the crystal field Hamiltonian.[65,67,102,139,140,141,142]

For the realization of the aforementioned challenges and objectives, it becomes apparent that the synthesis of new 4*f*-metal complexes is a fruitful route for the enhancement of the

understanding of the magnetic dynamics of lanthanide SMMs, hopefully developing systems with large barriers and blocking temperatures. To this end, the choice of bridging/chelating ligands is of vital importance not only for structural and coordination chemistry reasons but also for inducing magnetic coupling between two 4*f*-metal ions and harnessing the intrinsic anisotropy of the metal ion(s). In this chapter, the employment of the Schiff base ligand *N*-salicylidene-2-amino-5-chlorobenzoic acid ($sacbH_2$, Scheme 4.1) in 4*f*-metal chemistry is reported. This has led to the dinuclear complex $[Dy_2(NO_3)_4(sacbH)_2(H_2O)_2(MeCN)_2]$ exhibiting SMM properties with a large barrier for the magnetization reversal and hysteresis loops in the *M vs. H* data at 5 K. In addition, the isostructural $\{Gd^{III}_2\}$ and $\{Tb^{III}_2\}$ complexes were isolated and subsequently characterized. None of the dinuclear complexes exhibited emission properties in the solid-state.

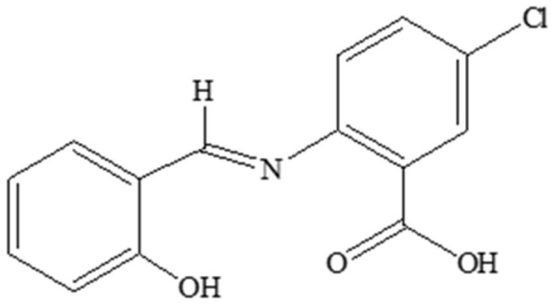

$sacbH_2$

Scheme 4.1. Structural formula and abbreviation of the Schiff base ligand *N*-salicylidene-2-amino-5-chlorobenzoic acid ($sacbH_2$) used in this study.

4.2 ***Experimental Section***

4.2.1 Physical Measurements

Elemental analysis: Elemental analyses (C, H, and N) were performed on a Perkin-Elmer 2400 Series II Analyzer.

FT-IR spectroscopy: Infrared spectra were recorded in the solid state on a Bruker FT-IR spectrometer (ALPHA's Platinum ATR single reflection) in the 4000-400 cm^{-1} range.

Magnetic susceptibility measurements: Magnetic susceptibility studies were performed at the State Key Laboratory of Rare Earth Resource Utilization, part of the Changchun Institute of Applied Chemistry in the Chinese Academy of Sciences. Data were collected in the temperature range 1.9-300 K using a Quantum Design MPMS XL-7 SQUID magnetometer equipped with a 7 T magnet. Pascal's constants were used to estimate the diamagnetic corrections, which were subtracted from the experimental susceptibilities to give the molar paramagnetic susceptibilities (χ_M).[61]

***Ab initio* calculations:** *Ab initio* CASSCF/RASSI/SINGLE_ANISO calculations with MOLCAS 7.8 were carried out on the crystallographically determined coordinates of $\{Dy_2\}$ complex to determine the *g*-tensors and the relative energies of the Kramers' doublets in the $^6H_{15/2}$ ground state of the Dy^{III} ions (*vide infra*).

4.2.2 Synthesis

General considerations: All reactions were performed under aerobic conditions using chemicals and solvents as received. The Schiff base ligand $sacbH_2$ was prepared, purified, and characterized as described elsewhere.[143]

[$Gd_2(NO_3)_4(sacbH)_2(MeCN)_2(H_2O)_2$] (11): To a stirred, yellow solution of $sacbH_2$ (0.12 g, 0.40 mmol) and NEt_3 (0.11 mL, 0.80 mmol) in MeCN (20 mL) was added solid $Gd(NO_3)_3 \cdot 6H_2O$ (0.09 g, 0.20 mmol). The resulting deep yellow suspension was stirred for 20 min, during which time all of the solids dissolved. The solution was then filtered, and the filtrate was left to evaporate slowly at room temperature. After four days, X-ray quality orange plate-like crystals of **11** had appeared and were collected by filtration, washed with cold MeCN (2 × 2 mL), and dried in air. The yield was 46 %. The air-dried solid was analyzed as **11**. Anal. Calcd: C, 31.25; H, 2.29; N, 9.11 %. Found: C, 31.36; H, 2.42; N, 9.02 %. Selected IR data (ATR): *v*= 3378 (w), 2933 (w), 2303 (w), 2276 (w), 1597 (s), 1563 (m), 1469 (sb), 1411 (m), 1391 (m), 1359 (s), 1316 (s), 1281 (s), 1224 (s), 1181 (s), 1141 (s), 1107 (s), 1014 (m), 908 (m), 888 (m), 816 (m), 789 (w), 768 (m), 744 (m), 719 (m), 690 (m), 573 (m), 528 (m), 487(m), 462(m), 421(w).

[$Tb_2(NO_3)_4(sacbH)_2(MeCN)_2(H_2O)_2$] (12): This complex was prepared in the same manner as complex **11** but using $Tb(NO_3)_3 \cdot 5H_2O$ (0.09 g, 0.20 mmol) as the Ln salt. Again, after seven days, orange plate-like crystals of **12** had appeared. The crystals were collected by filtration, washed with cold MeCN (2 × 2 mL) and dried in air. The yield was 42 %. The air-dried solid was analyzed as **12**. Anal. Calcd: C, 31.16; H, 2.29; N, 9.09 %. Found: C, 31.23; H, 2.43; N, 9.01 %. Selected IR data (ATR): *v*= 3377 (w), 2932 (w), 2302 (w), 2274 (w), 1603 (s), 1525 (m), 1454 (sb), 1389 (m), 1362 (s), 1301 (s), 1225 (s), 1180 (s), 1140 (s), 1105 (s), 1016 (m), 908 (m), 886 (m), 817 (m), 785 (w), 759 (m), 741 (m), 716 (m), 658 (m), 572 (m), 528 (m), 489 (m), 463 (m), 420 (w).

[$Dy_2(NO_3)_4(sacbH)_2(H_2O)_2(MeCN)_2$] (13): This complex was prepared in the same manner as complex **11** but using $Dy(NO_3)_3 \cdot 5H_2O$ (0.09 g, 0.20 mmol) as the Ln salt. After four

days, orange plate-like crystals of **13** had appeared. The crystals were collected by filtration, washed with cold MeCN (2 × 2 mL) and dried in air. The yield was 45 %. The air-dried solid was analyzed as **13**. Anal. Calcd: C, 30.98; H, 2.28; N, 9.03. Found: C, 31.12; H, 2.39; N, 8.91. Selected IR data (ATR): *v*= 3384 (m), 2304 (w), 1599 (vs), 1469 (vs), 1413 (vs), 1391 (vs), 1360 (s), 1325 (m), 1285 (m), 1225 (s), 1181 (s), 1163 (s), 1141 (s), 1107 (m), 1015 (s), 909 (m), 888 (m), 816 (s), 790 (m), 768 (m), 746 (s), 719 (s), 690 (m), 574 (s), 544 (s), 529 (s), 488 (m), 463 (s), 423 (s).

4.2.3 Single-crystal X-Ray Crystallography

Single-crystals of complexes **11**-**13** were selected and mounted on cryoloops using inert oil.[89] Diffraction data were collected at 150(2) K on a Bruker X8 Kappa APEX II Charge-Coupled Device (CCD) area detector diffractometer controlled by the APEX2 software package (MoKα graphite-monochromated radiation, λ = 0.71073 Å) and equipped with an Oxford Cryosystems series 700 cryostream monitored remotely with the software interface Cryopad.[91] Images were processed with the SAINT software,[92] and absorption effects corrected with the multiscan method implemented in SADABS.[121] The structure was solved using the algorithm implemented in SHELXT-2014,[94,95] and refined by successive full-matrix least-squares cycles on F^2 using the latest SHELXL-v.2014.[94,96] The non-hydrogen atoms were successfully refined using anisotropic displacement parameters. The hydrogen atoms bonded to carbon were placed at their idealized positions using the appropriate *HFIX* instructions in SHELXL and included in subsequent refinement cycles in riding-motion approximation with isotropic thermal displacements parameters (U_{iso}) fixed at 1.2 or 1.5 × U_{eq} of the relative atom. In addition, the

hydrogen atoms of the coordinated water molecules were visible in the difference Fourier maps and placed in the structural model with the O-H and H···H distances restrained to 0.90(2) and 1.50(2) Å, respectively, in order to ensure a chemically reasonable geometry for the molecule [U_{iso}(H) = 1.5 × U_{eq}(O)]. The programs used for the molecular graphics were MERCURY[144] and DIAMOND.[145] Unit cell parameters and structure solution and refinement data for complexes **11**-**13** are listed in Table 4.1.

Table 4.1. Crystal and structure refinement details for complexes **11**-**13**.

	11	**12**	**13**
Formula	$C_{32}H_{28}Gd_2Cl_2N_8O_{20}$	$C_{32}H_{28}Tb_2Cl_2N_8O_{20}$	$C_{32}H_{28}Dy_2Cl_2N_8O_{20}$
Fw / g mol^{-1}	1230.03	1233.38	1240.52
Crystal type	Orange plate	Orange plate	Orange plate
Crystal size / mm^3	0.10 × 0.06 × 0.06	0.11 × 0.05 × 0.07	0.12 × 0.05 × 0.04
Crystal system	Triclinic	Triclinic	Triclinic
Space group	*P*-1	*P*-1	*P*-1
a / Å	8.5704(6)	8.529(3)	8.5421(6)
b / Å	10.4758(6)	10.4094(4)	10.4051(8)
c / Å	12.9067(11)	12.8568(10)	12.8795(10)
α / °	66.293(1)	66.348(1)	66.309(2)
β / °	74.639(1)	74.930(1)	74.672(2)
γ / °	81.185(1)	82.417(1)	81.563(3)
V / Å^3	1022.53(11)	1008.27(11)	1009.92(13)
Z	1	1	1

T / K	150(2)	150(2)	150(2)
D_c / g cm^{-3}	1.965	1.985	2.040
μ / mm^{-1}	3.786	3.801	3.896
θ range	3.555 - 28.323	3.643 - 27.076	3.667 - 27.484
Index ranges	$-12 \le h \le 11$	$-11 \le h \le 11$	$-11 \le h \le 10$
	$-6 \le k \le 12$	$-7 \le k \le 12$	$-7 \le k \le 13$
	$-17 \le l \le 17$	$-16 \le l \le 16$	$-16 \le l \le 16$
Reflections collected	8656	8879	8237
Independent reflections	4457 (R_{int} = 0.0322)	4129 (R_{int} = 0.0267)	4387 (R_{int} = 0.0307)
Data completeness	to θ = 25.123°, 96%	to θ = 25.365°, 95%	to θ = 25.242°, 95.5%
Final R indices	$R1$ = 0.0343	$R1$ = 0.0357	$R1$ = 0.0308
$[I>2\sigma(I)]^{a,b}$	$wR2$ = 0.0628	$wR2$ = 0.0697	$wR2$ = 0.0613
Final R indices	$R1$ = 0.0391	$R1$ = 0.0388	$R1$ = 0.0360
(all data)	$wR2$ = 0.0692	$wR2$ = 0.0786	$wR2$ = 0.0635
$(\Delta\rho)_{max,min}$ / e Å^{-3}	0.814 and -0.744	0.831 and -0.769	0.862 and -0.721

[a] $R1 = \Sigma(||F_o| - |F_c||)/\Sigma|F_o|$. [b] $wR2 = [\Sigma[w(F_o^2 - F_c^2)^2]/ \Sigma[w(F_o^2)^2]]^{1/2}$, $w = 1/[\sigma^2(F_o^2) + [(ap)^2 + bp]$, where $p = [\max(F_o^2, 0) + 2F_c^2]/3$.

4.3 ***Results and Discussion***

4.3.1 Synthetic Comments

The organic chelating/bridging ligand sacbH$_2$ has been previously used in Ni^{II} chemistry as a means of obtaining very high-nuclearity cluster compounds with nanoscale dimensions and interesting magnetic properties; as a result, {Ni$_{11}$}, {Ni$_{18}$} and {Ni$_{26}$} complexes have been isolated and characterized.[48,143,146] However, sacbH$_2$ has never been used in the coordination chemistry of lanthanide ions.

Complexes **11-13** were prepared by vigorously stirring one equivalent of each Ln^{III} salt together with two and four equivalents of the Schiff base ligand and NEt$_3$, respectively, in MeCN for 20 min. The resulting solutions were left to slowly evaporate at room temperature and suitable single-crystals for X-ray crystallography were obtained after ~4-7 days. Although the experimental and stoichiometric Ln^{III}:sacbH$_2$:NEt$_3$ molar ratios of 1:2:4 and 1:1:1, respectively, were very different, the resulting products were always the dinuclear complexes **11-13**. However, it should be mentioned that the stoichiometric reactions do not lead to crystalline materials of **11-13** but only to orange precipitates that have identical IR spectra and similar elemental analyses data with those of **11-13**.

4.3.2 Description of Structures

Complexes **11-13** are isostructural and thus only the structure of representative complex **13** will be described in detail. Complex **13** possesses an inversion center at the mid-point of the Dy1···Dy1′ distance (Figure 4.1). The two Dy^{III} atoms are doubly bridged by the deprotonated carboxylato O atoms of two nearly planar, η^1:η^1:η^1:μ sacbH$^-$ ligands. The Dy···Dy distance is 5.098(2) Å and the Dy-O/N bond lengths are within the expected range reported for similar compounds (Table 4.2).[46,147] Four bidentate chelating NO$_3^-$ and two monodentate H$_2$O and

MeCN molecules are terminally bound to the metal centers and they are displaced out of the nearly planar $\{Dy_2(\mu\text{-}O_2CR)_2\}^{4+}$ core. Nine-coordination at each metal ion is completed by the deprotonated phenoxido O atom of sacbH$^-$. The phenol H atom appears to have migrated to the imino N atom which therefore becomes positively charged and is unbound. The structure of **13** is stabilized by six strong intramolecular H bonds which involve the nitrato and aquo ligands, as well as the carboxylato/phenoxido O atoms and N-H group of sacbH$^-$ (Figure 4.2). In terms of intermolecular interactions, there are only some weak H-bonding contacts (Figure 4.3), and the shortest intermolecular Dy···Dy distance is 8.542 Å.

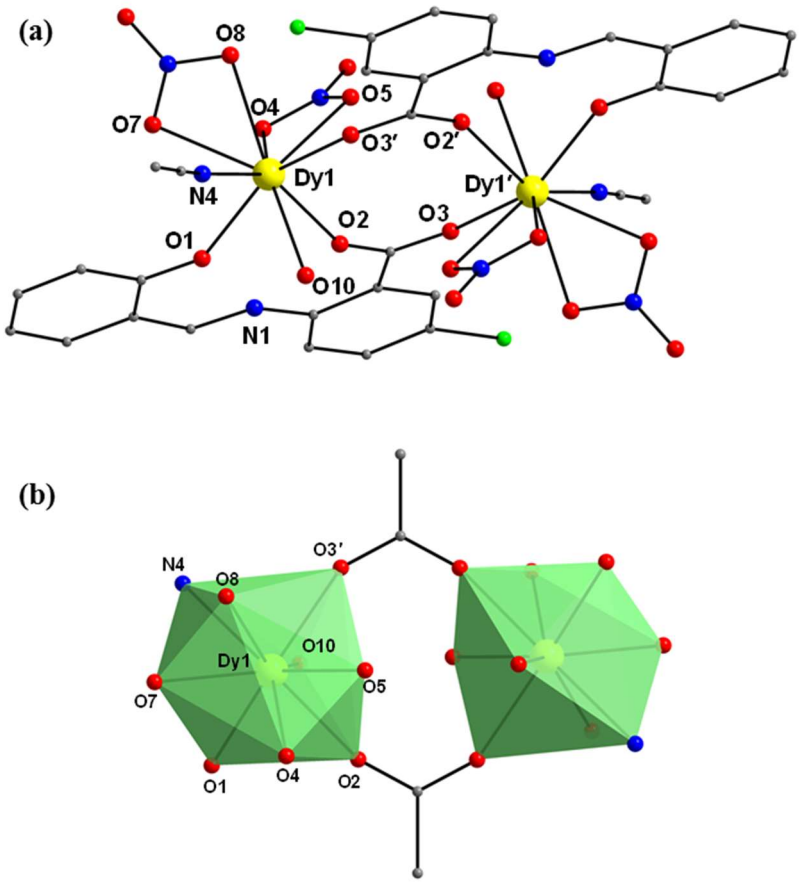

Figure 4.1. (a) Molecular structure of **13**, and **(b)** a simplified representation of the same structure using the observed Dy^{III} coordination polyhedra. H atoms are omitted for clarity.

Primed and unprimed atoms are related by symmetry. Color scheme: Dy^{III}, yellow; O, red; N, blue; Cl, green; C, gray.

Table 4.2. Selected interatomic distances (Å) for complex **13**.[a]

Dy(1)-O(1)	2.231(3)	Dy(1)-O(7)	2.472(3)
Dy(1)-O(2)	2.347(3)	Dy(1)-O(8)	2.445(3)
Dy(1)-O(3′)	2.305(3)	Dy(1)-O(10)	2.459(3)
Dy(1)-O(4)	2.589(3)	Dy(1)-N(4)	2.511(4)
Dy(1)-O(5)	2.500(3)	Dy(1)···Dy(1′)	5.098(2)

[a] Symmetry code: ′ = 1-*x*, 1-*y*, 1-*z*.

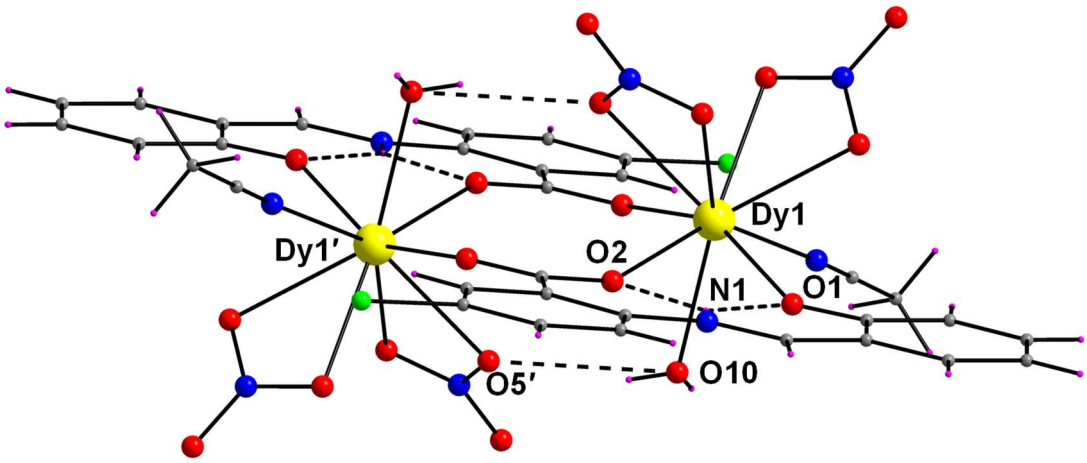

Figure 4.2. Molecular structure of **13** showing the intramolecular hydrogen bonding interactions (dashed lines). Their dimensions are: N(1)-H(1)···O(1) = 2.641(4) Å; N(1)-H(1)···O(2) = 2.674(4) Å; O(10)-H(1W)···O(5′) = 2.828(4) Å. Color scheme: Dy^{III}, yellow; O, red; N, blue; Cl, green; C, gray; H, purple.

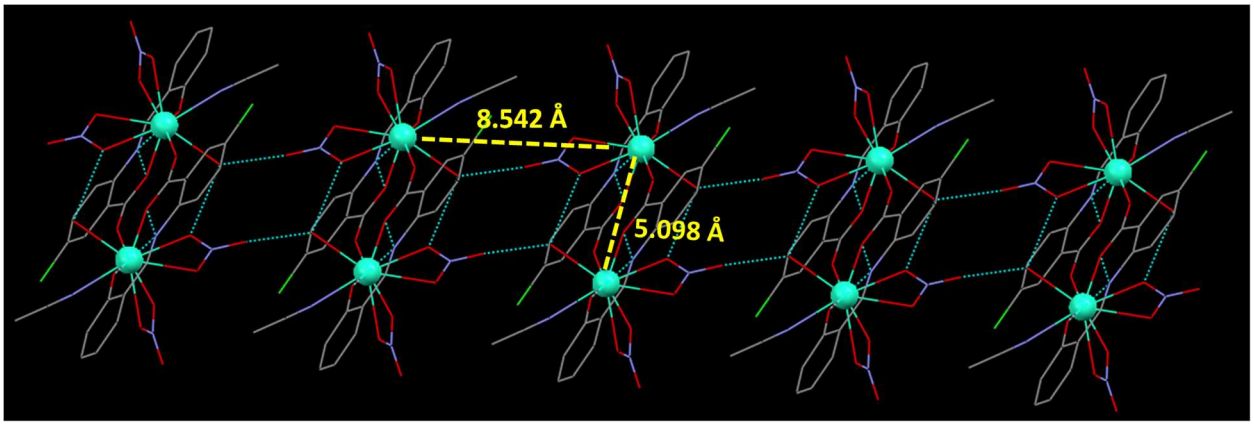

Figure 4.3. Intra- and intermolecular Dy···Dy distances resulting from the carboxylato bridging ligation and weak intermolecular H-bonding interactions (donor = H_2O; acceptor = NO_3^-), respectively.

A search of literature reveals that the most common coordination number for the lanthanide ions in dinuclear complexes is eight.[148] There are also dimers of nine-coordinate *4f*-metal ions with monocapped square antiprismatic, dodecahedral and distorted pentagonal interpenetrating tetrahedral geometries.[105a,149] SHAPE analysis[11a,150] reveals that the closest coordination geometry that describes the nine-coordinate Dy^{III} centers in **13** is spherical tricapped trigonal prismatic (CShM = 1.65; Figure 4.4 and Table 4.3) with virtual D_{3h} point group symmetry. According to Alvarez and coworkers, the unusual spherical tricapped trigonal prismatic polyhedron (s-TCTPR) tends to have the capping vertices at the same distance from the center of the polyhedron.[151] This was indeed the case for **13** (Figure 4.1b); the distance from Dy1 to the three equatorial capping O donor atoms (O5, O7 and O10), which belong to NO_3^- and H_2O ligands, are 2.500(3), 2.472(3) and 2.459(3) Å, respectively. The two axial triangular faces of the prism comprise the atoms O3′/O4/N8 and O1/O2/O4, most of which belong to the deprotonated donor atoms of the $sacbH^-$ ligand. The bond distances between these atoms and the central Dy^{III}

ion are much shorter (2.231(3)-2.347(3) Å) than those of the equatorial capping atoms. Thus, the anionic donors from the sacbH$^-$ ligand are far closer to the Dy^{III} ions than the three equatorial ligands and thus will dominate the electronic structure. This confers a relatively strong and axial crystal field above and below the *4f*-metal ions, which could potentially enhance the oblate nature of the electron density of Dy^{III} in its electronic ground state and hopefully stabilize an axial $m_J = \pm 15/2$ Kramers' doublet with a large anisotropy barrier.[152]

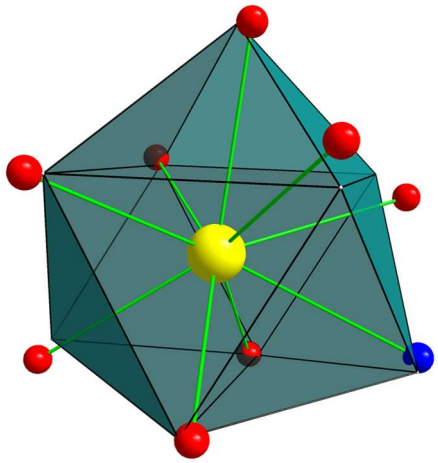

Figure 4.4. Spherical tricapped trigonal prismatic geometry of Dy1 and Dy1′ atoms in the structure of **13**. Points connected by the black lines define the vertices of the ideal polyhedron. Color scheme: Dy^{III}, yellow; O, red; N, blue.

Table 4.3. Shape measures of the nine-coordinate Dy(1,1′)^a coordination polyhedron in **13**. The values in boldface indicate the closest polyhedron according to the Continuous Shape Measures.

Polyhedron	Dy(1,1′)
EP-9	34.769
OPY-9	21.798

HBPY-9	17.941
JTC-9	15.140
JCCU-9	10.170
CCU-9	8.983
JCSAPR-9	2.746
CSAPR-9	1.751
JTCTPR-9	2.836
TCTPR-9	**1.650**
JTDIC-9	11.487
HH-9	12.223
MFF-9	2.129

[a] Abbreviations: EP-9, Enneagon; OPY-9, Octagonal pyramid; HBPY-9, Heptagonal bipyramid; JTC-9, Johnson triangular cupola; JCCU-9, Capped cube; CCU-9, Spherical-relaxed capped cube; JCSAPR-9, Capped square antiprism; CSAPR-9, Spherical capped square antiprism; JTCTPR-9, Tricapped trigonal prism; TCTPR-9, Spherical tricapped trigonal prism; JTDIC-9, Tridiminished icosahedron; HH-9, Hula-hoop; MFF-9, Muffin.

4.3.3 Static Magnetic Properties

Direct current (*dc*) magnetic susceptibility measurements of complexes **11-13** were performed in the 2-300 K range under an applied magnetic field of 0.1 T. The obtained data for all complexes are shown as $\chi_M T$ *vs.* T plots in Figure 4.5 for $\{Gd^{III}_2\}$ (**11**) and Figure 4.6 for both $\{Tb^{III}_2\}$ (**12**) and $\{Dy^{III}_2\}$ (**13**) complexes. The room-temperature $\chi_M T$ values are very close to

the theoretical ones (15.75 cm^3Kmol^{-1} for **11**; 23.64 cm^3Kmol^{-1} for **12**; 28.34 cm^3Kmol^{-1} for **13**) for two non-interacting Gd^{III} ($^8S_{7/2}$, S = 7/2, L = 0, g = 2), Tb^{III} ($^7F_6$, S = 3, L = 3, g = 3/2) and Dy^{III} ($^6H_{15/2}$, S = 5/2, L = 5, g = 4/3) ions, respectively. For the isotropic $\{Gd^{III}_2\}$ (**11**) complex, the $\chi_M T$ product remains constant at a value of 15.58 cm^3Kmol^{-1} until ~10 K and then rapidly decreases to a minimum value of 15.38 cm^3Kmol^{-1} at 2 K. The PHI[153] software was used to fit the susceptibility data of **11** adopting a 1-J model. An excellent fit (Figure 4.5) was obtained resulting in J = -0.01(2) cm^{-1} and g = 1.99(1). The very small and negative value of J for the $\{Gd_2\}$ complex indicates the presence of very weak antiferromagnetic exchange interactions between the two metal centers, as expected for Gd^{III} complexes bridged by bidentate carboxylate ligands.[87,110] For the anisotropic $\{Tb^{III}_2\}$ (**12**), the thermal evolution of the magnetic susceptibility remains almost constant at 22.11 cm^3Kmol^{-1} until ~70 K and then steadily decreases to a value of 14.58 cm^3Kmol^{-1} at 2 K, while for the $\{Dy^{III}_2\}$ (**13**) complex the $\chi_M T$ product declines smoothly on cooling until ~100 K and then sharply, reaching a value of 24.36 cm^3Kmol^{-1} at 2 K. The decrease in $\chi_M T$ when the temperature is lowered is mainly due to the depopulation of the crystal field (CF) m_J states and possibly very weak intramolecular antiferromagnetic interactions between the Ln^{III} ions.

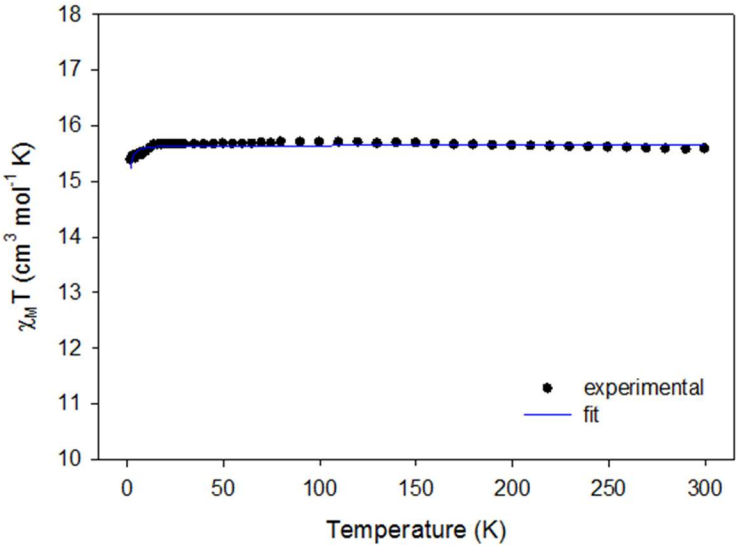

Figure 4.5. Temperature dependence of the $\chi_M T$ product for complex **11** at 0.1 T. Solid blue line is the result of the fit for the $\{Gd_2\}$ compound, as described in the text.

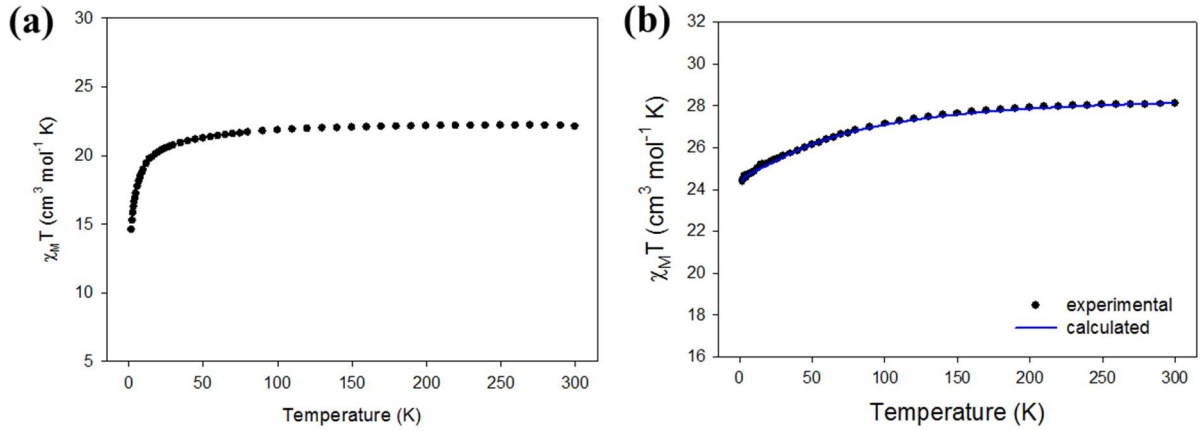

Figure 4.6. Temperature dependence of the $\chi_M T$ product for complexes **(a) 12**, and **(b) 13** at 0.1 T. The solid blue line corresponds to the curve generated from the *ab initio* studies for complex **13**.

The field dependence of the magnetization of complexes **11-13** is shown in Figures 4.7 and 4.8. The magnetization of complexes **11** and **12** reach saturated values of 13.8 $N\mu_B$ and 18.2

$N\mu_B$ at the highest fields and lowest temperatures, which are in excellent agreement with the theoretical values of 14 $N\mu_B$ and 18 $N\mu_B$ for two uncoupled Gd^{III} and Tb^{III} ions, respectively. In the case of **13**, the field dependence of the magnetization at 1.9, 3 and 5 K shows a relatively rapid increase at low fields without reaching saturation at 7 T, which indicates significant magnetic anisotropy (Figure 4.8b). Furthermore, the magnetization value at 7 T is ~11.5 $N\mu_B$, which is much lower than the expected value for two Dy^{III} ions ($M_S/N\mu_B = ng_JJ = 20\ N\mu_B$) and is due to the CF effects that induce strong magnetic anisotropy. The $\chi_M'T$ value (χ_M' is the in-phase *ac* susceptibility) at its plateau temperature region is ~27 cm^3Kmol^{-1}, which agrees well with the expected value for randomly oriented crystals of a molecule with two Dy^{III} ions, each with a $m_J = \pm 15/2$ Ising ground Kramers' doublet (Figure 4.9).[154]

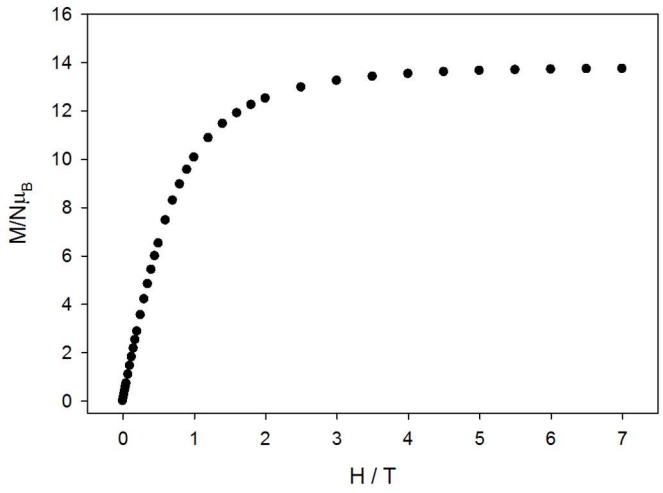

Figure 4.7. Plot of magnetization (*M*) *vs*. field (*H*) for complex **11** at 1.9 K.

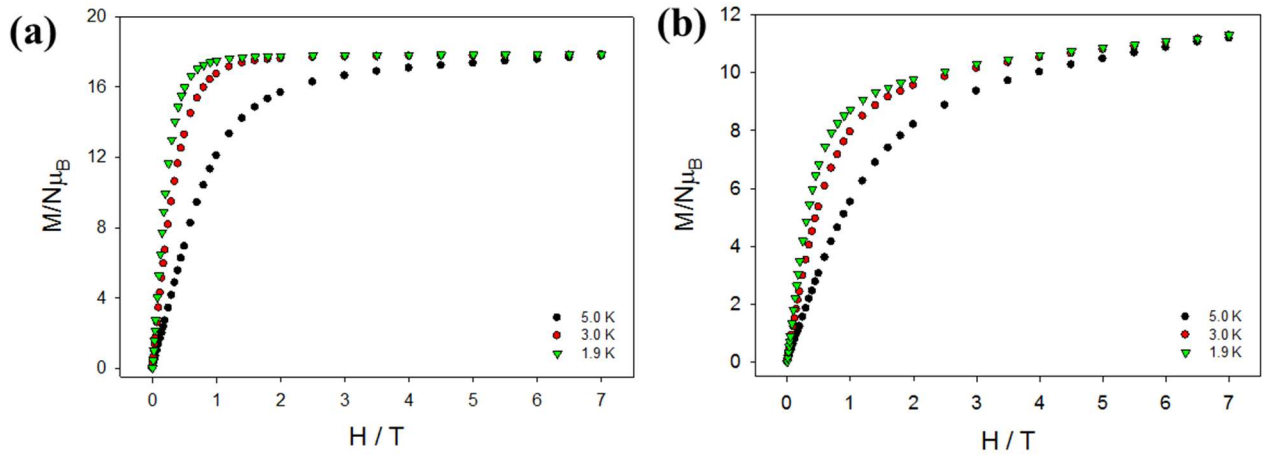

Figure 4.8. Plots of magnetization (*M*) *vs*. field (*H*) for complexes **(a) 12** and **(b) 13** at three different low temperatures.

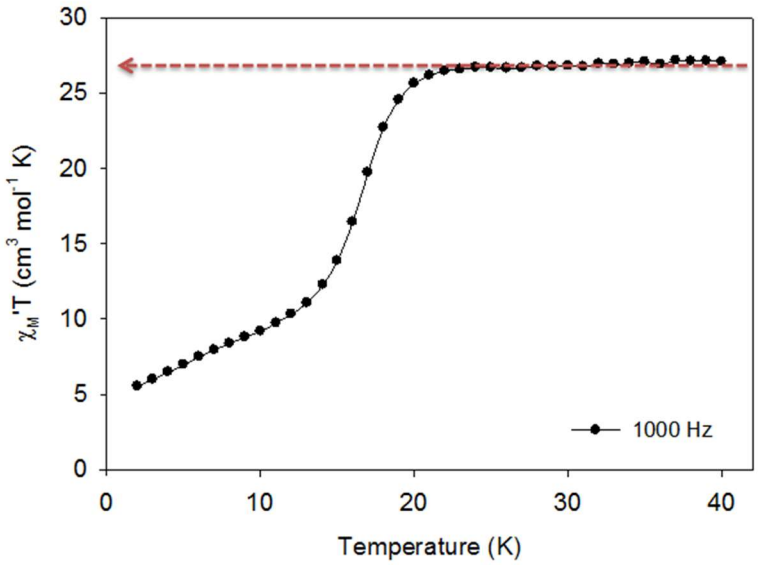

Figure 4.9. In-phase (χ_M') (as $\chi_M'T$) *vs*. *T ac* susceptibility signals for **13** in a 3.0 G field oscillating at the indicated frequency.

4.3.4. Dynamic Magnetic Properties

To probe the magnetic dynamics of **13**, alternating current (*ac*) magnetic susceptibility measurements, as a function of both temperature (Figure 4.10) and frequency (Figure 4.11), were initially performed in zero applied *dc* field. *Ac* magnetic susceptibility studies were also performed in complex **12** but no out-of-phase signals were observed in the absence or presence of an external *dc* field, suggesting that this {Tb_2} complex is not a SMM. In contrast, complex **13** displays frequency dependence of in-phase (χ_M') and out-of-phase (χ_M'') susceptibilities at temperatures below 25 K, suggesting the presence of slow relaxation of the magnetization consistent with the presence of an SMM. The out-of-phase peaks at high temperatures, indicative of a slow relaxation process, overlap with tails of signals at the low-T regime, which is a clear sign of fast QTM. The dependence of χ_M' and χ_M'' signals on the *ac* frequency at each temperature (1.9-22 K, Figure 4.11) allowed me to fit the data to a generalized Debye function and extract the temperature-dependent relaxation times (τ). In this respect, the temperature dependence of the relaxation times can provide useful information about the operative magnetic relaxation processes at particular temperatures for a given system. In particular, in the presence of an activation barrier with respect to magnetization reversal, the system must exchange energy with the lattice (in the form of phonons) to ascend to the top of the barrier before relaxation can occur.[155] Such a relaxation mechanism, known as an Orbach process, leads to an exponential dependence of τ upon temperature which allows one to construct an Arrhenius plot and determine the effective energy barrier, U_{eff}, and pre-exponential factor, τ_0, for the system. The data used for the fitting of **13** were for the thermally activated relaxation in the high-temperature regime, where a fit of τ to the Arrhenius law [$\ln\tau = \ln\tau_0 + U_{eff}/k_BT$] afforded an effective energy barrier U_{eff} = 109.3(1) K (76.0(1) cm^{-1}) and $\tau_0 = 1.4(1) \times 10^{-7}$ s (Figure 4.12). In contrast, the low-temperature data could not be fit using this method since the values of τ deviate from

linearity due to the interplay between QTM and thermally assisted relaxation processes, (*vide infra*).

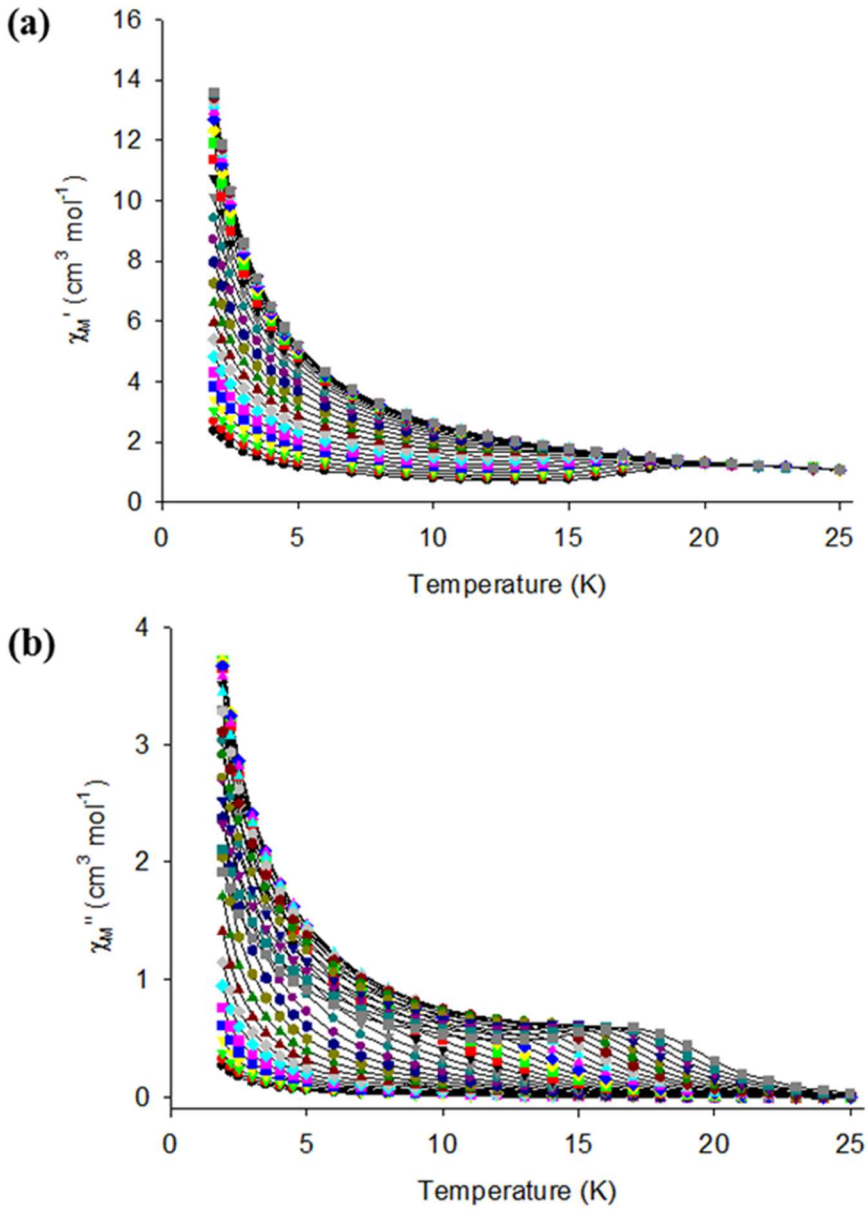

Figure 4.10. Temperature dependence of the **(a)** in-phase (χ_M') and **(b)** out-of-phase (χ_M'') *ac* magnetic susceptibilities in zero *dc* field for **13**, measured in a 3.0 G *ac* field oscillating at frequencies of 1-1488 Hz (30 frequencies in total). The solid lines are guides only.

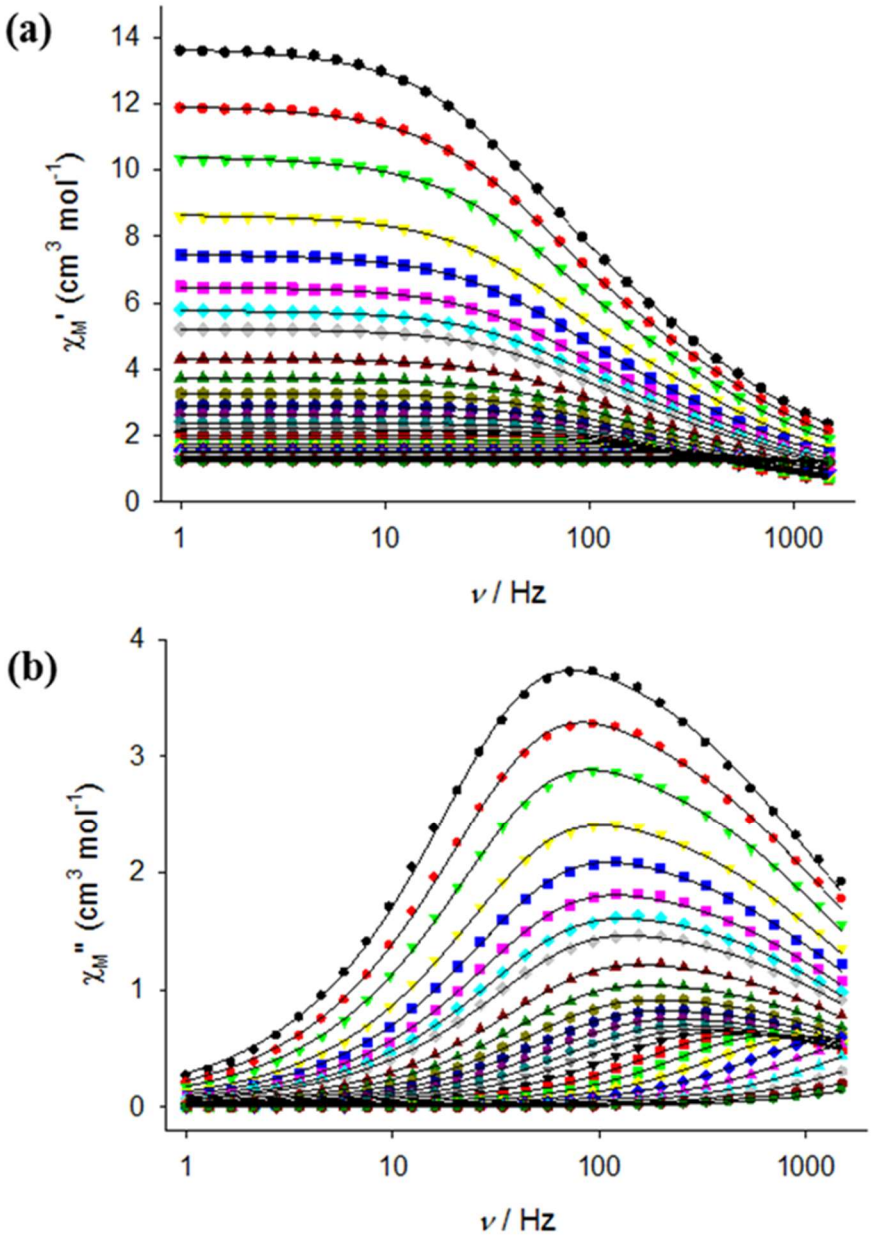

Figure 4.11. Frequency dependence of **(a)** the in-phase (χ_M') and **(b)** out-of-phase (χ_M'') *ac* magnetic susceptibilities in zero *dc* field for **13**, measured in a 3.0 G *ac* field at the temperature range 1.9-22 K (25 temperatures in total). Solid lines represent fits to the data, as described in the main text.

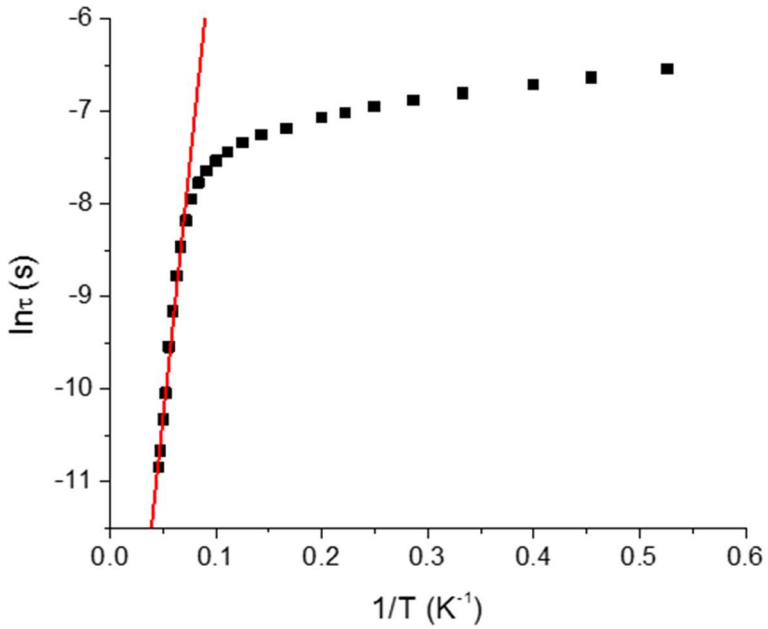

Figure 4.12. Arrhenius plot showing the relaxation of magnetization of **13** under zero applied *dc* field. The red line corresponds to the fit of the high-temperature data; see the text for the fit parameters.

For Kramers' ions, in the majority of coordination geometries, the presence of an easy-axis anisotropy, dipole-dipole and hyperfine interactions permit the mixing of the ground states of the two Kramers' ions in zero *dc* field, thus promoting the QTM relaxation pathway over thermal relaxation processes.[64,156] In fact, the Cole-Cole plots (Figure 4.13) for **13** in the temperature range 1.9-22 K exhibit semicircular shapes and the data were fit using a generalized Debye model.[157] The α values were in the range 0.31-0.02, suggesting the presence of multiple relaxation processes, most likely due to a combination of QTM and thermally assisted relaxation pathways.[158]

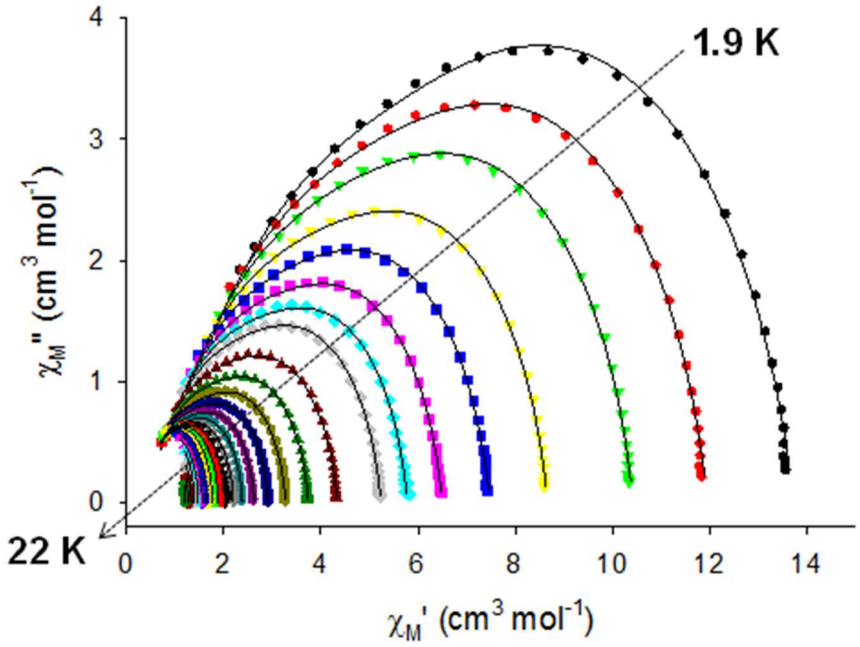

Figure 4.13. Cole-Cole plot for **13** obtained using the *ac* susceptibility data in zero applied *dc* field. The solid lines correspond to the best fit obtained with a generalized Debye model.

The obtained energy barrier of ~109 K for **13**, under a zero static *dc* field, is among the largest U_{eff} values reported for dinuclear, non-organometallic Dy^{III} SMMs.[105a,148,149] In order to reduce or even eliminate QTM, *ac* studies -as a function of both temperature (Figures 4.14 and 4.15) and frequency (Figure 4.16)- were also performed under an applied, optimum *dc* field of 1000 Oe. Indeed, entirely visible, frequency-dependent in-phase and out-of-phase signals were observed in the temperature range ~7-27 K, suggesting the presence of slow magnetization relaxation that is thermally assisted. The *ac* signals were not dramatically shifted in terms of temperature range when compared with the *ac* signals at zero *dc* field (Figure 4.10). At temperatures below ~7 K, a second fast relaxation process due to QTM was still present and is accompanied by the appearance of tails of χ_M'' signals. At a given temperature, the position of the χ_M'' peak maximum is the point at which the angular frequency ($\omega = 2\pi\nu$) of the oscillating

field equals the magnetization relaxation rate ($1/\tau$, where τ is the relaxation time); relaxation rate *vs*. T_{max} data can thus be obtained from the position of the peak maxima. Hence, out-of-phase *ac* measurements at different oscillation frequencies, where entirely visible χ_M'' peak maxima are observed, are a valuable source of rate *vs. T* kinetic data that can be fit to the Arrhenius relationship. Therefore, the χ_M''*vs. T* data of **13** above 7 K, where the peak maxima are entirely resolved, were fit for all *ac* frequencies and the T_{max} for each oscillation frequency were obtained. An Arrhenius plot (Figure 4.17) was constructed and this revealed two linear (activated) regimes that correspond to two thermally assisted processes. The fit of the data gave the following set of values: U_{eff} = 128.2(4) K (89.0(4) cm^{-1}) and $\tau_0 = 1.1(2) \times 10^{-7}$ s for $T > 11$ K and U_{eff} = 62.3(4) K (43.3(4) cm^{-1}) and $\tau_0 = 2.7(2) \times 10^{-5}$ s for $T < 11$ K.

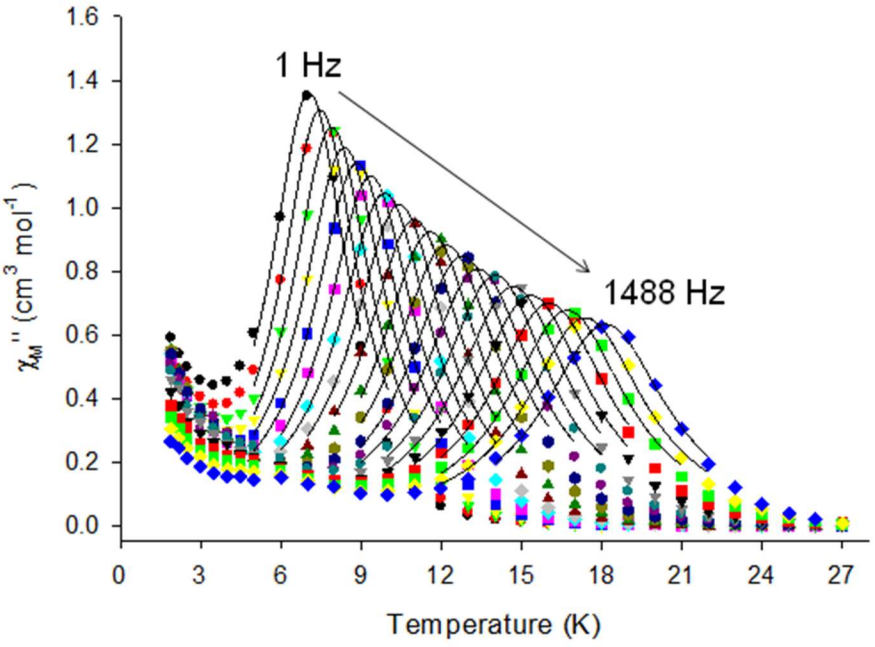

Figure 4.14. Temperature dependence of the out-of-phase (χ_M'') *ac* magnetic susceptibilities in a 1000 Oe *dc* field for **13**, measured in a 3.0 G *ac* field oscillating at frequencies of 1-1488 Hz. Solid lines represent fits to the data; see the text for details.

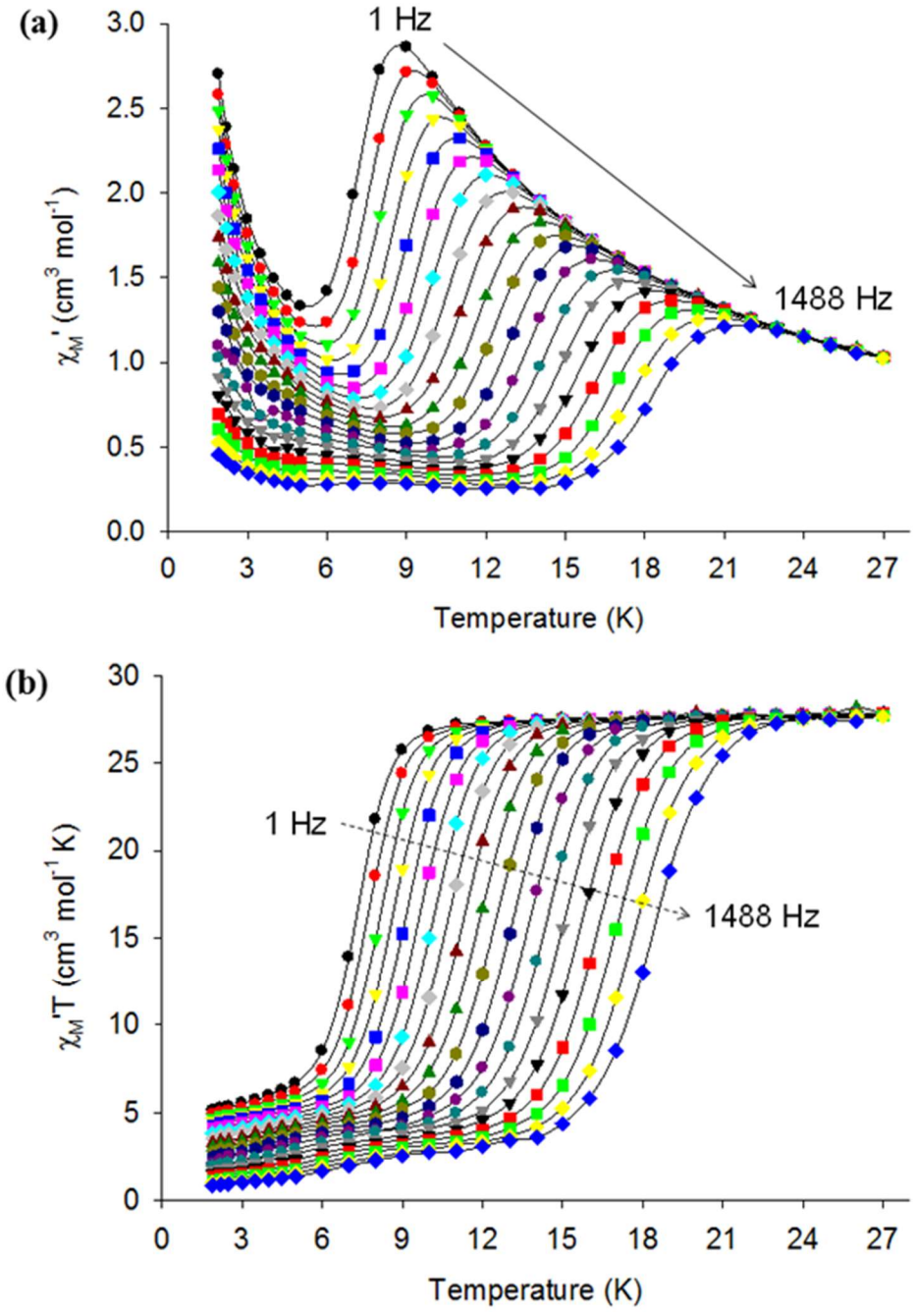

Figure 4.15. In-phase [as χ_M' **(a)** and $\chi_M'T$ **(b)**] *vs*. *T ac* susceptibility signals for **13** under an applied *dc* field of 1000 Oe and in a 3.0 G *ac* field oscillating at the indicated frequencies. The solid lines are guides only.

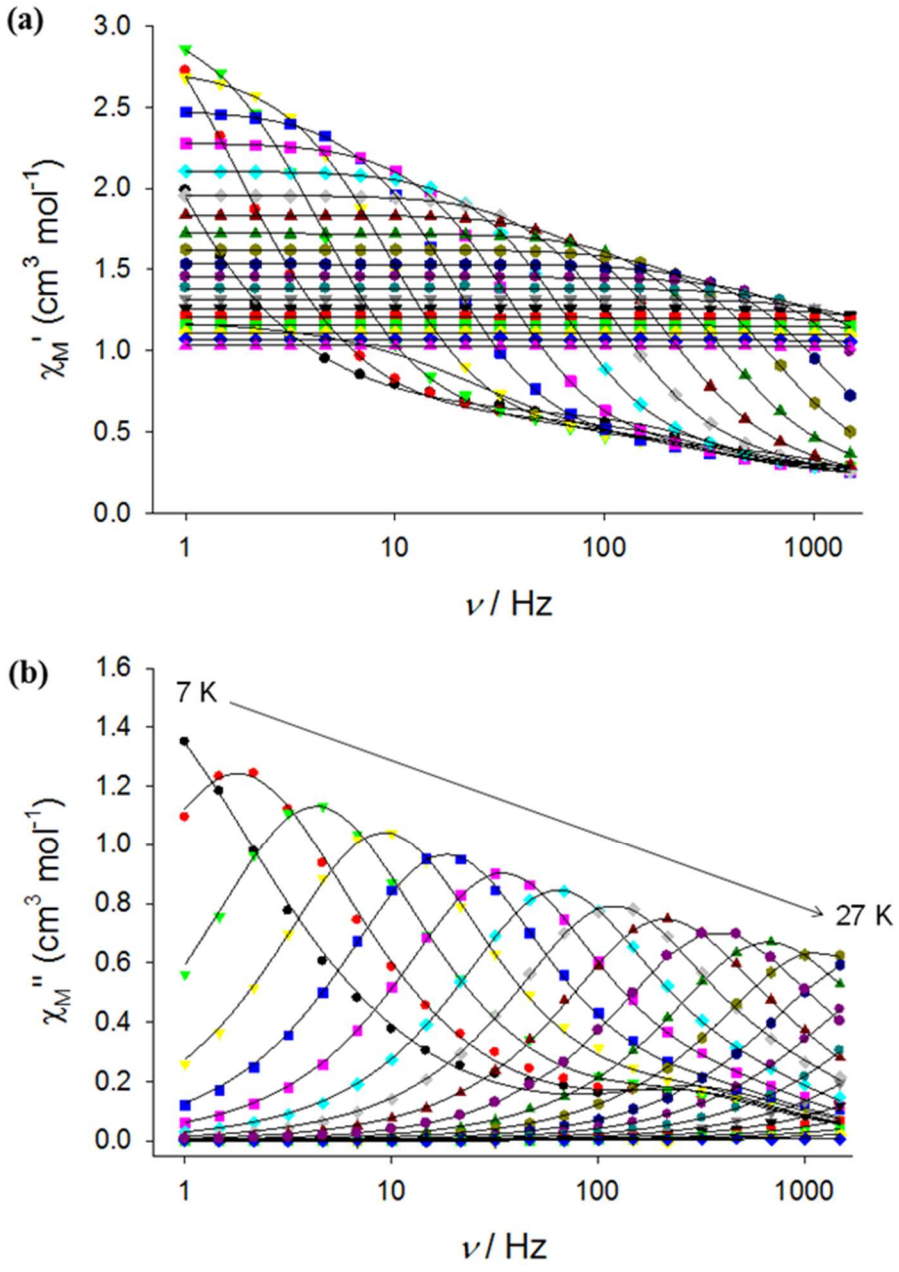

Figure 4.16. Frequency dependence of the **(a)** in-phase (χ_M') and **(b)** out-of-phase (χ_M'') *ac* magnetic susceptibilities in 1000 Oe *dc* field for **13**, measured in a 3.0 G *ac* field at the temperature range 7-27 K (21 temperatures in total). Solid lines represent fits to the data, as described in the main text.

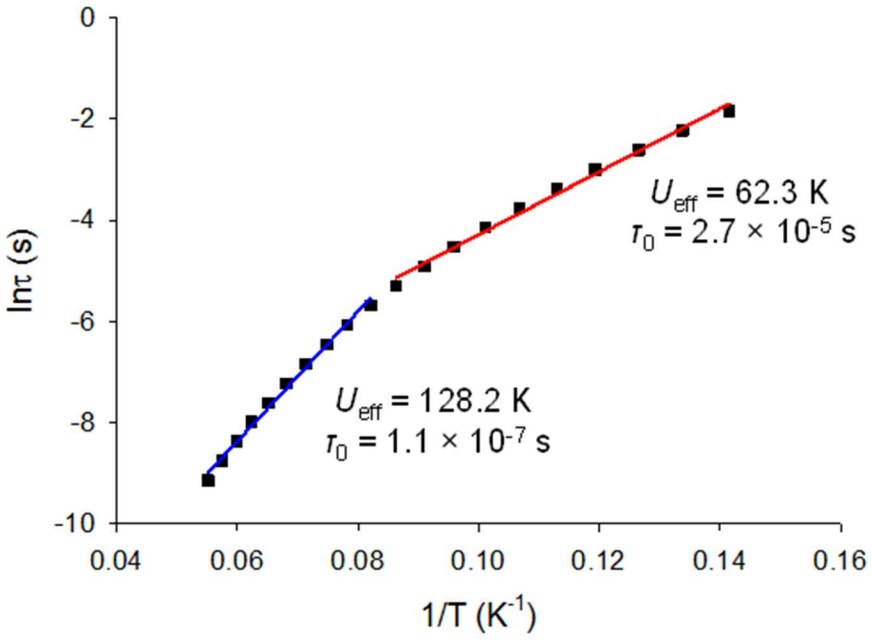

Figure 4.17. Arrhenius plot of **13** under a 1000 Oe applied *dc* field. The blue and red lines correspond to the fit of the high- and low-temperature data, respectively; see the text and inset for the fit parameters.

The unsaturated Arrhenius plot confirms the reduction of QTM in **13** under the applied optimum *dc* field, at temperatures higher than 7 K. The presence of multiple relaxation barriers was further explored *via* the construction of a Cole-Cole plot (Figure 4.18), using the generalized Debye model in the temperature range 7-27 K. Asymmetrical semicircles were nicely fit with α values ranging from 0.28 to 0.03, indicating the simultaneous presence of more than one relaxation processes.

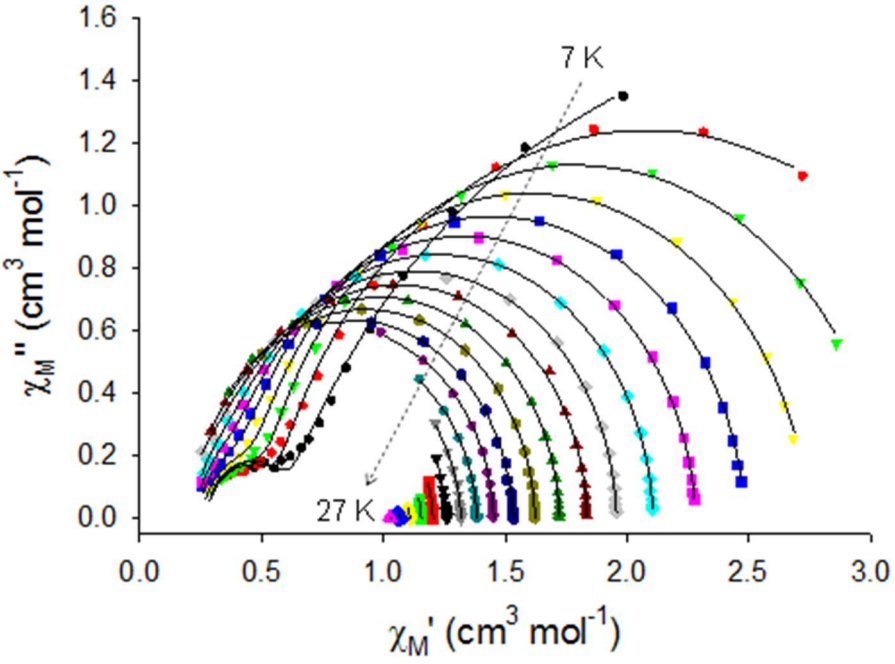

Figure 4.18. Cole-Cole plot for **13** obtained using the *ac* susceptibility data in 1000 Oe applied *dc* field. The solid lines correspond to the best fit obtained with a generalized Debye model.

4.3.5. Magnetization *vs. dc* Field Hysteresis Studies

To confirm the SMM behavior of **13**, hysteresis studies were performed on a single crystal of **13** at temperatures down to 0.03 K using a micro-SQUID apparatus. The obtained magnetization *vs.* applied *dc* field responses are shown in Figure 4.19, which includes both a temperature dependence at a constant field sweep rate of 0.140 T/s (Figure 4.19a) and a field sweep rate dependence at a constant temperature of 0.03 K (Figure 4.19b). Typical "butterfly"-shaped hysteresis loops were indeed observed below 5 K, whose coercivities increase with decreasing temperature and increasing field sweep rate, as expected for the superparamagnetic-like properties of an SMM below its blocking temperature (T_B). The data thus confirm that complex **13** is a new addition to the family of *4f*-based dinuclear SMMs with a T_B ~5 K, one of

the highest blocking temperatures below which hysteresis loops in the field of lanthanide SMMs were observed.[43,67,159] In addition, the hysteresis loops allowed to estimate the weak magnetic coupling between the two Dy^{III} ions. Indeed, the zero-field quantum resonance starts already before reaching zero field, thus establishing an antiferromagnetic coupling. It is also broadened by about 50 mT, which should mainly arise from exchange coupling and dipole interactions; both are expected to be weak because for the large distance and the orientation of the magnetic anisotropy axes, as depicted in Figure 4.20. Further broadening most likely arises from intermolecular interactions.[159a]

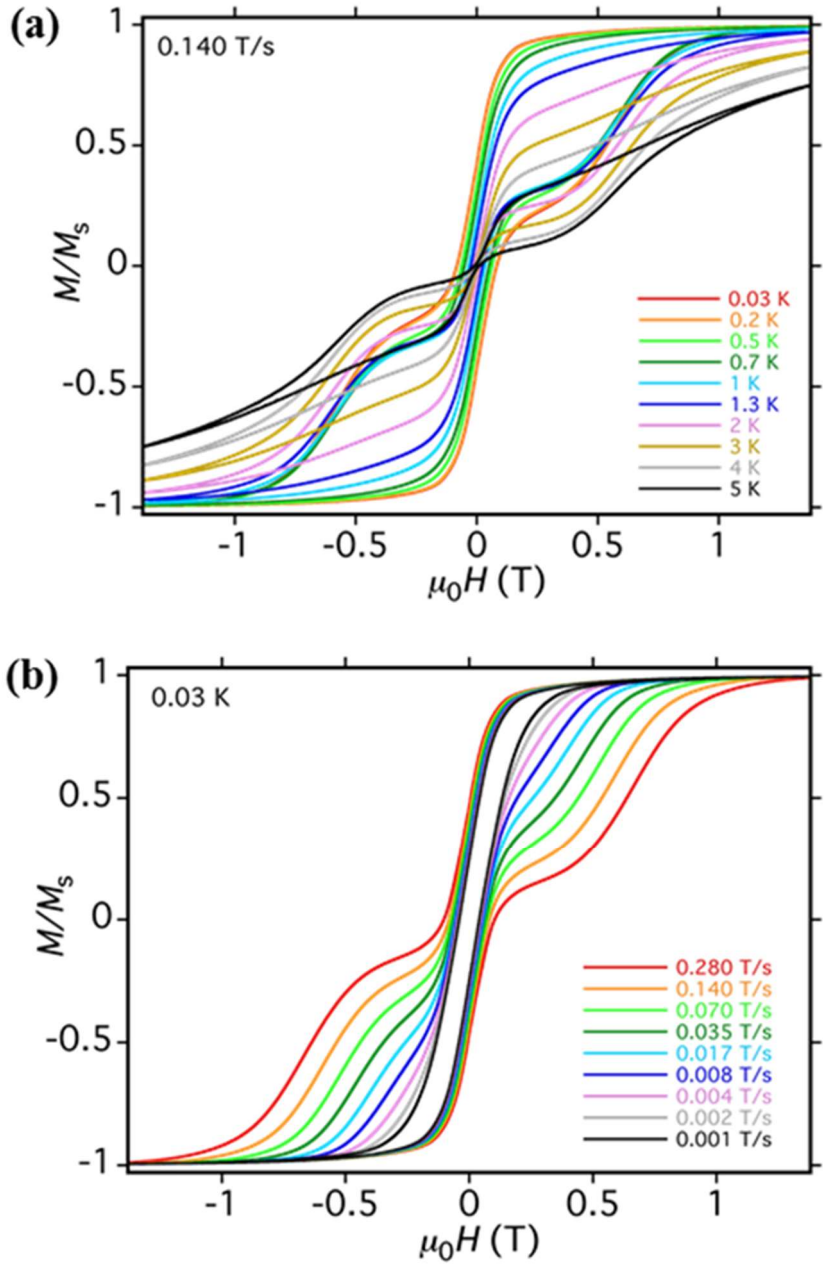

Figure 4.19. Magnetization (*M*) *vs. dc* field hysteresis loops for a single crystal of **13 (a)** at the indicated temperatures and a fixed field sweep rate of 0.140 T/s, and **(b)** at the indicated field sweep rates and a fixed temperature of 0.03 K (bottom). The magnetization is normalized to its saturation value, M_S.

4.3.6. Computational Studies

Further insight into the electronic structure and magnetic blocking of the dinuclear complex **13** was acquired by performing *ab initio* calculations with the MOLCAS program[69] and were of CASSCF/RASSI/SINGLE_ANISO type.[160] This computational approach has been successfully applied for the investigation of many lanthanide compounds to date.[24,57,63,68,82,133,134,148,149,161] In particular, this computational methodology has proven to be reliable for determining the *g*-tensors, the orientation of the local magnetic axes in the lowest electronic states of metal sites, and the relative energies of the Kramers' doublets in the $^6H_{15/2}$ ground state of Dy^{III} ions.[162] Recently, it was shown to also give a trustworthy spectrum of the CF splitting of the lowest *J* manifolds.[163] Current *ab initio* methods are not suitable for treating several magnetic centers simultaneously; thus, appropriate fragmentation was imposed. In the present calculations, diamagnetic Lu^{III} was used in place of neighboring magnetic Dy^{III}, and the positions of all other atoms of complex **13** were maintained as in the experimental X-ray structure. All atoms were described by ANO-RCC relativistic basis sets[164] available within the MOLCAS package. Contractions were accounted for by utilizing the ANO-RCC basis set library as well as the Douglas-Kroll-Hess Hamiltonian.[165] To determine if there is an influence of the basis sets on the calculations, three basis set models were applied (Table 4.4); however, here are only presented the results obtained using the large basis set that, based on previous experience, most accurately represents the system.[142] The active space of the CASSCF method includes nine electrons from the last shell spanning seven *4f*-orbitals of the Dy^{III} ion. Strong spin-orbit coupling was introduced into the calculations in the RASSI module, where 21 sextet and 128 quartet spin-free states were mixed. The doublet states were omitted due to limited computer resources. Local

magnetic properties were calculated in the SINGLE_ANISO module, which uses the resulting spin-orbit multiplets from the RASSI procedure.[69,160] Furthermore, the *ab initio* calculated low-lying spin–orbit states on individual Dy centers were employed in the phenomenological Lines model describing the exchange interaction between the Dy centers. The dipolar magnetic interaction was computed exactly and added to the Lines exchange matrix by using the *ab initio* results. Diagonalization of the total interaction matrix (exchange and dipolar) yields the spectrum of coupled eigenstates, which is further used as the basis for the description of the magnetic properties of the $\{Dy^{III}_2\}$ compound **13**. For these purposes, the POLY_ANISO program was employed.[166]

Table 4.4. Contractions of the ANO-RCC basis sets employed in *ab initio* calculations.

Short Basis Set	Medium Basis Set	Large Basis Set
Dy.ANO-RCC-VDZP	Dy.ANO-RCC-VQZP	Dy.ANO-RCC-VQZP
O.ANO-RCC-VDZP	O.ANO-RCC-VTZP	O.ANO-RCC-VTZP
(coordinated)	(coordinated)	(coordinated)
O.ANO-RCC-MB	O.ANO-RCC-VDZP	O.ANO-RCC-VDZP
N.ANO-RCC-VDZP	N.ANO-RCC-VTZP	N.ANO-RCC-VTZP
(coordinated)	(coordinated)	(coordinated)
N.ANO-RCC-MB	N.ANO-RCC-VDZP	N.ANO-RCC-VDZP
Lu.ANO-RCC-VDZP	Lu.ANO-RCC-VQZP	Lu.ANO-RCC-VQZP
Cl.ANO-RCC-MB	Cl.ANO-RCC-VDZP	Cl.ANO-RCC-VDZP
C.ANO-RCC-MB	C.ANO-RCC-MB	C.ANO-RCC-VDZP
H.ANO-RCC-MB	H.ANO-RCC-MB	H.ANO-RCC-VDZP

As shown in Table 4.5, *ab initio* studies reveal a large energy separation between the ground and first excited doublets for the two symmetry related Dy^{III} ions in the complex. The ground state KDs are highly axial and close to pure Ising anisotropy ($g_z = 20$ with $g_x = g_y \sim 0$). The first excited KDs are also almost close to Ising with $m_J = 13/2$ ($g_z = 17$, g_x, $g_y < 0.5$).[82] The magnetic axes between the ground and first excited KDs for both Dy sites are fairly collinear, forming an angle of 9.74° (Table 4.5). This deviation from co-linearity together with some transverse magnetization in both the ground and first excited state KDs will, however, facilitate the presence of QTM and Orbach relaxation processes.[82] The calculated value for $\Delta E_1 = 149$ cm^{-1} from the *ab initio* calculations is larger than the experimentally determined U_{eff} values for the first excited state Kramers' doublet indicating that even in a 1000 Oe applied *dc* field ground-state QTM is not completely suppressed. In addition, the main magnetic axes of the Dy sites in **13** form a small angle with the shortest chemical bond (Dy1-O1) of 11.85° (Figure 4.20). The short Dy1-O1 distance is a sign of the dominant covalent effect of the O1 atom on the ligand field of Dy1. Recall that O1 belongs to the deprotonated phenoxido group of the ligand $sacbH^-$ bearing the highest negative charge among all atoms in the first coordination sphere of the Dy center. In fact, it is quite common that the main magnetic axis of strongly axial Dy compounds or fragments is oriented along the ligand atom that exerts the strongest perturbation (i.e., usually it is the closest to the Dy ligand atom).[67,141,167] In the case of **13**, the anisotropy axes appear to orient towards the axial triangular faces of the spherical tricapped trigonal prismatic Dy^{III} polyhedron, thus avoiding the equatorial capping atoms that would otherwise reduce the magnetization dynamics. As discussed earlier, in the presence of a small applied *dc* field, complex **13** displays multiple relaxation processes. In this respect, *ab initio* calculations support

our proposition that the two closely spaced relaxation processes below 25 K are consistent with interplay between quantum tunneling and Orbach mechanisms involving both ground and first excited state Kramers' doublets (Figure 4.21).

Table 4.5. *Ab Initio* calculated energy spectrum, *g*-tensors and angle between magnetic axes of the KDs on the crystallographically unique Dy^{III} site of complex **13** using the large basis set.

KD	ΔE (cm^{-1})	g_x	g_y	g_z	Angle (°)
1	0.00	0.01	0.01	19.79	0.00
2	149.35	0.11	0.15	16.98	9.74
3	270.36	2.15	4.65	12.55	84.59
4	309.36	1.94	4.80	8.14	54.53
5	392.56	8.86	7.36	1.94	72.42
6	440.35	1.97	4.35	11.57	150.87
7	494.01	0.94	1.41	17.74	6.08
8	578.71	0.13	0.19	19.51	28.84

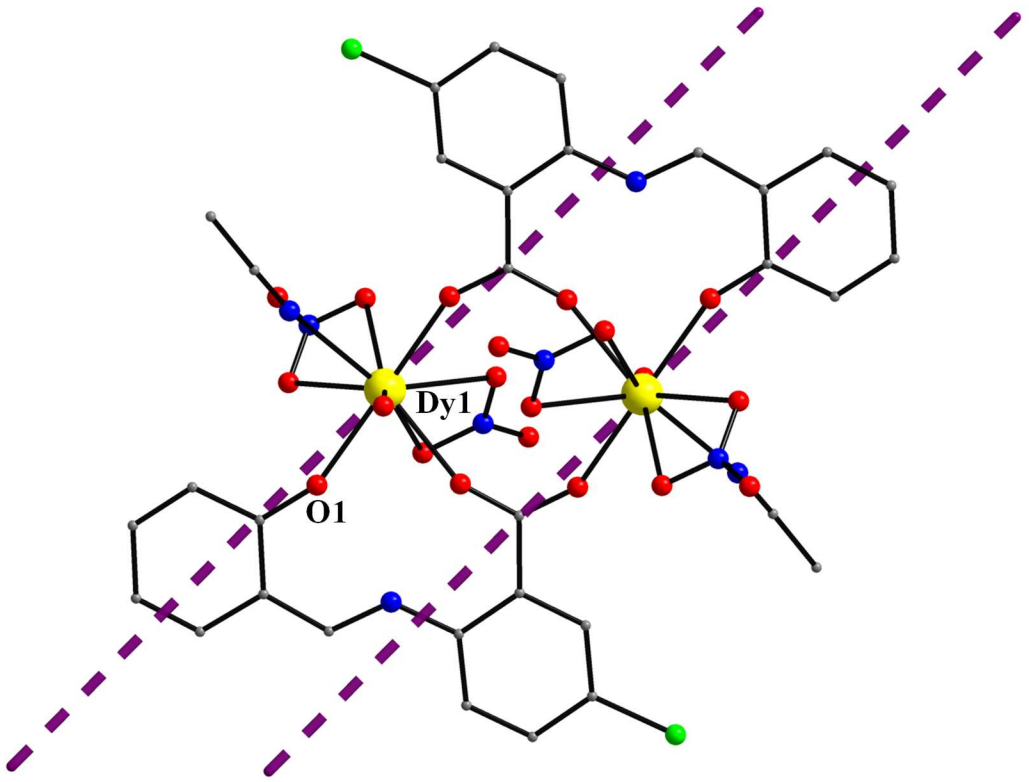

Figure 4.20. Orientations of the ground-state magnetic anisotropy axes for the two symmetry related Dy^{III} ions present in **13**.

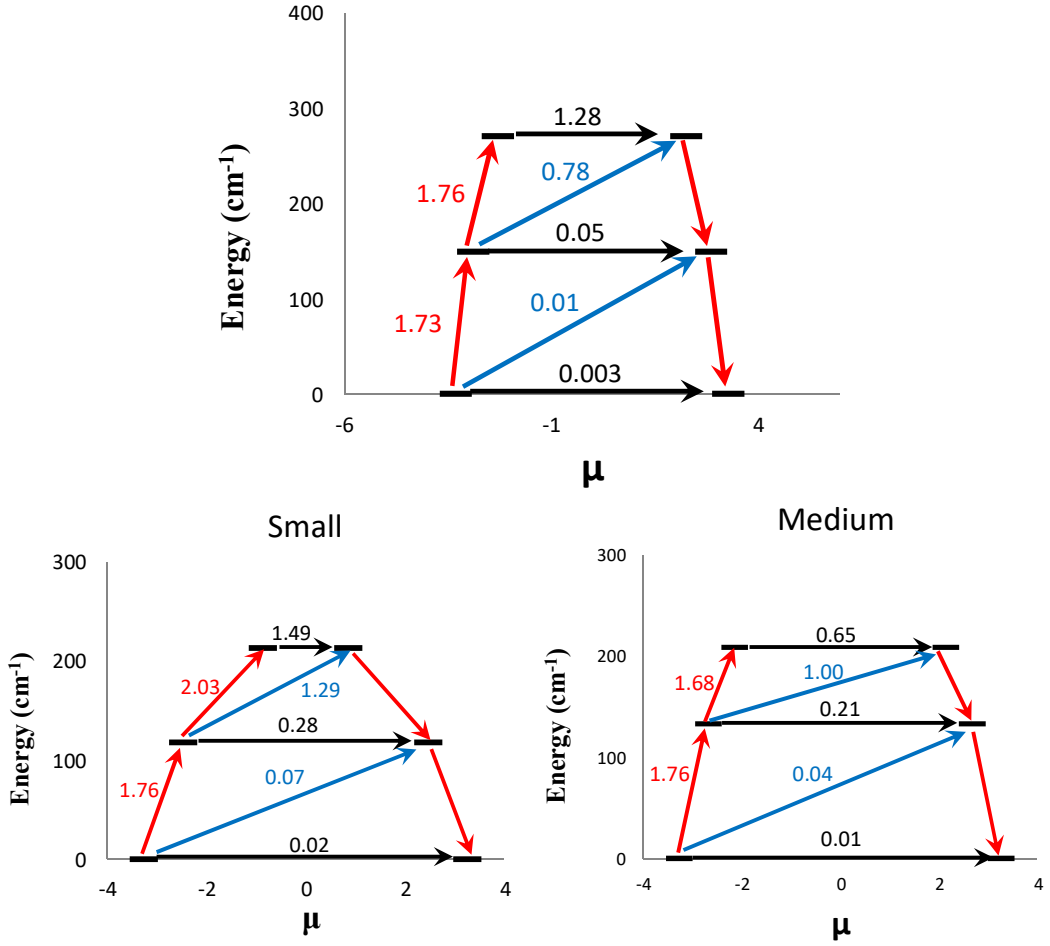

Figure 4.21. Low-lying electronic structure for **13** showing the Kramers' doublets for the Dy^{III} ions and possible relaxation pathways (indicative energies; large basis set (top), small and medium basis sets (bottom)). The thick black lines represent the Kramers' doublets as a function of their magnetic moment along the main anisotropy axes. The black arrows indicate ground state QTM or thermally assisted-QTM *via* the first and second excited state Kramers' doublets. Blue arrows show possible Orbach processes. Red arrows show the thermally assisted relaxation processes.

Once the results for individual metal sites had been obtained, *ab initio* calculations were further employed to compute the exchange spectrum and magnetic properties of complex **13**

using the POLY_ANISO program.[166,168] The exchange interaction between lanthanide sites was considered within the Lines model,[169] whereas the contribution of the intramolecular dipole-dipole magnetic coupling was accounted for exactly, given that all necessary data were available from the *ab initio* calculations. Best-fit Lines parameters for the exchange interactions in **13** are listed in Table 4.6. On the basis of the resulting exchange spectrum of the entire system, all macroscopic magnetic properties were computed. The magnetic interaction (exchange and dipolar) between the lowest KDs on sites can be calculated in good approximation by the noncollinear Ising Hamiltonian: $\hat{H}_{exch} = -J\hat{S}_{z1}\hat{S}_{z2}$, where $J = J_{exchange} + J_{dipolar}$ is the total magnetic interactions between the metal centers and $\hat{S}_{zi} = 1/2$ is the pseudospin of the ground doublet state of the corresponding Dy sites.

Table 4.6. Exchange and dipolar interactions and the corresponding low-lying exchange spectrum of **13** (cm^{-1}).

Interaction	**13**
Dipolar[a]	-0.0120
Exchange	0.0092
Total	-0.0028
Doublet	Total low-lying spectrum
1	0.00
2	4.72×10^{-7}
3	3.00×10^{-1}
4	3.00×10^{-1}

Doublet	g_z values in the two low-lying exchange doublet states[b]
1	39.58
2	0.00

[a] Only the z_1z_2 term of the dipolar interaction is shown here. All terms were included in the POLY_ANISO calculation. [b] $g_{x,y} = 0$ for non-Kramers' doublets, in view of the Griffith theorem.

As already inferred from the performed magnetic studies of **13**, the shape of the low-temperature and low-field molar magnetization facilitates the presence of weak interactions between the metal centers. This is not unexpected due to the bidentate η^1:η^1:μ-bridging carboxylate groups of $sacbH^-$, which induce a long pathway, hindering any significant magnetic exchange interaction between the two metal centers. This is also a significantly different magnetic behavior than that previously seen in the majority of $\{Dy_2\}$ SMMs, where the metal centers are coupled fairly strongly due to the presence of monodentate μ-OR^- bridges. Indeed, a reasonable theoretical description of measured magnetic susceptibility and molar magnetization is accomplished by assigning a very weak to negligible value to the intramolecular magnetic interaction between the Dy^{III} centers (Table 4.6). The results from adopting the short and medium basis sets were very similar to those obtained for the large basis set. As expected from the structural arrangement of the metal ions in **13**, both the exchange and dipolar interactions are weak in magnitude due to the presence of three-atom bridges and the large Dy···Dy distances. In addition, these interactions act in the opposite direction, that is, toward stabilizing the antiferromagnetically coupled non-magnetic state (Table 4.6).

4.4 ***Conclusions and Perspectives***

In conclusion, a new family of symmetric, dinuclear lanthanide complexes is herein reported, with the most interesting of all three members being the $\{Dy^{III}_2\}$ complex **13**. In **13**, the Dy^{III} ions adopt a unique spherical tricapped trigonal prismatic geometry. The negatively charged donor atoms of the Schiff base ligand, *N*-salicylidene-2-amino-5-chlorobenzoic acid were found to occupy the axial triangular phases of the prism, thus facilitating the presence of a strong axial magnetic anisotropy, supported by *ab initio* calculations. As a result, the reported $\{Dy_2\}$ compound exhibits SMM properties with a large energy barrier for the magnetization reversal and hysteresis loops below 5 K, one of the largest temperatures below which a magnetization blockage is observed in *4f*-metal based SMMs. DFT studies on previously reported compounds have shown that the negative charge on the phenoxido oxygen atoms should have a much greater magnitude than those found on the water, carboxylate and nitrate ligands. The phenoxido donor atoms in **13** are regarded as occupying axial positions, which enhances the oblate nature of the electron density of Dy^{III} in its electronic ground state, producing a relatively large anisotropy barrier. The combined magneto-structural and *ab initio* studies of **13** demonstrate the ability of *common* coordination numbers (i.e., 9) with *rare* coordination geometries (i.e., spherical tricapped trigonal prismatic) to promote a strong axial anisotropy that permits dinuclear Dy^{III} complexes to act as efficient SMMs.

The Stamatatos group is currently directing our efforts toward the replacement of the negatively charged ligands from the capping sites of the equatorial plane with neutral groups in order to enhance the electrostatic interactions between the Dy^{III} ions and the atoms in the axial triangular faces, thus enhancing the axiality of the ligand field and, subsequently, the anisotropy barrier. Synthetic endeavors can be also focused on the isolation of all isostructural to **11**-**13**

complexes bearing anisotropic *4f*-metal ions and the elucidation of the synergetic effect of the spherical tricapped trigonal prismatic geometry with the nature (oblate or prolate) of the electron density of each lanthanide ion. To further probe the QTM effect, diluted samples of **13** will be prepared in several Dy:Y molar ratios by co-crystallization with the isostructural $\{Y_2\}$ complex. From a chemical reactivity perspective, it would be interesting to study: (i) the effect of the inorganic anion present in the Dy^{III} salt; (ii) the nature of the reaction solvent, and (iii) the influence of the crystallization process on the structural identities and magnetic properties of the reported dinuclear compounds.

References

[1] *(a)* Cotton, S. *Lanthanide and Actinide Chemistry*, West Sussex: John Willey & Sons, **2006**. *(b)* Housecroft, E. C.; Sharpe, G. A. *Inorganic Chemistry*, Pearson, **2012**. *(c)* Soni, P. L.; Soni, V. Coordination Chemistry, *Metal Complexes Transition Metal Chemistry with Lanthanides and Actinides, Chapter 7: Inner Transition or f-block Elements: The Lanthanides*, CRC Press, Taylor and Francis Group, **2013**. *(d)* Bünzli, J.- C. G. *J. Coord. Chem.* **2014**, *67*, 3706. *(e)* Huang, C.; Bian, Z. *Rare Earth Coordination Chemistry, Chapter 1: Introduction*, Wiley, **2010**.

[2] Eliseeva, S. V.; Bünzli, J.- C. *New J. Chem.* **2011**, *35*, 1165.

[3] http://geology.com/articles/rare-earth-elements/

[4] https://www.statista.com/statistics/277268/rare-earth-reserves-by-country/

[5] Charalampides, G.; Vatalis, I. K.; Baklavaridis, A.; Benetis P.- N. *Proc. Econ. and Finan.* **2015**, *24*, 126.

[6] *(a)* Benelli, C.; Gatteschi, D. *Introduction to Molecular Magnetism: From Transition Metals to Lanthanides*, 1st ed., Wiley-VCH, **2015**. *(b)* Tang, J.; Zhang, P. *Lanthanide Single Molecule Magnets*, Springer, **2015**.

[7] https://en.wikibooks.org/wiki/General_Chemistry/Shells_and_Orbitals#The_f_orbitals

[8] Lang, F. P.; Smith, C. B. *J. Chem. Educ.* **2010**, *87*, 875.

[9] https://upload.wikimedia.org/wikipedia/commons/3/30/LS_coupling.svg, Creative Commons License.

[10] *(a)* Pilar, L. F. *Elementary Quantum Chemistry, Chapter 8: The Quantum States of Atoms,* Dover Publications, Mineola, NY, **1990**. *(b)* Rudowicz, C.; Karbowiak, M. *Coord. Chem. Rev.* **2015**, *287*, 28. *(c)* Jiang, S.- D.; Wang, B.- W.; Gao, S. *Molecular Nanomagnets and Related Phenomena, Chapter 2: Advances in Lanthanide Single-Ion Magnets*, Oxford University Press,

2006. *(d)* DeVorkin, D. H. *Henry Norris Russell: Dean of American Astronomers*, Princeton University Press, **2000**. *(e)* Luzon, J.; Sessoli, R. *Dalton Trans.* **2012**, *41*, 13556. *(f)* Ratner, A. M.; Schatz, C. G. *Introduction to Quantum Mechanics in Chemistry*, Prentice Hall, NY, **2001**.

[11] *(a)* Alvarez, S.; Alemany, P.; Casanova, D.; Cirera, J.; Llunell, M.; Avnir, D. *Coord. Chem. Rev.* **2005**, *249*, 1693. *(b)* Zabrodsky, H.; Peleg, S.; Anvir, D. *J. Am. Chem. Soc.* **1992**, *114*, 7843.

[12] Werner, A. Z. *Z. Anorg. Chem.* **1897**, *14*, 21.

[13] For a discussion of the term "coordination cluster", see: Kostakis, G. E.; Ako, A. M.; Powell, A. K. *Chem. Soc. Rev.* **2010**, *39*, 2238.

[14] For a discussion on the various meanings of the term "cluster" in several areas of inorganic chemistry, see: Chisholm, M. H. *Polyhedron* **1998**, *17*, 2773.

[15] Stamatatos, Th. C.; Efthymiou, C. G.; Stoumpos, C. C.; Perlepes, S. P. *Eur. J. Inorg. Chem.* **2009**, 3361.

[16] *(a)* Whitehead, G. F. S.; Moro, F.; Timco, G. A.; Wernsdorfer, W.; Teat, S. J.; Winpenny, R. E. P. *Angew. Chem. Int. Ed.* **2013**, *125*, 10116. *(b)* Scott, R. T. W.; Parsons, S.; Murugesu, M.; Wernsdorfer, W.; Christou, G.; Brechin, E. K. *Angew. Chem. Int. Ed.* **2005**, *44*, 6540. *(c)* Manoli, M.; Inglis, R.; Manos, M. J.; Nastopoulos, V.; Wernsdorfer, W.; Brechin, E. K.; Tasiopoulos, A. J. *Angew. Chem. Int. Ed.* **2011**, *50*, 4441. *(d)* Murugesu, M.; Clérac, R.; Anson, C. E.; Powell, A. K. *Inorg. Chem.* **2004**, *43*, 7269. *(e)* Bi, Y.; Wang, X.- T.; Liao, W.; Wang, X.; Zhang, H.; Gao, S. *J. Am. Chem. Soc.* **2009**, *131*, 11650. *(f)* Liu, T.; Zhang, Y.- J.; Wang, Z.- M.; Gao, S. *J. Am. Chem. Soc.* **2008**, *130*, 10500. *(g)* Langley, S. K.; Scott, R. A.; Chilton, N. F; Moubaraki, B.; Murray, K. S. *Chem. Commun.* **2011**, *47*, 6281. *(h)* Moushi, E. E.; Lampropoulos, C.;

Wernsdorfer, W.; Nastopoulos, V.; Christou, G.; Tasiopoulos, A. J. *J. Am. Chem. Soc.* **2010**, *132*, 16146.

[17] For example, see: http://cen.acs.org/articles/94/web/2016/10/Molecular-machines-garner-2016-Nobel-Prize-in-Chemistry.html

[18] Tasiopoulos, A. J.; Vinslava, A.; Wernsdorfer, W.; Abboud, K. A.; Christou, G. *Angew. Chem. Int. Ed.* **2004**, *43*, 2117.

[19] Zheng, Z. *Chem. Commun.* **2001**, 2521.

[20] Peng, J.- B.; Kong, X.- J.; Zhang, Q.- C.; Orendáč, M.; Prokleška, J.; Ren, Y.- P. Long, L.- S.; Zheng Z.; Zheng, L.- S. *J. Am. Chem. Soc.* **2014**, *136*, 17938.

[21] Gu, X.; Xue, D. *Inorg. Chem.*, **2007**, *46*, 3212.

[22] *(a)* Roesky, P. W.; Canseco-Melchor, G.; Zulys, A. *Chem. Commun.* **2004**, 738. *(b)* Hubert-Pfalzgraf, L. G. *Inorg. Chem. Commun.* **2003**, *6*, 102.

[23] *(a)* Singh-Wilmot, M. A.; Sinclair, R. A.; Andrews, M.; Rowland, C.; Cahill, C. L.; Murugesu, M. *Polyhedron* **2013**, *53*, 187. *(b)* Romanelli, M.; Kumar, G. A.; Emge, T. J.; Riman, R. E.; Brennan, J. G. *Angew. Chem. Int. Ed.* **2008**, *47*, 6049. *(c)* Moore, B. F.; Kumar, G. A.; Tan, M.-C.; Kohl, J.; Riman, R. E.; Brik, M. G.; Emge, T. J.; Brennan, J. G. *J. Am. Chem. Soc.* **2011**, *133*, 373.

[24] *(a)* Woodruff, D. N.; Winpenny, R. E. P.; Layfield, R. A. *Chem. Rev.* **2013**, *113*, 5110. *(b)* Wills, A. S. *Annu. Rep. Prog. Chem. Sect. A: Inorg. Chem.* **2004**, *100*, 509.

[25] *(a)* Wang, R.; Carducci, M. D.; Zheng, Z. *Inorg. Chem.* **2000**, *39*, 1836. *(b)* Mudring, A.- V.; Timofte, T.; Babai, A. *Inorg. Chem.* **2006**, *45*, 5162. *(c)* Andrews, P. C.; Gee, W. J.; Junk, P. C.; Massi, M. *New J. Chem.* **2013**, *37*, 35.

[26] Poncelet, O.; Sartain, W. J.; Hubert-Pfalzgraf, L. G.; Folting, K.; Caulton, K. G. *Inorg. Chem.* **1989**, *28*, 263.

[27] *(a)* Gamer, M. T.; Lan, Y.; Roesky, P. W.; Powell, A. K.; Clérac, R. *Inorg. Chem.* **2008**, *47*, 6581. *(b)* Tang, J.; Hewitt, I.; Madhu, N. T.; Chastanet, G.; Wernsdorfer, W.; Anson, C. E.; Benelli, C.; Sessoli, R.; Powell, A. K. *Angew. Chem. Int. Ed.* **2006**, *45*, 1729.

[28] *(a)* Kajiwara, T.; Katagiri, K.; Hasegawa, M.; Ishii, A.; Ferbinteanu, M.; Takaishi, S.; Ito, T.; Yamashita, M.; Iki, N. *Inorg. Chem.* **1996**, *45*, 4880. *(b)* Kornienko, A.; Emge, T. J.; Kumar, G. A.; Riman, R. E.; Brennan, J. G. *J. Am. Chem. Soc.* **2005**, *122*, 3501.

[29] Wagner, T. A.; Roesky, W. P. *Eur. J. Inorg. Chem.* **2016**, 782.

[30] *(a)* Burgstein, M. R.; Gamer, M. T.; Roesky, P. W. *J. Am. Chem. Soc.* **2004**, *126*, 5213. *(b)* Burgstein, M. R.; Roesky, P. W. *Angew. Chem. Int. Ed.* **2000**, *39*, 549.

[31] Wang, R.; Zheng, Z.; Jin, T.; Staples, R. J. *Angew. Chem. Int. Ed.* **1999**, *38*, 1813.

[32] Milios, C. J.; Winpenny, R. E. P. *Struct. Bond.* **2015**, *164*, 1.

[33] Bünzli, J.- C. G.; Eliseeva, S. V. *Chem. Sci.* **2013**, 1939.

[34] *(a)* Jo, M. H.; Grose, J. E.; Baheti, K.; Deshmukh, M. M.; Sokol, J. J.; Rumberger, E. M.; Hendrickson, D. N.; Long, J. R.; Park, H.; Ralph, D. C. *Nano Lett.* **2006**, *6*, 2014. *(b)* Coronado, E.; Martí-Gastaldo, C.; Tatay, S. *Appl. Surf. Sci.* **2007**, *254*, 225.

[35] *(a)* Schmidt, S.; Prodius, D.; Mereacre, V.; Kostakis, G. E.; Powell, A. K. *Chem. Commun.* **2013**, *49*, 1696. *(b)* Brunet, G.; Habib, F.; Cook, C.; Pathmalingam, T.; Loiseau, F.; Korobkov, I.; Burchell, T. J.; Beauchemin, A. M.; Murugesu, M. *Chem. Commun.* **2012**, *48*, 1287. *(c)* Blackman, A. *Eur. J. Inorg. Chem.* **2008**, 2633. *(d)* Chesman, A. S. R.; Turner, D. R.; Moubaraki, B.; Murray, K. S.; Deacon, G. B.; Batten, S. R. *Eur. J. Inorg. Chem.* **2010**, 59.

[36] *(a)* Winpenny, R. E. P. *J. Chem. Soc., Dalton Trans.* **2002**, 1. *(b)* Winpenny, R. E. P. *Adv. Inorg. Chem.* **2001**, *52*, 1.

[37] *(a)* Robertson, N.; Yee, G. *Molecular Materials*, (Eds.: Bruce, D. W.; O′ Hare, D.; Walton, R. I.), Wiley, Warwick, **2010**. *(b)* Orchard, A. F. *Magnetochemistry*, Oxford University Press, Oxford, **2003**. *(c)* Carlin, R. L. *Magnetochemistry*, Springer-Verlag, Berlin, **1986**. *(d)* Kahn, O. *Molecular Magnetism*, VCH Publishers, New York, **1993**.

[38] Worku, D.; Negussie, M.; Raju, V. J. T.; Theodros, S.; Jonsson, J. A. *Bull. Chem. Soc. Ethiop.* **2002**, 29.

[39] *(a)* Schiff, H. *Ann. Chim.* **1864**, *131*, 118. *(b)* Smith, A. P.; Fraser, C. L. *In Comprehensive Coordination Chemistry II, Vol. 1*, Lever, A. B. P., Ed., Elsevier, Amsterdam, **2003**, p.p. 411-446.

[40] Clayden, J.; Greeves, N.; Warren, S. *Organic Chemistry, 2nd ed*., Oxford, New York, USA, **2012**, p. 231.

[41] *(a)* Casas, J. S.; Garcia-Tasende, M. S.; Sordo, J. *Coord. Chem. Rev.* **2000**, *209*, 197. *(b)* Kuzmina, L. G.; Struchikov, V. T. *Cryst. Struct. Commun.* **1979**, *8*, 715.

[42] Andruh, M. *Dalton Trans.* **2015**, *44*, 16633.

[43] Long, J.; Habib, F.; Lin, P.- H.; Korobkov, I.; Enright, G.; Ungur, L.; Wernsdorfer, W.; Chibotaru, L. F.; Murugesu, M. *J. Am. Chem. Soc.* **2011**, *133*, 5319.

[44] Dinca, A. S.; Shova, S.; Ion, A. E.; Maxim, C.; Lloret, F.; Julve, M.; Andruh, M. *Dalton Trans.* **2015**, *44*, 7148.

[45] Alexandropoulos, D. I.; Nguyen, T. N.; Cuhna-Silva, L.; Zafiropoulos, T. F.; Escuer, A.; Christou, G.; Stamatatos, Th. C. *Inorg. Chem.* **2013**, *52*, 1179.

[46] Anastasiadis, N. C.; Kalofolias, D. A.; Philippidis, A.; Tzani, S.; Raptopoulou, C. P.; Psycharis, V.; Milios, C. J.; Escuer, A., Perlepes, S. P. *Dalton Trans.* **2015**, *44*, 10200.

[47] Mukherjee, S.; Chaudhari, A. K.; Xue, S.; Tang, J.; Ghosh, S. K. *Inorg. Chem. Commun.* **2013**, *35*, 144.

[48] *(a)* Athanasopoulou, A. A.; Pilkington, M.; Raptopoulou, C. P.; Escuer, A.; Stamatatos. T. C. *Chem. Commun.* **2014**, *50*, 14942. *(b)* Perlepe, P. S.; Cunha-Silva, L.; Bekiari, V.; Gagnon, K. J.; Teat, S. J.; Escuer, A.; Stamatatos, Th. C. *Dalton Trans.* **2016**, *45*, 10256. *(c)* Perlepe, P. S.; Cunha-Silva, L.; Gagnon, K. J.; Teat, S. J.; Lampropoulos, C.; Escuer, A.; Stamatatos, Th. C. *Inorg. Chem.* **2016**, *55*, 1270.

[49] Gatteschi, D.; Sessoli, R.; Villain, J. *Molecular Nanomagnets*, Oxford University Press, **2006**.

[50] Miller, J. S.; Epstein, A. J. *Angew. Chem. Int. Ed.* **1994**, *33*, 385.

[51] *(a)* Christou, G.; Gatteschi, D.; Hendrickson, D. N.; Sessoli, R. *MRS Bull.* **2000**, *25*, 66. *(b)* Aromí, G.; Brechin, E. K. *Struct. Bond.* **2006**, *122*, 1. *(c)* Bircher, R.; Chaboussant, G.; Dobe, C.; Güdel, H. U.; Ochsenbein, S. T.; Sieber, A.; Waldman, O. *Adv. Funct. Mater.* **2006**, *16*, 209. *(d)* Murrie, M.; Price, D. J. *Annu. Rep. Prog. Chem., Sect. A* **2007**, *103*, 20.

[52] *(a)* Sessoli, R.; Gatteschi, D.; Caneschi, A.; Novak, M. A. *Nature* **1993**, *365*, 141. *(b)* Sessoli, R.; Tsai, H.- L.; Schake, A. R.; Wang, S.; Vincent, J. B.; Folting, K.; Gatteschi, D.; Christou, G.; Hendrickson, D. N. *J. Am. Chem. Soc.* **1993**, *115*, 1804.

[53] Lis, T. *Acta Crystallogr., Sect. B* **1980**, *36*, 2042.

[54] *(a)* Boyd, P. D. W.; Li, Q.; Vincent, J. B.; Folting, K.; Chang, H. R.; Streib, W. E.; Huffman, J. C.; Christou, G.; Hendrickson, D. N. *J. Am. Chem. Soc.* **1988**, *110*, 8537. *(b)* Caneschi, A.; Gatteschi, D.; Sessoli, R.; Barra, A. L.; Brunel, L. C.; Guillot, M. *J. Am. Chem. Soc*. **1991**, *113*, 5873.

[55] Ardavan, A.; Rival, O.; Morton, J. J. L.; Blundell, S. J.; Tyryshkin, A. M.; Timco, G. A.; Winpenny, R. E. P. *Phys. Rev. Lett.* **2007**, *98*, 057201.

[56] Leuenberger, M. N.; Loss, D. *Nature* **2001**, *410*, 789.

[57] Ishikawa, N.; Sugita, M.; Ishikawa, T.; Koshihara, S.; Kaizu, Y. *J. Am. Chem. Soc.* **2003**, *125*, 8694.

[58] *(a)* Alexandropoulos, D. I. *PhD Thesis: Single-Molecule Magnets and Multifunctional Molecular Magnetic Materials Based on Polynuclear Metal Complex*es, Brock University, **2015**. *(b)* Stares, E. *PhD Thesis: Novel Magnetic Materials Based on Macrocyclic Ligands: Towards High Relaxivity Contrast Agents and Mononuclear Single-Molecule Magnets,* Brock University, **2015**.

[59] Perlepe, P. S. *MSc Thesis: High-Spin and Emissive Molecular Materials: Synthesis and Characterization of New Polynuclear Ni^{II} Complexes from the Use of Aromatic Schiff Bases as Bridging Ligands*, Brock University, **2016.**

[60] Miller, J. S.; Epstein, A. J. *MRS Bull.* **2000***, 25,* 21.

[61] Bain, G. A.; Berry, J. F. *J. Chem. Educ*. **2008**, *85*, 532.

[62] Rinehart, J. D.; Long, J. R. *Chem. Sci.* **2011**, *2*, 2078.

[63] Ungur, L.; Le Roy, J. J.; Korobkov, I.; Murugesu, M.; Chibotaru, L. F. *Angew. Chem. Int. Ed.* **2014**, *53*, 4413.

[64] Liddle, S. T.; van Slageren, J. *Chem. Soc. Rev.* **2015**, *44*, 6655.

[65] Ding, Y.- S.; Chilton, N. F.; Winpenny, R. E. P.; Zheng, Y.-Z. *Angew. Chem. Int. Ed.* **2016**, *55*, 16071.

[66] Guo, Y.- N.; Xu, G.- F.; Gamez, P.; Zhao, L.; Lin, S.- Y.; Deng, R.; Tang, J.; Zhang, H.- J. *J. Am. Chem. Soc.* **2010**, *132*, 8538.

[67] Rinehart, J. D.; Fang, M.; Evans, J. W.; Long, R. J. *J. Am. Chem. Soc.* **2011,** *133*, 14236.

[68] Layfield, R. A.; Murugesu, M. *Lanthanides and Actinides in Molecular Magnetism*, Wiley-VCH, **2015**.

[69] Aquilante, F.; Vico, L. D.; Ferre, N.; Ghigo, G.; Malmqvist, P. A. A.; Neogrady, P.; Pedersen, T. B.; Pitonak, M.; Reiher, M.; Roos, B.O.; Serrano-Andres, L.; Urban, M.; Veryazov, V.; Lindh, R. *J. Comput. Chem.* **2010,** *31*, 224.

[70] *(a)* Lakowicz, J. R. *Principles of Fluorescence Spectroscopy*, Springer, New York, **2006**. *(b)* Stokes, G. G. *Phil. Trans. R. Soc. London* **1852**, *142*, 463. *(c)* Krasovickij, B. M.; Bolotin, B. M. *Org. Luminesc. Mater.*, VCH, Weinheim, **1988**.

[71] Jabłoński, A. *Nature* **1933**, *131*, 839.

[72] *(a)* Nijegorodov, N; Luhanga, P. V. C.; Nkoma, J. S.; Winkoun, D. P. *Spectrochim. Acta Part A: Molecular and Biomolecular Spectroscopy* **2006**, *64*, 1. *(b)* McClure, D. S. *J. Chem. Phys.* **1949**, *17*, 665. *(c)* McClure, D. S. *J. Chem. Phys.* **1949**, *17*, 905.

[73] Valeur, B. *Molecular Fluorescence: Principles and Applications*, Wiley-VCH, New York, **2001**.

[74] Bünzli, J.- C. G.; Piguet, C. *Chem. Soc. Rev.* **2005**, *34*, 1048.

[75] Deng, Z.; Bai, F.; Xing, Y.; Xing, N; Xu, L. *Open J. Inorg. Chem.* **2013**, *3*, 76.

[76] Bünzli, J.- C. G.; Eliseeva, V. S.; *Lanthanide Luminescence: Basics of Lanthanide Photophysics* p. 1-45, Springer, Berlin, **2010**.

[77] Filipescu, N.; Sager, W. F.; Serafin, F. A. *J. Phys. Chem.* **1964**, *68*, 3324.

[78] *(a)* Petoud, S.; Bünzli, J.- C. G.; Glanzman, T.; Piguet, C.; Xiang, Q.; Thummel, R. P. *J. Lumin.* **1999**, *82*, 69. *(b)* Faustino, W. M.; Malta, O. L.; de Sa, G. F. *J. Chem. Phys.* **2005**, *122*, 054109. *(c)* Malta, O. L. *J. Lumin.* **1997**, *71*, 229. *(d)* D'Aleo, A.; Picot, A.; Beeby, A.; Williams,

J. A. G.; Le Guennic, B.; Andraud, C.; Maury, O. *Inorg. Chem.* **2008**, *47*, 10258. *(e)* Fonger, W. H.; Struck, C. W. *J. Chem. Phys.* **1970**, *52*, 6364.

[79] Shuvaev, S.; Utochnikova, V.; Marciniak, Ł.; Freidzon, A.; Sinev, I.; Van Deun, R.; Freire, R. O.; Zubavichus, Y.; Grünertd, W.; Kuzminaa, N. *Dalton Trans.* **2014**, *43*, 3121.

[80] *(a)* Lazarides, T.; Sykes, D.; Faulkner, S.; Barbieri, A.; Ward, M. D. *Chem.-Eur. J.* **2008**, *14*, 9389. *(b)* Ward, M. D. *Coord. Chem. Rev.* **2007**, *251*, 1663. *(c)* Ronson, T. K.; Lazarides, T.; Adams, H.; Pope, S. J. A.; Sykes, D.; Faulkner, S.; Coles, S. J.; Hursthouse, M. B.; Clegg, W.; Harrington, R. W.; Ward, M. D. *Chem.-Eur. J.* **2005**, *12*, 9299. *(d)* Lazarides, T.; Adams, H.; Sykes, D.; Faulkner, S.; Calogero, G.; Ward, M. D. *Dalton Trans.* **2008**, 691. *(e)* Shavaleev, N. M.; Moorcraft, L. P.; Pope, S. J. A.; Bell, Z. R.; Faulkner, S.; Ward, M. D. *Chem. Commun.* **2003**, 1134. *(f)* Chen, F. F.; Bian, Z. Q.; Liu, Z. W.; Nie, D. B.; Chen, Z. Q.; Huang, C. H. *Inorg. Chem.* **2008**, *47*, 2507. *(g)* Imbert, D.; Cantuel, M.; Bünzli, J.- C. G.; Bernardinelli, G.; Piguet, C. *J. Am. Chem. Soc.* **2003**, *125*, 15698.

[81] For example, see: *(a)* Ababei, R; Pichon, C.; Roubeau, O.; Li, Y.- G.; Bréfuel, N.; Buisson, L.; Guionneau, P.; Mathonière C.; Clérac, R. *J. Am. Chem. Soc.* **2013**, *135*, 14840. *(b)* Long, J.; Rouquette, J.; Thibaud, J. M.; Ferreira, R. A. S.; Carlos, L. D.; Donnadieu, B.; Vieru, V.; Chibotaru, L. F.; Konczewicz, L.; Haines, J.; Guari, Y.; Larionova, J. *Angew. Chem. Int. Ed.* **2015**, *54*, 2236. *(c)* Coronado, E.; Galán-Mascarós, J. R.; Murcia-Martínez, A.; Romero, F. M.; Tarazón, A. "*Organic Conductors, Superconductors and Magnets: From Synthesis to Molecular Electronics*", NATO ASI Series, Eds. L. Ouahab, E. Yagubskii, Kluwer Academic Publishers **2004**, *139*, p. 127-142.

[82] Blagg, R. J.; Ungur, L.; Tuna, F.; Speak, J.; Comar, P.; Collison, D. N.; Wernsdorfer, W.; McInnes, E. J. L.; Chibotaru, L.; Winpenny, R. E. P. *Nature Chem.* **2013**, *5*, 673.

[83] *(a)* Gatteschi, D.; Sessoli, R. *Angew. Chem. Int. Ed.* **2003**, *42*, 268. *(b)* Sorace, L.; Benelli, C.; Gatteschi, D. *Chem. Soc. Rev.*, **2011**, *40*, 3092. *(c)* Sorace, L.; Gatteschi, D. in "*Lanthanides and Actinides in Molecular Magnetism*", 1st Ed., Layfield, R. A.; Murugesu, M.; Wiley-VCH, **2015**.

[84] Bagai, R.; Christou, G. *Chem. Soc. Rev.* **2009**, *38*, 1011.

[85] *(a)* Ward, M. D. *Coord. Chem. Rev.* **2010**, *254,* 2634. *(b)* Förster, T. *Chem. Phys. Let.* **1971**, *12*, 422.

[86] *(a)* Bi, Y.; Wang, X.- T.; Liao, W.; Wang, X.; Deng, R., Zhang, H.; Gao, S. *Inorg. Chem.* **2009**, *48*, 11743. *(b)* Burrow, C. E.; Burchell, T. J.; Lin, P.- H.; Habib, F.; Wernsdorfer, W.; Clérac, R.; Murugesu, M. *Inorg. Chem.* **2009**, *48*, 8051. *(c)* Li, C.- J.; Peng, M.- X.; Leng, J.- D.; Yang, M.- M.; Li, Z.; Tong, M.- L. *CrystEngComm* **2008**, *10,* 1645.

[87] *(a)* Alexandropoulos, D. I.; Mukherjee, S.; Papatriantafyllopoulou, C.; Raptopoulou, C. P.; Psycharis, V.; Bekiari, V.; Christou, G.; Stamatatos, Th. C. *Inorg. Chem.* **2011**, *50*, 11276. *(b)* Menelaou, M.; Ouharrou, F.; Rodríguez, L.; Roubeau, O.; Teat, S. J.; Aliaga-Alcalde, N. *Chem. Eur. J.* **2012**, *18*, 11545. *(c)* Alexandropoulos, D. I.; Cunha-Silva, L.; Pham, L.; Bekiari, V.; Christou, G.; Stamatatos, Th. C. *Inorg. Chem.* **2014**, *53*, 3220. *(d)* Canaj, A. B.; Tzimopoulos, D. I.; Philippidis, A.; Kostakis, G. E.; Milios, C. J. *Inorg. Chem.* **2012**, *51*, 7451.

[88] Kagkelari, A.; Papaefstathiou, G. S.; Raptopoulou, C. P.; Zafiropoulos, T. F. *Polyhedron* **2009**, *28*, 3279.

[89] Kottke, T.; Stalke, D. *J. App. Cryst.* **1993**, *26*, 615.

[90] APEX2, *Data Collection Software Version 2012.4, Bruker AXS, Delft, The Netherlands*, **2012**.

[91] Cryopad, *Remote monitoring and control, Version 1.451, Oxford Cryosystems, Oxford, United Kingdom*, **2006**.

[92] SAINT+, *Data Integration Engine v. 8.27b*©, **1997-2012**, Bruker AXS, Madison, Wisconsin, USA.

[93] Sheldrick, G. M. *SADABS 2012/1, Bruker AXS Area Detector Scaling and Absorption Correction Program*, **2012**, Bruker AXS, Madison, Wisconsin, USA.

[94] Sheldrick, G. M. *Acta Cryst. A* **2008**, *64*, 112.

[95] Sheldrick, G. M. *SHELXT v. 2014/3, Program for Crystal Structure Solution, University of Göttingen*, **2014**.

[96] Sheldrick, G. M. *SHELXL v. 2014, Program for Crystal Structure Refinement, University of Göttingen*, **2014**.

[97] Spek, A. L. *J. Appl. Crystallogr.* **2003**, *36*, 7.

[98] Van der Sluis, P.; Spek, A. L. *Acta Cryst. A* **1990**, *46*, 194.

[99] Brown, I. D.; Altermatt, D. *Acta Crystallogr. Sect. B* **1985**, 244. An O BVS in the ~1.7-2.0, ~1.0-1.2, and ~0.2-0.4 ranges is indicative of non-, single- and double-protonation, respectively.

[100] *(a)* Liu, X.; McAllister, J. A.; de Miranda, M. P.; McInnes, E. J. L.; Kilner, C. A.; Halcrow, M. A. *Chem. Eur. J.* **2004**, *10*, 1827. *(b)* Guedes, G. P.; Soriano, S.; Comerlato, N. M.; Speziali, N. L.; Novak, M. A.; Vaz, M. G. F. *Inorg. Chem. Commun.* **2013**, *37*, 101. *(c)* Petit, S.; Neugebauer, P.; Pilet, G.; Chastanet, G.; Barra, A.- L.; Antunes, A. B.; Wernsdorfer, W.; Luneau, D. *Inorg. Chem.* **2012**, *51*, 6645.

[101] Bhula, R.; Weatherburn, D. C. *Angew. Chem. Int. Ed.* **1991**, *30*, 688.

[102] Zhang, P.; Guo, Y.- N.; Tang, J. *Coord. Chem. Rev.* **2013**, *257*, 1728.

[103] Mondal, K. C.; Kostakis, G. E.; Lan, Y.; Powell, A. K. *Polyhedron* **2013**, *66*, 268.

[104] *(a)* Ishikawa, N.; Sugita, M.; Ishikawa, T.; Koshihara, S.- y.; Kaizu, Y. *J. Phys. Chem. B* **2004**, *108*, 11265. *(b)* Ishikawa, N.; Mizuno, Y.; Takamatsu, S.; Ishikawa, T.; Koshihara, S.- y. *Inorg. Chem.* **2008**, *47*, 10217.

[105] *(a)* Lin, P.- H.; Sun, W.- B.; Yu, M.- F.; Li, G.- M.; Yan, P.- F.; Murugesu, M. *Chem. Commun.* **2011**, *47*, 10993. *(b)* Lin, P.- H.; Sun, W.- B.; Tian, Y.- M.; Yan, P.- F.; Ungur, L.; Chibotaru, L. F.; Murugesu, M. *Dalton Trans.* **2012**, *41*, 12349. *(c)* Westin, L. G.; Kritikos, M.; Caneschi, A. *Chem. Commun*. **2003**, 1012.

[106] Bartolomé, J.; Filoti, G.; Kuncser, V.; Schinteie, G.; Mereacre, V.; Anson, C. E.; Powell, A. K.; Prodius, D.; Turta, C. *Phys. Rev. B* **2009**, *80*, 014430.

[107] *(a)* Sabbatini, N.; Guardigli, M.; Lehn, J.- M. *Coord. Chem. Rev.* **1993**, *123*, 201. *(b)* Lehn, J.- M. *Angew. Chem. Int. Ed.* **1990**, *29*, 1304.

[108] *(a)* Binnemans, K. *Chem. Rev.* **2009**, *109*, 4283. *(b)* Bekiari, V.; Lianos, P. *Adv. Mater.* **2000**, *12*, 1603.

[109] For the photophysical properties of $saph^{2-}$ in solution, see: Kagkelari, A.; Bekiari, V.; Stathatos, E.; Papaefstathiou, G. S.; Raptopoulou, C. P.; Zafiropoulos, Th. F.; Lianos, P. *J. Luminesc.* **2009**, *129*, 578.

[110] Alexandropoulos, D. I.; Fournet, A.; Cunha-Silva, L.; Mowson, A. M.; Bekiari, V.; Christou, G.; Stamatatos, Th. C. *Inorg. Chem.* **2014**, *53*, 5420.

[111] Quahab, L. *"Multifunctional Molecular Materials"*, Pan Stanford Publishing, **2013**.

[112] Provent, C.; Williams, A. F. *"The Chirality of Polynuclear Transition Metal Complexes"* in Transition Metals in Supramolecular Chemistry, ed. J.- P. Sauvage, John Wiley & Sons Ltd, **1999**.

[113] *(a)* Cucinotta, G.; Perfetti, M.; Luzon, J.; Etienne, M.; Car, P.- E.; Caneschi, A.; Calvez, G.; Bernot, K.; Sessoli, R. *Angew. Chem. Int. Ed.* **2012**, *51*, 1606. *(b)* Boulon, M.- E.; Cucinotta, G.; Luzon, J.; Degl'Innocenti, C.; Perfetti, M.; Bernot, K.; Calvez, G.; Caneschi, A.; Sessoli, R. *Angew. Chem. Int. Ed.* **2013**, *52*, 350.

[114] *(a)* Bogani, L.; Wernsdorfer, W. *Nat. Mater.* **2008**, *7*, 179. *(b)* Vincent, R.; Klyatskaya, S.; Ruben, M.; Wernsdorfer, W.; Balestro, F. *Nature* **2012**, *488*, 357. *(c)* Urdampilleta, M.; Klyatskaya, S.; Cleuziou, J.- P.; Ruben, M.; Wernsdorfer, W. *Nat. Mater.* **2011**, *10*, 502.

[115] del Carmen Giménez-López, M.; Moro, F.; La Torre, A.; Gómez-García, C. J.; Brown, P. D.; van Slageren, J.; Khlobystov, A. N. *Nature Comm.* **2011**, *407*, 1415.

[116] *(a)* Mannini, M.; Pineider, F.; Sainctavit, P.; Danieli, C.; Otero, E.; Sciancalepore, C.; Talarisco, A. M.; Arrio, M.- A.; Cornia, A.; Gatteschi, D.; Sessoli, R. *Nat. Mater.* **2009**, *8*, 194. *(b)* Katoh, K.; Isshiki, H.; Komeda, T.; Yamashita, M. *Coord. Chem. Rev.* **2011**, *255*, 2124.

[117] *(a)* Lin, S.- Y.; Wernsdorfer, W.; Ungur, L.; Powell, A. K.; Guo, Y.- N.; Tang, J.; Zhao, L.; Chibotaru, L. F.; Zhang, H.- J. *Angew. Chem. Int. Ed.* **2012**, *51*, 12767. *(b)* Ke, H.; Gamez, P.; Zhao, L.; Xu, G.- F.; Xue, S.; Tang, J. *Inorg. Chem.* **2010**, *49*, 7549. *(c)* Tian, H.; Wang, M.; Zhao, L.; Guo, Y.- N.; Guo, Y.; Tang, J.; Liu, Z. *Chem. Eur. J.* **2012**, *18*, 442. *(d)* Ungur, L.; Langley, S. K.; Hooper, T. N.; Moubaraki, B.; Brechin, E. K.; Murray, K. S.; Chibotaru, L. F. *J. Am. Chem. Soc.* **2012**, *134*, 18554.

[118] *(a)* Yousaf, M.; Liu, Q.; Huang, J.; Qian, Y.; Chan, A. S.- C. *Inorg. Chem. Commun.* **2000**, *3*, 105. *(b)* Gang, Y.; Zhang, C.; Li, Y. J. *Suzhou University (Natural Science Edition)* **2008**, *24*, 69.

[119] APEX2, *Data Collection Software Version 2.1-RC13, Brucker AXS, Delf, The Netherlands,* **2006**.

[120] SAINT+, *Data Integration Engine v. 7.23b©,* **1997-2012***, Bruker AXS*, Madison, Wisconsin, USA.

[121] Sheldrick, G. M. *SADABS v.2.01, Bruker AXS Area Detector Scaling and Absorption Correction Program*, **1998**, Bruker AXS, Madison, Wisconsin, USA.

[122] Sheldrick, G. M. *SHELXS-97, Program for Crystal Structure Refinement, University of Göttingen*, **1997**.

[123] Spek, A. L. *J. Appl. Crystallogr.* **1990**, *46*, C34.

[124] Langley, S. K.; Moubaraki, B.; Murray, K. S. *Inorg. Chem.* **2012**, *51*, 3947.

[125] Hooper, T. N.; Inglis, R.; Palacios, M. A.; Nichol, G. S.; Pitak, M. B.; Coles, S. J.; Lorusso, G.; Evangelisti, M.; Brechin, E. K. *Chem. Commun.* **2014**, *50*, 3498.

[126] Koumousi, E. S.; Manos, M. J.; Lampropoulos, C.; Tasiopoulos, A. J.; Wernsdorfer, W.; Christou, G.; Stamatatos, Th. C. *Inorg. Chem.* **2010**, *49*, 3077.

[127] *(a)* Fleming, S.; Gutsche, C. D.; Harrowfield, J. M.; Ogden, M. I.; Skelton, B. W.; Stewart, D. F.; White, A. H. *Dalton Trans.* **2003**, 3319. *(b)* Guo, F.- S.; Guo, P.- H.; Meng, Z.- S.; Tong, M.- L. *Polyhedron* **2011**, *30*, 3079. *(c)* Bretonniere, Y.; Mazzanti, M.; Pecaut, J.; Olmstead, M. M. *J. Am. Chem. Soc.* **2002**, *124*, 9012. *(d)* Tang, X.- L.; Wang, W.- H.; Dou, W.; Jiang, J.; Liu, W.- S.; Qin, W.- W.; Zhang, G.- L.; Zhang, H.- R.; Yu, K.- B.; Zheng, L.- M. *Angew. Chem. Int. Ed.* **2009**, *48*, 3499. *(e)* Sharples, J. W.; Zheng, Y.- Z.; Tuna, F.; McInnes, E. J. L.; Collison, D. *Chem. Commun.* **2011**, *47*, 7650. *(f)* Taylor, S. M.; Sanz, S.; McIntosh, R. D.; Beavers, C. M.; Teat, S. J.; Brechin, E. K.; Dalgarno, S. J. *Chem.- Eur. J.* **2012**, *18*, 16014.

[128] Deacon, G. B.; Forsyth, C. M.; Junk, P. C.; Urbatsch, A. *Eur. J. Inorg. Chem.* **2010**, 2787.

[129] *(a)* Guo, Y.- N.; Chen, X.- H.; Xue, S.; Tang, J. *Inorg. Chem.* **2012**, *51*, 4035. *(b)* Miao, Y.- L.; Liu, J.- L.; Li, J.- Y.; Leng, J.- D.; Ou, Y.- C.; Tong, M.- L. *Dalton Trans.* **2011**, *40*, 10229.

(c) Chesman, A. S. R.; Turner, D. R.; Moubaraki, B.; Murray, K. S.; Deacon, G. B.; Batten, S. R. *Dalton Trans.* **2012**, *41*, 3751. *(d)* Tian, H.; Zhao, L.; Guo, Y.- N.; Guo, Y.; Tang, J.; Liu, Z. *Chem. Commun.* **2012**, *48*, 708. *(e)* Savard, D.; Lin, P.- H.; Burchell, T. J.; Korobkov, I.; Wernsdorfer, W.; Clérac, R.; Murugesu, M. *Inorg. Chem.* **2009**, *48*, 11748. *(f)* Chandrasekhar, V.; Bag, P.; Colacio, E. *Inorg. Chem.* **2013**, *52*, 4562. *(g)* Zangana, K. H.; Pineda, E. M.; Schnack, J.; Winpenny, R. E. P. *Dalton Trans.* **2013**, *42*, 14045. *(h)* Fang, M.; Zhao, H.; Prosvirin, A. V.; Pinkowicz, D.; Zhao, B.; Cheng, P.; Wernsdorfer, W.; Brechin, E. K.; Dunbar, K. R. *Dalton Trans.* **2013**, *42*, 14693.

[130] Yang, X.; Jones, R. A.; Wong, W.- K. *Chem. Commun.* **2008**, 3266.

[131] *(a)* Orfanoudaki, M.; Tamiolakis, I.; Siczek, M.; Lis, T.; Armatas, G. S.; Pergantis, S. A.; Milios, C. J. *Dalton Trans.* **2011**, *40*, 4793. *(b)* Winter, R. S.; Yan, J.; Busche, C.; Mathieson, J. S.; Prescimone, A.; Brechin, E. K.; Long, D.- L.; Cronin, L. *Chem. Eur. J.* **2013**, *19*, 2976.

[132] Bekiari, V.; Thiakou, K. A.; Raptopoulou, C. P.; Perlepes, S. P.; Lianos, P. J. *Luminesc.* **2008**, *128*, 481.

[133] *(a)* Zhang, P.; Zhang, L.; Wang, C.; Xue, S.; Lin, S.- Y.; Tang, J. *J. Am. Chem. Soc.* **2014**, *136*, 4484. *(b)* Pugh, T.; Chilton, N. F.; Layfield, R. A. *Angew. Chem. Int. Ed.* **2016**, *55*, 11082.

[134] *(a)* Rinehart, J. D.; Fang, M.; Evans, W. J.; Long, J. R. *Nature Chem.* **2011**, *3*, 538. *(b)* Habib, F.; Murugesu, M. *Chem. Soc. Rev.* **2013**, *42*, 3278. *(c)* Tuna, F.; Smith, C. A.; Bodensteiner, M.; Ungur, L.; Chibotaru, L. F.; McInnes, E. J. L.; Winpenny, R. E. P.; Collison, D.; Layfield, R. A. *Angew. Chem. Int. Ed.* **2012**, *51*, 6976.

[135] *(a)* Papatriantafyllopoulou, C.; Moushi, E. E.; Christou, G.; Tasiopoulos, A. J. *Chem. Soc. Rev.* **2016**, *45*, 1597. *(b)* Craig, G. A.; Murrie, M. *Chem. Soc. Rev.* **2015**, *44*, 2135. *(c)* Frost, J. M.; Harriman, K. L. M.; Murugesu, M. *Chem. Sci.* **2016**, *7*, 2470.

[136] *(a)* Neese, F.; Pantazis, D. *Faraday Discuss.* **2011**, *148*, 229. *(b)* Sessoli, R.; Powell, A. K. *Coord. Chem. Rev.* **2009**, *253*, 2328. *(c)* Feltham, H. L. C.; Brooker, S. *Coord. Chem. Rev.* **2014**, *276*, 1. *(d)* Gavey, E. L.; Rawson, J. M. *"Magnetic measurements"* in "Comprehensive Supramolecular Chemistry, II" (Eds. Atwood, J.; Barbour, L.), 2017 (in press).

[137] Kyatskaya, S.; Galán-Mascarós, J. R.; Bogani, L.; Hennrich, F.; Kappes, M.; Wernsdorfer, W.; Ruben, M. *J. Am. Chem. Soc.* **2009**, *131*, 15143.

[138] Denchev, V. S.; Boixo, S.; Isakov, S. V.; Ding, N.; Babbush, R.; Smelyanskiy, V.; Martinis, J.; Neven, H. *Phys. Rev. X* **2016**, *6*, 031015.

[139] Guo, Y.- N.; Xu, G.-F.; Guo, Y.; Tang, J. *Dalton Trans.* **2011**, *40*, 9953.

[140] *(a)* Liu, J.; Chen, Y.- C.; Liu, J.- L.; Vieru, V.; Ungur, L.; Jia, J.- H.; Chibotaru, L. F.; Lan, Y.; Wernsdorfer, W.; Gao, S.; Chen, X.- M.; Tong, M.- L. *J. Am. Chem. Soc.* **2016**, *138*, 5441. *(b)* Chen, Y.- C.; Liu, J.- L.; Ungur, L.; Liu, J.; Li, Q.- W.; Wang, L.- F.; Ni, Z.- P.; Chibotaru, L. F.; Chen, X.- M.; Tong, M.- L. *J. Am. Chem. Soc.* **2016**, *138*, 2829.

[141] Gavey, E. L.; Pilkington, M. *Coord. Chem. Rev.* **2015**, *296*, 125.

[142] Gavey, E. L.; Al Hareri, M.; Regier, J.; Carlos, L. D.; Ferreira, R. A. S.; Razavi, F. S.; Rawson, J. M.; Pilkington, M. *J. Mater. Chem. C*, **2015**, *3*, 7738.

[143] Perlepe, P. S.; Athanasopoulou, A. A.; Alexopoulou, K. I.; Raptopoulou, C. P.; Psycharis, V.; Escuer, A.; Perlepes, S. P.; Stamatatos, Th. C. *Dalton. Trans.* **2014**, *43*, 16605.

[144] Bruno, I. J.; Cole, J. C.; Edgington, P. R.; Kessler, M. K.; Macrae, C. F.; McCabe, P.; Pearson, J.; Taylor, R. *Acta Crystallogr., Sect. B* **2002**, *58*, 389.

[145] Bradenburg, K. *DIAMOND, Release 3.1f, Crystal Impact GbR*; Bonn, Germany, **2008**.

[146] Athanasopoulou, A. A.; Raptopoulou, C. P.; Escuer, A.; Stamatatos, Th. C. *RSC Adv.* **2014**, *4*, 12680.

[147] *(a)* Kuo, C.- J.; Holmberg, R. J.; Lin, P.- H. *Dalton Trans.* **2015**, *44*, 19758. *(b)* Anastasiadis, N. C.; Granadeiro, C. M.; Klouras, N.; Cunha-Silva, L.; Raptopoulou, C. P.; Psycharis, C.; Bekiari, V.; Balula, S. S.; Escuer, A.; Perlepes, S. P. *Inorg. Chem.* **2013**, *52*, 4145. *(c)* Comba, P.; Großhauser, M.; Klingeler, R.; Koo, C.; Lan, Y.; Müller, D.; Park, J.; Powell, A.; Riley, M. J.; Wadepohl, H. *Inorg. Chem.* **2015**, *54*, 11247.

[148] For representative examples, see: *(a)* Zhang, J.; Zhang, H.; Chen, Y.; Zhang, X.; Li, Y.; Liu, W.; Dong, Y. *Dalton Trans.* **2016**, *45*, 16463. *(b)* Zhang, L.; Jung, J.; Zhang, P.; Guo, M.; Zhao, L.; Tang, J.; Le Guennic, B. *Chem. Eur. J.* **2016**, *22*, 1392. *(c)* Guo, Y.; Xu, G.; Wernsdorfer, W.; Ungur, L.; Guo, Y.; Tang, J.; Zhang, H.; Chibotaru, L. F.; Powell, A. K. *J. Am. Chem. Soc.* **2011**, *133*, 11948. *(d)* Shen, H.; Wang, W.; Gao, H.; Cui, J. *RSC Adv.* **2016**, *6*, 34165. *(e)* Yang, F.; Zhou, Q.; Zeng, G.; Li, G.; Gao, L.; Shi, Z.; Feng, S. *Dalton Trans.* **2014**, *43*, 1238. *(f)* Wang, W.; Zhang, H.; Wang, S.; Shen, H.; Gao, H.; Cui, J.; Zhao, B. *Inorg. Chem.* **2015**, *54*, 10610. *(g)* Lin, P.; Burchell, T. J.; Clérac, R.; Murugesu, M. *Angew. Chem. Int. Ed.* **2008**, *47*, 8848. *(h)* Liang, L.; Peng, G.; Li, G.; Lan, Y.; Powell, A. K.; Deng, H. *Dalton Trans.* **2012**, *41*, 5816. *(i)* Sulway, S. A.; Layfield, R. A.; Tuna, F.; Wernsdorfer, W.; Winpenny, R. E. P. *Chem. Commun.* **2012**, *48*, 1508.

[149] *(a)* Zhang, H.; Lin, S.- Y.; Xue, S.; Wang, C.; Tang, J. *Dalton Trans.* **2014**, *43*, 6262. *(b)* Wang, Y.; Han, C.; Zhang, Y.; Liu, Q.; Liu, C.; Yin, S. *Inorg. Chem.* **2016**, *55*, 5578. *(c)* Peng, Y.; Mereacre, V.; Baniodeh, A.; Lan, Y.; Schlageter, M.; Kostakis, G. E.; Powell, A. K. *Inorg. Chem.* **2016**, *55*, 68. *(d)* Ke, H.; Zhang, S.; Li, X.; Wei, Q.; Xie, G.; Wang, W.; Chen, S. *Dalton Trans.* **2015**, *44*, 21025. *(e)* Bag, P.; Rastogi, C. K.; Biswas, S.; Sivakumar, S.; Mereacre, V.; Chandrasekhar, V. *Dalton Trans.* **2015**, *44*, 4328. *(f)* Song, Y.; Luo, F.; Luo, M.; Liao, Z.; Sun, G.; Tian, X.; Zhu, Y.; Yuan, Z.; Liu, S.; Xu, W.; Feng, X. *Chem. Commun.* **2012**, *48*, 1006. *(g)*

Ma, Y.; Xu, G.- F.; Yang, X.; Li, L.- C.; Tang, J.; Yan, S.- P.; Cheng, P.; Liao, D.- Z. *Chem. Commun.* **2010**, *46*, 8264. *(h)* Sun, L.; Zhang, S.; Qiao, C.; Chen, S.; Yin, B.; Wang, W.; Wei, Q.; Xie, G.; Gao, S. *Inorg. Chem.* **2016**, *55*, 10587. *(i)* Yutronkie, N. J.; Kühne, I. A.; Korobkov, I.; Brusso, J. L.; Murugesu, M. *Chem. Commun.* **2016**, *52*, 677. *(j)* Hutchings, A.- J.; Habib, F.; Holmberg, R. J.; Korobkov, I.; Murugesu, M. *Inorg. Chem.* **2014**, *53*, 2102. *(k)* Lin, P.- H.; Korobkov, I.; Burchell, T. J.; Murugesu, M. *Dalton Trans.* **2012**, *41*, 13649. *(l)* Guo, Y.- N.; Chen, X.- H.; Xue, S.; Tang, J. *Inorg. Chem.* **2011**, *50*, 9705.

[150] *(a)* Llunell, M.; Casanova, D.; Girera, J.; Alemany, P.; Alvarez, S. *SHAPE*, version 2.0, Barcelona, Spain, **2010**. *(b)* Zabrodsky, H.; Peleg, S.; Avnir, D. *J. Am. Chem. Soc.* **1993**, *115*, 8278.

[151] Ruiz-Martinez, A.; Casanova, D.; Alvarez, S. *Chem. Eur. J.* **2008**, *14*, 1291.

[152] Chilton, N. F.; Collison, D.; McInnes, E. J. L.; Winpenny, R. E. P.; Soncini, A. *Nature Commun.* **2013**, *4*, 1.

[153] Chilton, N. F.; Anderson, R. P.; Turner, L. D.; Soncini, A.; Murray, K. S. *J. Comput. Chem.* **2013**, *34*, 1164.

[154] Costes, J. P.; Titos-Padilla, S.; Oyarzabal, I.; Gupta, T.; Duhayon, C.; Rajaraman, G.; Colacio, E. *Chem. Eur. J.* **2015**, *21*, 15785.

[155] Demir, S.; Zadrozny, J. M.; Nippe, M.; Long, J. R. *J. Am. Chem. Soc.* **2012**, *134*, 18546.

[156] Costes, J. P.; Titos-Padilla, S.; Oyarzabal, I.; Gupta, T.; Duhayon, C.; Rajaraman, G.; Colacio, E. *Inorg. Chem.* **2016**, *55*, 4428.

[157] *(a)* Cole, K. S.; Cole, R. H. *"Dispersion and Absorption in Dielectrics I. Alternating Current Characteristics", J. Chem. Phys.* **1941**, *9*, 341-351. *(b)* Grahl, M.; Kotzler, J.; Sessler, I *J. Magn. Magn. Mater.* **1990**, *90-1*, 187.

[158] *(a)* Watanabe, A.; Yamashita, A.; Nakano, M.; Yamamura, T.; Kajiwara, T. Multi-Path *Chem. Eur. J.* **2011**, *17*, 7428. *(b)* Anwar, M. U.; Thompson, L. K.; Dawe, L. N.; Habib, F.; Murugesu, M. *Chem. Commun.* **2012**, *48*, 4576. *(c)* Habib, F.; Brunet, G.; Vieru, V.; Korobkov, I.; Chibotaru, L. F.; Murugesu, M. *J. Am. Chem. Soc.* **2013**, *135*, 13242.

[159] *(a)* Habib, F.; Long, J.; Lin, P.- H.; Korobkov, I.; Ungur, L.; Wernsdorfer, W.; Chibotaru, L. F.; Murugesu, M. *Chem. Sci.* **2012**, *3*, 2158. *(b)* Xue, S.; Guo, Y.- N.; Ungur, L.; Tang, J.; Chibotaru, L. F. *Chem. Eur. J.* **2015**, *21*, 14099.

[160] *(a)* Malmqvist, P.; Roos, B. O.; Schimmelpfennig, B. *Chem. Phys. Lett.* **2002**, *357*, 230. *(b)* Chibotaru, L. F.; Ungur, L. *J. Chem. Phys.* **2012**, *137*, 064112.

[161] *(a)* Mukherjee, S.; Lu, J.; Velmurugan, G.; Singh, S.; Rajaraman, G.; Tang, J.; Ghosh, S. K. *Inorg. Chem.* **2016**, *55*, 11283. *(b)* Ungur, L.; Chibotaru, L. F. *Phys. Chem. Chem. Phys.* **2011**, *13*, 20086.

[162] Chibotaru, L. F.; Ungur, L.; Aronica, C.; Elmoll, H.; Pilet, G.; Luneau, D. *J. Am. Chem. Soc.* **2008**, *130*, 12445.

[163] Marx, R.; Moro, F.; Dorfel, M.; Ungur, L.; Waters, M.; Jiang, S. D.; Orlita, Taylor, M. J.; Frey, W.; Chibotaru, L. F.; van Slageren, J. *Chem. Sci.* **2014**, *5*, 3287.

[164] Roos, B. O.; Veryazov, V.; V. Widmark, P.- O. *Theor. Chem. Acc.* **2004**, *111*, 345.

[165] Reiher, M. *WIREs Comput. Mol. Sci.* **2012**, *2*, 139.

[166] Ungur, L.; Thewissen, M.; Costes, J.- P.; Wernsdorfer, W.; Chibotaru, L. F. *Inorg. Chem.* **2013**, *52*, 6328.

[167] Gagliardi, L.; Lindh, R.; Karlström, G. *J. Chem. Phys.* **2004**, *121*, 4494.

[168] Ungur, L.; Chibotaru, L. F. *SINGLE_ANISO and POLY_ANISO*; KU Leuven, **2013**.

[169] *(a)* Lines, M. E. *J. Chem. Phys.* **1971**, *55*, 2977-2984. *(b)* Griffith, J. S. *Phys. Rev.* **1963**, *132*, 316.

Appendix

- IR spectra of the organic ligands and complexes **1-13**.
- NMR spectra of the sachH_2-based ligands.

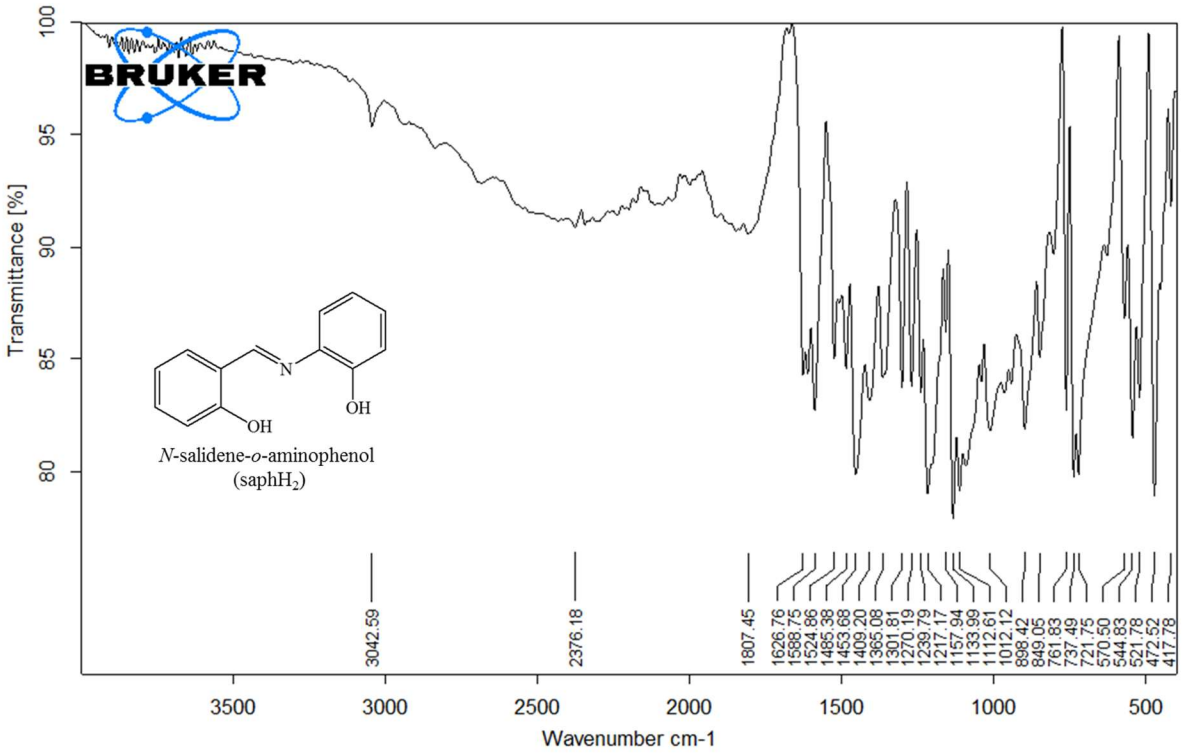

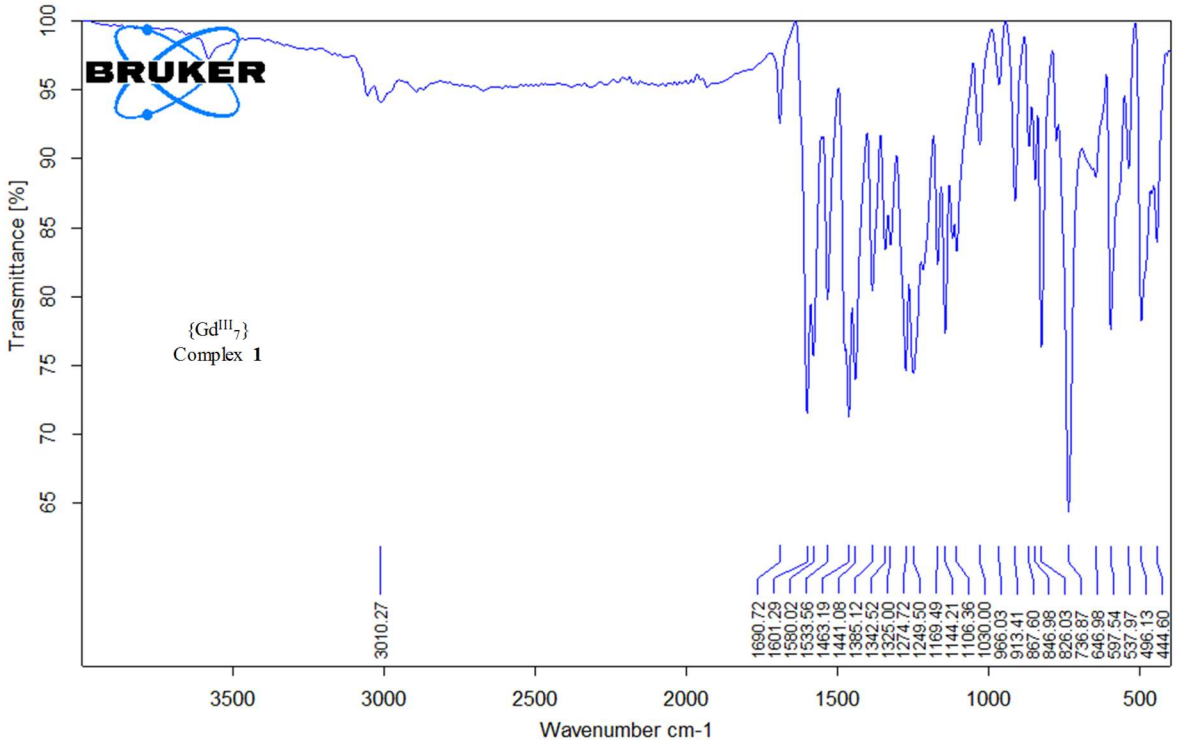
BRUKER
Transmittance [%]
100
95
90
85
80
75
70
65
{Gd$^{III}_{7}$}
Complex 1
3010.27
1690.72
1601.29
1580.02
1533.56
1463.19
1441.08
1385.12
1342.52
1325.00
1274.72
1249.50
1169.49
1144.21
1106.36
1030.00
966.03
913.41
867.60
846.98
826.03
736.87
646.98
597.54
537.97
496.13
444.60
3500
3000
2500
2000
1500
1000
500
Wavenumber cm-1

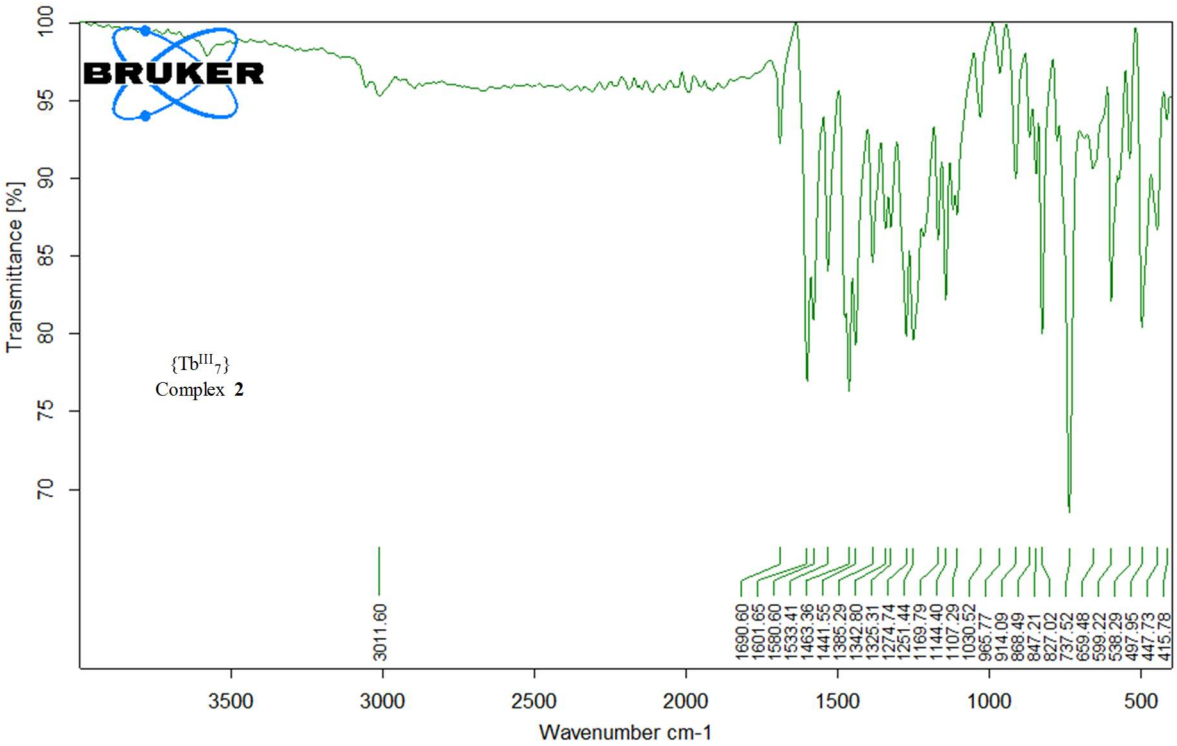
BRUKER
Transmittance [%]
100
95
90
85
80
75
70
{Tb$^{III}_{7}$}
Complex 2
3011.60
1690.60
1601.65
1580.60
1533.41
1463.36
1441.55
1385.29
1342.80
1325.31
1274.74
1251.44
1169.79
1144.40
1107.29
1030.52
965.77
914.09
868.49
847.21
827.02
737.52
659.48
599.22
538.29
497.95
447.73
415.78
3500
3000
2500
2000
1500
1000
500
Wavenumber cm-1

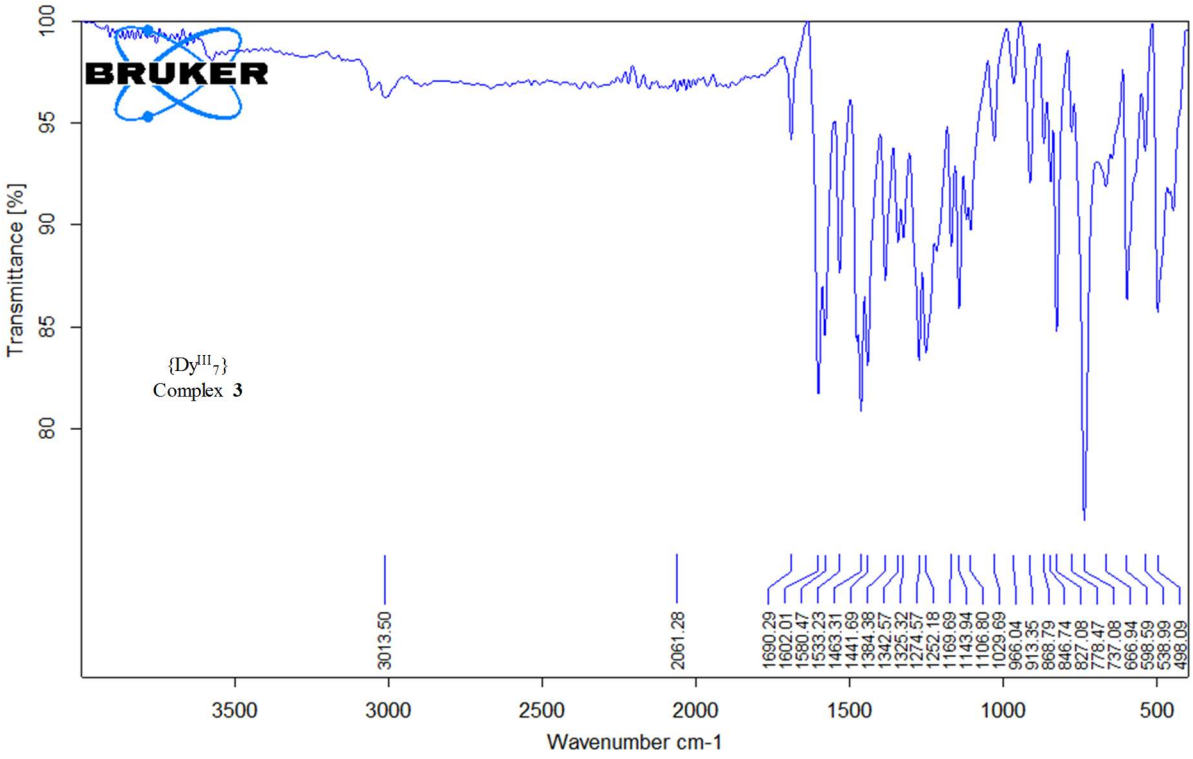
BRUKER
Transmittance [%]
100
95
90
85
80
{Dy$^{III}_7$}
Complex 3
3013.50
2061.28
1690.29
1602.01
1580.47
1533.23
1463.31
1441.69
1384.38
1342.57
1325.32
1274.57
1252.18
1169.69
1143.94
1106.80
1029.69
966.04
913.35
868.79
846.74
827.08
778.47
737.08
666.94
598.59
538.99
498.09
3500
3000
2500
2000
1500
1000
500
Wavenumber cm-1

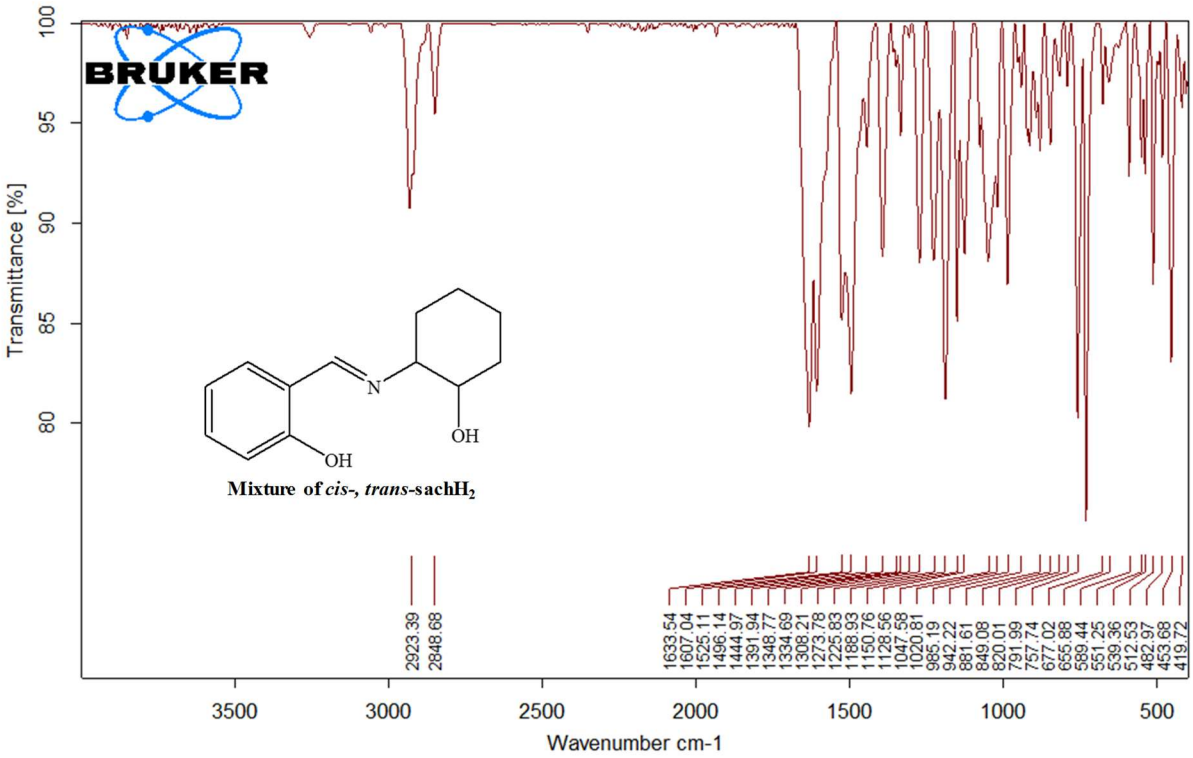
BRUKER
Transmittance [%]
100
95
90
85
80
N
OH
OH
Mixture of *cis*-, *trans*-sachH$_2$
2923.39
2848.68
1633.54
1607.04
1525.11
1496.14
1444.97
1391.94
1348.77
1334.69
1308.21
1273.78
1225.83
1188.93
1150.76
1128.56
1047.58
1020.81
985.19
942.22
881.61
849.08
820.01
791.99
757.74
677.02
655.88
589.44
551.25
539.36
512.53
482.97
453.68
419.72
3500
3000
2500
2000
1500
1000
500
Wavenumber cm-1

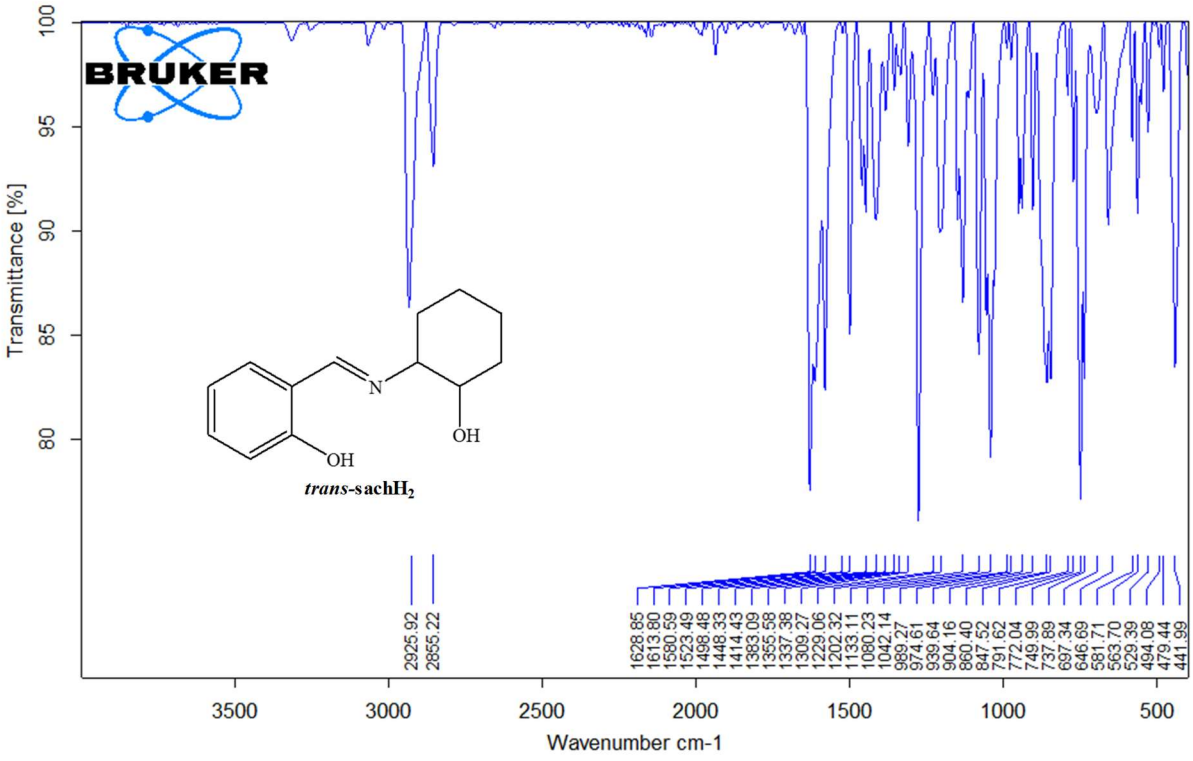
BRUKER
Transmittance [%]
100
95
90
85
80
OH
N
OH
trans-sachH2
2925.92
2855.22
1628.85
1613.80
1580.59
1523.49
1498.48
1448.33
1414.43
1383.09
1355.58
1337.38
1309.27
1229.06
1202.32
1133.11
1080.23
1042.14
999.27
974.61
939.64
904.16
860.40
847.52
791.62
772.04
749.99
737.89
697.34
646.69
581.71
563.70
529.39
494.08
479.44
441.99
3500
3000
2500
2000
1500
1000
500
Wavenumber cm-1

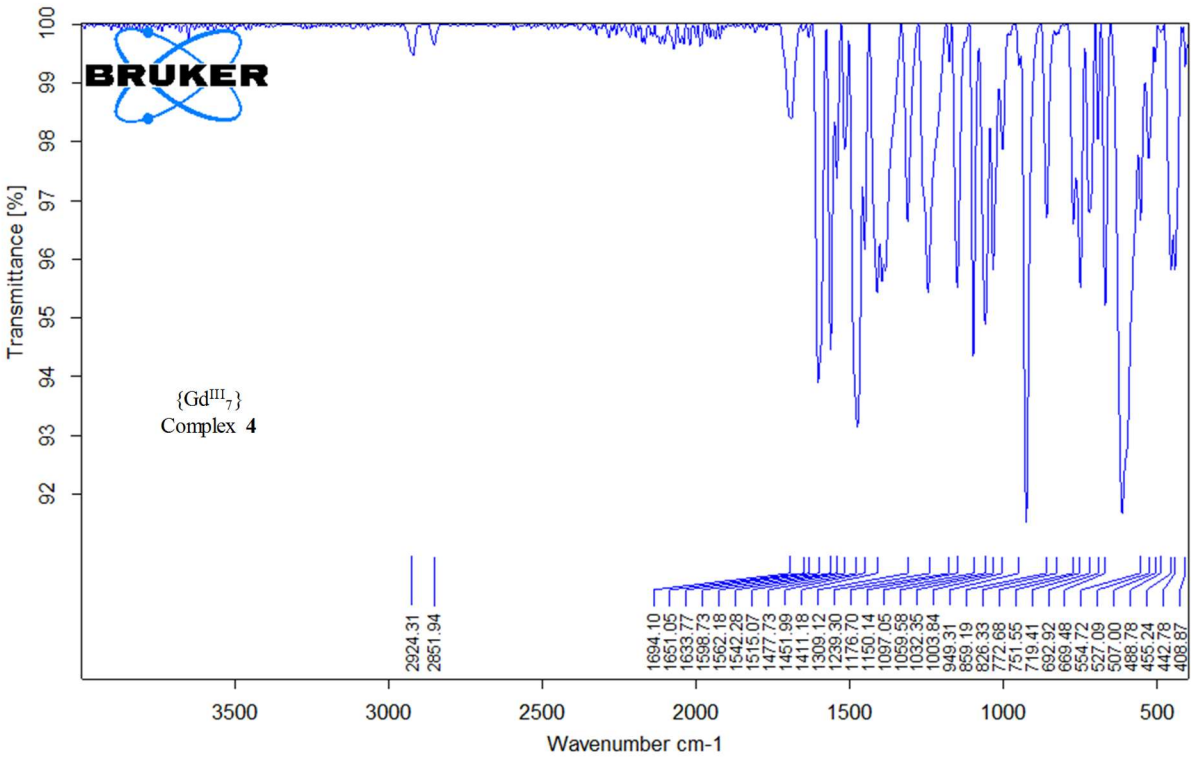
BRUKER
Transmittance [%]
100
99
98
97
96
95
94
93
92
{Gd^III_7}
Complex 4
2924.31
2851.94
1694.10
1651.05
1633.77
1598.73
1562.18
1542.28
1515.07
1477.73
1451.99
1411.18
1309.12
1239.30
1176.70
1150.14
1097.05
1059.98
1032.35
1003.84
949.31
859.19
826.33
772.68
751.55
719.41
692.92
669.48
554.72
527.09
507.00
488.78
455.24
442.78
408.87
3500
3000
2500
2000
1500
1000
500
Wavenumber cm-1

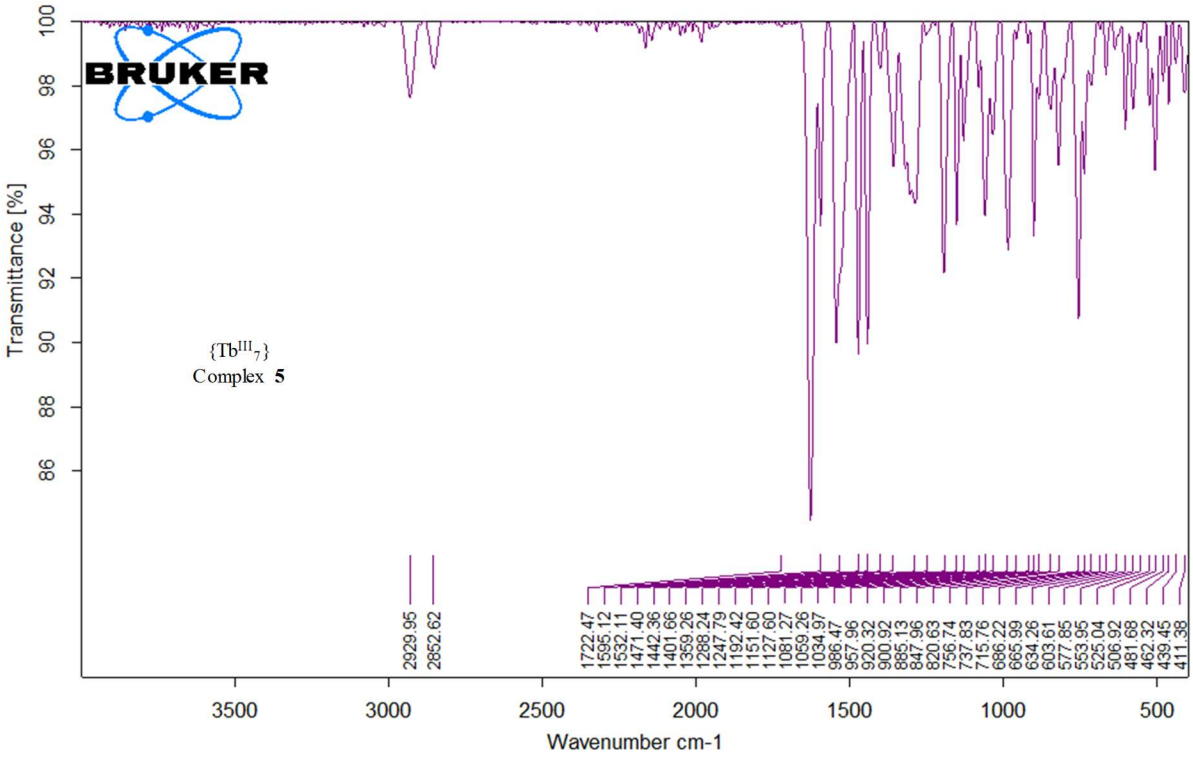
BRUKER
Transmittance [%]
100
98
96
94
92
90
88
86
{Tb$^{III}_7$}
Complex 5
2929.95
2852.62
1722.47
1595.12
1532.11
1471.40
1442.36
1401.66
1359.26
1288.24
1247.79
1192.42
1151.60
1127.60
1081.27
1059.26
1034.97
986.47
957.96
920.32
900.92
885.13
847.96
820.63
756.74
737.83
715.76
686.22
665.99
634.26
603.61
577.85
553.95
525.04
506.92
481.68
462.32
439.45
411.38
3500
3000
2500
2000
1500
1000
500
Wavenumber cm-1

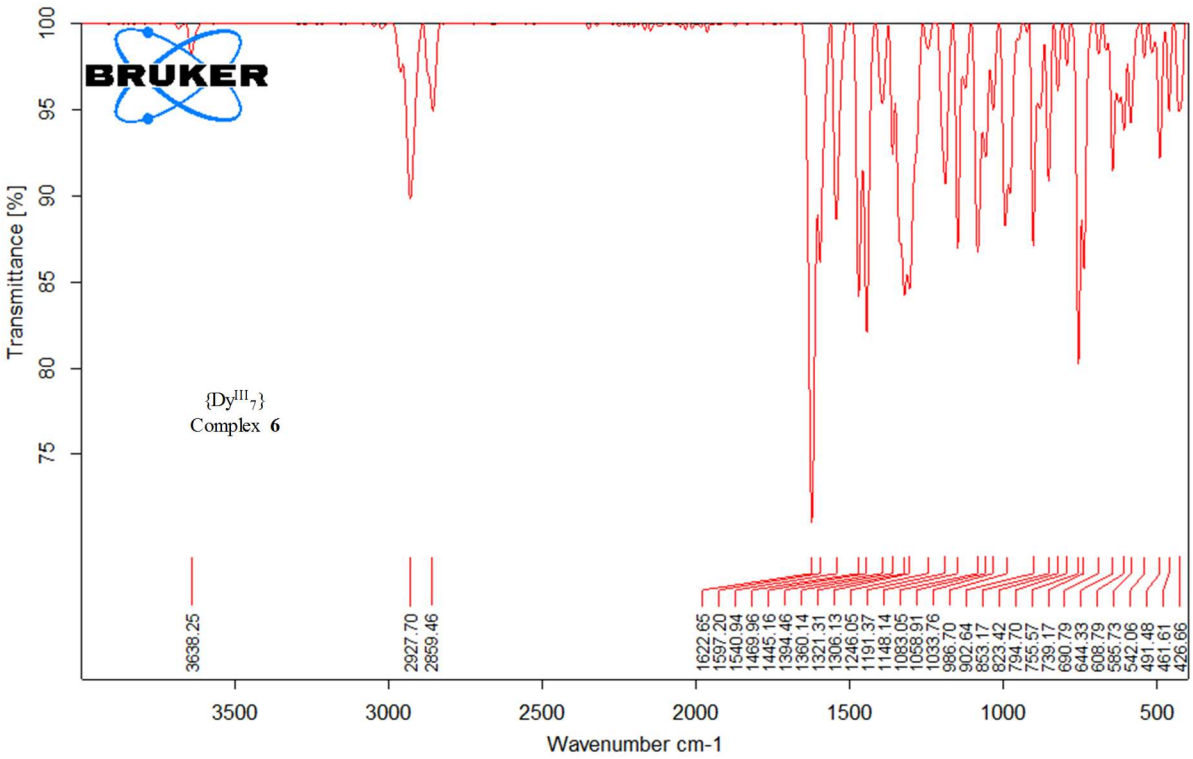
BRUKER
Transmittance [%]
100
95
90
85
80
75
{Dy$^{III}_7$}
Complex 6
3638.25
2927.70
2859.46
1622.65
1597.20
1540.94
1469.96
1445.16
1394.46
1360.14
1321.31
1306.13
1246.05
1191.37
1148.14
1083.05
1058.91
1033.76
986.70
902.64
853.17
823.42
794.70
755.57
739.17
690.79
644.33
608.79
585.73
542.06
491.48
461.61
426.66
3500
3000
2500
2000
1500
1000
500
Wavenumber cm-1

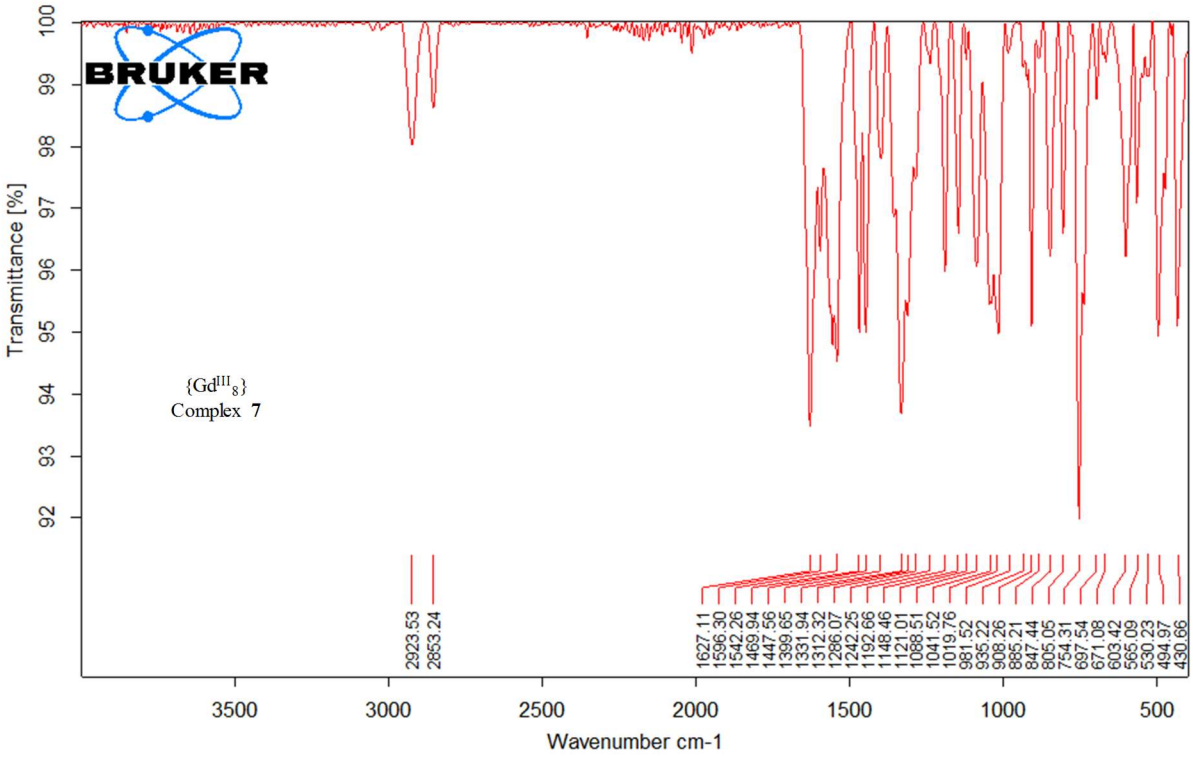
BRUKER
Transmittance [%]
100
99
98
97
96
95
94
93
92
{Gd$^{III}_8$}
Complex 7
2923.53
2853.24
1627.11
1596.30
1542.26
1469.94
1447.56
1399.65
1331.94
1312.32
1286.07
1242.25
1192.66
1148.46
1121.01
1088.51
1041.52
1019.76
981.52
935.22
908.26
885.21
847.44
805.05
754.31
697.54
671.08
603.42
565.09
530.23
494.97
430.66
3500
3000
2500
2000
1500
1000
500
Wavenumber cm-1

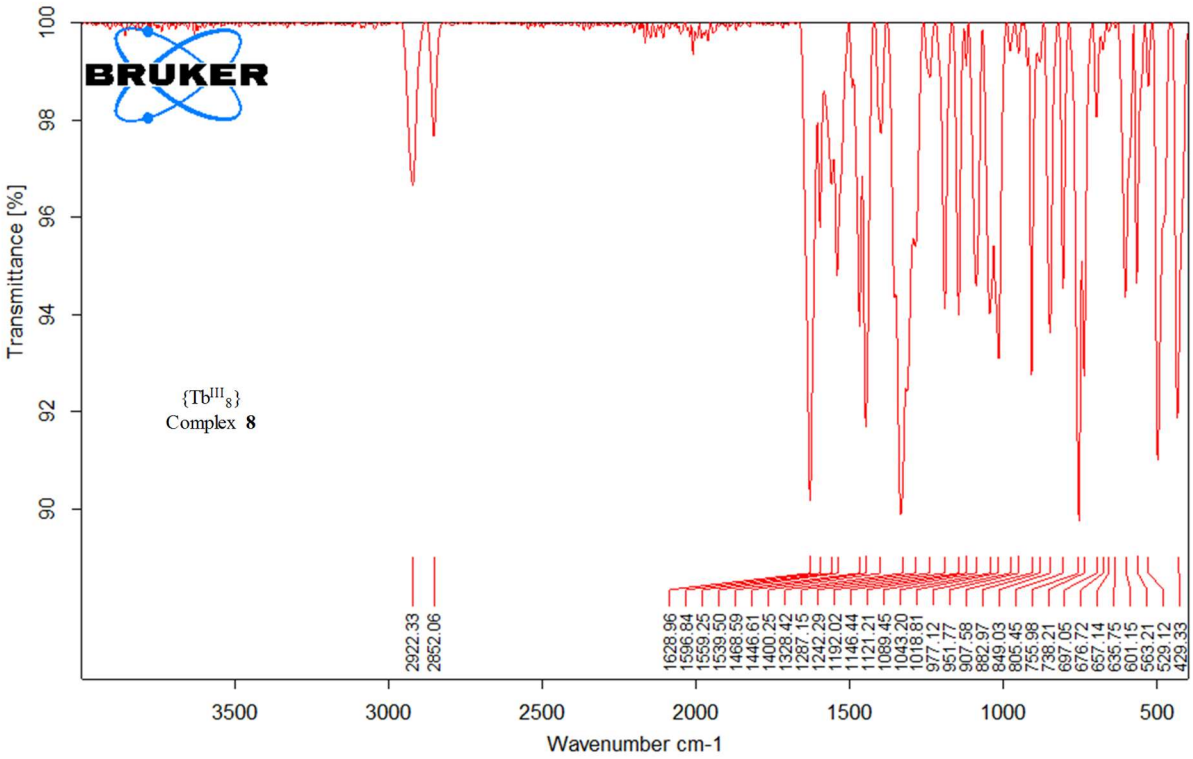
BRUKER
Transmittance [%]
100
98
96
94
92
90
{Tb$^{III}_8$}
Complex 8
2922.33
2852.06
1628.96
1596.84
1559.25
1539.50
1468.59
1446.61
1400.25
1328.42
1287.15
1242.29
1192.02
1146.44
1121.21
1089.45
1043.20
1018.81
977.12
951.77
907.58
882.97
849.03
805.45
755.98
738.21
697.05
676.72
657.14
635.75
601.15
563.21
529.12
429.33
3500
3000
2500
2000
1500
1000
500
Wavenumber cm-1

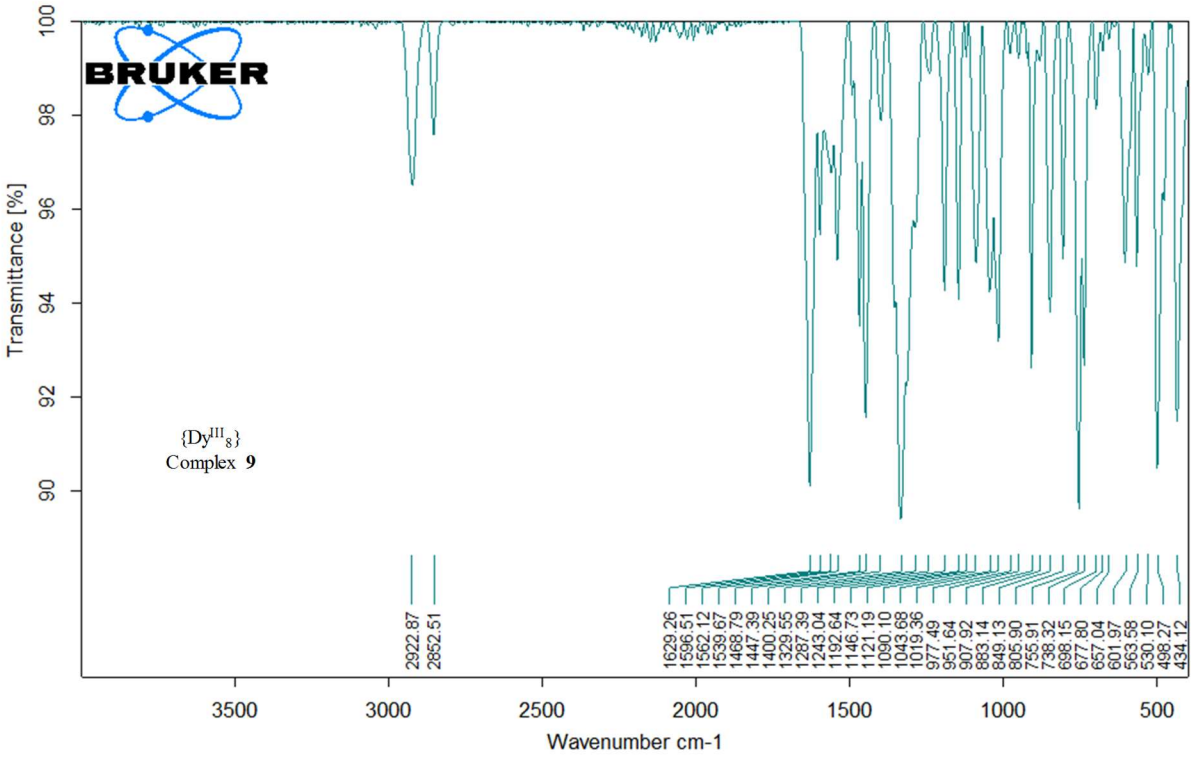
BRUKER
Transmittance [%]
100
98
96
94
92
90
{Dy$^{III}_8$}
Complex 9
2922.87
2852.51
1629.26
1596.51
1562.12
1539.67
1468.79
1447.39
1400.25
1329.55
1287.39
1243.04
1192.64
1146.73
1121.19
1090.10
1043.68
1019.36
977.49
951.64
907.92
883.14
849.13
805.90
755.91
738.32
698.15
677.80
657.04
601.97
563.58
530.10
498.27
434.12
3500
3000
2500
2000
1500
1000
500
Wavenumber cm-1

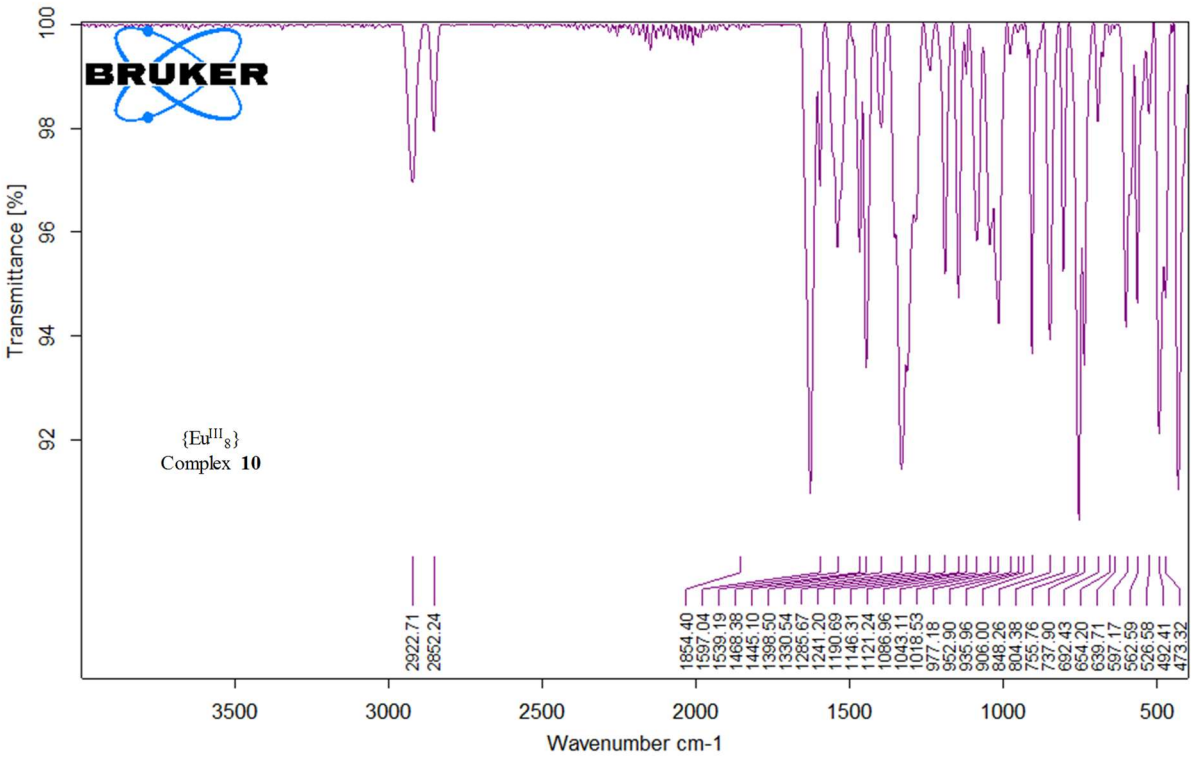
BRUKER
Transmittance [%]
100
98
96
94
92
{Eu$^{III}_8$}
Complex 10
2922.71
2852.24
1854.40
1597.04
1539.19
1468.38
1445.10
1398.50
1330.54
1285.67
1241.20
1190.69
1146.31
1121.24
1086.96
1043.11
1018.53
977.18
952.90
935.96
906.00
848.26
804.38
755.76
737.90
692.43
654.20
639.71
597.17
562.59
526.58
492.41
473.32
3500
3000
2500
2000
1500
1000
500
Wavenumber cm-1

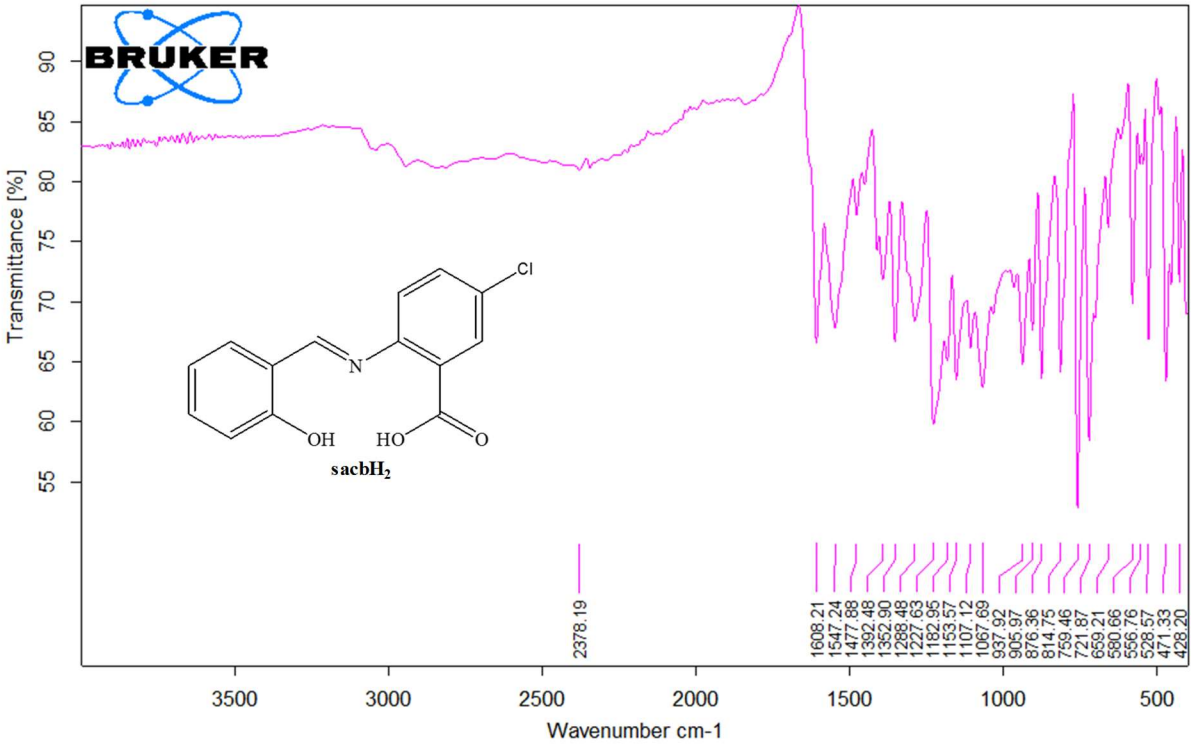
BRUKER
Transmittance [%]
Wavenumber cm-1
Cl
N
OH
HO
O
sacbH2
2378.19
1608.21
1547.24
1477.88
1392.48
1352.90
1288.48
1227.63
1182.95
1153.57
1107.12
1067.69
937.92
905.97
876.36
814.75
759.46
721.87
659.21
580.66
556.76
528.57
471.33
428.20

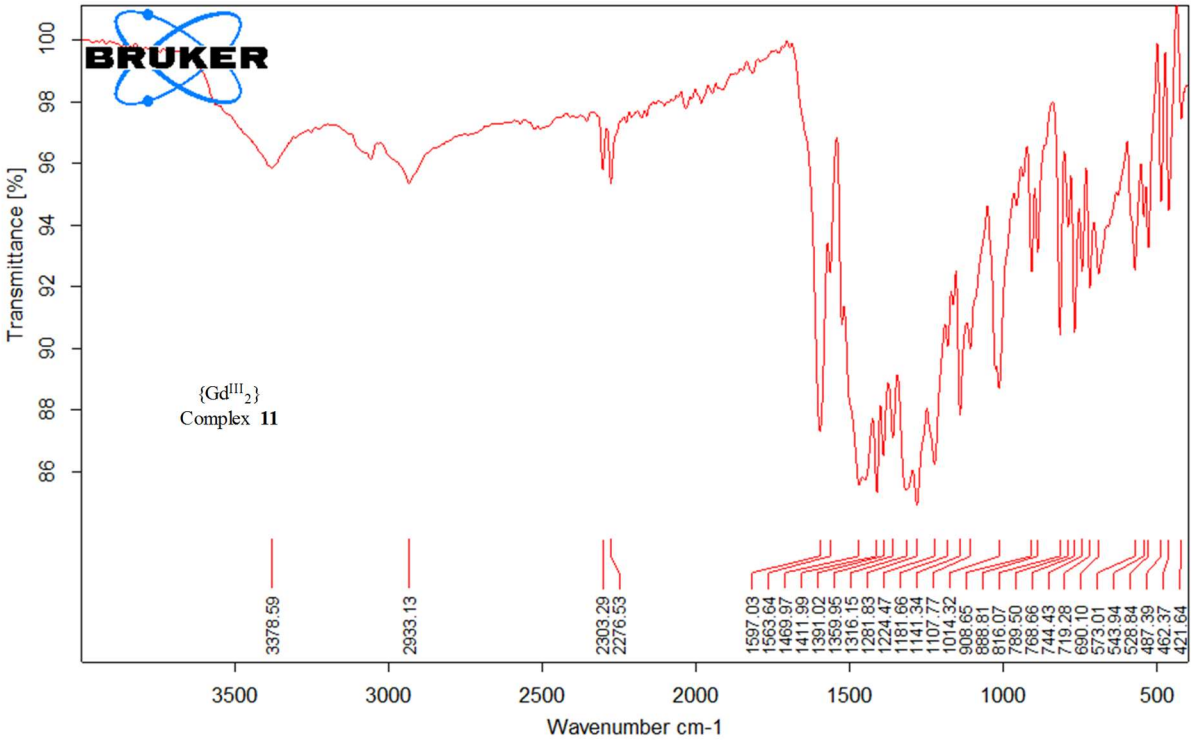
BRUKER
Transmittance [%]
Wavenumber cm-1
{Gd^III_2}
Complex 11
3378.59
2933.13
2303.29
2276.53
1597.03
1563.64
1469.97
1411.39
1391.02
1359.95
1316.15
1281.83
1224.47
1181.66
1141.34
1107.77
1014.32
908.65
888.81
816.07
789.50
768.66
744.43
719.28
690.10
573.01
543.94
528.84
487.39
462.37
421.64

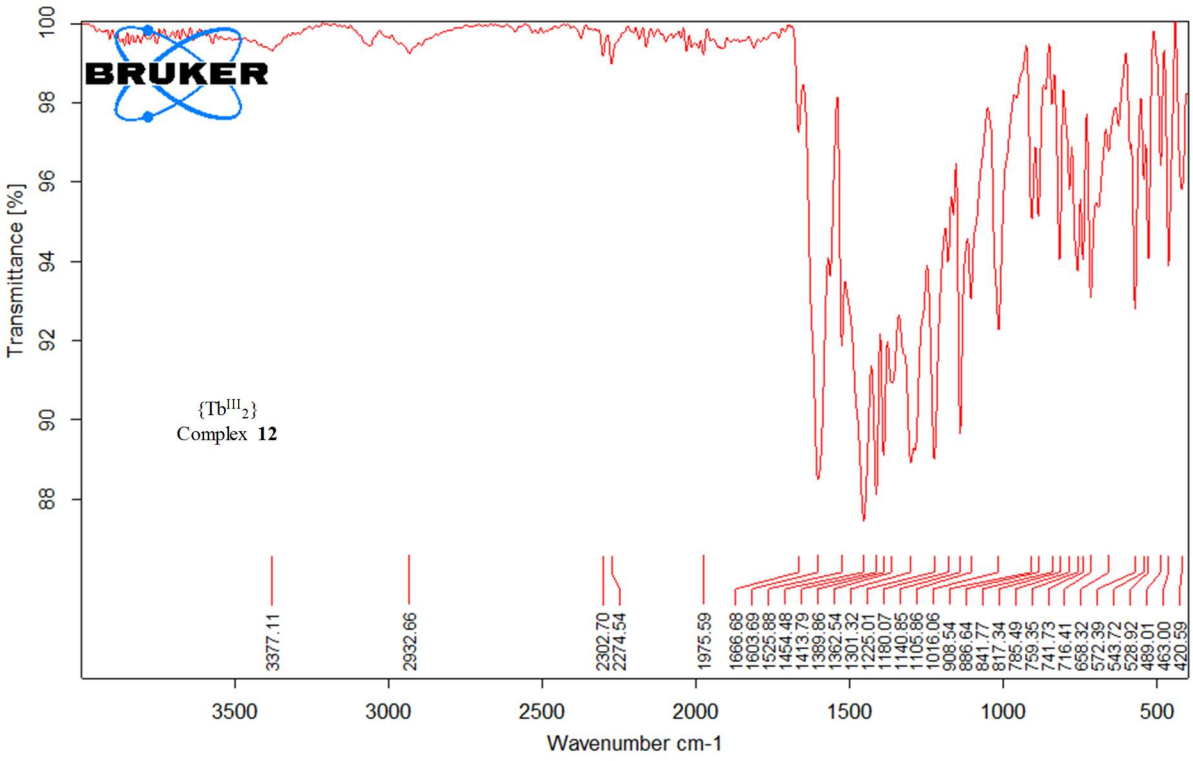
BRUKER
Transmittance [%]
100
98
96
94
92
90
88
{Tb$^{III}_2$}
Complex 12
3377.11
2932.66
2302.70
2274.54
1975.59
1666.68
1603.69
1525.88
1454.48
1413.79
1389.86
1362.54
1301.32
1225.01
1180.07
1140.85
1105.86
1016.06
908.54
886.64
841.77
817.34
785.49
759.35
741.73
716.41
658.32
572.39
543.72
528.92
489.01
463.00
420.59
3500
3000
2500
2000
1500
1000
500
Wavenumber cm-1

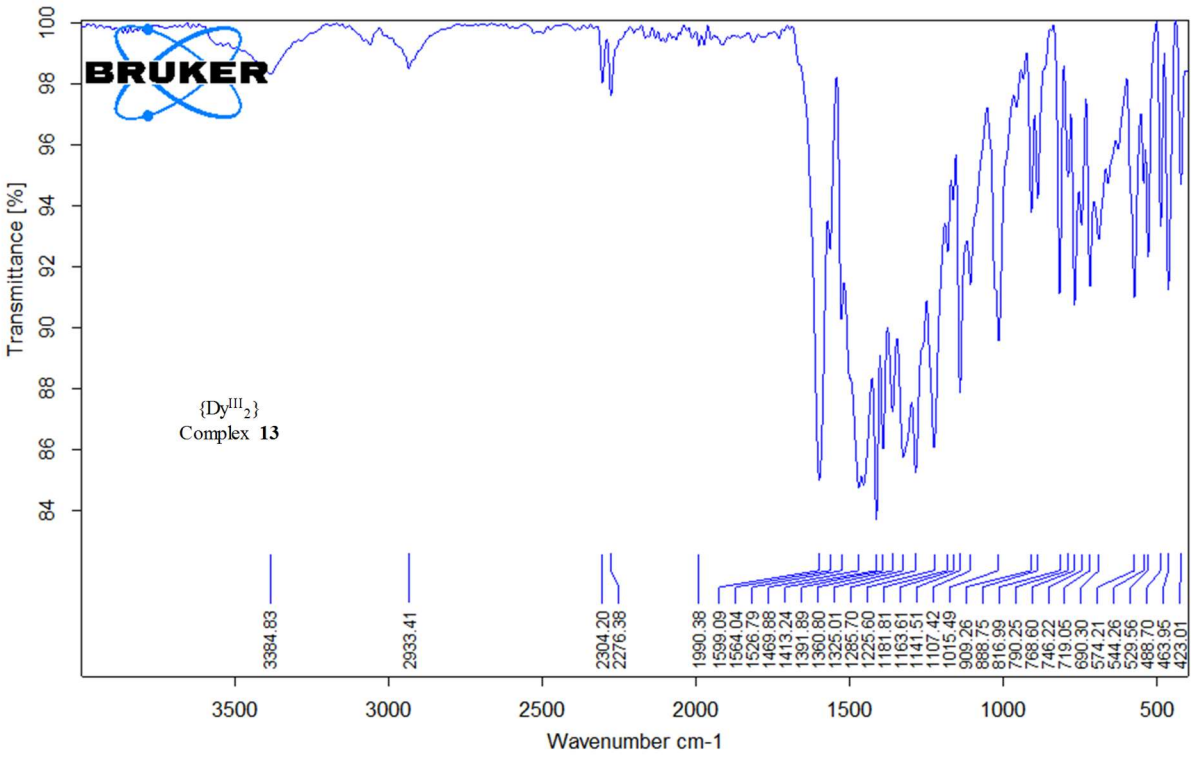
BRUKER
Transmittance [%]
100
98
96
94
92
90
88
86
84
{Dy$^{III}_2$}
Complex 13
3384.83
2933.41
2304.20
2276.38
1990.38
1599.09
1564.04
1526.79
1469.88
1413.24
1391.89
1360.80
1325.01
1285.70
1225.60
1181.81
1163.61
1141.51
1107.42
1015.49
909.26
888.75
816.99
790.25
768.60
746.22
719.05
690.30
574.21
544.26
529.56
488.70
463.95
423.01
3500
3000
2500
2000
1500
1000
500
Wavenumber cm-1

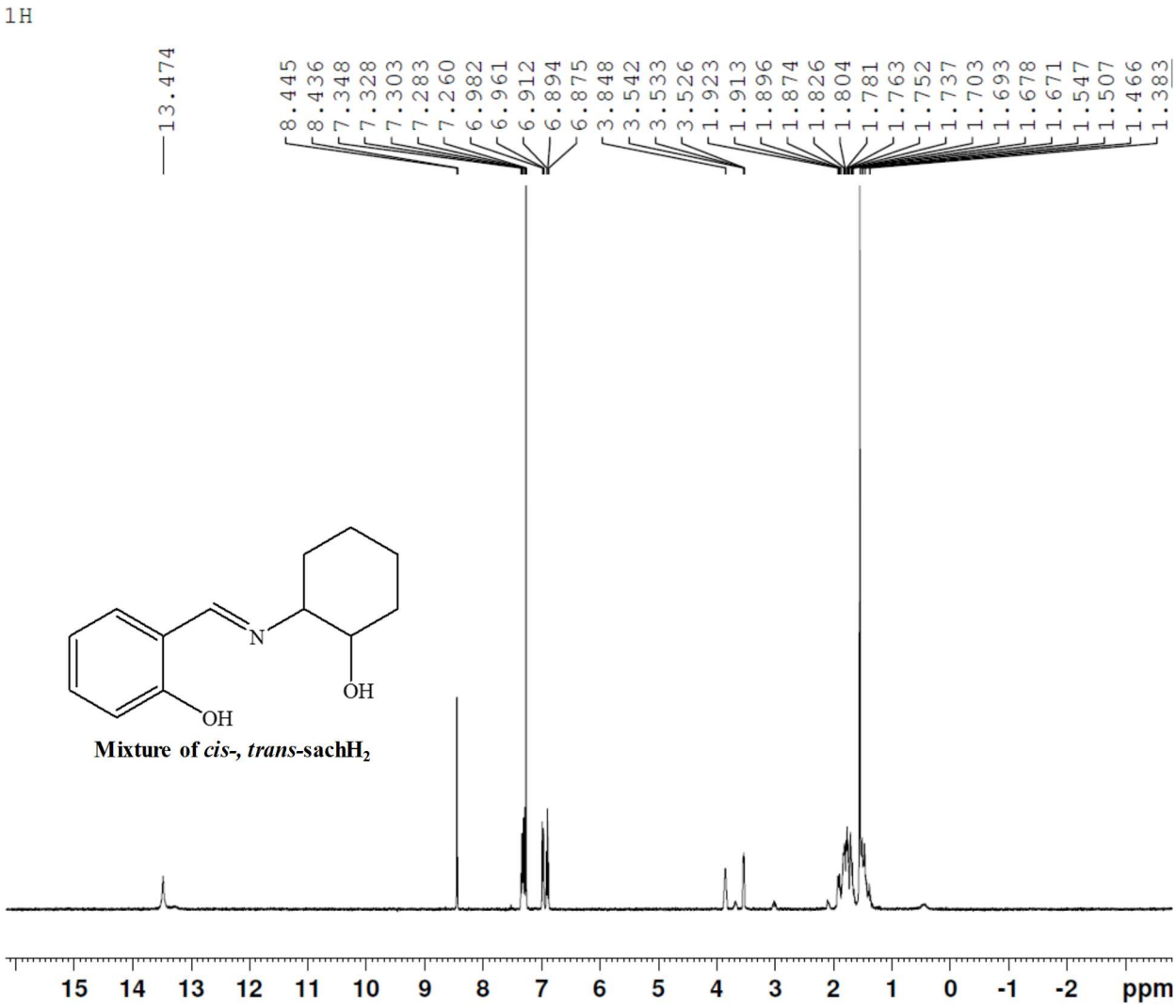

Mixture of *cis*-, *trans*-sachH$_2$

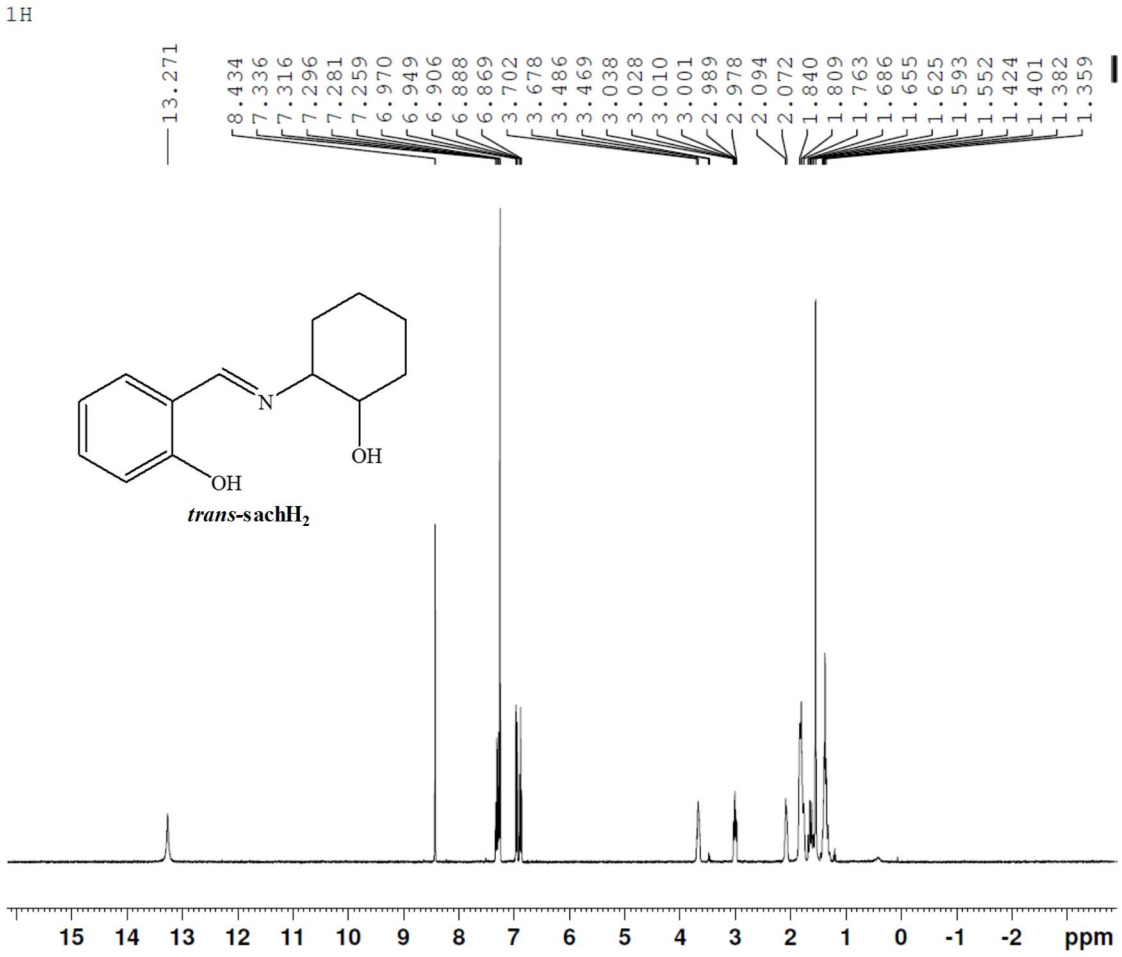

***trans*-sachH$_2$**